# Polymorphism in Post-Dichalcogenide Two-Dimensional Materials

*Hadallia Bergeron,[1] Dmitry Lebedev,[1] and Mark C. Hersam[1,2,3,*]*

[1]Department of Materials Science and Engineering, Northwestern University, Evanston Illinois 60208, United States

[2]Department of Chemistry, Northwestern University, Evanston Illinois 60208, United States

[3]Department of Electrical and Computer Engineering, Northwestern University, Evanston Illinois 60208, United States

*Corresponding author: m-hersam@northwestern.edu

## Abstract

Two-dimensional (2D) materials exhibit a wide range of atomic structures, compositions, and associated versatility of properties. Furthermore, for a given composition, a variety of different crystal structures (*i.e.*, polymorphs) can be observed. Polymorphism in 2D materials presents a fertile landscape for designing novel architectures and imparting new functionalities. The objective of this Review is to identify the polymorphs of emerging 2D materials, describe their polymorph-dependent properties, and outline methods used for polymorph control. Since traditional 2D materials (e.g., graphene, hexagonal boron nitride, and transition metal dichalcogenides) have already been studied extensively, the focus here is on polymorphism in post-dichalcogenide 2D materials including group III, IV, and V elemental 2D materials, layered group III, IV, and V metal chalcogenides, and 2D transition metal halides. In addition to providing a comprehensive survey of recent experimental and theoretical literature, this Review identifies the most promising

opportunities for future research including how 2D polymorph engineering can provide a pathway to materials by design.

# Table of Contents

# 1. Introduction

## *1.1. Polymorphism*

Polymorphism is a fundamental principle of nature and a widespread phenomenon affecting various scientific disciplines. In the context of crystallography, polymorphism is the "occurrence of different crystal structures for the same chemical entity."[1] Herein, the "chemical entity" can include small variances in chemical composition to account for non-stoichiometric defective or doped compounds. Readers may also be familiar with polymorphism from the field of genetics, where it refers to variants in a particular DNA sequence,[2] or in organic chemistry, where it describes supramolecular isomerism, which has been the subject of concentrated research efforts in pharmacology.[3–5] Whereas in the aforementioned fields the importance of polymorph engineering is well-established, this concept is still incipient for two-dimensional (2D) materials. However, 2D materials exhibit rich polymorphism that has profound implications for higher-order materials engineering in the atomically thin limit. Polymorphism is at the root of crystal engineering and the materials science paradigm – *i.e.*, to control structure is to control properties.

Therefore, polymorph engineering offers a unique pathway to the grand challenge of rational design of 2D materials with predefined architectures and functionalities.

The manifestation of polymorphism presents both a challenge and an opportunity. For instance, competing polymorphs can make the synthesis of pure phases difficult as is the case for several 2D materials discussed here (*e.g.*, borophene and indium selenide), where single-phase synthesis has not yet been mastered. On the other hand, polymorphism provides opportunities for additional structure and property control beyond chemical composition, thus enabling the discovery and engineering of novel 2D polymorphs. Similar to bulk materials, various processing conditions exert structural control over 2D polymorphic materials including temperature, pressure, and related environmental variables. However, the 2D regime also offers additional environmental variables to influence the occurrence of polymorphs, particularly the dominance of surface effects (*e.g.*, the influence of thickness or substrates) in the 2D limit. Consequently, structures that are not observed in the bulk can be stabilized in the 2D regime, which implies fundamentally different opportunities for polymorph engineering in atomically thin materials.

Polymorphism encompasses several different categories of structural variation. The most intuitive notion of polymorphism is when a single composition can form different crystal structures of entirely different symmetry and periodicity. The archetypal example of this is bulk elemental carbon, which can take the form of graphite (space group $P6_3/mmc$, lattice constants $a$ = 2.46 Å and $c$ = 6.71 Å) and diamond (space group $Fd\bar{3}m$, $a$ = 3.56 Å) among others.[6] The various structures of carbon are also referred to as "allotropes," a term used to describe polymorphs of elemental materials.[1] More subtle forms of polymorphism also exist such as polytypism. Polytypism applies to close-packed or layered materials, where polytypes are characterized by constituent layers with identical structures but different periodicities perpendicular to the layer

plane (*i.e.*, different stacking).[7] Since van der Waals (vdW) layered materials have weak interlayer interactions, polytypism is a commonly observed and highly relevant form of polymorphism for multilayer 2D materials. Taking the example of graphite, the hexagonal (2H) polytype with a bilayer unit cell accounts for most naturally occurring crystals, but a higher-energy rhombohedral modification with a trilayer unit cell can be obtained *via* mechanical grinding.[8] For 2D materials, this concept can be taken further to artificial polytypes, as was recently demonstrated in twisted bilayer graphene. By stacking two graphene layers with a small twist angle (magic angle of ~1.1 $^{o}$), a moiré pattern appears that results in the formation of flat bands[9,10] and unique correlated electronic states,[11,12] including superconductivity.[13,14] The aforementioned examples of carbon polymorphism are instances where the various forms can coexist over a range of experimental conditions. In contrast, some polymorphs are effectively exclusive to different environmental conditions. For example, $sp^2$-coordinated glassy carbon can be compressed into an amorphous high-pressure $sp^3$-coordinated allotrope, but unlike diamond, it rapidly recovers its original $sp^2$ coordination upon return to ambient conditions.[15]

Implicit in the discussion of polymorphism is the concept of (meta)stability. It is possible to observe higher-energy metastable structures other than the ground state structure(s) under the right conditions. The energetic discrepancies between polymorphs can range from effectively degenerate to barely experimentally feasible, but compounds recognized as being concomitantly polymorphic generally exhibit structures with similar lattice energies. In addition, kinetic influences are also crucial to the observation of polymorphs. Kinetics often dictate whether polymorphs are observed to coexist or are exclusive, and whether individual structures are effectively stable (*i.e.*, long-lived metastable state) or transiently observed.

## *1.2. Polymorphism in Post-Dichalcogenide 2D Materials*

This Review explores the identity and control of 2D polymorphs in the recent post-dichalcogenide 2D literature – namely, recently emerging 2D materials following the advent of the transition metal dichalcogenides (TMDs) such as $MoS_2$, $WS_2$, $MoSe_2$, $WSe_2$, and $MoTe_2$. TMDs also exhibit polymorphism with their structures and phase engineering already having been detailed in previous reviews.[16–22] In contrast, the focus of this Review is 2D polymorphism in group III, IV, and V elemental materials, layered group III, IV, and V metal chalcogenides, and vdW transition metal halides (TMHs). For each class of materials, the emphasis is placed on polymorphs that are 2D or vdW-layered in nature, rather than non-layered three-dimensional (3D) structures. The covered 2D materials exhibit a wide range of polymorphic variations including entirely different monolayer structures, multilayer stacking polytypes, as well as polymorphs that coexist under the same conditions or are mutually exclusive. Furthermore, 2D materials also demonstrate substrate-induced monolayer reconstructions such that many monolayer materials have calculated ground state freestanding forms that are altered when interacting with a substrate, resulting in novel polymorphs in the ultrathin limit. The increased contribution of surface energy in 2D materials also enables thickness-induced structural transformations. In addition to substrate and thickness effects, more conventional means of polymorph control such as manipulation of synthesis conditions (*e.g.*, temperature and pressure) or post-synthesis processing (*e.g.*, thermal annealing) will be discussed. We do not discuss 2D structural variations arising from complex ground states or other complex physical phenomena (*e.g.*, charge density wave formation or superconductivity), even though the formation of such a ground state may result in commensurate or incommensurate lattice distortions that could fall under the definition of polymorphism. Currently, the 2D materials literature generally does not refer to these phases as polymorphs and instead treats them from a physical perspective.[20,23–25]

For each material class, the 2D structures and polymorph-dependent properties are presented, followed by a discussion of methods for achieving polymorph control. The Review includes both experimental and theoretical work, which are interwoven throughout. The Review concludes with a discussion on outstanding challenges and opportunities in polymorph engineering for 2D materials by design.

## *1.3. Experimental Distinction of 2D Polymorphs*

Resolving the structure of 2D polymorphs often presents its own challenge. In particular, X-ray diffraction (XRD), which is commonly employed for bulk crystals, has limited applicability to the ultrathin and platelet nature of 2D films or individual exfoliated crystals, reducing both the number and intensity of Bragg peaks for indexing. Polytypes tend to be particularly difficult to distinguish using diffraction experiments since they often show similarities in overall symmetry in addition to identical intralayer structures. Since the occurrence of stacking faults is also associated with polytypic crystals, it is important to reliably differentiate between polymorphs and local defects. Techniques that have proven to be particularly beneficial in clarifying the polymorphs of 2D materials include grazing incidence XRD, scanning tunneling microscopy (STM), selected area electron diffraction (SAED), and transmission electronic microscopy (TEM), especially high-angle annular dark-field (HAADF) scanning TEM (STEM). These techniques are especially powerful when paired with other methods that provide complementary information, such as Raman spectroscopy and second harmonic generation (SHG). Furthermore, many 2D materials are currently limited to synthesis and characterization in ultrahigh vacuum conditions, such that the elucidation of their structures is almost exclusively reliant on STM. In these cases, carbon monoxide (CO)-functionalized atomic force microscopy has been a powerful tool in interpreting the observed 2D structures.

## *1.4. Nomenclature*

The nomenclature used to denote polymorphs of an element or compound is not uniformly standardized, which can lead to confusion. As Herbstein aptly puts it, the research community generally treats "well-intentioned suggestions with disdain, leaving its practitioners to sort out the confusion for themselves."[1] The nomenclature for 2D polymorphs is no exception. To minimize ambiguity, this Review uses descriptive nomenclature that invokes the structure discussed, in addition to providing the space group for each polymorph. This nomenclature breaks down into two main approaches: (1) the use of structural prototypes as reference points (*e.g.*, "$CdI_2$-type"), (2) the use of descriptive names such as "hexagonal buckled" (*hb*) or "asymmetric washboard" (*aw*). This practice helps identify common structures among 2D materials. For example, this nomenclature makes clear that the group V elements and group IV metal chalcogenides both exhibit similar structures (*hb* and *aw*, specifically), which might not be apparent under different conventions. Furthermore, the naming and recognition of polymorphs is highly dependent upon literature precedent, so alternate names for single polymorphs that appear in the literature are provided whenever possible. In particular, other common naming schemes utilize colors, *Strukturbericht* designation, or lowercase Greek letters (which are usually given alphabetically in order of discovery, stability, or temperature). For instance, the most stable structure of arsenic can be described as grey arsenic, A7-arsenic, or $\alpha$-arsenic. In this Review, the structure will be referred to as *hb*-arsenic since it is composed of layers of hexagonal buckled atoms. Despite this effort at consistency in nomenclature, some minor exceptions will be employed: (1) notations for overlayer structures are given as the overlayer unit cell periodicity with respect to the substrate unit cell ($n \times m$), and (2) vacancy-concentration-based nomenclature is used for borophene and will be introduced in the corresponding section.

Polytypes also have their own nomenclature. Here, Ramsdell notation[26] is used in addition to ABC notation. The former takes the form nZ, where n is given by the number of vdW layers in a unit cell and Z is given by the crystal and lattice systems of the structure: H indicates a hexagonal crystal and lattice systems, T indicates a trigonal crystal system with a hexagonal Bravais lattice, and R indicates a trigonal crystal system with a rhombohedral Bravais lattice.[27] Additionally, subscripts can be used in Ramsdell notation to denote different stacking orders of the same unit cell size and symmetry (*e.g.*, $2H_a$, $2H_b$).[7,28] In this Review, the Ramsdell notation is used with respect to the vdW layers of a material (*i.e.*, the ensemble of strongly bonded atomic sheets separated by vdW gaps), in contrast to some literature that refers to the individual atomic layers within a vdW layer.[29] Additionally, ABC notation is employed to denote the relationship between vdW layers in the unit cell of a polytype. Using graphite as an example, the most common polytype is known as 2H-graphite, where two atomic layers of carbon are stacked in a translationally offset AB sequence to form a unit cell of a hexagonal lattice. Furthermore, the expanded "AbACaC" notation is used to detail the relative position of cations (usually lowercase letter) and anions (usually uppercase letter) in different vdW layers. This notation is commonly used for TMDs. For example, AbACaC stacking implies that the unit cell consists of two layers in the out-of-plane direction, namely an AbA and a CaC layer separated by a vdW gap. The layers are shifted or rotated such that cations in the latter layer (a) are located on top of anions in the former layer (A). Therefore, AbACaC stacking indicates three distinct columns of atoms in the out-of-plane direction, whereas an AbABaB stacking pattern would only have two.

Lastly, while the terms "dimorphs" or "trimorphs" are sometimes used to denote the occurrence of two or three polymorphic forms of a compound, respectively, this Review foregoes this specification and instead uses the general term "polymorphs" to denote any number of

polymorphic variations. This terminology is more accommodating to the future discovery of additional structures for a given compound.

# 2. Elemental 2D Materials

## *2.1. Group III Elements*

With the synthesis of 2D boron (i.e., 'borophene') in 2015,[30,31] the 2D material family expanded to include group III elements. Beyond boron, potential structures and synthesis conditions have been investigated for other 2D group III elements such as Al,[32,33] Ga,[34] and In,[35] but the literature is quite limited. Consequently, borophene currently represent the most reliably synthesized monolayer group III element.

### 2.1.1. Structures and properties of 2D boron polymorphs

In the bulk, boron exhibits complex structures and several different polymorphs, although none of these structures are layered. The complexity of boron structures is attributed to its trivalent electronic configuration, forming highly diverse bonding motifs that have attracted the interest of researchers for decades.[36,37] As a result, several 2D boron polymorphs were predicted far before the experimental realization of borophene using molecular beam epitaxy (MBE) on Ag(111).[30,31] The borophene structures that have been synthetically realized thus far are based on the triangular buckled lattice shown in **Figure 1,** which has a calculated unit cell of dimension $a$ = 1.62 Å and $b$ = 2.85 Å with a buckling height of 0.86 Å.[38] While this 2D structure was believed to be the most stable for almost a decade,[39,40] later work determined that a periodically defective derivative of the triangular buckled lattice, known as the α sheet, was more energetically favorable.[41,42] The α sheet is a flat structure composed of hollow hexagons (HHs) with a vacancy concentration $v = m/N$ =

1/9 (**Figure 1**), where $m$ is the number of HHs for $N$ triangular lattice sites. The structures of borophene are often referred to by their HH concentration, such that the pristine triangular buckled structure and the α sheet correspond to $v_0$ and $v_{1/9}$ phases, respectively. The α sheet has a calculated unit cell of dimension $a = b = 5.05$ Å, and Wu *et al.* found that a slight buckling of ± 0.17 Å makes the structure more stable.[43] Since the HH regions act as electron acceptors and the pristine triangular regions acts as donors, the two motifs complement each other to form a more stable overall structure.[41]

Subsequent studies found polymorphs with higher vacancy concentrations ($v > 1/9$) to be slightly more energetically favorable.[43–46] A computational study by Penev *et al.* indicated that buckling is present for structures of $v < 1/9$, while higher HH concentrations are flat,[44] although slight buckling can occur when placed on a substrate.[47] Calculations show that HH-based structures are separated by small energetic differences, implying that coexistence of polymorphs can be expected at finite temperatures.[44,46] Indeed, the observed MBE-synthesized structures contain HHs, with the most commonly reported structures being the $\beta_{12}$ sheet ($v_{1/6}$) and the $\chi_3$ sheet ($v_{1/5}$) on Ag(111). The $v_{1/6}$ and $v_{1/5}$ phases are also referred to as the S1 and S2 phases, respectively. The HH concentration notation is used in this text to identify the polymorphs shown in **Figure 1**. However, multiple HH arrangements can exist for a certain HH concentration.[43] In the case of borophene on Ag(111), the $v_{1/6}$ and $v_{1/5}$ exhibit the specific arrangements of the $\beta_{12}$ and $\chi_3$ sheets shown in **Figure 1**. The $v_{1/6}$ monolayer has a rectangular unit cell (calculated lattice parameters of $a = 2.92$ Å, $b = 5.08$ Å), while the $v_{1/5}$ monolayer has a hexagonal unit cell (calculated lattice parameters of $a = b = 4.55$ Å).[38] While the exact structures of the borophene phases on Ag(111) were ambiguous when initially observed with conventional STM, Liu *et al.* later used atomic force microscopy with a CO-functionalized tip to directly image the spatial distribution of HHs.[48] The

authors determined that the $v_{1/6}$ and $v_{1/5}$ models account for all observed phases on Ag(111), with crystallographic rotations with respect to the substrate giving rise to the various STM observations. Overall, experimental efforts have confirmed polymorphism in borophene, and the challenge now lies in realizing synthetic conditions that enable phase purity or periodic polymorph superlattices.

The 2D boron polymorphs observed experimentally are all metallic in character, which is consistent with multiple computational studies.[44,41,30,49,50] A potential exception is the α sheet ($v_{1/9}$), which Wu *et al.* calculated to be a narrow bandgap semiconductor,[43] but the experimental observation of this structure requires further investigation.[51] In a study by Silvestre *et al.*, the $v_0$ structure was found to exhibit a more anisotropic band structure than the $v_{1/6}$ and $v_{1/5}$ structures.[52] Additionally, the authors found that the π* states in the $v_{1/6}$ structure are more localized than in the $v_{1/5}$ structure. However, the distinctions are subtle and experimental measurements show that the $v_{1/6}$ and $v_{1/5}$ structures on Ag(111) are electronically similar.[30,48] Evidence of Dirac fermions in the $v_{1/6}$ and $v_{1/5}$ structures has also been reported,[53,54] although a large mismatch exists for the $v_{1/6}$ structure between the observed and predicted Dirac point with respect to the Fermi level. Gupta *et al.* proposed that the observation of the Dirac-like dispersion in the $v_{1/6}$ phase on Ag(111) is due to a predicted topologically nontrivial Dirac nodal line.[55] The authors also predicted the existence of two Dirac cones in $v_{1/6}$ borophene, which become gapped on Ag(111).

Superconductivity has also been predicted for the $v_0$, $v_{1/9}$, $v_{1/6}$, and $v_{1/5}$ borophene structures with the transition temperature being polymorph dependent.[56–58] While the predicted transition temperatures are around 10-20 K in the freestanding monolayers, the interaction with an Ag(111) substrate could reduce the values down to below 5 K. The presence of Dirac fermions[59,60] and superconductivity[61] is also predicted for other borophene polymorphs that have not yet observed experimentally but could be stabilized by a metal substrate. The HH concentration also has an

effect on the thermal and mechanical properties of borophene.[62–64] In particular, the $v_{1/6}$ polymorph has been calculated to possess an exceptionally high in-plane modulus to bending stiffness ratio (568 $nm^{-2}$), indicating a highly flexible material. Additionally, reports by Kulish *et al.*[65] and Xiang *et al.*[66] detail the polymorph-dependent chemical properties of borophene, which include surface reactivity and metal ion adsorption and migration. Kulish *et al.* found that the $v_{1/6}$ phase is generally more reactive than the $v_{1/9}$ and $v_0$ phases, while Xiang *et al*. contend that the $v_0$ phase shows more anisotropic metal ion migration pathways in comparison to other borophene structures. For further reading on the synthesis, properties, and applications of borophene, please see the reviews by Mannix *et al.,*[36] Zhang *et al.*,[37] and Li *et al.*[67]

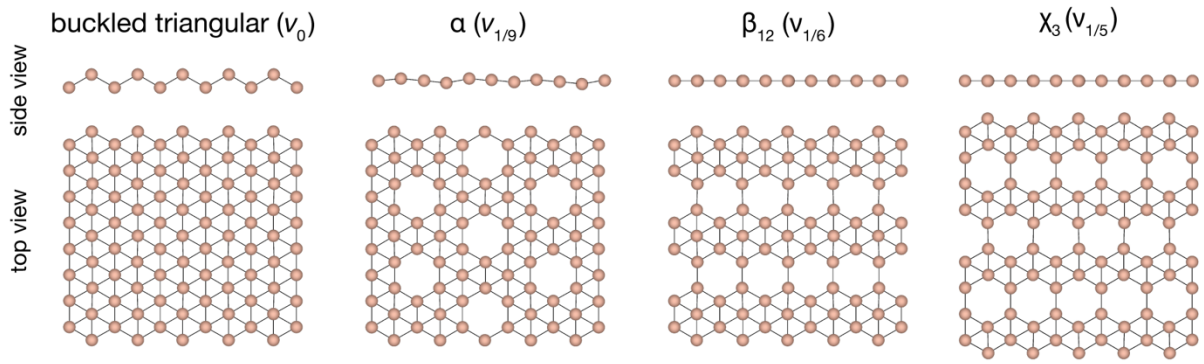


**Figure 1. 2D polymorphs of borophene.** Commonly reported monolayer polymorphs of borophene. The $v_{1/6}$ and $v_{1/5}$ structures have been experimentally observed on Ag(111). Modification of the buckled triangular ($v_0$) structure with various HH concentrations results in the other presented polymorphs.

## 2.1.2. Polymorph control of 2D boron

**2.1.2.1. Substrates.** Since 2D boron is metastable, its growth requires the presence of a stabilizing substrate. So far, metallic substrates have played that role and are thus critical in experimentally accessing 2D borophene polymorphs. In particular, borophene is thought to be stabilized by the charge transfer and chemical hybridization provided by metal substrates.[68] Silver was predicted as a suitable substrate prior to its use in the first borophene growth experiments. Liu *et al*. had

suggested the use of Ag or Au based on the lack of boride formation and sufficiently strong interaction with boron for surface adhesion while still promoting a 2D, rather than 3D, growth mode for boron superstructures.[69] Furthermore, depending on the type of metal, different HH concentrations are favored.[68] In this manner, the substrate can provide a borophene polymorph selection mechanism. Since Ag, Cu, and Ni donate electrons to borophene, these substrates are expected to favor the formation of borophene with a high HH concentration. On the other hand, since Au withdraws electrons, lower HH concentrations are expected. This trend is supported by the observation of $\nu_{1/6}$ and $\nu_{1/5}$ structures on Ag(111)[48] and $\nu_{1/12}$ structures on Au(111).[50] Currently, Ag(111) is the most prevalent substrate for borophene growth. The observed borophene phases on Ag(111) can be assigned to either $\nu_{1/6}$ or $\nu_{1/5}$ structures, both of which can adopt various rotational orientations with respect to the metal substrate.[48] A report by Campbell *et al.* verified that the $\nu_{1/6}$ and $\nu_{1/5}$ polymorphs on Ag(111) are chemically discrete from the Ag(111) substrate and described by a relatively weak film-substrate interaction. Experimental images of the $\nu_{1/6}$ and $\nu_{1/5}$ structures obtained from atomic force microscopy using a CO-functionalized tip are shown in **Figure 2a**. Furthermore, multiple studies report the coexistence of the $\nu_{1/6}$ and $\nu_{1/5}$ structures, attesting to the polymorphism of borophene.[25,30,31,70] An STM image of a region containing intermixed $\nu_{1/6}$ and $\nu_{1/5}$ domains is presented in **Figure 2b**. As suggested by Silvestre *et al.*, the formation of periodically alternating domains of the $\nu_{1/6}$ and $\nu_{1/5}$ phases could be leveraged to form electronic stripes or transport channels.[52]

In contrast to Ag(111), Vinogradov *et al.* observed only a single a phase of borophene grown *via* MBE on Ir(111).[71] The proposed structure for their STM observations consists of a HH density of $\nu = 1/6$, however the HHs are arranged differently from the $\nu_{1/6}$ polymorph discussed above. The authors calculated the exfoliation energy for borophene on Ir(111) to be five times

greater than borophene on Ag(111), indicating a stronger film-substrate interaction. Similarly, Wu *et al.* reported the synthesis of single-phase borophene on Cu(111), where the single crystal domains are microns in lateral size.[70] The observed STM topography and its proposed structural model are presented in **Figure 2c-e**. The proposed structure on Cu(111) corresponds to a HH density of $\nu$ = 1/5 but the HH arrangement differs from the $\nu_{1/5}$ polymorph discussed above. Calculations by the authors indicate that there is significant charge transfer between borophene and Cu(111) but no covalent bonding. Additionally, honeycomb (i.e., graphene-like) borophene has been reported on Al(111).[72] However, borophene synthesis on substrates other than Ag(111) still need to be reproduced, which will allow their structures to be verified and investigated in more detail. Given the convolution of electronic and structural information obtained in STM, complementary methods such as atomic force microscopy using a CO-functionalized tip will aid in confirming the structural models for new borophene phases. Ultimately, the synthesis of borophene on diverse substrates with a variety of structures supports the notion that substrate choice is a key strategy for engineering the polymorphism of borophene.

**2.1.2.2. Synthesis conditions.** Borophene synthesis has been most commonly demonstrated on Ag(111) compared to other substrates. Recently, the temperatures for which the various phases of borophene are obtained was detailed by Liu *et al.* as depicted in **Figure 2f**.[48] Specifically, the formation of the $\nu_{1/6}$ polymorph is favored at substrate temperatures below 450 ºC. Above 450 ºC, a mixture of $\nu_{1/6}$ and $\nu_{1/5}$ phases are observed until the $\nu_{1/5}$ structure dominates at ~500 ºC. At ~525 ºC and above, the $\nu_{1/5}$ phase coexists with 30º-rotated $\nu_{1/6}$ and $\nu_{1/5}$ domains in addition to incommensurately rotated $\nu_{1/5}$ phases. This trend is in agreement with simulations performed by Karmodak *et al.*[73] and a report by Wu *et al.*,[70] both of which determined the $\nu_{1/6}$ structure to be formed on Ag(111) at lower temperatures than the $\nu_{1/5}$ structure.

While similar temperatures are used for the synthesis of borophene on Au(111), Kiraly *et al.* reported that the total dose of boron required was an order of magnitude greater than on Ag(111). The authors attributed this discrepancy to dissolution of boron into the bulk of the Au substrate, which later segregates to the surface upon cooling. Similarly, dissolution of boron into Ir(111) was reported by Vinogradov *et al.*, such that 3D boron clusters segregate to the surface after excessive boron dosing.[71] Recrystallization from subsurface boron in Cu(111) was also reported by Wu *et al*.[74] Further studies are needed to fully understand the surface segregation synthesis mechanism for borophene and its implications for polymorphic control.

**2.1.2.3. Post-synthesis processing.** The structure of borophene can also be modified through additional processing following boron deposition. For example, thermal post-annealing of borophene domains at 650 K has been demonstrated to convert most $v_{1/6}$ domains to the $v_{1/5}$ structure,[31] which is in agreement with the $v_{1/5}$ phase being favored at higher temperatures during growth. Moreover, Zhang *et al.* suggested that charge doping *via* a gate voltage could alter the HH concentration of borophene monolayers.[75] This concept is based on the previously discussed formation of HHs in borophene as a self-doping mechanism that contributes to structural stability. External control of the charge doping with a gate voltage could provide a dynamic method for polymorph control in borophene, although this intriguing possibility has not yet been demonstrated experimentally.

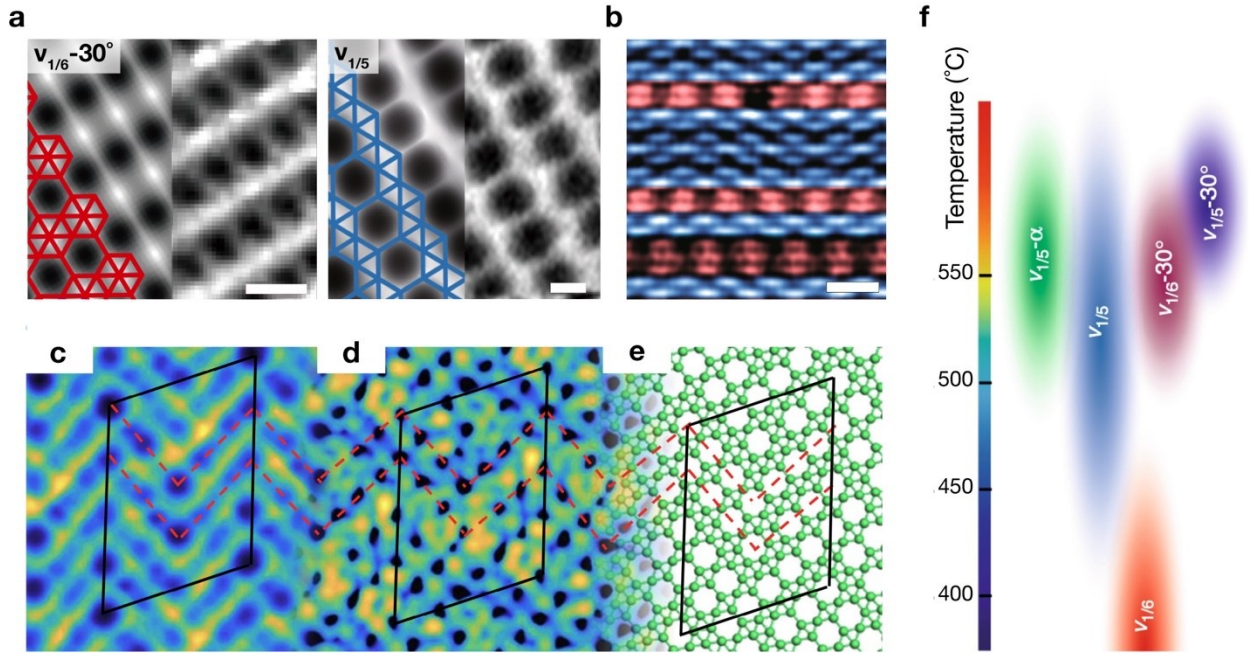


**Figure 2. Experimental demonstrations of polymorphic control in borophene. a)** Ultra-high vacuum atomic force microscopy images obtained using a CO-functionalized tip of the $\nu_{1/6}$ – 30° and $\nu_{1/5}$ phases of borophene grown on Ag(111) *via* MBE. The simulated atomic force microscopy images, overlaid with the structural models, are shown on the left of each image, and the experimental images are shown on the right. The scale bars for the $\nu_{1/6}$ – 30° and $\nu_{1/5}$ images are 5 Å and 2 Å, respectively. **b)** Bare-tipped STM image of the coexistence of the $\nu_{1/6}$ (red) and $\nu_{1/5}$ (blue) borophene phases on Ag(111). The scale bar is 2 nm. **c)** STM image obtained with a CO-functionalized tip of borophene grown on Cu(111) *via* MBE. Growth on Cu(111) is reported to promote large domains of single-crystal borophene without competing phases. **d)** DFT-simulated image of the constant tunneling current isosurface corresponding to the proposed borophene structure in **e)**. The proposed structure has a HH concentration of $\nu$ = 1/5, but the HH arrangement is different from the $\nu_{1/5}$ phase of borophene on Ag(111). The unit cell is outlined in black and has a dimension of 15.96 Å × 21.84 Å. **f)** Phases of borophene obtained *via* MBE on Ag(111) at different temperatures. Increasing the substrate temperature during deposition results in the coexistence of multiple phases, including $\nu_{1/5}$ structures that are rotationally incommensurate to the underlying Ag(111) substrate crystallography (denoted by $\nu_{1/5}$-α where α is an arbitrary angle). **a), b),** and **f)** are adapted from Ref.[48] Copyright 2019 Springer Nature under a Creative Commons Attribution 4.0 International License https://creativecommons.org/licenses/by/4.0. **c-e)** are adapted with permission from Ref.[70] Copyright 2018 Springer Nature.

## *2.2. Group IV Elements*

### 2.2.1. Structures and properties of 2D group IV elemental polymorphs

While graphene adopts a planar honeycomb structure, the other 2D group IV elemental materials (e.g., Si, Ge, Sn) form a buckled honeycomb arrangement that will be referred to here as the hexagonal buckled (*hb*) structure (**Figure 3a**). This structural disparity arises from the ability of carbon to maintain π bonding through $sp^2$ hybridization, while this bonding motif is weakened in heavier group IV elements. As explained by Şahin *et al.,* the bond distance between nearest neighbor atoms increases with increasing atomic mass.[76] In turn the $p_z$ orbital overlap decreases and weakens the π bond. Since the weaker π bond can no longer maintain the planarity of the structure, out-of-plane buckling arises that is stabilized by an increase in $sp^3$ bonding character. Consequently, the degree of buckling and $sp^3$ bonding character in the 2D structures of group IV elements increases as the atomic mass increases, approaching the pure $sp^3$ bonding observed in their bulk face-centered cubic structures.[77–79] In other words, the 2D group IV elements become more 3D-like when moving down the periodic table from carbon to tin. Nevertheless, 2D *hb* structures are predicted to be stable for Si, Ge, and Sn.[80,76,81,82] One report also found 2D Pb to be stable in a highly buckled *hb* structure,[83] although another study claimed that it was unstable.[82] In light of the inconclusive results on 2D Pb, the discussion in this text will focus on 2D Si, Ge, and Sn. A summary of the calculated freestanding structures and bandgaps for the discussed 2D group IV elemental materials is provided in **Table 1**. For further reading on the synthesis, properties, and applications of these materials, please see the review articles by Molle *et al.*,[77] Vishnoi *et al.,*[84] Glavin *et al.,*[85] and Si *et al.*[86]

Similar to graphene, Dirac cones are expected for *hb* group IV elemental materials.[80,87] However, due to significant spin-orbit coupling (SOC) for heavier elements, a gap opens at the Dirac point (**Table 1**) and distorts the linear Dirac cones.[88] In addition, as studied computationally by Liu *et al.*, the buckled honeycomb structure exhibits much larger SOC in comparison to planar

graphene. As a result, in tandem with the intrinsically larger SOC due to higher atomic mass, the gap is significantly larger in silicene, germanene, and stanene than graphene.[78] The quantum spin Hall effect in *hb* Si, Ge, and Sn is also predicted at temperatures above that of liquid nitrogen.[78] The SOC is sensitive to the degree of buckling such that higher buckling angles result in greater gaps at the Dirac point. The gap is thus expected to be largest for stanene with a magnitude of ~0.1 eV.[78,81] The gap can be enhanced with further structural and chemical modification, such as chemical functionalization.[89,81,90,91] In particular, halogens such as iodine have been calculated to increase the bandgap of stanene to 0.3-0.4 eV.

In addition to the *hb* polymorph, structures composed of dumbbell units have also been proposed for Si, Ge, and Sn.[92–97] The formation of a dumbbell unit is presented in **Figure 3b**. For silicene, an array of dumbbell units has been suggested at high Si deposition conditions.[93] In addition, Matusalem *et al.* found the dumbbell arrangements to be more energetically favorable than the *hb* structure for freestanding Si, Ge, and Sn.[96] Tang *et al.* explained that the dumbbell geometry enables more $sp^3$-like hybridization in the atoms to stabilize the 2D structure.[95] The structures based on dumbbell units are predicted to be semiconductors with indirect bandgaps. However, robust experimental verification of these dumbbell structures has not yet been achieved.

The structures of 2D group IV elemental materials are further affected by the substrates upon which they are grown. Whereas most 2D materials can be exfoliated from the bulk, this method is not readily available to the 2D group IV elements due to a lack of layered bulk allotropes and the favoring of $sp^3$-like coordination that precludes true vdW interlayer coupling in multilayer *hb* structures. Therefore, the use of substrates has been crucial in stabilizing the ultrathin layers of *hb* group IV elements.[98] Specifically, the synthesis of 2D group IV elemental materials is mostly restricted to MBE, although top-down chemical exfoliation methods are being explored.[99] The

strong film-substrate interactions in MBE-grown group IV elemental films can result in reconstructions that deviate from the structure of their calculated freestanding forms. Consequently, polymorphism in the 2D group IV elements includes the various reconstructions or superstructures observed due to coupling with their substrates. Moreover, the sensitivity of these materials to ambient conditions limits most of their characterization to STM and other *in situ* ultra-high vacuum (UHV) techniques, which complicates the verification of their observed 2D structures. Consequently, significant controversy exists in the literature concerning the structures and compositions of the materials reported as silicene, germanene, and stanene.

The structural modifications induced in 2D group IV elements by growth substrates in turn affect their symmetry and electronic properties. For example, Lin *et al.* found that the 4 × 4 silicene superstructure on Ag(111) breaks the symmetry of pristine *hb*-silicene resulting in a loss of Dirac fermion characteristics.[100] While *hb*-stanene is predicted to exhibit a narrow bandgap, the growth of stanene on $Bi_2Te_3$(111) renders it metallic due to the topologically metallic states of the substrate.[101] While the influence of the substrate often leads to discrepancies between observations and theoretical predictions of the free-standing material, these discrepancies sometimes provide enhanced functionality. For example, Liao *et al.* recently demonstrated superconductivity in few-layer stanene on PbTe(111)/$Bi_2Te_3$ substrates where the thickness of the PbTe(111) layer enabled modulation of the superconducting behavior.[102]

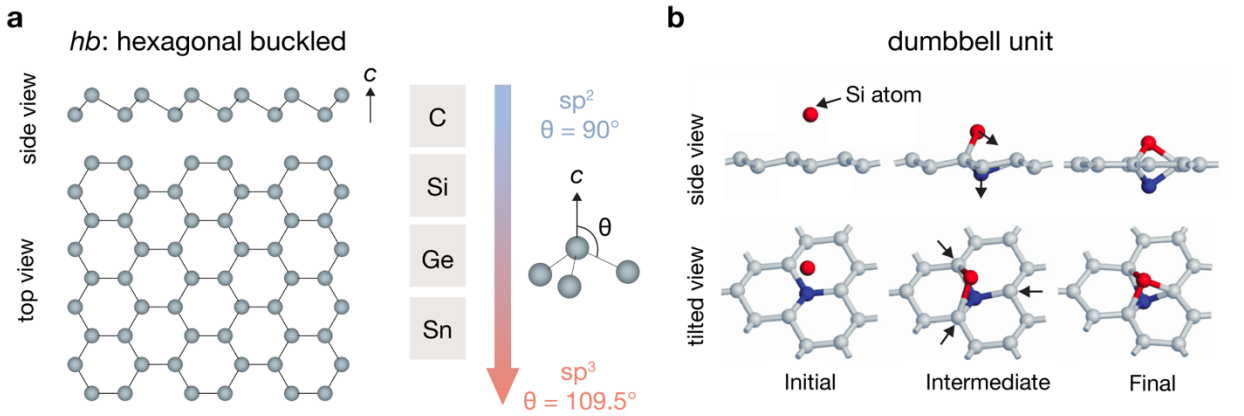


**Figure 3. 2D polymorphs of group IV elements. a)** Structure of monolayer group IV elemental materials. The severity of the buckling increases with the atomic number and approaches the bulk $sp^3$ structure. **b)** Formation of the proposed dumbbell unit structure as an alternative energetically favorable 2D structure. However, it should be noted that periodic 2D structures made from dumbbell units have not yet been robustly substantiated through experimental observations. Adapted with permission from Ref.[93] Copyright 2014 American Physical Society.

**Table 1. Calculated structures and bandgaps of freestanding monolayer group IV elements.**

| | structure type | space group | lattice parameter (Å) | buckling distance (Å) | bandgap type | bandgap, with SOC (eV) | ref(s) |
|---|---|---|---|---|---|---|---|
| **Si** | *hb* | $P\bar{3}m1$ | 3.83 | 0.44 | Semimetal[a] | 0.0016-0.0079 | [76,78] |
| **Ge** | *hb* | $P\bar{3}m1$ | 3.97 | 0.64 | Semimetal[a] | 0.024-0.093 | [76,78] |
| **Sn** | *hb* | $P\bar{3}m1$ | 4.67 | 0.85 | Direct | 0.073-0.129 | [78,82] |

[a]The inclusion of SOC in the calculations opens narrow bandgaps in Si and Ge.

## 2.2.2. Polymorph control of 2D group IV elemental materials

**2.2.2.1. Substrates.** The synthesis substrate plays an essential role in stabilizing the 2D structures of group IV elements. For silicene in particular, most reports of its synthesis have been using MBE on Ag(111),[103–107] where it forms three reproducible superstructures: (3 × 3)/(4 × 4), (√7)/(2√3 × 2√3)R30°, and (√7 × √7)/(√13 × √13)R13.9° with respect to freestanding *hb*-Si/Ag(111) unit cells given as $(i \times j)/(n \times m)$, respectively.[108,109] In this text, the notation of the superstructure with respect to the substrate unit cell $(n \times m)$ will be used. The three reproducible phases of silicene on Ag(111) are thus the 4 × 4, (2√3 × 2√3)R30°, and (√13 × √13)R13.9° superstructures, where the

Rθº notation indicates a rotation of the overlayer lattice of θ degrees with respect to the substrate lattice. Pawlak *et al.* recently utilized atomic force microscopy with a CO-functionalized tip to image these three structures (**Figure 4a**).[108] The 4 × 4 phase is the most stable and studied phase,[109] and is generally believed to correspond to *hb*-Si with a buckling of about 0.8 Å.[108] Additionally, the synthesis of silicene has been reported on Ir(111),[110] Ru(001),[111] $ZrBr_2$(001),[112] ZrC(111),[113] and Pb(111).[114] Compared to silicene, the number of studies of germanene synthesis are fewer, but most of them also employ metallic substrates. Germanene was first reported using MBE on Pt(111) as a √19×√19 superstructure.[115] Subsequently, germanene synthesis has been pursued using MBE on additional metal substrates such as Au(111),[116–118] Ag(111),[119,120] Al(111), [121–123] Cu(111)[124] and Sb(111).[125] Stanene synthesis has also been reported on metallic substrates such as Sb(111),[126] Cu(111),[127] Ag(111),[128] and Au(111), where multiple phases have been observed in the latter case.[129,130] Additionally, stanene synthesis has been achieved on semiconducting substrates. Due to commensurate lattices, the synthesis of *hb*-stanene without a reconstruction was achieved by Zhu *et al*. with MBE on a $Bi_2Te_3$(111) substrate,[101] although compressive strain increased the buckling of the *hb* structure to 1.2 Å instead of the expected value of 0.85 Å for freestanding *hb*-stanene. In this case, stanene was found to be metallic due to metallic $Bi_2Te_3$ surface states. In later reports, the epitaxial growth of *hb*-Sn on PbTe(111)/$Bi_2Te_3$(111) was also demonstrated where the stanene $p_z$ orbitals are hybridized with both the substrate on the bottom (Te-terminated PbTe(111)) and presumed hydrogen functionalization on top. The authors attribute the resulting sizeable bandgap of 0.32 eV to the presumed hydrogen passivation, which also imparted high chemical stability in ambient conditions. Since stanene grows epitaxially on PbTe(111), Zang *et al.* were able to change the lattice constant of the stanene from an estimated 4.46 Å to 4.52 Å by changing the thickness of the underlying PbTe(111) layer on $Bi_2Te_3$. Liao *et al.* similarly used the thickness

of the PbTe(111) substrate to tune the superconducting transition temperature of passivated multilayer stanene on PbTe(111)/$Bi_2Te_3$(111).[102] The epitaxial growth of few-layer stanene films has also been investigated on semiconducting InSb(111), where evidence of 2D Dirac-like cones were observed by Xu *et al.*,[131] and a topologically nontrivial band structure was observed by Xu *et al.*[132] and Rogalev *et al.*[133] Finally, vdW substrates such as highly oriented pyrolytic graphite (HOPG)[134] and $MoS_2$[135] have been utilized for the growth of silicene and germanene, but the results have been mixed, presumably due to insufficiently strong film-substrate interactions.[136,137]

In contrast to pure vdW materials, the 2D group IV elements require additional stabilization, which explains why metal substrates have been most widely employed. For example, Gao *et al.* studied the growth mechanism of silicene on Ag (111) and found that initial silicene clusters were stabilized by the Ag(111) surface as a result of the passivation of unsaturated edge Si atoms by Ag free electrons and the *p-d* hybridization between inner Si atoms and the Ag substrate.[138] Hence, strong film-substrate interactions appear necessary to obtain the *hb* structure in group IV elements.[139] When weakly interacting vdW substrates are used, the formation of bulk-like silicon or germanium clusters has been reported.[136,137,140] While metal substrates can provide the strength of interaction necessary for stabilization, they strongly disturb the Dirac states and other intrinsic properties. Indeed, many reports suggest that the Dirac-like cones for silicene are destroyed on Ag(111) substrates by Si-Ag hybridization,[141,142,100,143,144] although the topic is still debated.[145] Similarly, a computational study by Wang *et al.* concluded that many metal substrates destroy the Dirac cones in germanene,[146] which may explain why conclusive experimental observation of Dirac-like cones in germanene have not yet been achieved.

Strong substrate interactions also make the 2D group IV elements susceptible to the formation of surface alloys. Along these lines, several studies of the structure of ($\sqrt{3} \times \sqrt{3}$)R30º

silicene on Ag(111) obtained at high temperatures have suggested that this phase is a bulk-like silicon terminated with a Ag surface alloy rather than multilayer silicene.[147–152] Similarly, the observed structures of germanene and stanene on several metal substrates are purportedly surface alloys, rather than *hb*-germanene or *hb*-stanene reconstructions, including germanium on Pt(111),[153,154] Au(111),[155,156] and Al(111),[157–159] as well as tin on Ag(111).[160]

The strength of interaction between the group IV element and the substrate also has implications for the degree of buckling observed. Deng *et al.* used a strongly interacting Cu(111) substrate to synthesize a planar honeycomb stanene film instead of the buckled structure (**Figure 4b**).[161] The planar structure is not reconstructed and corresponds to a 2 × 2 Cu(111) supercell. The authors calculated the adsorption energy of the Sn atoms to the Cu(111) substrate as ~1.16 eV/atom, which is considerably higher than the calculated binding energies for Si on Ag(111) of ~0.7 eV/atom. The authors thus attribute the stanene planarity in this case to the energetically favorable maximization of all Sn atoms in contact with the Cu(111) surface. This structure has been predicted to enable topologically derived boundary states, which is consistent with the scanning tunneling spectroscopy (STS) results shown in **Figure 4c**. In particular, STS indicates the presence of an edge state in an energy range that matches the energy of the SOC-induced gap observed in angle-resolved photoemission spectroscopy (ARPES) experiments (−1.25 eV ± 0.15 eV).

Overall, the search for substrates that can stabilize the 2D group IV elemental materials without destroying their predicted intrinsic properties remains a challenge. Future experimental efforts may be guided by the many substrates that have been predicted to preserve the Dirac-like dispersion expected from the freestanding *hb* structures of the group IV elements including $Al_2O_3$(001),[139] H-terminated SiC,[162] Cl-terminated SiC,[163] epitaxial graphene on SiC,[164,165]

hBN,[162,166] $CaF_2$,[163] and CdTe.[167] A more detailed discussion on the prospects of synthesizing ultrathin films of group IV elements on non-metallic substrates is given in a review by Galbiati *et al.*[168]

**2.2.2.2. Synthesis conditions.** The deposition conditions used during the synthesis of 2D group IV elements also affect their structure and composition. For example, the deposition temperature of Si on Ag(111) can be used to select for one silicene superstructure over another, although the control is limited since coexistence of phases is often observed. In particular, a dominant 4 × 4 phase can be obtained at lower substrate temperatures around 470-600 K.[105–107] The (2√3 × 2√3)R30º and (√13 × √13)R13.9º superstructures are reported to coexist with the 4 × 4 phase at higher temperatures with the (2√3 × 2√3)R30º phase generally becoming dominant with increasing temperature.[106,109] Increasing the deposition temperatures above 600 K results in the formation of bulk-like silicon terminated with a Ag-Si alloy,[151,169,170] while exceedingly low temperatures (< 400 K) result in disordered deposition.[171] Similarly, the formation of Ge alloys with the substrate is reported for temperatures above 900 K on Pt(111)[154] and 600 K on Au (111).[117] For the synthesis of stanene on PbTe(111), a deposition procedure has been developed to prevent diffusion of Sn atoms into the substrate lattice. Specifically, Zang *et al.* used a low-temperature deposition of Sn on PbTe(111) at 150 K followed by a post-anneal a 400 K to obtain *hb*-stanene.[172] A previous study by Liang *et al.* also found that alloying of Sn on Cu (111) could be prevented by decreasing the substrate temperature from 300 K to 100 K. While alloy formation was not discussed by Deng *et al.*, their procedure entailed Sn deposition on Cu(111) at 200 K.[161] The authors report that temperatures below 243 K are necessary to maintain the planar structure of stanene and that domains of the buckled phase are obtained at higher temperatures. However, the previous study

by Liang *et al*. suggests that Sn-Cu alloy formation is another factor that dictates the optimal deposition temperature, in addition to the planarity of the stanene structure.

Structural control over 2D group IV elements can also be achieved using the deposition rate and/or coverage. For example, the silicene ($\sqrt{13} \times \sqrt{13}$)R13.9º structure on Ag(111) can be obtained at the same conditions as the 4 × 4 superstructure for longer deposition times.[105] A study by Arafune *et al*. on the phase evolution of silicene structures on Ag(111) illustrates the dynamic nature of silicene growth as a function of deposition time. The authors observed that a film of primarily 4 × 4 *hb*-silicene on Ag(111) transitioned to a mixture of 4 different superstructures upon further deposition of Si.[107] Similarly, a structural evolution of silicene from a herringbone arrangement to a honeycomb $\sqrt{7} \times \sqrt{7}$ superstructure on Ru(001) has been reported upon increased Si coverage.[111] The effect of deposition coverage on the structure of germanium domains on Ag(111) was investigated by Lin *et al.*, which considered the interesting case of dealloying. Initial Ge deposition (< 1/3 of a monolayer) proceeded *via* the formation of an $Ag_2Ge$ alloy with further deposition resulting in a dealloying process.[119] The dealloying began with a highly strained striped germanium phase (**Figure 4d**, top) commensurate with the Ag(111)-($\sqrt{3} \times \sqrt{3}$)R30º unit cell, where further deposition resulted in the conversion of the striped domains to an incommensurate honeycomb phase (**Figure 4d**, bottom) that resembles freestanding germanene. The authors found that the structural change to the quasi-freestanding phase was accompanied with a transition to a band structure resembling germanene, although Dirac cones were not observed. This structural evolution was also observed by Chiniwar *et al.*[120] Dealloying processes have also been reported for stanene synthesis on Ag(111)[128] and Au(111).[130] Hence, it is possible to obtain films of *hb* group IV elements on metal substrates that initially form an alloy through a dealloying process

upon additional deposition. However, this relatively complicated phase evolution leads to challenges in achieving high homogeneity in the resulting 2D materials.

**2.2.2.3. Post-synthesis processing.** Most reports of structural control in the 2D group IV elemental materials exploit control during synthesis. However, a few accounts focus on the manipulation of the structures after deposition. Using post-annealing at 523 K, Grazianetti *et al.* were able to convert a network of small silicene domains with various superstructures on Ag(111) into large domains of the 4 × 4 and (√13 × √13)R13.9º superstructures.[173] Additionally, Huang *et al.* proposed the application of pressure to transform germanene and stanene bilayers into topologically nontrivial flat honeycomb structures with a bulk gap of ~0.1 eV.[174]

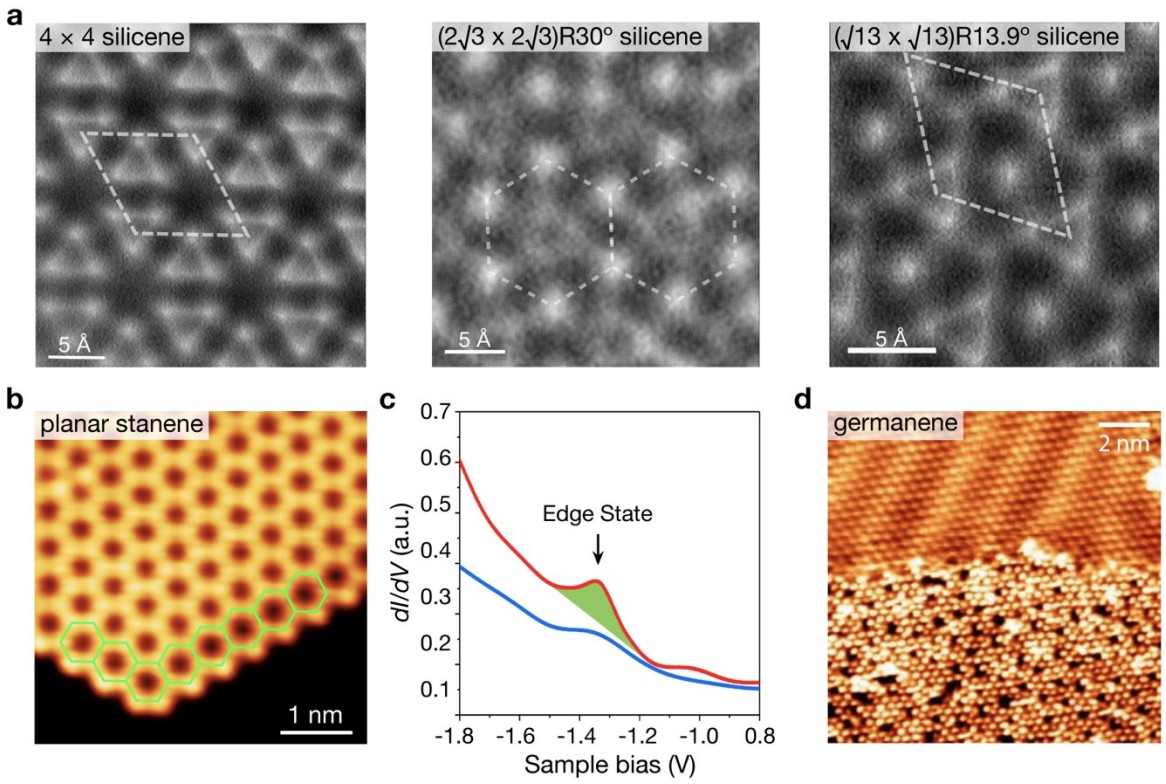


**Figure 4. Experimental demonstrations of polymorphic control in 2D group IV elemental materials.** **a)** Ultra-high vacuum atomic force microscopy images obtained using a CO-functionalized tip of the three reproducibly observed reconstructed silicene phases grown *via* MBE on Ag(111). Adapted with permission from Ref.[108] **b)** STM image of planar stanene grown *via* low-temperature MBE on Cu(111) and **c)** STS of the edge (red) and center (blue) of a planar stanene domain, indicating the presence of an edge state in an energy range that matches the energy of the SOC-induced gap observed in ARPES (−1.25 eV ± 0.15 eV).

The stabilization of the planar polymorph was attributed to the strong interaction of Sn with the Cu(111) substrate. Adapted with permission from Ref.[161] Copyright 2018 Springer Nature. **d)** Coexistence of a partially commensurate "striped" phase (top) and quasi-freestanding incommensurate honeycomb phase (bottom) of germanene grown *via* MBE on Ag(111). The quasi-freestanding phase is reported to form after the striped phase by dealloying of Ge from the Ag(111) surface upon further Ge deposition. Adapted with permission from Ref.[119] Copyright 2018 American Physical Society.

## *2.3. Group V Elements*

### 2.3.1. Structures and properties of 2D group V elemental polymorphs

Many of the group V elemental materials (P, As, Sb, Bi), or pnictogens, exist as layered polymorphs in the bulk that can be exfoliated into 2D form. In particular, there are three types of monolayer structures observed in the layered elemental group V materials: hexagonal buckled (*hb*), symmetric washboard (*sw*), and asymmetric washboard (*aw*) (**Figure 5a**). The *hb* structure is the most symmetric of the three polymorphs and is analogous to that observed in the group IV elemental 2D materials. Recall that this structure resembles the planar hexagonal lattice of graphene, but with significant out-of-plane buckling such that there are two distinct atomic planes in the monolayer structure. The monolayer *hb* structure can be converted to a graphene-like planar hexagonal lattice if the buckling is eliminated with external forces, such as strain or chemical functionalization.[175–179] In its bulk form, the layered *hb* structure is known as the rhombohedral A7 (*Strukturbericht* designation) or α-As structure type. At this point, it is important to make a note regarding nomenclature of group V elemental structures. In the 2D material literature, the "β" designation is often used to refer to the monolayer *hb* structure while "α" is used to refer to the monolayer *sw* structure, which can cause confusion. For example, atomically thin α-As is sometimes referred to as "β-As" in the 2D material literature, even though they both correspond to the *hb* structure. To avoid this confusion, the "α" and "β" designations will not be used here to

identify 2D group V elemental polymorphs. The bulk A7 structure can be derived as a distortion of the simple cubic structure with a rhombohedral shear and displacement along the [111] direction.[180] The distortion is explained by the existence of a Peierls electronic instability from the half-filled *p* bands.[181] While the intralayer bonding in the A7 (multilayer *hb*) structure is of much greater strength than the interlayer bonding, the layers are not explicitly vdW-bonded and have a weakly covalent nature that increases from As to Bi.[182,183]

The monolayer *sw* structure is also composed of six-membered rings, but they are puckered into a chair-like confirmation. The result is an orthorhombic lattice with two distinct atomic planes. This puckered structure is best known as the structure of monolayer black phosphorus (phosphorene). The bulk black phosphorus structure is also referred to as the A17 structure (*Strukturbericht* designation).[184] The *aw* structure is similar to the *sw* structure, but with an additional out-of-plane offset or buckling between neighboring atoms in the two atomic layers. As a result, the *aw* polymorph is lower in symmetry with four distinct atomic planes in the monolayer. The relationship between the A7 (*hb*) and A17 (*sw/aw*) polymorphs was investigated in a study by Boulfelfel *et al.*[184] The authors predicted the observation of *sw/aw* structures in other group V elements with *hb* ground state structures (As, Sb, Bi). These predictions were later corroborated by Zhang *et al.*[185] in their computational assessment of the stability of 2D structures of the group V elements and have since been confirmed experimentally. A summary of the commonly observed monolayer group V polymorphs is presented in **Figure 5b**. Additionally, the existence of a square-octagon polymorph for this class of materials composed of tiled square and octagonal rings of atoms has been predicted by many but has yet to be observed experimentally.[186–190] In contrast to the other pnictogens, nitrogen does not exhibit a layered bulk solid. While nitrogen is usually observed in a molecular form, a report has synthesized a covalently bonded cubic gauche phase of

nitrogen at extreme temperatures and pressures.[191] The existence of a solid 2D phase of nitrogene in the *hb*[192] or square-octagon[187] structure has been predicted, but not yet confirmed experimentally, although attempts have been made in this direction.[193]

Phosphorus is the most widely studied of the group V elemental materials in the 2D material literature. The layered *sw* polymorph, known as black phosphorus or α-P, is thermodynamically stable at ambient conditions and usually formed at high pressure, although synthesis at lower pressures has also been achieved.[194] The investigation of 2D *sw*-P was enabled in 2014 *via* mechanical exfoliation from bulk black phosphorus.[195–197] At high pressures, the black phosphorus structure transitions to the A7 structure (layered *hb* structure).[198] While the *hb* structure of phosphorus, named "blue phosphorus", was predicted by Zhu *et al.* to be stable in the monolayer form,[199] top-down exfoliation is not possible for 2D *hb*-P since the bulk A7 structure is thermodynamically unstable in ambient conditions. Consequently, the realization of 2D *hb*-P was not achieved until 2016 through MBE on Au(111).[200] As of now, MBE on Au(111) remains the sole pathway through which 2D *hb*-P can be obtained, and a recent report has called this structure into question.[201] Outside of the *sw* and *hb* monolayers, several other 2D polymorphs have been proposed in computational studies[202–208] beyond the square-octagon structure.[186]

For the heavier group V elements (As, Sb, Bi), the most stable polymorph in the bulk is the A7 (layered *hb*) structure.[209] This form is also termed gray arsenic, gray antimony, and metallic bismuth.[210] In the bulk, elemental arsenic can also adopt a metastable layered *sw* (A17) structure.[211] For 2D arsenene, several computational studies have predicted both the *hb* and *sw* monolayers to be stable.[212–214,189] Similarly, 2D antimonene and 2D bismuthene have been predicted to be stable in the monolayer *hb* structure as well as the *aw* structure, the latter of which is not observed in the bulk.[215–218] For bismuthene, the *sw* form may also be obtained when stabilized with appropriate

substrates,[218–220] but the asymmetric structure is more common in the 2D form. Furthermore, the application of strain to *hb*-antimonene and *hb*-bismuthene is predicted to yield planar hexagonal lattices.[178,221]

Whereas the *hb* monolayer structure is isotropic, the *sw* and *aw* monolayers are both anisotropic and result in anisotropic properties. Several computational studies have reported anisotropic electrical conductance, thermal conductance, and mechanical properties along the armchair and zigzag directions in *sw*-phosphorene and *sw*-arsenene.[216,222–224] Furthermore, linear dichroism in light absorption of *sw*-phosphorene has been predicted.[222] These attributes have since been verified experimentally,[195,225–228] with 2D *sw*-As demonstrating extreme charge carrier anisotropies. In *sw*-As, the ratio of the hole carrier mobility in the armchair direction (10,606 $cm^2 V^{-1} s^{-1}$) to the zigzag direction (60.7 $cm^2 V^{-1} s^{-1}$) is ~175.[228] Anisotropic hole carrier mobilities have also been confirmed in *sw*-P.[195] A report by Chen *et al.* further compared the properties of the *hb* and *sw/aw* monolayer polymorphs.[229] In their calculations, the authors observed that the *hb* structure of As, Sb, and Bi generally had lower electrical conductance but higher thermal conductance than the *sw*/*aw* counterpart. Furthermore, the Seebeck coefficient is greater in the *hb* structure, with the exception of As where the two polymorphs are comparable. Altogether, these results suggests that *hb*-Sb is a promising thermoelectric material with a predicted ZT of 2.15 at room temperature. Based on the calculated electronic properties of the *hb* and *sw* structures of monolayer phosphorene and arsenene, the *sw* polymorph is expected to have significantly higher mobilities (up to orders of magnitude in disparity for arsenene).[185,212,230,231] The lesser degree of undulation in the monolayer *hb* polymorph compared to the *sw*/*aw* polymorphs may also have implications for their chemical reactivity and interaction with molecules due to different steric environments.[232]

While both the *hb* and *sw* polymorphs are centrosymmetric, the *aw* structure is noncentrosymmetric. The breaking of inversion symmetry in the *aw* polymorph holds promise for the emergence of spontaneous polarization. A report by Xiao *et al.* on *aw*-structured group V elemental monolayers predicted sizable in-plane ferroelectricity and antiferroelectricity with Curie temperatures above room-temperature.[233] The *aw*-structured materials are also expected to display other spontaneous polarization phenomena such as piezoelectricity, although the magnitude of these additional polarizations is not yet known. In addition, a recent computational study by Guo *et al.* has predicted large intrinsic SHG in *aw* monolayers.[234]

As atomic mass increases, SOC becomes more significant. Consequently, *hb*-Bi is predicted to be a topological insulator.[235–237] The existence of these topological nontrivial states is also expected to be sensitive to structural modifications. For example, the application of strain in *hb*-arsenene and *hb*-antimonene has been reported to result in topologically nontrivial states.[238–241] Furthermore, hexagonal planar structures of antimonene and bismuthene have been proposed as 2D topological crystalline insulators.[178] Accordingly, several studies have reported the observation of conductive edge states in planar bismuthene,[242] *hb*-bismuthene,[243] and *hb*-antimonene films.[244] In contrast, monolayer *aw*-Bi is anticipated to be trivial. However, Lu *et al.*[219] reported the existence of topological edge states when the *aw* structure of bismuthene approaches the higher symmetry *sw* structure through weakening of out-of-plane buckling. The effects of different stacking configurations in the 2D group V polymorphs have been studied in several computational reports but not yet corroborated with experimental studies.[214,245,246] A summary of the structures and bandgaps for the discussed 2D group V elemental materials is provided in **Table 2**. For further reading on the synthesis, properties, and applications of these materials, please see the review articles by Gusmão *et al.*,[194] Zhang *et al.,*[247] Ersan *et al.,*[248] Vishnoi *et al.,*[84] and Wu and Hao.[249]

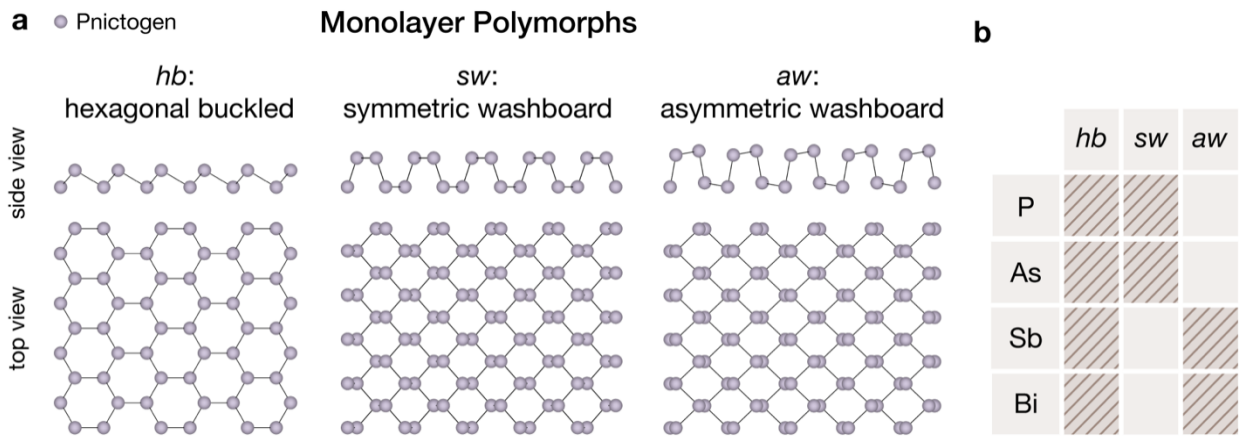


**Figure 5. 2D polymorphs of group V elements. a)** Monolayer polymorphs of layered group V (pnictogen) elemental materials. The *aw* structure differs from the *sw* structure by an out-of-plane buckling in the two atomic planes of the *sw* structure (see side view). **b)** Summary of the commonly observed polymorphs for each element. Although reports exist of *sw*-bismuthene grown on substrates,[219,220] the freestanding form has been calculated to be unstable.[218]

**Table 2. Structures and bandgaps of monolayer and bulk group V elements**.

| | Monolayer | | | Bulk | | | | | |
|---|---|---|---|---|---|---|---|---|---|
| | **structure type** | **lattice parameters (Å)** | **bandgap (eV)** | **name** | **structure type** | **space group** | **lattice parameters (Å)** | **bandgap (eV)** | **ref(s)** |
| **P** | *hb* | $a$ = 3.326[a] | 2-3[a, c]<br>1.1, on Au(111) | blue phosphorus | A7 | $R\bar{3}m$ | $a$ = 3.324[a]<br>$c$ = 5.63[a] | 1.1[a,c] | 199,250 |
| | *sw* | $a$ = 3.32[a]<br>$b$ = 4.58[a] | 1.51[a,b], 1.94[a,b]<br>2[b] | black phosphorus | A17 | *Cmca* | $a$ = 3.3164<br>$b$ = 10.484<br>$c$ = 4.3793 | 0.335[b] | 222,251–253 |
| **As** | *hb* | $a$ = 3.607[a] | 2.10 [a,c] | grey arsenic | A7 | $R\bar{3}m$ | $a$ = 3.7598<br>$c$ = 10.5475 | Semimetal | 213,214,254 |
| | *sw* | $a$ = 3.677[a]<br>$b$ = 4.765[a] | 1.47[a,c] | black arsenic | A17 | *Cmca* | $a$ = 3.74[a]<br>$b$ = 10.76[a]<br>$c$ = 4.36[a] | 0.31[a,b] | 211,213,214,228 |
| **Sb** | *hb* | $a$ = 4.04[a] | 0.76[a,c], 1.55[a,c] | grey antimony | A7 | $R\bar{3}m$ | $a$ = 4.31<br>$c$ = 11.27 | Semimetal | 215,216 |
| | *aw* | $a$ = 4.28[a]<br>$b$ = 4.74[a] | 0.28[a,c], 0.34[a,c] | - | distorted A17 | - | - | - | 215,216 |
| **Bi** | *hb* | $a$ = 4.38[a] | 0.32[a,b],<br>0.45[a,c] | metallic bismuth | A7 | $R\bar{3}m$ | $a$ = 4.546<br>$c$ = 11.863 | Semimetal | 218,255,256 |
| | *aw* | $a$ = 4.55[a]<br>$b$ = 4.94[a] | 0.39[a,c] | - | distorted A17 | - | - | - | 218,255 |

[a] calculated value
[b] direct bandgap
[c] indirect bandgap

## 2.3.2. Polymorph control of 2D group V elemental materials

**2.3.2.1. Synthesis conditions.** Since many group V elemental materials exhibit several polymorphs, including non-layered structures, precise control of the synthesis conditions is necessary to prevent the formation of other phases. For example, a report by Smith *et al.* describes the formation of red and pyrophoric white phosphorus during attempts at the vapor-phase synthesis of 2D black phosphorus.[257] The possibility of pyrophoric competing phases implies that the formation of black (*sw*) phosphorus during vapor-phase synthesis is difficult and dangerous. As a result, efforts at the synthesis of phosphorene have mostly focused on the conversion of thin films of red phosphorus to the black phosphorus structure. This polymorphic conversion typically requires high pressures and recent attempts have yielded thick films or thick nanoflakes, rather than the desired continuous monolayer.[257–259] Rajabali *et al.* avoided the high pressure pathway by instead using plasma treatment at 300 ºC to crystallize red phosphorus films into thick black phosphorus nanoflakes.[260] Meanwhile, synthesis of *hb*-P has been limited to MBE on Au(111), where the typical substrate temperature during deposition is between 180 ºC and 350 ºC.[200,250,261] The lack of reports of *hb*-P on other substrates suggest that film-substrate interactions are the dominant factor in realizing this phase as is discussed later in section 2.3.2.2.

The vapor-phase synthesis of 2D *hb*-As is also subject to the formation of alternate phases. A recent report by Hu *et al.* concerning PVD of *hb*-As nanoflakes states that the growth temperatures were specifically chosen to avoid impurity phases.[262] In particular, temperatures above 300 ºC are required to prevent a mixture of *hb* and *sw* arsenic, while slow cooling prevents the formation of metastable and light-sensitive yellow arsenic. Consequently, the authors used a growth temperature of 325 ºC in their study. This temperature range is in agreement with a subsequent report on the MBE of monolayer *hb*-As on Ag(111) using substrate temperatures of

200 ºC to 350 ºC.[263] On the other hand, the bottom-up synthesis of 2D *sw*-As has yet to be achieved. Due to its metastability, the synthesis of bulk *sw*-As (black arsenic) requires stabilization by the presence of impurities. While black arsenic is usually found as a rare mineral, Antonatos *et al.* recently reported the synthesis of bulk *sw*-As using growth temperatures of 100-200 ºC with mercury vapors.[264] These bulk synthetic crystals can then be used as a source of 2D *sw*-As following exfoliation.[228,265] For bismuthene, the role of the substrate temperature during synthesis has also been demonstrated to favor the formation of one polymorph over another. In particular, pulsed laser deposition (PLD) of bismuth on substrates at room temperature resulted in *aw*-Bi, whereas substrate temperatures of 100 ºC resulted in *hb*-Bi.[266] Additionally, the authors of this study found the film thickness to be an essential parameter in the polymorphic control of bismuthene. Typically, the *aw* structure only exists below a few layers, as discussed further in section 2.3.2.3. However, Jankowski *et al.* were able to obtain exclusively *aw*-Bi films up to 14 nm in thickness by cooling the substrate to 40 K during UHV growth using a Bi source.[267] Growth at a higher temperature of 400 K resulted in a competition between *aw*-Bi and *hb*-Bi domains, while growth at 450 K and above favored *hb*-Bi exclusively.

**2.3.2.2. Substrates.** The role of the substrate has proven to be one of the main methods of polymorphic control in the group V elemental materials. In the case of *hb* (blue) phosphorene, its synthesis has only been achieved on Au(111), which suggests that this substrate plays a crucial role in stabilizing the *hb* structure for phosphorus. A computational study by Han *et al.* showed that the formation energy ($E_f$) of *hb*-P on Au(111) is significantly lower than freestanding *hb*-P, and that *hb*-P is favored over *sw*-P on Au(111).[268] The interaction of *hb*-phosphorene with the Au(111) surface is also believed to strongly modulate its properties. Specifically, the structure of *hb*-phosphorene is reconstructed as shown in **Figure 6a**, resulting in a significant difference

between the observed and theoretical lattice parameters and bandgaps.[250] A recent study by Zhao *et al.* has called into question the structure of *hb*-P on Au (111).[201] The authors instead explain the experimental STM images as Au-P complexes formed from a strong interaction of the P atoms with the Au substrate. The formation of Au-P complexes has been further corroborated by a recent independent report by Tian *et al*.[269] In their STM study, the structures formed upon deposition of phosphorus at ~250 ºC (within the typically reported *hb*-P synthesis window) are attributed to Au-P networks, which are calculated to have lower $E_f$ than *hb*-P on Au(111). Given the previous controversies regarding elemental monolayer structures on metals (section 2.2.2.1), further investigation into the role of the substrate in *hb*-phosphorene synthesis is warranted. For example, it would be valuable to explore alternative substrates for the synthesis of *hb*-phosphorene, particularly substrates that are likely to possess weak enough interactions with phosphorus to prevent alloying but strong enough interactions to stabilize the 2D structure. This 'goldilocks' problem was previously explored in a computational study by Gao *et al.*[270] Suggested alternative substrates include Ag(111) and GaN(001).[268,271]

Experimental studies into the role of the substrate in obtaining *sw*-phosphorene are scarce. However, given its orthorhombic lattice, a rectangular substrate is most likely to yield the *sw* polymorph. For example, the rectangular-latticed surface of Sn(100) was computationally determined to be a suitable substrate for *sw*-phosphorene growth instead of *hb*-phosphorene.[272] The use of a substrate template in the synthesis of *sw*-P was recently demonstrated by Xu *et al.* (**Figure 6b**).[273] In their growth scheme, templates of $Au_3SnP_7$ domains were used to yield large crystals (up to millimeters) of *sw* (black) phosphorus. The resulting crystals were fairly thick (10+ nm), but exhibited high crystallinity and field-effect mobilities (1200 $cm^2\ V^{-1}\ s^{-1}$) exceeding previous attempts at 2D *sw*-phosphorus growth (160 $cm^2\ V^{-1}\ s^{-1}$).[259] Although the synthesis of

continuous monolayer films of *sw*-phosphorene remains elusive, this report indicates the importance of substrate/template choice for future growth efforts.

Recent experimental efforts towards the growth of antimonene best illustrate the ability of the growth substrate to exert polymorphic control. Three polymorphs of antimonene (*hb*-Sb, *aw*-Sb, and planar hexagonal Sb) have been realized through the use of different substrates. Several substrates with hexagonal symmetry have been used to grow *hb*-antimonene, including $Bi_2Te_3$ and $Sb_2Te_3$,[274] Ge(111),[275] $PdTe_2$,[276] Cu (111),[244,277] Pb (111),[278] $Cu_3O_2$, [279] and graphene.[280] An STM image of *hb*-Sb on $PdTe_2$ is shown in **Figure 6c**. In contrast, when substrates with rectangular symmetry are used, the *aw* polymorph of antimonene is formed. In a report by Shi *et al.,* monolayer *aw*-Sb was templated by a rectangular-latticed $T_d$-$WTe_2$ substrate.[281] As shown by the STM image in **Figure 6d**, the Sb overlayer possesses a rectangular lattice indicative of *aw*-Sb. Additionally, Märkl *et al.* observed the coexistence of *aw*-Sb and *hb*-Sb when deposited on *aw*-Bi.[282] As reported by Shao *et al.*, when a more strongly interacting substrate such as Ag(111) is used, planar hexagonal antimonene can be formed.[283] An STM image of planar antimonene on Ag(111) is shown in **Figure 6e**. However, metallic substrates often alter the intrinsic properties of the overlaid materials. Therefore, Zhang *et al.* has proposed the use of hBN and hydrogenated SiC as substrates for planar antimonene. Indeed, planar bismuthene on SiC has been achieved experimentally with conductive edge states and a bandgap of ~0.8 eV. However, the bismuthene was covalently bonded to the SiC, which helps explain the relatively large bandgap.[242]

The strength of the substrate interaction also has implications for the structures of ultrathin bismuth films. On some substrates, a pseudocubic structure is observed. Yagunima *et al.* suggested this structure to be *aw*-Bi when the interaction between the Bi and the substrate is relatively weak.[284] The authors observed that bismuth films on Si(111)-7 × 7 would easily delaminate from

their substrate, suggesting the presence of a vdW gap between the film and substrate. The substrate dependence in the formation of this vdW *aw*-Bi structure in ultrathin bismuth films was further investigated by Kokubo *et al.,* who found no explicit dependence on substrate symmetry.[285] The 2D *aw*-Bi structure has also been reported for the MBE growth of bismuth on $NbTe_2$,[243,286] $TaS_2$,[287] $TiSe_2$,[288] and EG/SiC.[289] Furthermore, a report by Lu *et al.* indicates that the degree of out-of-plane buckling in *aw*-Bi is dependent on the degree of charge transfer from the growth substrate. In their observations, significant charge doping from the HOPG substrate reduced the buckling or "asymmetry" in *aw*-Bi. As a result, the authors observed gapless edge states and an insulating gap at 77 K, which they attributed to the low buckling of the *aw*-Bi that approached the *sw* structure (**Figure 6f)**.[219] Low-buckled *sw*-like 2D Bi on HOPG was also observed by Kowalcyk *et al.*,[220] along with Dirac-like band dispersions. The structure of monolayer *aw*-bismuth, and potentially other group V elements, is thus sensitive to subtle effects in the film-substrate interaction.

**2.3.2.3. Thickness.** In the MBE growth of ultrathin bismuth, a thickness dependence in the structure of the film has been observed. Specifically, below a critical thickness of 2 vdW monolayers, bismuth films tend to grow in a pseudo-cubic mode different from the bulk A7 (*hb*) structure.[284,290,291] This phenomenon was first investigated by Nagao *et al.* with bismuth deposition on Si(111)-7 × 7, and the structure was determined to be the nanoallotrope of *aw*-Bi.[290] Beyond 2 vdW layers, the entire film was observed to transform into *hb*-Bi with additional deposition. Nagao *et al.* and Yagunima *et al.* proposed that the origin of this thickness-dependent structural transformation is a surface effect rather than a substrate effect.[290,284] In particular, the *aw* polymorph is the result of a minimization in the energy of the ultrathin film through the saturation of out-of-plane dangling bonds in the vdW *aw*-structure. As the films grow thicker, this surface effect becomes less dominant and starts to favor the stable bulk *hb* structure, which is not purely

vdW layered. This phenomenon is in contrast to a substrate effect where a strong film-substrate interaction forces a new structure. In fact, a pseudo-cubic structure explained by bulk-like *hb* bonding, rather than *aw* bonding, is proposed for ultrathin bismuth films grown on more strongly interacting substrates like β-$\sqrt{3}$ ×$\sqrt{3}$-Bi.[284,285] Moreover, the observation of the *aw*-Bi structure does not appear to depend explicitly on the substrate symmetry. For example, orthorhombic *aw*-bismuthene was observed when grown *via* MBE on vdW-layered $NbSe_2$ with six-fold symmetry (**Figure 6g**). These observations support the mechanism of *aw*-Bi stabilization being a thickness effect and prompts the question of how this phenomenon could be leveraged further. For example, a report by Walker *et al.* proposed that the initial growth of vdW *aw*-Bi enables the facile dry transfer of large-area single-crystal *hb*-Bi films from the Si(111) substrate.[292] Overall, the thickness-induced structural transformation in ultrathin bismuth films gives credence to the search for 2D polymorphs not observed in the bulk.

**2.3.2.4. Post-synthesis processing.** Thermal treatments after the synthesis of 2D bismuth films have been shown to result in structural conversions. For example, Kawakami *et al.* found that annealing of *aw*-Bi films on Au(111) at 470 K transformed them into the *hb* structure.[293] Jankowski *et al.* observed a similar transitional temperature of 450 K with ultrathin bismuth films on *c*-plane sapphire.[267] These results indicate that the *hb* structure is more stable than the *aw* polymorph in bismuth films, which is consistent with the absence of bulk *aw*-Bi. Given that the various 2D polymorphs of phosphorene, arsenene, and antimonene also have different stabilities,[294,189,216] the use of cooling or heating could also be used in these cases to access different structures. However, thermally induced structural transformations between polymorphs in these 2D materials have yet to be investigated. Other post-synthesis treatments for controlling the structure of 2D group V elements have been considered computationally. For instance, the functionalization of *hb*-

structured As, Sb, and Bi monolayers with hydrogen or halogens was predicted to convert the structures to a planar hexagonal form.[175,177,295] Additionally, the application of mechanical forces or the introduction of defects have been suggested as pathways to access several novel phosphorene polymorphs.[199,296]

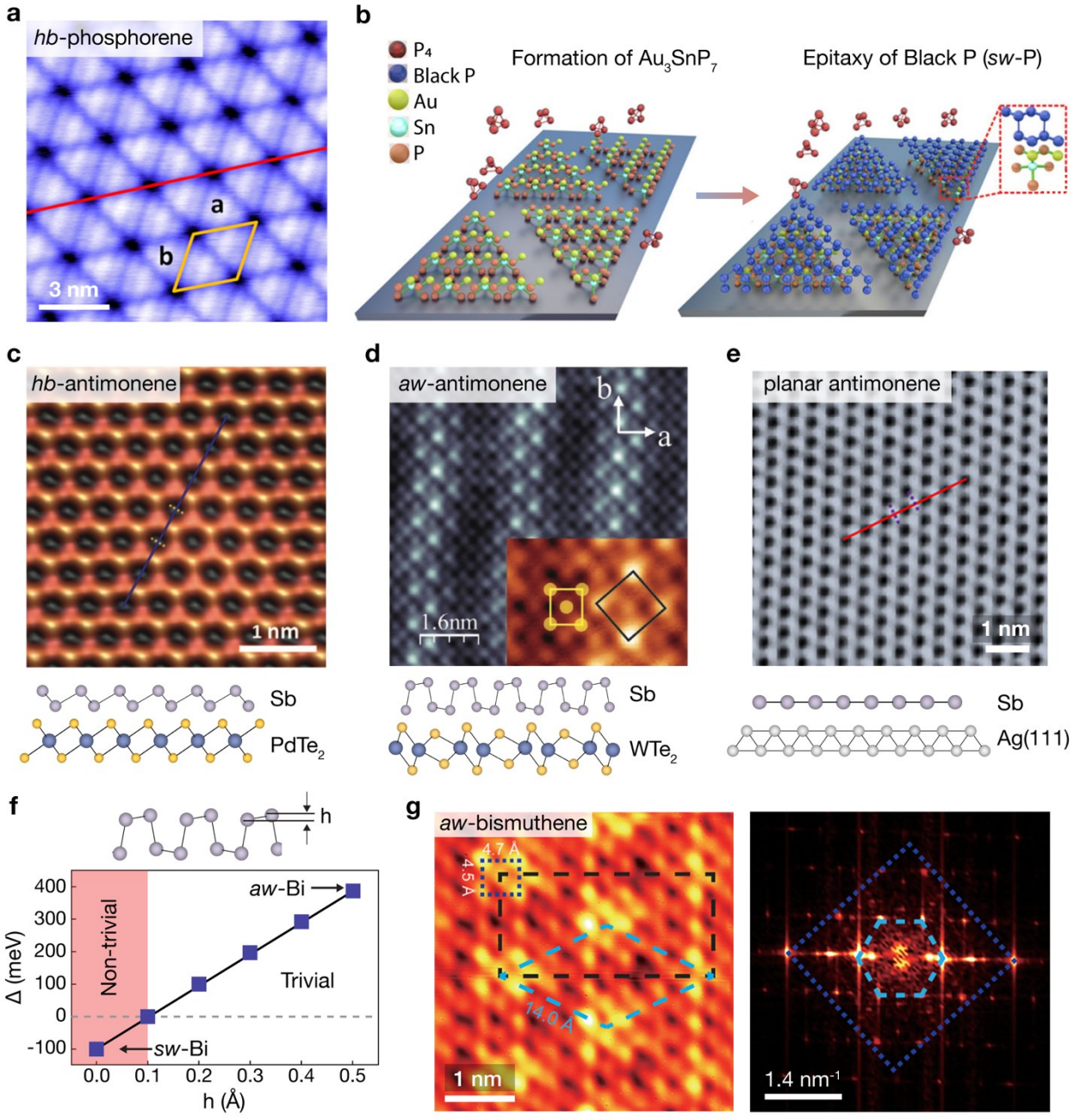


**Figure 6. Experimental demonstrations of polymorphic control in 2D group V elemental materials. a)** High-resolution STM image of *hb* (blue) phosphorene grown via MBE on Au(111). Due to strong interaction with the Au(111) substrate, *hb*-phosphorene is reconstructed in this case. Adapted with

permission from Ref.[200] Copyright 2016 American Chemical Society. **b)** The growth of large crystal domains of *sw* (black) phosphorus down to 10 nm in thickness was realized using $Au_3SnP_7$ template crystals, which have comparable structural features to *sw*-P. Adapted with permission from Ref.[273] Copyright 2020 Springer Nature under a Creative Commons Attribution 4.0 International License https://creativecommons.org/licenses/by/4.0/. **c-e)** STM images of the various polymorphs of antimonene obtained *via* MBE on different substrates: **c)** *hb*-antimonene on hexagonal $PdTe_2$ (adapted with permission from Ref.[276] Copyright 2016. John Wiley and Sons), **d)** *aw*-antimonene on orthorhombic $WTe_2$ (adapted with permission from Ref.[281] Copyright 2018 John Wiley and Sons), and **e)** planar antimonene on Ag(111) (adapted with permission from Ref.[283] Copyright 2018 American Chemical Society). **f)** Buckling height (h) dependent energy gap at the Dirac point of monolayer *aw*-bismuthene. As the buckling is reduced and approaches the *sw* structure, non-trivial topological properties emerge. Adapted with permission from Ref.[219] Copyright 2015 American Chemical Society. **g)** STM image (left) and its fast Fourier transform (right) obtained from the orthorhombic lattice of *aw*-bismuthene grown *via* MBE on a $NbSe_2$ substrate with six-fold symmetry. The preference of the *aw* polymorph over the *hb* structure in bismuth films below a few vdW layers in thickness has been observed on many substrates. Adapted with permission from Ref.[286] Copyright 2019 American Chemical Society.

# 3. Post-Transition Metal Chalcogenides

## *3.1. Group III Metal Chalcogenides*

### 3.1.1. Structures and properties of 2D group III metal chalcogenide polymorphs

The group III metal chalcogenides adopt many stoichiometries with a general formula $M^{III}{}_nX_m$, where $M^{III}$ = Ga, In and $X$ = S, Se, Te. However, most of the layered group III metal chalcogenides are of the stoichiometry $M^{III}{}_2X_2 = M^{III}X$ and $M^{III}{}_2X_3$. These structures consist of hexagonal single layers stacked with out-of-plane vdW bonding. The vdW single layers have an internal atomic layer arrangement of the form *X-M-M-X* and *X-M-X-M-X* for the $M^{III}X$ and $M^{III}{}_2X_3$ compositions, respectively (**Figure 7a)**. An exception is GaTe, which is most stable in a monoclinic structure (**Figure 7b**). The layered group III metal chalcogenides demonstrate various stacking polytypes,[297] which is well documented for InSe, GaSe, α-$In_2Se_3$, and β-$In_2Se_3$. Group III metal chalcogenides that possess layered polymorphs but have not been significantly studied in the 2D materials community include $In_2S_3$,[298] $In_3Se_4$,[299] $In_4Se_3$,[300] InTe,[301] $In_2Te_3$,[302] and $Ga_2Te_3$.[302] Consequently,

the following discussion will focus on the layered group III metal chalcogenides that have been heavily studied by the 2D community – namely, those of composition $M^{III}X$ = GaS, GaSe, GaTe, and InSe and $M^{III}_2X_3$ = $In_2Se_3$. A summary of the structures and bandgaps for these 2D group III metal chalcogenides can be found in **Table 3**. For further discussion on the synthesis, properties, and applications of 2D group III metal chalcogenides, please see the review articles by Wasala *et al.*,[303] Yang *et al.*,[304] and Cai *et al*.[305]

**3.1.1.1. $M^{III}X$ compounds.** Most of the layered $M^{III}X$ compounds exhibit a ground state InSe-type intralayer structure. These compounds include GaS, GaSe, and InSe. GaTe can also exist in the hexagonal InSe-type structure (*h*-GaTe) at high pressures, but its stable structure in the bulk is the more complex layered monoclinic structure (*m*-GaTe) depicted in **Figure 7b**.[306,307] For the InSe-type structures, three stacking polytypes are commonly observed: $2H_b$, $2H_c$, and 3R, which are known as the ε, β, and γ polytypes, respectively. The β and γ designations are also used in the $M_2X_3$ literature but denote different intralayer structures instead of stacking polytypes. To avoid confusion, we will use the Ramsdell notation (*e.g.,* 2H, 3R) to denote polytypes. Here, we differentiate the InSe-type 2H structures ($2H_b$ and $2H_c$) in analogy to the TMD literature, wherein the $2H_b$ and $2H_c$ structures have AbACaC and AbABaB atomic layer stacking motifs, respectively.[28] Both the $2H_b$ and 3R polytypes correspond to translational offsets between layers with AB and ABC vdW layer stacking, respectively. The $2H_c$ polytype has a 60º rotation between layers, such that the chalcogen atom column lies above the metal atoms and vice versa (AA' vdW layer stacking). In terms of the individual atomic layers, the $2H_b$ and $2H_c$ stacking in InSe-type $M^{III}Xs$ exhibit AbbACaaC and AbbABaaB arrangements, respectively. The $2H_b$, $2H_c$, and 3R stacking polytypes for InSe-type $M^{III}Xs$ are depicted in **Figure 7c**, and the polytypes most commonly observed for the materials discussed are summarized in **Figure 7d**. While most of these

compounds show polytypism, GaS and *h*-GaTe have only been reported in the $2H_c$ form.[308] Additionally, a first-principles calculation report by Kou *et al.* suggests that InSe may be stable in other monolayer structures, although these structures have not been observed experimentally.[309]

Since the polymorphism in most of the $M^{III}Xs$ arises from differences in stacking, the distinction in their properties primarily results from differences in their symmetries. Both InSe-type and *m*-GaTe monolayers are noncentrosymmetric. However, for the InSe-type materials, different symmetries can be achieved *via* the different stacking orders in their polytypes. In particular, the $2H_b$ and 3R polytypes for the InSe-type $M^{III}Xs$ are noncentrosymmetric, whereas the $2H_c$ stacking is centrosymmetric for even numbers of vdW layers. Since noncentrosymmetric materials are applicable for nonlinear optics[310] and anticipated to display spontaneous polarizations,[311] much attention has been directed at studying the noncentrosymmetric $M^{III}X$ polytypes. Indeed, InSe-type monolayer $M^{III}X$s are predicted by Li *et al.* to demonstrate piezoelectricity,[312] and in contrast to centrosymmetric TMDs, the $2H_b$ and 3R polytypes of the InSe-type $M^{III}X$s sustain a piezoelectric response in the multilayer form. In-plane piezoelectricity has also been confirmed in 3R-InSe by Dai *et al.*[313] Furthermore, SHG in the $M^{III}X$s has been the subject of many recent studies. Zhou *et al.* observed enhanced SHG in $2H_b$-GaSe bilayers grown using chemical vapor deposition (CVD) and nearly zero SHG signal in synthesized $2H_c$-GaSe bilayers.[314] This result demonstrates the promise of noncentrosymmetric multilayer $M^{III}X$s in high-intensity SHG, which has since been confirmed experimentally in multilayer 3R-InSe[315] and $2H_b$-InSe,[316–318] in addition to being further investigated computationally[319,320] Electronically, the $2H_b$, $2H_c$, and 3R polytypes of the InSe-type $M^{III}X$s are expected to be similar.[321–323] However, Sun *et al.*[324] calculated the carrier mobilities of $2H_c$-InSe to be larger than 3R-InSe (up to ~1.5× in the thick limit).

In contrast to the InSe-type monolayer structure, *m*-GaTe exhibits in-plane anisotropy. Huang *et al*. experimentally verified the anisotropy in exfoliated 2D flakes of *m*-GaTe using optical extinction and Raman spectroscopy.[325] Since *m*-GaTe has broken inversion symmetry, it has also been shown to exhibit SHG.[326] In addition, a recent density functional theory (DFT) study by Kosobutsky *et al.* suggests that *m*-GaTe shows a lesser degree of bandgap tunability as a function thickness than *h*-GaTe.[327]

**3.1.1.2. $In_2Se_3$.** There are two monolayer structures of vdW-layered $In_2Se_3$ polymorphs – namely, α-$In_2Se_3$ and β-$In_2Se_3$, the latter of which shares the same intralayer structure as $Bi_2Te_3$ (see section 3.3.1.1). Bulk $In_2Se_3$ also has non-layered polymorphs.[328] Similar to the InSe-type $M^{III}X$ compounds, the layered structures of $In_2Se_3$ show stacking polytypes. α-$In_2Se_3$ stacks in both the 2H and 3R polytypes, while β-$In_2Se_3$ stacks in the 1T, 2H, and 3R polytypes (**Figure 7d**).[329,330] The 1T polytype corresponds to AA stacking where the single layers are stacked directly on top of each other with no offset. 1T β-$In_2Se_3$ is also known as the high-temperature δ-$In_2Se_3$ phase.[331] The 2H polytype for $In_2Se_3$ has an AB stacking pattern with a 60º rotation between layers, while the 3R polytype has an ABC stacking pattern with only a translational offset between the layers. Additionally, distorted β structures, denoted as β', have been observed for 2D $In_2Se_3$. One of the structures reported is the result of a 1D periodic modulation along the high-symmetry direction,[332,333] and the other is a new structure with a rectangular lattice, although both are not yet fully understood.[334–336]

Since the α-$In_2Se_3$ structure is noncentrosymmetric and β-$In_2Se_3$ is centrosymmetric, the two polymorphs have significant distinctions in their properties. Firstly, α-$In_2Se_3$ is predicted to demonstrate robust room-temperature spontaneous polarization,[337] including intrinsic in-plane and out-of-plane ferroelectricity that persists down to monolayer thickness.[338] This behavior is in

contrast to conventional ferroelectric thin films in which the effect is supressed past a critical thickness. Xiao *et al.* experimentally confirmed the room temperature out-of-plane ferroelectricity of 2D α-$In_2Se_3$,[339] while Xue *et al.*[340] and Cui *et al.*[341] showed the room temperature in-plane ferroelectricity of 2D α-$In_2Se_3$. Out-of-plane and in-plane piezoelectricity have also been experimentally confirmed in 2D α-$In_2Se_3$.[342,343,313] In contrast, centrosymmetric β-$In_2Se_3$ does not exhibit ferroelectricity or piezoelectricity. However, if the β-$In_2Se_3$ structure is distorted and the inversion symmetry is broken, it could result in spontaneous polarizations. In particular, Zheng *et al.*[332] showed room temperature in-plane ferroelectricity in distorted β'-$In_2Se_3$ multilayer crystals. In terms of electronic transport properties, Tao and Gu[344] and Feng *et al.*[345] both found β-$In_2Se_3$ to be more conductive than α-$In_2Se_3$.

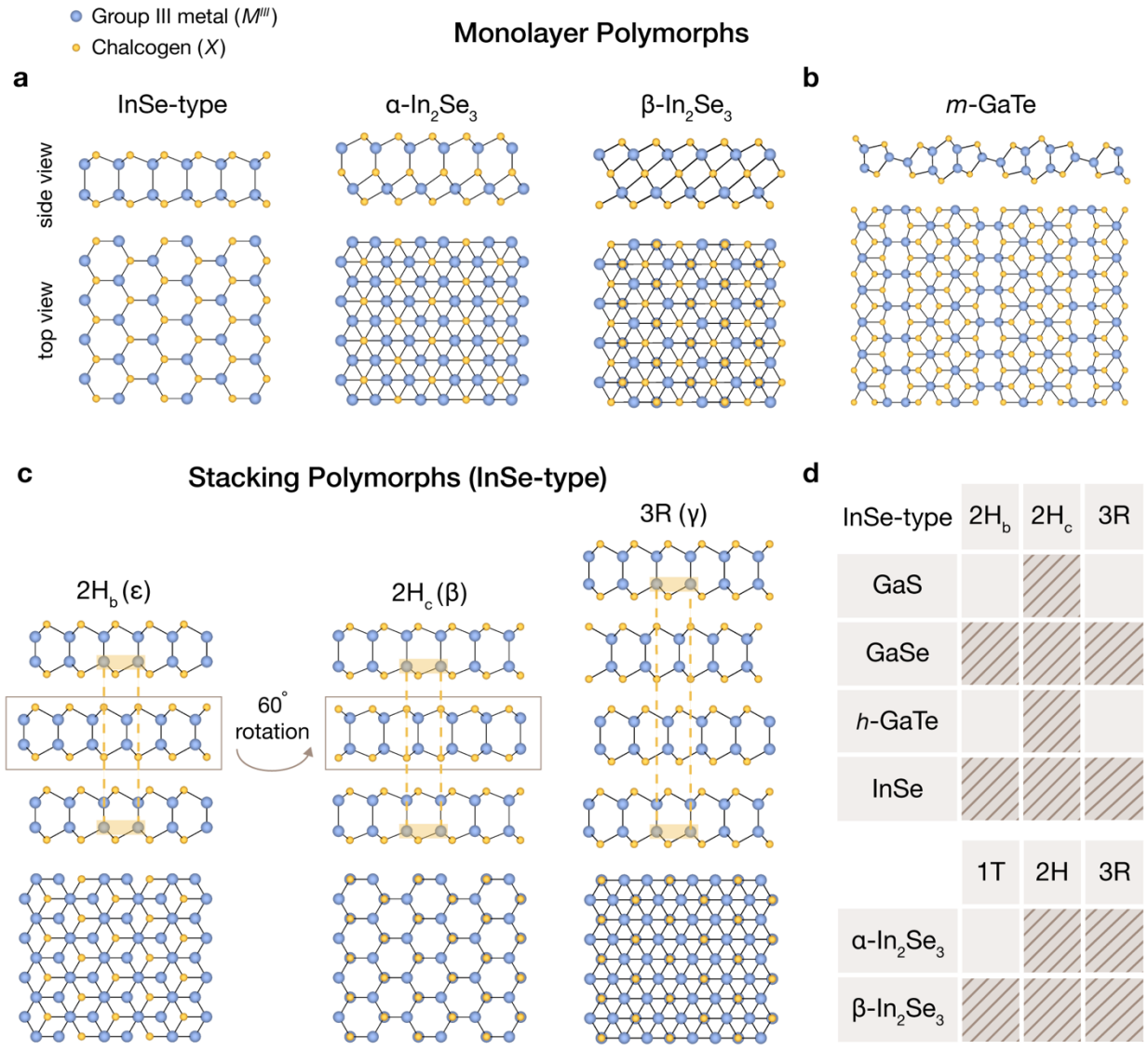


**Figure 7. 2D polymorphs of group III metal chalcogenides. a)** Monolayer polymorphs of InSe-type $M^{III}X$ compounds *(i.e.*, GaS, GaSe, *h*-GaTe, and InSe) and $In_2Se_3$. **b)** Structure of monoclinic GaTe (*m*-GaTe). **c)** Stacking polytypes for the InSe-type structures. The shaded yellow rectangle and dashed lines indicate the stacking to equivalent layers. The $2H_b$ and 3R polytypes corresponds to AB and ABC stacking, respectively. The $2H_c$ polytype corresponds to AA' stacking where the alternating layers are 60º rotated such that the metal atoms are stacked directly on top of the chalcogen atoms. The stacking polymorphs for $In_2Se_3$ are not shown here but are given by the 1T (AA stacking), 2H (AB stacking with 60º rotations between alternating layers), and 3R (ABC stacking with translational offset between layers) polytypes. **d)** Summary of commonly observed 2D group III metal chalcogenide stacking polytypes.

**Table 3. Structures and bandgaps of monolayer and bulk group III metal chalcogenides.**

| | Monolayer | | | Bulk | | | | | |
|---|---|---|---|---|---|---|---|---|---|
| | **structure type** | **lattice parameters (Å)** | **bandgap (eV)** | **polymorph or polytype** | **stacking order** | **space group** | **lattice parameters (Å)** | **bandgap (eV)** | **ref(s)** |
| **GaS** | InSe | $a = 3.64^{a}$ | $2.35^{a,c}$ - $3.325^{a,c}$ | $2H_c$ (β) | AA' | $P6_3/mmc$ | $a = 3.581$<br>$c = 15.450$ | 2.53 (I) | 346–349 |
| **GaSe** | InSe | $a = 3.82^{a}$ | $1.77^{a,c,d}$ - $3.001^{a,c,d}$ | $2H_b$ (ε) | AB | $P\bar{6}m2$ | $a = 3.755$<br>$c = 15.946$ | $1.786^{a,c,d}$<br>$2.065^{,c}$ | 323,348–352 |
| | | | | $2H_c$ (β) | AA' | $P6_3/mmc$ | $a = 3.755$<br>$c = 15.940$ | $1.949^{a,c,d}$<br>$2.117^{c}$ | |
| | | | | 3R (γ) | ABC | $R3m$ | $a = 3.755$<br>$c = 23.92$ | $1.963^{a,c,d}$<br>$2.065^{,c}$ | |
| **GaTe** | *m*-GaTe | $a = 23.14^{a}$<br>$b = 4.05^{a}$ | $1.370^{a,b}$ - $2.063^{a,b}$ | *m*-GaTe | - | $C2/m$ | $a = 17.32$<br>$b = 4.05$<br>$c = 10.54$<br>β = 104.4º | $1.620^{a,b}$<br>$1.66^{b}$ | 353,354 |
| | InSe (*h*-GaTe) | $a = 4.13^{a}$ | $1.44^{a,c}$ - $2.30^{a,c}$ | $2H_c$ (β) (*h*-GaTe) | AA' | $P6_3/mmc$ | $a = 4.06$<br>$c = 16.96$ | $0.79^{a,c}$<br>- | 346,348,355 |
| **InSe** | InSe | $a = 4.10^{a}$ | $2.97^{a,c}$ | $2H_b$ (ε) | AB | $P\bar{6}m2$ | $a = 4.00$<br>$c = 16.640$ | $1.697^{a,b}$ | 323,348,356–358 |
| | | | | $2H_c$ (β) | AA' | $P6_3/mmc$ | $a = 4.00$<br>$c = 16.640$ | $1.232^{a,b}$ | |
| | | | | 3R (γ) | ABC | $R3m$ | $a = 4.00$<br>$c = 25.32$ | $1.204^{a,b}$<br>$1.26^{,b}$ | |

| | structure type | lattice parameters (Å) | bandgap (eV) | polymorph/ polytype | stacking order | space group | lattice parameters (Å) | bandgap (eV) | ref(s) |
|---|---|---|---|---|---|---|---|---|---|
| **$In_2Se_3$** | α-$In_2Se_3$ | $a$ = 4.106[a] | 1.46[a,c] -1.92[a,c] 1.55[c,d] | 2H-α | AA’ | $P6_3mc$ | $a$ = 4.023 $c$ = 19.217 | - | 329,338,356,359,360 |
| | | | | 3R-α | ABC | $R3m$ | $a$ = 4.026 $c$ = 28.750 | 1.365[b] | |
| | β-$In_2Se_3$ ($Bi_2Te_3$-type) | $a$ = 4.048[a] | 1.15[a,c], 1.29[a,c] 1.55[c] | 1T-β | AA | $P\bar{3}m1$ | $a$ = 4.04 $c$ = 9.76 | - | 330,338,356,360–362 |
| | | | | 2H-β | AA’ | $P6_3mc$ | $a$ = 4.06 $c$ = 19.48 | - | |
| | | | | 3R-β | ABC | $R\bar{3}m$ | $a$ = 4.05 $c$ = 29.41 | 1.308[b] | |

[a] calculated value
[b] direct bandgap
[c] indirect bandgap
[d] the indirect bandgap value is close to the direct bandgap value

### 3.1.2. Polymorph control of 2D group III metal chalcogenides

**3.1.2.1. Synthesis conditions.** Due to competing polymorphs or stoichiometries, small changes in growth conditions can significantly affect the phase of synthesized group III metal chalcogenides. As studied by Huang *et al.*, the successful CVD of 2D InSe was restricted to a narrow region with low Se sublimation temperature and high $H_2$ content in an Ar carrier gas (**Figure 8a**).[316] In conditions of excess Se (from high Se sublimation temperatures) or in the absence of $H_2$ gas, 2D $In_2Se_3$ was formed. On the other hand, too low a concentration of Se or too high a concentration of $H_2$ resulted in overall poor-quality growth. For the indium-selenium system specifically, it is common to observe the formation of different compositional phases where the reaction temperature is one of the primary parameters used to control the phase of the deposited material. This method of control is well illustrated by the work of Balakrishnan *et al.*, wherein four different phases of indium chalcogenides were obtained by varying the physical vapor deposition (PVD) growth temperature.[363] They exploited the temperature gradient of a tube furnace to obtain thick nanoflakes of γ-$In_2Se_3$, β-$In_2Se_3$, α-$In_2Se_3$, and 3R-InSe along a substrate temperature gradient of 580 °C to 500 °C. It is important to note here that there is also an implicit precursor concentration gradient in the PVD method used. The reaction temperature was also tuned by Hu *et al.* for the chemical vapor transport (CVT) of 2D $2H_c$-InSe on mica at 400 °C, while 2D α-$In_2Se_3$ was synthesized at 450 °C.[364] Both of these reports suggest a narrow temperature region in which these various structures can be obtained and attest to the difficulty in achieving single-phase growth. In the MBE of 2D GaSe, higher temperatures of 575 °C resulted in pure epitaxial $2H_b$-GaSe on GaN, while lower temperatures (350-450 °C) improved continuity of the films but resulted in a mixture of $2H_b$-GaSe and $2H_c$-GaSe.[365] This behavior is consistent with reports that the $2H_b$ polytype of GaSe is more stable than $2H_c$-GaSe.[366] Similarly, *h*-GaTe is metastable[367] but can be obtained

using PVD on mica at lower temperatures (600 °C) than the more stable *m*-GaTe polymorph at 760 °C.[368] A mixture of the two polymorphs are obtained between these temperatures.

A recent report on the CVD of indium chalcogenides demonstrates the combination of various parameters for specific polymorphs. Using a high temperature of 850 °C for the In source ($In_2O_3$) and 750 °C for the substrate, Liu *et al.* obtained nanoscale structures of 2H α-$In_2Se_3$ on $SiO_2$ for upstream substrate positions and γ-$In_2Se_3$ when the substrate was positioned further downstream.[330] By decreasing the temperature of both the $In_2O_3$ and substrate by ~100 °C, 1T β-$In_2Se_3$ was synthesized. On the other hand, switching the substrate to HOPG under those same conditions resulted in 2H β-$In_2Se_3$. Overall, precise level of control over these $In_2Se_3$ polymorphs is difficult to achieve. As demonstrated by **Figure 8b**, CVD of $In_2Se_3$ on $SiO_2$ can result in a mixture of 1T β-$In_2Se_3$, 3R β-$In_2Se_3$, and 2H α-$In_2Se_3$.

The cooling rate of materials grown at elevated temperatures presents another parameter for controlling the ultimate structure of 2D $M^{III}{}_nX_m$ crystals. In a report on the CVD of 2D $In_2Se_3$ by Cui *et al.*, slow cooling (0.1 °C/min) favored the formation of α-$In_2Se_3$ over β-$In_2Se_3$.[341] Crystals synthesized with fast cooling were instead dominated by β-$In_2Se_3$. This result is consistent with previous accounts of bulk β-$In_2Se_3$ as a high-temperature phase of α-$In_2Se_3$ that reverts back to bulk α-$In_2Se_3$ upon cooling.[369] In combination with a 2D thickness effect (section 3.1.2.3),[344] quenching may help to isolate the high-temperature form at room temperature. In another report, Lin *et al.* observed that slow cooling rates (< 5°C/min ) following PVD resulted in α-$In_2Se_3$ while fast cooling rates (>100 °C/min) resulted in a $In_2Se_3$ superlattice phase.[370]

**3.1.2.2. Substrates.** The choice of substrate in the growth of 2D $M^{III}{}_nX_m$ crystals has been shown to affect the synthesized structure. By using *c*-plane sapphire and Si(111) as substrates in the metal-organic CVD (MOCVD) of $In_2Se_3$, Zhang *et al.* obtained epitaxial 2D β-$In_2Se_3$.[371] In contrast, the

use of amorphous $SiO_2$ resulted in nonlayered γ-$In_2Se_3$. Similarly, Bae *et al.* attributed the MBE-growth of *h*-GaTe on GaAs(001) to a better match in symmetry to the GaAs(001) surface than the *m*-GaTe polymorph.[372] However, upon further GaTe deposition, the additional growth was monoclinic, presumably due to relaxation of the structure into its more stable form as the epitaxial strain near the interface with the GaAs substrate diminished. Despite the existence of a quasi vdW gap, Yonezawa *et al*. reported a GaSe film with an alternative structure to the expected InSe-type structure (also referred to as 'wurtzite-like').[373] Instead, the GaSe layers near the interface with a Ge(111) substrate showed a zinc blende-like structure where the top and bottom Ga-Se bonds point in opposite directions. The authors thus make the case that despite the vdW gap, the substrate can still significantly influence the structure of the deposited 2D material. Structural preferences are also affected by substrate pre-treatments. As reported by Diep *et al.*, the MBE growth of GaSe films on GaAs(001) favored $2H_b$-GaSe, whereas growth on Se-terminated GaAs(001) resulted in $2H_c$-GaSe.[374]

**3.1.2.3. Post-synthesis processing.** The processing of 2D group III metal chalcogenides after synthesis is a frequently used method of phase conversion. In particular, thermal annealing is a prevalent way to transform one 2D group III metal chalcogenide into another. Tao and Gu converted exfoliated 2D α-$In_2Se_3$ into β-$In_2Se_3$ by annealing the flakes in argon at 533-633 K, depending on the flake thickness.[344] The authors also observed a superlattice with the conversion to β-$In_2Se_3$, as has also been observed for other reports of 2D β-$In_2Se_3$.[335] Furthermore, a dramatic decrease in resistivity is accompanied with the conversion into β-$In_2Se_3$. This result was corroborated by Feng *et al.*[345] who followed the same procedure to obtain higher field-effect mobilities (18× greater to 22.8 $cm^2V^{-1}s^{-1}$) and better photodetector performance from multilayer β-$In_2Se_3$ flakes that were thermally converted from α-$In_2Se_3$. A favorable increase in current was

observed, but the $I_{on}/I_{off}$ ratio was severely compromised due to metallic behavior. Interestingly, this behavior was also observed by Feng *et al.* in annealed 2D $2H_c$-InSe.[375] In their report, an exfoliated $2H_c$-InSe flake was annealed at 573 K in an $H_2$/argon reducing atmosphere, and the annealed crystal demonstrated an increased mobility (4× greater to 299.1 $cm^2V^{-1}s^{-1}$) and photoresponsivity, but orders of magnitude lower $I_{on}/I_{off}$ ratio. The authors determined the effect to be the result of the formation of an InSe superlattice. In contrast, a prior report by Osman *et al.* on annealed 2D $2H_c$-InSe found degradation of mobility (4× reduced from 10.32 $cm^2V^{-1}s^{-1}$ to 2.37 $cm^2V^{-1}s^{-1}$) and photodetector performance after thermal processing.[376] In that case, the exfoliated $2H_c$-InSe was annealed at 200-400 °C in an argon atmosphere without $H_2$, which resulted in partial conversion of the crystals to γ-$In_2Se_3$. Thermally induced phase transitions can also be monitored using the SHG signal intensity as has been demonstrated for the conversion of noncentrosymmetric α-$In_2Se_3$ to centrosymmetric β-$In_2Se_3$. Xue *et al.* observed a loss of SHG intensity after annealing an exfoliated α-$In_2Se_3$ crystal to 573 K,[340] and Xiao *et al.* observed the dramatic decrease of SHG signal intensity during annealing of a 4-layer thick exfoliated α-$In_2Se_3$ crystal to 700 K (which is presumably due to a transition to β-$In_2Se_3$).[339] In addition to thermal annealing, laser annealing can be used to induce a phase transformation and holds the considerable advantage of patternable conversion. As shown in **Figure 8c**, Yu *et al.* demonstrated this concept using a femtosecond laser to partially convert *h*-GaTe into *m*-GaTe,[368] which is the more stable polymorph.[367]

Cooling can also lead to structural phase transitions in the 2D group III metal chalcogenides. Zhang *et al.* recently reported the reversible phase conversion between β-$In_2Se_3$ at room temperature and a distorted β' $In_2Se_3$ structure at 77 K.[335] As shown in the STM images of **Figure 8d,** the hexagonal lattice of β-$In_2Se_3$ transformed to a rectangular lattice at low temperatures. The hexagonal lattice is recovered upon warming to room temperature. A subsequent report by Dong *et al.* on β-$In_2Se_3$

grown on $WS_2$ demonstrated the existence of a thickness dependence for this phenomenon,[336] with the transition temperature increasing with an increasing number of layers.

While the application of hydrostatic pressure is a commonly employed method to control polymorphism in bulk group III metal chalcogenides, relatively few reports use pressure as a structural tuning parameter for the 2D group III metal chalcogenides. Su *et al.* recently used hydrostatic pressure to alter the symmetry of $2H_b$-InSe.[377] They observed a continuous transition from three-fold symmetry to mirror symmetry as a hydrostatic pressure of up to 8.2 GPa was applied. The symmetry was monitored *via* the polarization of the SHG signal from the 2D $2H_b$-InSe sample and was found to be reversible upon return to atmospheric pressure. Su *et al.* attributed the change in symmetry to sliding of adjacent vdW layers under pressure.

The application of an electric current has also been shown to control $In_2Se_3$ polymorphs. Choi *et al.* demonstrated the reversible electrically-driven conversion between β-$In_2Se_3$ and γ-$In_2Se_3$.[378] This transformation is mediated by Joule heating from the applied current, which is consistent with the previous understanding of γ-$In_2Se_3$ as a higher temperature phase compared to β-$In_2Se_3$.[369] Starting with an exfoliated α-$In_2Se_3$ crystal, the device was annealed to 250 °C to convert the crystal to β-$In_2Se_3$. Pulses of 3 V and 0.7 V were then used to RESET or SET the device into its high (γ-$In_2Se_3$) or low (β-$In_2Se_3$) resistance states, respectively. Lastly, a report by Kou *et al.* suggests that charge doping, such as through electron injection or alkali metal adsorption, can be used to stabilize yet unrealized polymorphs of InSe with different intralayer structures.[309]

**3.1.2.3. Thickness.** Another factor in the polymorph control of 2D group III metal chalcogenides is the thickness of the material. Upon exfoliation of bulk *m*-GaTe crystals, Zhao *et al.* observed its spontaneous transformation into *h*-GaTe.[379] As shown in **Figure 8e**, the selected area electron diffraction (SAED) patterns of bulk GaTe and exfoliated 2D GaTe were of a monoclinic and

hexagonal lattice, respectively. The transformation occurred below a critical thickness of 4 layers. The authors performed first-principles calculations, which supported the explanation that the transformation occurred due to the balance between the interlayer interactions and surface energy shifting toward *h*-GaTe as the surface energy contribution becomes more dominant in thinner layers. Furthermore, nanoscale thicknesses in $In_2Se_3$ have been found to stabilize the β-$In_2Se_3$ polymorph at room temperature.[344,345] In the bulk, the high-temperature β-$In_2Se_3$ phase normally reverts back into α-$In_2Se_3$ at room temperature,[369] but a study by Tao and Gu suggests that the nanoscale thickness of the crystal may stabilize the metastable phase at room temperature. The authors observed that the annealing temperature required for the phase transformation demonstrated a clear thickness dependence with higher temperatures required for thinner crystals.

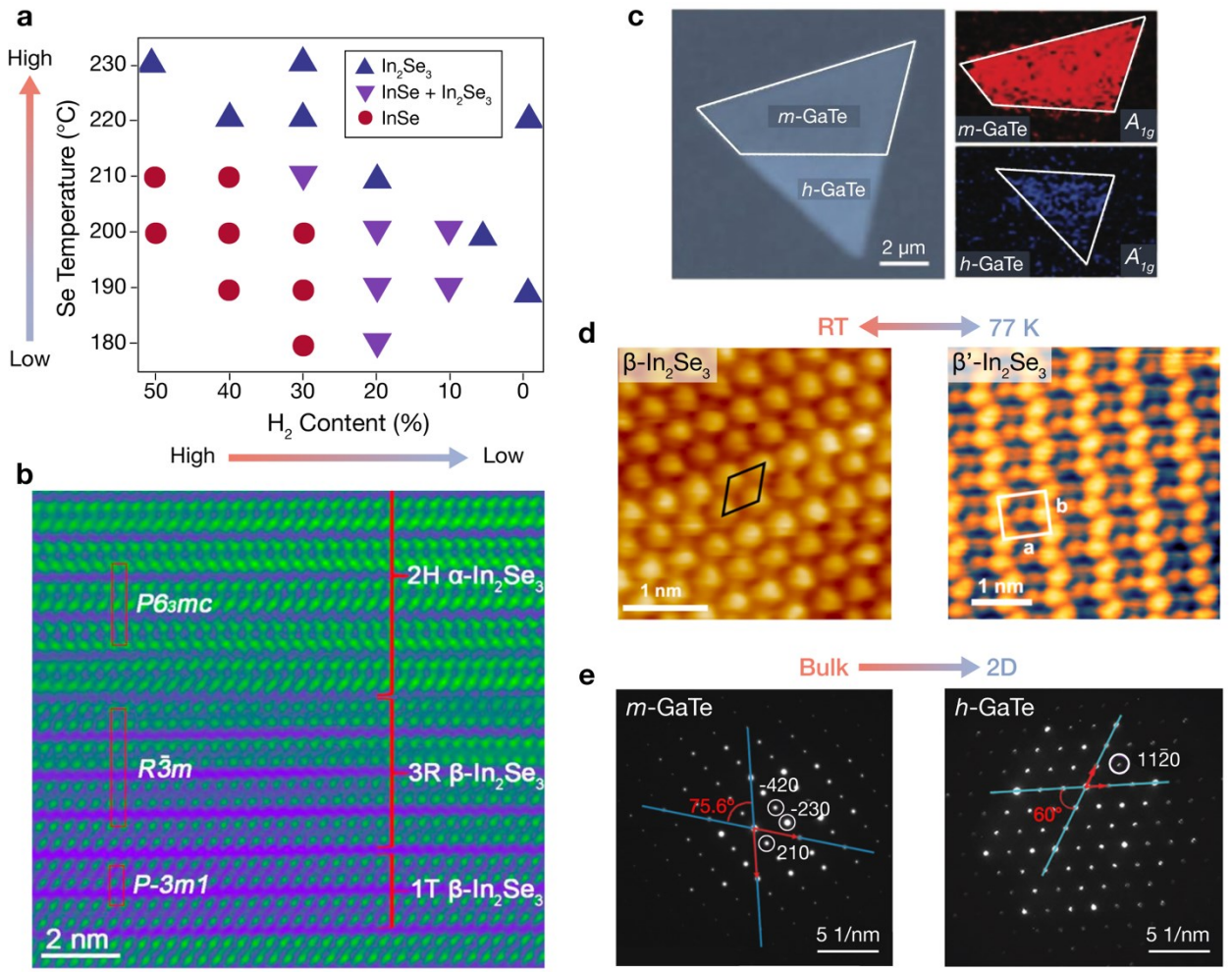


**Figure 8. Experimental demonstrations of polymorphic control in 2D group III metal chalcogenides.** **a)** Synthesis conditions for the CVD growth of InSe and $In_2Se_3$. Low Se sublimation temperatures and high $H_2$ content favor InSe over $In_2Se_3$. Adapted with permission from Ref.[316] Copyright 2018 John Wiley and Sons. **b)** HAADF STEM image showing the coexistence of α-$In_2Se_3$, β-$In_2Se_3$, and their stacking polytypes in a crystal synthesized *via* CVD. Reprinted with permission from Ref.[330] Copyright 2019 American Chemical Society. **c)** The laser-induced transformation of a section of a monolayer *h*-GaTe crystal to *m*-GaTe. Left: optical microscopy image of the partially converted monolayer *h*-GaTe domain. Right: Raman spectroscopy maps of the two domains in the optical microscopy image, showing significant *m*-GaTe $A_g$ Raman mode signal in the converted region (top) and *h*-GaTe Raman $A'_g$ Raman mode signal in the pristine region (bottom). Adapted with permission from Ref.[368] Copyright 2019 John Wiley and Sons. **d)** Atomic resolution STM image of exfoliated β-$In_2Se_3$ at RT (left) and distorted β'-$In_2Se_3$ at 77 K (right). The temperature-driven transformation is observed to be reversible. Adapted with permission from Ref.[335] Copyright 2019 American Chemical Society. **e)** The thickness-induced transformation of *m*-GaTe to *h*-GaTe upon exfoliation down to a few layers. The SAED patterns of the bulk (left) and exfoliated (right) crystals show the patterns expected for *m*-GaTe and *h*-GaTe, respectively. Adapted from Ref.[379] Copyright 2016 Royal Society of Chemistry.

## *3.2. Group IV Metal Chalcogenides*

### 3.2.1. Structures and properties of 2D group IV metal chalcogenide polymorphs

The layered group IV metal chalcogenides primarily exist in two compositions: $M^{IV}X$ and $M^{IV}X_2$, where $M^{IV}$ = Ge, Sn and $X$ = S, Se, Te. In contrast to the group III metal chalcogenides, the group IV metal chalcogenides have relatively simple binary phase diagrams, which implies that the $M^{IV}X$ and $M^{IV}X_2$ stoichiometries dominate the stable binary compositions.[380,381] However, the polytypism exhibited by the $M^{IV}X_2$s creates a rich phase space,[382–385] although this range of structures is relatively underexplored in the 2D literature. In addition to the $M^{IV}X$ and $M^{IV}X_2$ stoichiometries, the existence of layered $Ga_4Se_9$ has been reported.[386] Silicon chalcogenides are seldom studied, ambient unstable, and generally do not form layered structures.[387] The exception is $Si_2Te_3$, which crystallizes in a layered structure belonging to the $P\bar{3}1c$ space group.[388] The existence and structures of other silicon tellurides remain controversial.[389,390] Lead chalcogenides also do not form layered structures in the bulk.[391] The following discussion will focus on the stable 2D materials of $M^{IV}X$ = GeS, GeSe, GeTe, SnS, SnSe, SnTe and $M^{IV}X_2$ = $GeS_2$, $GeSe_2$, $SnS_2$, $SnSe_2$. A summary of the structures and bandgaps for these group IV metal chalcogenides is provided in **Table 4**. For further discussions on the synthesis, properties, and applications of 2D group IV metal chalcogenides, please see the review articles by Xia *et al.*,[392] Hu *et al.,*[393] and Boschker *et al.*[394]

**3.2.1.1. *MX* compounds**. For the monochalcogenides of GeS, GeSe, SnS, and SnSe, the most stable polymorph in ambient conditions is a vdW-layered GeS-type orthorhombic structure of the space group *Pnma*, which is known as the α phase of the aforementioned compounds.[383] The corresponding monolayer structure is the asymmetric washboard (*aw*) structure (**Figure 9a**). This

structure was calculated to be the most stable monolayer configuration for 2D GeS, GeSe, SnS, and SnSe.[395,396] While bulk SnTe exists in a cubic NaCl-type structure (space group *Fm*3*m*) at ambient conditions (β-SnTe),[383] it transforms into the *Pnma* (*aw*) structure at high pressures (γ-SnTe).[397] In the 2D limit, the *aw* structure was predicted to be stable for SnTe[395] and was confirmed experimentally in ultrathin films grown using MBE.[398] Bulk GeTe crystallizes in an *R3m* rhombohedral structure at ambient conditions (α-GeTe), which corresponds to a distorted NaCl structure that is also known as the A7 structure (*Strukturbericht* designation).[399,400] The A7 structure is similarly adopted by several group V elemental materials (section 2.3.1) and is shared by the low-temperature (< 100 K) SnTe phase (α-SnTe). The corresponding monolayer structure is the hexagonal buckled (*hb*) structure (**Figure 9a**). Moreover, the *hb* structure has been predicted to be stable for monolayer GeTe in a study by Li *et al.*,[401] and has been observed experimentally for both ultrathin GeTe and SnTe. The *aw* structure has also been predicted to be stable for GeTe,[395,402] but has yet to be observed. While bulk A7 (*hb*) GeTe displays short in-plane bonds and long out-of-plane bonds for a layered-like structure, it is not truly vdW bonded.[403] It should also be noted that for low-temperature bulk A7 (*hb*) SnTe, the rhombohedral distortion is much smaller than in GeTe, such that its lattice parameters are very close to its room temperature NaCl-type structure (β-SnTe), which is not vdW bonded in the out-of-plane direction.[404]

A summary of the structures observed in the group IV metal monochalcogenides is presented in **Figure 9b**. Many additional monolayer structures have been proposed but remain to be confirmed experimentally.[405–411,396,412] The stacking order in 2D $M^{IV}X$s is predicted to affect their properties,[413–416] but the observation of polytypic variation is not well documented in contrast to the $M^{IV}X_2$ compounds that show a variety of polytypes. The monolayer *aw* and *hb* structures of the $M^{IV}X$s are the same as the *aw* and *hb* structures observed in the group V elemental 2D materials

(*e.g.*, phosphorene, bismuthene), except that the atoms alternate between the metal and chalcogen. Similarly, these compounds have 10 electrons for each atom pair. As a result, the $M^{IV}X$s are known as analogues and isoelectronic counterparts to phosphorene and other group V elementals.[405,417]

In contrast to the *hb* structure, the *aw* monolayer demonstrates in-plane anisotropy,[418–422] including anisotropic spin-orbit splitting of the bands for applications in spin-transport devices.[423] Among the 2D *aw* $M^{IV}X$ compounds, GeS shows the greatest degree of in-plane anisotropy in its properties.[419,424,425] The 2D *aw* $M^{IV}X$ compounds are predicted to have large piezoelectric coefficients exceeding those of other 2D vdW materials due to their noncentrosymmetric structure in tandem with their flexibility along the armchair direction, which is the main polar direction. The 2D *aw* $M^{IV}X$ compounds are also predicted to be multiferroic, exhibiting both ferroelectricity and ferroelasticity.[426,427] Additionally, Wang *et al.* predicted large SHG susceptibility in these multiferroic compounds.[428] The first observation of 2D in-plane ferroelectricity was reported by Chang *et al.* in ultrathin *aw*-SnTe.[429] The Curie temperature was found to be much higher than in bulk SnTe, owing to the orthorhombic structure.[398] In-plane ferroelectricity, along with SHG, was also recently confirmed in ultrathin SnS by Bao *et al*.[430] However, due to the vdW layer stacking arrangement, even-numbered layers of the *aw* SnS structure, as well as the bulk form, are centrosymmetric with no net polarization or SHG. The bulk forms of other *aw* $M^{IV}X$ compounds are also centrosymmetric. Lastly, the lone electron pairs of the puckered *aw* structure are believed to be responsible for the difficulty in exfoliating and synthesizing single layers of these crystals.[431,432]

Since the rhombohedral distortion in the *hb* structure also results in a noncentrosymmetric structure, α-GeTe is well known as a ferroelectric material, including in the nanoscale limit.[433,434] Furthermore, GeTe is a phase change material with a sharp contrast in properties associated with

an amorphous to crystalline transition. This contrast is due to the presence of resonant bonding in the crystalline phase, although this bonding character is weakened by the rhombohedral distortion. This nuance to the GeTe bonding character imparts a high degree of electronic polarizability.[399] Although not as well studied, some characteristics of resonant bonding also exist in SnTe.[435] For 2D SnTe, the implications of the *aw* versus *hb* structure for its ferroelectric behavior was investigated by Kaloni *et al.*[436] In particular, they observed antiferroelectric coupling in ultrathin SnTe layers (< 6 layers), which converted to ferroelectric coupling with an increasing number of layers due to a transition from an orthorhombic (*aw*) to rhombohedral structure (*hb*). Furthermore, the cubic polymorph of SnTe was experimentally shown to be a topological crystalline insulator by Tanaka *et al.*[437] The authors suggested that despite the small rhombohedral distortion in *hb*-SnTe, which breaks the symmetry of one of the two mirror planes, it could also be a topological crystalline insulator.

**3.2.1.2. $M^{IV}X_2$ compounds.** For the $M^{IV}X_2$ compounds, two types of monolayer structures have been observed. The two germanium dichalcogenides ($GeS_2$ and $GeSe_2$) crystallize in the layered monoclinic *m*-$GeS_2$ structure,[438,439] whereas the tin dichalcogenides ($SnS_2$ and $SnSe_2$) instead form a $CdI_2$-type structure. The two structures are depicted in **Figure 9a** and summarized in **Figure 9c**. The monoclinic *m*-$GeS_2$-type structure is known as the β phase for both $GeS_2$ and $GeSe_2$ since it is a high-temperature modification, although it is stable at ambient conditions.[440,441] Additionally, $GeS_2$ and $GeSe_2$ exhibit other polymorphs (some layered) at different pressures and temperatures, but these structures are not yet studied in the 2D literature. Specifically, $GeS_2$ exhibits another monoclinic low-temperature structure with space group *Pc*,[442] not to be confused with the *m*-$GeS_2$ structure (space group $P2_1/c$) referred to here. The *m*-$GeS_2$ structure is anisotropic[443] and was shown by Yang *et al.* to have relatively weak interlayer coupling.[444] Calculations by Yan *et al.*

also found a nearly layer-independent bandgap in 2D $GeSe_2$ with experimental investigations revealing an anisotropic optical response.[445]

The $CdI_2$-type structure of $SnS_2$ and $SnSe_2$ is sometimes referred to as the 1T structure in the 2D literature, as derived from the TMDs.[446] The most common multilayer polytype for $SnS_2$ and $SnSe_2$ is 1T, although a plethora of other stacking polytypes exist in the bulk.[447–449] In a computation study by Seminovski *et al.*, the 1T polytype in $SnS_2$ was found to have a slightly larger indirect bandgap than the other common 2H polytype.[450] It should be noted that many texts refer to the 1T and 2H polytypes for $SnS_2$ and $SnSe_2$ as '2H' and '4H', respectively, in reference to the arrangement of *M*-*X* atomic layers within the vdW layer.[29] Hence, when reviewing the literature, it is helpful to refer to the lattice parameters for polytype clarity. In contrast to the *m*-$GeS_2$ structure, 2D $SnS_2$ and $SnSe_2$ are predicted to exhibit stronger interlayer coupling, as well as excitonic effects.[451] Additionally, superconductivity has been reported when 2D $SnSe_2$ was interfaced with graphene[452] or $SrTiO_3$,[453] gated by an electric-double-layer,[454] or intercalated with lithium compounds.[455]

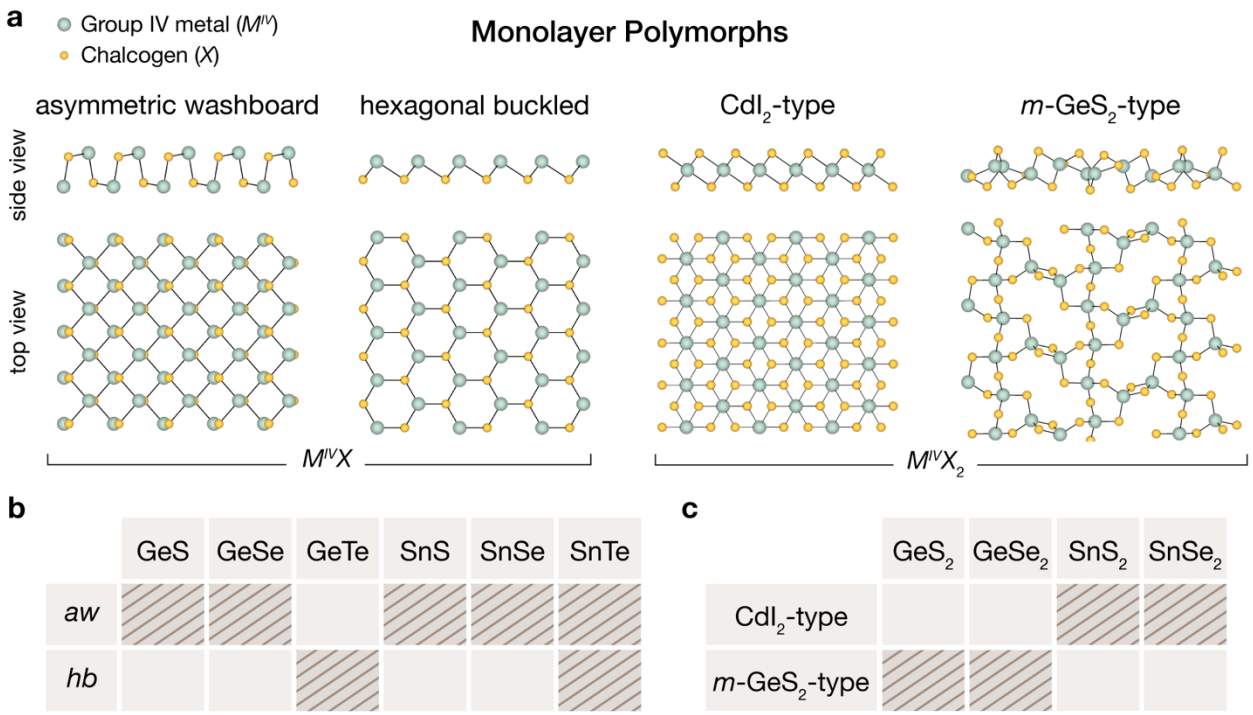


**Figure 9. 2D polymorphs of group IV metal chalcogenides. a)** Monolayer polymorphs of layered group IV metal chalcogenides with composition $M^{IV}X$ (left) and $M^{IV}X_2$ (right). **b,c)** Summary of commonly observed polymorphs for **(b)** $M^{IV}X$ and **(c)** $M^{IV}X_2$ compounds. The asymmetric washboard and hexagonal buckled structures are abbreviated as *aw* and *hb*, respectively.

**Table 4. Structures and bandgaps of monolayer and bulk group IV metal chalcogenides.**

| | Monolayer | | | Bulk | | | | | |
|---|---|---|---|---|---|---|---|---|---|
| | **structure type** | **lattice parameters (Å)** | **bandgap (eV)** | **name** | **structure type** | **space group** | **lattice parameters (Å)** | **bandgap (eV)** | **ref(s)** |
| **GeS** | *aw* | $a$ = 4.40[a,g]<br>$b$ =3.68[a,g] | 1.69 - 2.32[a,c] | α-GeS | GeS | *Pnma* | $a$ = 4.30<br>$b$ = 3.64<br>$c$ = 10.47 | 1.54 - 1.8[d] | 417,456 |
| **GeSe** | *aw* | $a$ = 4.26[a,g]<br>$b$ = 3.99[a,g] | 1.14 - 1.54[a,b] | α-GeSe | GeS | *Pnma* | $a$ = 4.39<br>$b$ = 3.83<br>$c$ = 10.83 | 1.14[c,d] | 417,457 |
| **GeTe** | *hb* | $a$ = 3.96[a] | 2.35 [a,c] | α-GeTe | A7 | *R*3*m* | $a$ = 4.156<br>$c$ = 10.663 | 0.3 - 0.8[b] | 401,458,459 |
| **SnS** | *aw* | $a$ = 4.24[a,g]<br>$b$ = 4.07[a,g] | 1.40 - 1.96[a,c,d] | α-SnS | GeS | *Pnma* | $a$ = 4.334<br>$b$ = 3.987<br>$c$ = 11.20 | 1.07 - 1.18[c,d] | 417,456 |
| **SnSe** | *aw* | $a$ = 4.36[a,g]<br>$b$ = 4.30[a,g] | 1.01 - 1.44[a,c,d] | α-SnSe | GeS | *Pnma* | $a$ = 4.445<br>$b$ = 4.153<br>$c$ = 11.501 | 0.96[c] | 417,460,461 |
| **SnTe** | *aw* | $a$ = 4.57[a]<br>$b$ = 4.56[a] | 0.70 - 1.02[a,c] | γ-SnTe | GeS | *Pnma* | $a$ = 4.48 [b]<br>$b$ = 4.37[b]<br>$c$ = 11.59[b] | 0.3[a,c,e] | 418,462,463 |
| | *hb* | - | - | α-SnTe | A7 | *R*3*m* | $a$ = 6.33[c]<br>$c$ = 6.33[c] | - | 404,464 |
| **$GeS_2$** | *m*-$GeS_2$ | - | - | β-$GeS_2$ | *m*-$GeS_2$ | $P2_1/c$ | $a$ = 6.720<br>$b$ = 16.101<br>$c$ = 11.436<br>β = 90.88º | 3.65[b] | 438,443 |
| **$GeSe_2$** | *m*-$GeS_2$ | $a$ = 7.104[a]<br>$b$ = 17.095[a] | 2.96[b] | β-$GeSe_2$ | *m*-$GeS_2$ | $P2_1/c$ | $a$ = 7.016<br>$b$ = 16.796<br>$c$ = 11.831<br>β = 90.65º | 2.7[b] | 439,445,465 |
| **$SnS_2$** | $CdI_2$<br>(1T monolayer) | $a$ = 3.68[a] | 2.41[a,c]<br>2.34[c] | 1T-$SnS_2$ | $CdI_2$ (1T) | $P\bar{3}m1$ | $a$ = 3.64<br>$c$ = 5.88 | 2.06[c], 2.157[c] | 451,466–468 |
| **$SnSe_2$** | $CdI_2$<br>(1T monolayer) | $a$ = 3.83[a] | 1.69[a,c]<br>1.8[c] on graphene | 1T-$SnSe_2$ | $CdI_2$ (1T) | $P\bar{3}m1$ | $a$ = 3.81<br>$c$ = 6.14 | 1.02[c] | 451,452,467,468 |

[a] calculated value
[b] direct bandgap
[c] indirect bandgap
[d] the indirect bandgap value is close to the direct bandgap value
[e] Obtained at high pressure
[f] The rhombohedral distortion is small enough to approach a cubic structure
[g] A structural transition to a square lattice ($a = b$) is predicted above certain temperatures[469–471]

### 3.2.2. Polymorph control of 2D group IV metal chalcogenides

The following discussion reviews recent efforts toward controlling the structure of 2D group IV metal chalcogenides. For the sake of experimental clarity, $M_{IV}X$ and $M_{IV}X_2$ compounds will be discussed together despite not being polymorphs of each other. For example, while SnS and $SnS_2$ are considered different chemical entities, the synthesis of 2D SnS is intimately related to the synthesis of 2D $SnS_2$ and are thus reviewed together.

**3.2.2.1. Synthesis conditions.** Most demonstrations of phase control in 2D group IV metal chalcogenides are based on manipulating the synthesis conditions. Firstly, the synthesis temperature in the CVD of 2D group IV metal chalcogenides is a crucial parameter in determining the resulting phase. Mutlu *et al.* used $SnO_2$ and S powders for the CVD of 2D tin chalcogenides and found that $SnS_2$ grows at lower temperatures of ~425 ºC, whereas SnS forms at a higher temperature of ~550 ºC.[472] Huang *et al.* observed a similar phenomenon in the CVD growth of SnSe and $SnSe_2$,[473] where 2D $SnSe_2$ was formed at ~430-470 ºC, whereas SnSe was formed at ~510 ºC. Both of these results are in agreement a previous study on the CVT of bulk tin chalcogenides wherein SnS grew at high temperature, $SnS_2$ at medium temperatures, and non-layered $Sn_2Se_3$ at low temperatures.[474] Additionally, a precursor concentration gradient can give rise to a variety of phases. Li *et al.* observed the presence of 2D nanocrystals of SnS, $SnS_2$ on top of SnS, and $SnS_2$ on mica substrates positioned from upstream (SnS) to downstream ($SnS_2$).[475] Since the temperature of the substrates was comparable, the authors attributed this phase evolution to the decreasing SnS:S vapor concentration from upstream (excess SnS) to downstream (excess S), although the exact precursor concentration ratios were not quantified. This concept was also corroborated in a study by Wang and Pang where thick SnSe or $SnSe_2$ flakes were obtained depending on the Se:$SnO_2$ precursor powder loading ratio.[476] SnSe was synthesized at a precursor

loading of 50 mg Se:20 mg $SnO_2$, and $SnSe_2$ was synthesized at a loading of 300 mg Se:20 mg $SnO_2$. A report by Zhang *et al*. mapped the phase of the synthesized 2D tin sulfide as a function of the CVD precursor concentration and temperature (**Figure 10a**).[477] In agreement with the previously mentioned accounts, the formation of SnS was favored at high temperatures, whereas $SnS_2$ was favored at lower temperatures. Counterintuitively, the relative increase of the sulfur precursor ($H_2S$) to the tin precursor ($SnCl_4$) favored the formation of SnS. After further investigation, this effect was found to be due to the reduction of $SnS_2$ into SnS by $H_2$ gas formed from the decomposition of the $H_2S$ precursor. Thus, increased $H_2S$ concentration resulted in increased $H_2$ concentration for the reduction of $SnS_2$ into SnS, enabling the deposition of SnS at even lower temperatures. This mechanism is in agreement with a previous report for the CVD of tin chalcogenide nanoflakes by Ahn *et al*.[478] The authors reported that SnS could be grown instead of $SnS_2$ at reaction temperatures of 620-680 ºC when $H_2$ was added to the $N_2$ carrier gas. When pure $N_2$ carrier gas was used, $SnS_2$ was synthesized. The structure of 2D SnTe can also be tuned *via* the reaction temperature. As shown in **Figure 10b**, Chang *et al.* observed higher percentages of *aw*-SnTe coverage on graphene with higher growth temperatures and low thicknesses.[479] At thicknesses greater than 8 vdW layers, either the cubic or *hb*-SnTe structure is favored (depending on the temperature of the measurement). This observation is in agreement with previous calculations by Chang *et al.*, which determined the *aw* phase to be more stable than *hb* at low thicknesses.

Notably, the aforementioned accounts of phase control in the synthesis of 2D group IV metal chalcogenides are concentrated on tin chalcogenides. With the exception of a recent report by Sutter *et al.,* in which a bulk Ge surface was sulfurized to form GeS and $GeS_2$,[480] phase control

of 2D germanium chalcogenides is limited, which may be due to the generally limited number of reports on the vapor-phase synthesis of 2D germanium chalcogenides.

**3.2.2.2. Substrates.** The role of the substrate in the structure of MBE-grown ultrathin GeTe films was recently studied. In particular, the growth of 2D GeTe films initiated as an amorphous layer on Si(111)-(7 x7) and Si(111)-(1 x 1)-H instead of crystalline *hb*-GeTe.[481,482] A study by Wang *et al.* revealed the spontaneous crystallization of GeTe films into *hb*-GeTe after a critical thickness of 4 layers when deposited on Si(111)-(1 x 1)-H.[482] The authors attributed this phenomenon to the emergence of resonant bonding, which their simulations suggested could only take place above a critical thickness. In contrast, the immediate crystallization of ultrathin GeTe was observed for deposition on Sb-terminated Si(111).[483] However, the periodicity in the initial layers was slightly larger than expected for *hb*-GeTe. The authors suggested that this alternate phase in GeTe films below 2 layers is either the cubic (without rhombohedral distortion) high-temperature structure of GeTe or is the result of disorder in the bonding. Hilmi *et al.* recently investigated the MBE growth of 2D GeTe on $Sb_2Te_3$-buffered Si(111) and also found an immediately crystalline *hb*-GeTe ultrathin film.[484] Furthermore, the $Sb_2Te_3$-buffered substrate enabled the formation of crystalline films at lower substrate temperatures than Si(111), which is supported by a previous study by Simpson *et al.*[485] The authors also observed lower GeTe post-deposition crystallization temperatures using $Sb_2Te_3$ substrates. For the formation of *aw*-SnTe, the role of the substrate is still unclear since all reports on 2D *aw*-SnTe have thus far only used epitaxial graphene on silicon carbide.[398,429,436,479] Additionally, the use of confined epitaxy was recently reported to achieve 2D $GeTe_2$. $GeTe_2$ is a metastable structure that has not been observed in the bulk due to its decomposition into GeTe and Te.[486] However, Wang *et al*. reported the formation of a monolayer of $CdI_2$-type $GeTe_2$ by templating its growth in a matrix of Te-rich $GeSb_2Te_4$.[487] Hence, the use of

substrates and their ability to template or apply strain to 2D materials may enable access to metastable structures.

**3.2.2.3. Post-synthesis processing.** The conversion of group IV metal chalcogenides from one structure into another has been demonstrated using thermal and irradiation processes. Zhou *et al*. converted $SnS_2$/graphene nanocomposites grown using hydrothermal synthesis into SnS/graphene nanocomposites using a 600 ºC annealing step in a tube furnace with argon gas flow.[488] The proposed mechanism is the loss of sulfur during the annealing. This mechanism is supported by the findings of Tian *et al.*,[489] shown in **Figure 10c,d**. In their report, a mechanically exfoliated 2D $CdI_2$-type $SnSe_2$ crystal is partially converted into *aw*-SnSe by vacuum annealing in a tube furnace at 300 ºC. The partial conversion is achieved by encapsulating a section of the $SnSe_2$ crystal with exfoliated hBN. As verified by Raman spectroscopy, the encapsulated area remained as $SnSe_2$, while the exposed region was converted to SnSe and accompanied by a reduction in thickness of ~4 nm. The implied mechanism of the $SnSe_2$ phase preservation is thus the prevention of selenium loss. The reverse conversion of 2D SnS into $SnS_2$ has been demonstrated by Sutter *et al.* using thermal annealing in excess sulfur.[490] The authors used a Knudsen cell to evaporate SnS powder and deposit 2D SnS domains on a bulk $SnS_2$ crystal substrate in UHV. At both higher and lower substrate temperatures than ~300 ºC, only SnS deposition was observed. However, at approximately 300 ºC, the conversion of deposited SnS domains into $SnS_2$ was observed, resulting in 2D $SnS_2$ with a twisted orientation with respect to the original $SnS_2$ substrate (**Figure 10e,f**). The authors suggested that this conversion can be attributed to the availability of excess sulfur from both the $SnS_2$ substrate and single sulfur species from the SnS powder source at temperatures of ~300 ºC. They support this explanation by demonstrating the conversion of 2D SnS crystals deposited on $MoS_2$ into 2D $SnS_2$ crystals following post-annealing in a tube furnace in the presence

of excess sulfur. This work demonstrates a pathway to twisted homostructures facilitated by phase conversion.

In addition to thermal annealing, the use of irradiation has also been shown to transform the structure of 2D group IV metal chalcogenides. Electron-beam irradiation in a TEM was used by Sutter *et al.* to convert $CdI_2$-type 2D $SnS_2$ and $SnSe_2$ into their *aw* monochalcogenide counterparts.[491] This conversion is driven by the loss of the chalcogen and was further promoted using increased substrate temperature. Using laser irradiation, Jeon *et al.* observed the evolution of GeTe structures in 80-nm-thick GeTe films.[458] In addition to *hb*-GeTe, the authors propose the existence of other structures, such as a monoclinic *Cm* structure, as calculated using DFT.

**3.2.2.3. Thickness.** As demonstrated by the phase diagram in **Figure 10b** for the growth of 2D SnTe, the structure of some 2D $M^{IV}X$ compounds can be affected by their thickness. As previously discussed, thickness has a significant effect on stabilizing *aw*-SnTe versus cubic (or *hb*) SnTe.[398,479] Similarly, the thickness of GeTe films also plays a role in the crystallization of *hb*-GeTe. On non-passivated substrates, films below a critical thickness of a few monolayers are amorphous before they crystallize into *hb*-GeTe above the thickness threshold.[482,483] Additionally, several computational studies have investigated the effect of thickness on the structure of *aw*-structured 2D $M^{IV}X$ compounds. For GeS, GeSe, SnS, and SnSe, reports have predicted the structural transition from the rectangular *aw* structure ($a \neq b$) to a square lattice ($a = b$) in the monolayer.[469–471] Mehboudi *et al.* calculated the critical temperatures for this transition to be $T_c$ = 175 ± 11K for SnSe and $T_c$ = 350 ± 16 K for GeSe, where the monolayer *aw* structure exists below $T_c$ and the square lattice structure above $T_c$.[469] Due to the higher symmetry in the square lattice, the material should be paraelectric. However, the direct observation of the square-latticed structure

in 2D GeS, GeSe, SnS, and SnSe has not yet been reported. The lattice parameters of SnTe and GeTe were also calculated to depend strongly on their thickness.[492]

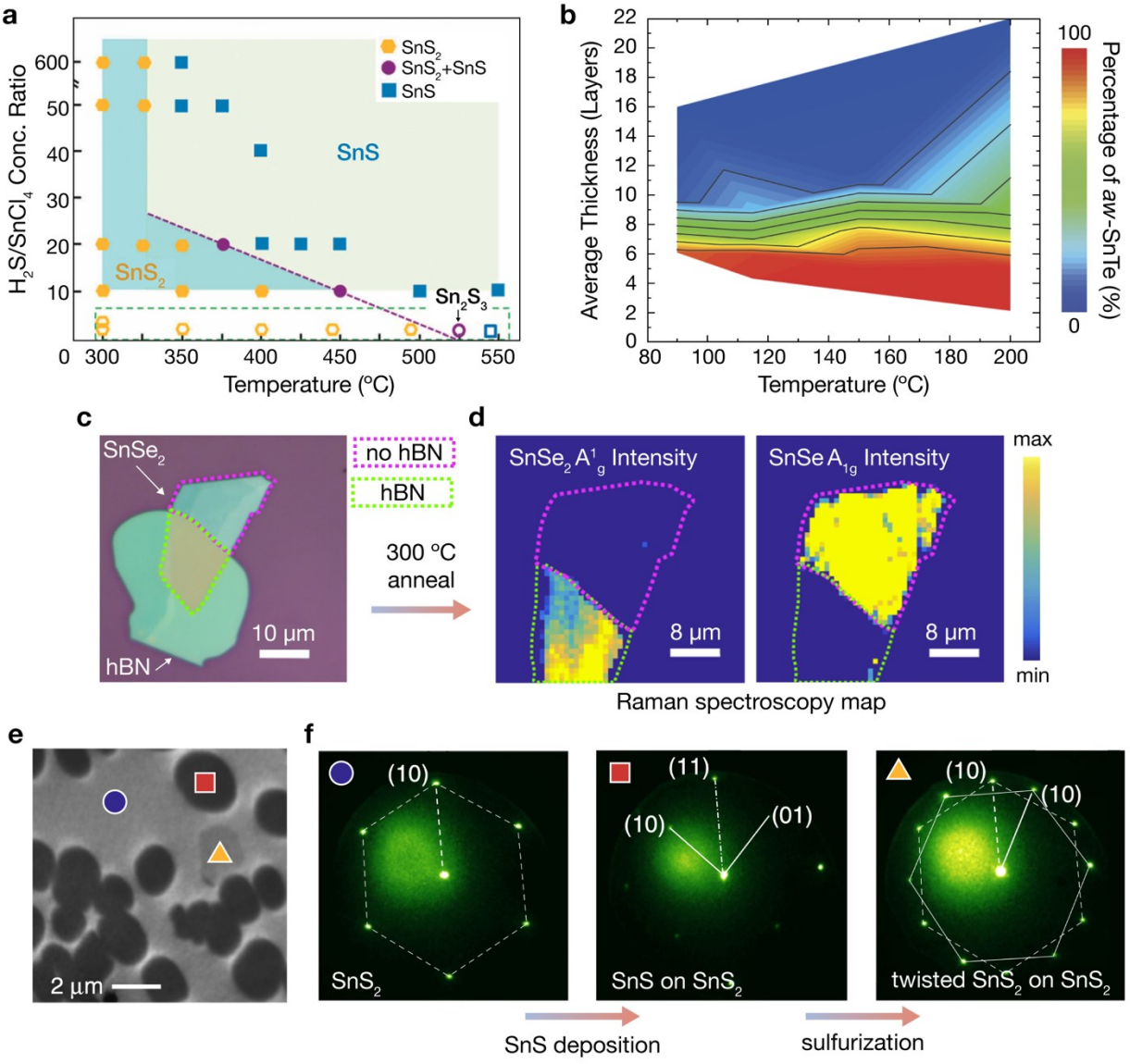


**Figure 10. Experimental demonstrations of polymorphic control in 2D group IV metal chalcogenides.** **a)** Synthesis conditions for the CVD growth of 2D SnS and $SnS_2$. High growth temperatures and high $H_2S$:$SnCl_4$ ratios favor SnS over $SnS_2$. Adapted with permission from Ref[477] Copyright 2018 Royal Society of Chemistry, which included data from Ref[493] (encompassed by the dashed green rectangle). **b)** The percentage of *aw*-SnTe (compared to cubic or *hb*-SnTe) as a function of the substrate temperature and average thickness of MBE-grown SnTe films. Adapted from Ref.[479] Copyright 2019 AIP Publishing under a Creative Commons Attribution 4.0 International License https://creativecommons.org/licenses/by/4.0/. **c)** Formation of a lateral heterojunction *via* thermal transformation of the hBN/$SnSe_2$ heterostructure shown in the optical image. **d)** Annealing the structure in **c)** results in $SnSe_2$ under the hBN and SnSe in the

unencapsulated region, as evidenced by the Raman maps showing significant $SnSe_2$ $A^1_g$ Raman peak intensity under the hBN (left) and significant SnSe $A_{1g}$ Raman peak intensity in the unencapsulated region (right). Adapted with permission from Ref.[489] Copyright 2018 American Chemical Society. **e)** Low-energy electron microscopy (LEEM) image showing the deposition of SnS (red square) and twisted-$SnS_2$ (yellow triangle) on the $SnS_2$ substrate (blue circle). **f)** Micro low-energy electron diffraction (LEED) of the hexagonal single crystal $SnS_2$ substrate (left), orthorhombic SnS islands upon SnS deposition (center), and a twisted hexagonal $SnS_2$ domain from sulfurization of deposited SnS (right). The sulfurization occurs from further SnS deposition at a temperature of ~300 ºC. Adapted from Ref.[490] Copyright 2019 Springer Nature under a Creative Commons Attribution 4.0 International License https://creativecommons.org/licenses/by/4.0/.

## *3.3. Group V Metal Chalcogenides*

### 3.3.1. Structures and properties of 2D group V metal chalcogenide polymorphs

Layered vdW group V metal chalcogenides mostly exist in the composition $M^V_2X_3$, where $M^V$ = As, Sb, Bi and X = S, Se, Te. Additionally, layered structures can be obtained from a continuous set of composition $(M^V_2)_m(M^V_2X_3)_n$ for the Sb-Te, Bi-Se and Bi-Te systems. More recently, metastable $As^VX$ and $M^VX_2$ compounds with layered structures have been accessed using high-pressure and high-temperature processing, and observed to persist at atmospheric pressure. These cases are discussed in further detail in section 3.3.2.

**3.3.1.1. $M^V_2X_3$ compounds.** Among the group V metal chalcogenides, α-$Sb_2Te_3$, α-$Bi_2Se_3$ and α-$Bi_2Te_3$ are the most explored and crystallize in the $Bi_2Te_3$-type structure at ambient conditions.[494–496] The $Bi_2Te_3$ structure type is also observed for β-$In_2Se_3$ (section 3.1.1.2), and consists of quintuple *X-M-X-M-X* layers stacked along the *c* direction with nearly octahedral coordination of the metal atoms (**Figure 11a**). Contrary to group III and IV metal chalcogenides (sections 3.1 and 3.2) and transition metal halides (section 4), polytypism is not common for group V metal chalcogenides. The $Bi_2Te_3$-type structure for these compounds is mostly observed in the 3R configuration (ABC stacking pattern with translational offsets between layers).

In contrast, the $As_2X_3$ compounds exhibit various layered structures at ambient conditions. For the sulfides ($As_2S_3$), only the monoclinic orpiment (α-$As_2S_3$, space group $P2_1/c$)[497–500] and the triclinic anorpiment (space group $P\bar{1}$)[501] polymorphs are layered. For $As_2Se_3$, the only polymorph at ambient conditions is α-$As_2Se_3$, which is isostructural to orpiment.[502,503] The crystal structures of orpiment and anorpiment are based on corrugated layers of six-membered rings of corner sharing [$AsS_3$] pyramids (**Figure 11a**). The polymorphs differ by the arrangement and orientation of the [$AsS_3$] pyramids within the layer as well as by the stacking of the neighboring layers.[501] Anorpiment has ~4% lower density in comparison to orpiment, which suggests weaker vdW interactions.[501] Both are naturally occurring minerals that are relatively hard to prepare in the laboratory since synthesis from elemental As and S yields amorphous glasses. While Espeau *et al*. successfully obtained orpiment by crystallizing a glass sample at 523 K for 1 year,[504] many researchers instead use naturally mined samples despite potential elemental contaminants such as Sb.[504–506] For $As_2Te_3$, three layered polymorphs are reported: α-$As_2Te_3$, β-$As_2Te_3$ and β`-$As_2Te_3$. The α-$As_2Te_3$ structure (space group $C2/m$) consists of complex zig-zag layers stacked along the *a* axis (**Figure 11a**).[507,508] β-$As_2Te_3$ has a $Bi_2Te_3$-type structure (space group $R\bar{3}m$), which transforms to α-$As_2Te_3$ upon heating to ~520 K.[508,509] Upon cooling to ~200 K, β-$As_2Te_3$ undergoes distortion and a 4-fold modulation along the *b* axis, yielding β`-$As_2Te_3$ (space group $P2_1/m$).[508] No experimental reports exist yet for layered nitrogen or phosphorus chalcogenides. However, recent theoretical studies predicted that monolayer forms of nitrogen or phosphorus chalcogenides could adopt the orpiment structure as well as another 2D polymorph that differs from the orpiment structure by the arrangement and orientation of the [$AsS_3$] pyramids, yet not of anorpiment type.[510,511]

A brief summary of the monolayer polymorphs of the of layered $M^{V}_2X_3$ compounds ($M^{V}$ = As, Sb, Bi and X = S, Se, Te) is presented in **Figure 11b**. The details of their structures and electronic properties are given in **Table 5**. The group V metal chalcogenides of composition $M^{V}_2X_3$ are well known as thermoelectric materials. The recent reviews by Wittig *et al*.,[512] Hong *et al*.,[513] Heremans *et al*.,[514] and Xu *et al*.[515] summarize the efforts of doping, alloying, and nanostructuring of isostructural α-$Bi_2Se_3$, α-$Bi_2Te_3$, α-$Sb_2Te$ for maximizing thermopower. In particular, the formation of solid solutions among these compounds is widely exploited for optimizing their thermoelectrical properties.[512,514] For chalcogen ratios of $X_1$:$X_2$ = 1:2, careful control over the growth can result in an ordered phase with $X_1$ atoms occupying the middle chalcogen layer for an $X_2$-$M$-$X_1$-$M$-$X_2$ quintuple layer (tetradymite structure). Such phases are reported for $Bi_2Te_2S$, $Bi_2Te_2Se$, $Bi_2Se_2S$, $Sb_2Te_2S$, and $Sb_2Te_2Se$, and are detailed in the review by Heremans *et al*.[514] Additionally, isostructural β-$As_2Te_3$ has also been explored for thermoelectric properties, with a *ZT* value up to 0.7 at 423 K for ~1% Bi substitution.[516–518] While α-$As_2Te_3$ has a lower *ZT* of 0.001, it can be significantly increased to 0.8 at 523 K with 2.5% Sn substitution.[519,520]

Concurrent with theoretical predictions in 2009,[521] α-$Bi_2Se_3$, α-$Bi_2Te_3$ and α-$Sb_2Te_3$ were experimentally reported to be 3D topological insulators,[522–526] which is discussed in detail by Hasan and Kane[527] and Heremans *et al*.[514] Given that 3D topological insulators feature topologically protected metallic surface states compared to an insulating bulk, the vdW-layered nature of α-$Bi_2Se_3$, α-$Bi_2Te_3$ and α-$Sb_2Te_3$ enables thickness tunability for controlling the contribution of the surface versus bulk states. In particular, experimental studies of gate-tunable conductance in thin crystals of α-$Bi_2Se_3$ and α-$Bi_2Te_3$ were able to resolve the contribution of surface and bulk currents.[528–532] Thickness-dependent experimental studies indicate that the

topological surface states persist down to 4 layers in α-$Sb_2Te_3$,[533] 6 layers in α-$Bi_2Se_3$,[534–536] and 2 layers in α-$Bi_2Te_3$.[537]

The thermoelectric properties of α-$Bi_2Se_3$, α-$Bi_2Te_3$ and α-$Sb_2Te_3$ are strongly related to their topological nature[538] and hence also vary with crystal thickness. Multiple theoretical studies predicted enhancement of *ZT* in few-layer samples[539–545] and solid solutions,[546–548] although experimental studies reveal more complex behavior. While enhancement of thermoelectric properties was found for few-layer α-$Bi_2Se_3$[549] and α-$Bi_2Te_3$,[550,551] later studies by Hinsche *et al.* and Guo *et al.* report the decrease of thermopower for thin samples of ALD-grown α-$Sb_2Te_3$[552] and MBE-grown α-$Bi_2Se_3$,[553] respectively. Further studies are needed to understand the effect of the larger contribution of metallic surface states on the thermoelectric properties of topologically nontrivial thin $M^V_2X_3$ samples.

Meanwhile, studies into the properties of 2D arsenic chalcogenides remain limited. Recently, Šiškins *et al.* exfoliated orpiment down to monolayer thickness and studied its mechanical and optical anisotropy. These researchers found a Young's modulus ratio for the *a* and *c* directions of $E_a/E_c = 1.7$, which is similar to black phosphorus.[505] Few-layer orpiment and α-$As_2Se_3$ have also been studied computationally and predicted to have indirect bandgaps of 3 - 3.3 eV and 2.3 - 2.6 eV, respectively.[554–556]

**3.3.2.1. $(M^V_2)_m(M^V_2X_3)_n$ compounds.** A continuous set of composition $(M^V_2)_m(M^V_2X_3)_n$ is observed for the Sb-Te (referred to as δ and γ phases in early works),[557,558] Bi-Se,[559–562] and Bi-Te[562–564] systems. The structures are composed of various ratios of stacks of $M^V_2X_3$ blocks (atomic quintuple layers of *X-M-X-M-X* in the $Bi_2Te_3$-type structure) and $M^V_2$ blocks (atomic bilayers of Sb or Bi). The $M^V_2$ structure can be recognized as the *hb* arrangement of elemental Sb and Bi (**Figure 5a**). The most studied members of the series include the 1:1 $M^V$:*X* composition (m = 1, n

= 2) of SbTe[563], BiSe[563] and BiTe[565,566] (**Figure 11c**), 2:1 $M^{V}$:$X$ composition (m = 2, n = 1) of $Sb_2Te$[567] and $Bi_2Te$,[568,569] (**Figure 11c**), and 4:3 $M^{V}$:$X$ composition (m = 1, n = 1) of $Sb_4Te_3$,[570] $Bi_4Se_3$[571], $Bi_4Te_3$.[572] Since there are two types of building blocks in these crystal structures, three interlayer gaps are possible between the blocks: the gap between quintuple layers ($M^{V}_2X_3$ to $M^{V}_2X_3$), the gap between the metal atomic bilayers ($M^{V}_2$ to $M^{V}_2$), and the gap between the two aforementioned blocks ($M^{V}_2X_3$ to $M^{V}_2$). The nature of the interlayer bonding between the blocks differs for Sb and Bi compounds. In the case of antimony tellurides, all three gaps are vdW in nature[558,573,574] and the $Sb_2Te_3$-$Sb_2Te_3$, $Sb_2$-$Sb_2$, and $Sb_2Te_3$-$Sb_2$ interlayer distances are 2.7 Å, 2.2-2.3 Å, and 2.4-2.5 Å, respectively. For comparison, the $Sb_2Te_3$-$Sb_2Te_3$ interlayer distance is 2.8 Å in the α-$Sb_2Te_3$ structure.[558] In the case of bismuth selenides and tellurides, the distances between $Bi_2X_3$ blocks remain large (2.6-2.7 Å) and hence the bonding is vdW. In contrast, the $Bi_2X_3$-$Bi_2$ interlayer distances are shorter (2.2 Å) as compared to the Sb-Te system and the bonding is considered to be weakly covalent.[560,575] As a result, the crystal structure of BiTe features vdW gaps between adjacent $Bi_2Te_3$ blocks (**Figure 11c**), whereas the crystal structure of $Bi_4Te_3$, which consists of alternating $Bi_2$ and $Bi_2Te_3$ blocks, does not feature any vdW gaps. While in most cases a given $(M^{V}_2)_m(M^{V}_2X_3)_n$ composition corresponds to a specific structure, the *n, m* pair does not uniquely define the stacking order. For example, the structure of $Sb_4Te_3$ has been observed both with[576] and without[577] the $Sb_2$-$Sb_2$ sequence, and MBE growth results in the mixture of both.[570] The $Bi_2$-$Bi_2$ sequence is less common in comparison to the $Sb_2$-$Sb_2$ sequence in the antimony tellurides, although reports exist of $Bi_2Te$ as well as further members of the series featuring $Bi_2$-$Bi_2$ neighbors.[568,569] In accordance with the trend for the *hb*-structured group V elements (section 2.3.1), the interlayer interaction (*i.e.*, *hb-hb* interaction) for $Bi_2$-$Bi_2$ sequences is stronger than for $Sb_2$-$Sb_2$.

Similar to the $M^{V}_2X_3$ compounds, members of the $(M^{V}_2)_m(M^{V}_2X_3)_n$ series show topologically nontrivial properties and are thermoelectrics.[568,574,578–582] Different surface terminations and termination-dependent electronic properties have been identified for cleaved $Sb_2Te$[573] and $Bi_4Se_3$[580] crystals by ARPES studies where a complex interplay between structure and surface electronic properties was discovered. BiTe was recently discovered to be a dual 3D topological insulator (weak topological insulator and topological crystalline insulator phases simultaneously) and also showed termination-dependent surface states.[565,575] These findings suggest ample opportunity for further study of the members of $(M^{V}_2)_m(M^{V}_2X_3)_n$ series in the 2D limit.

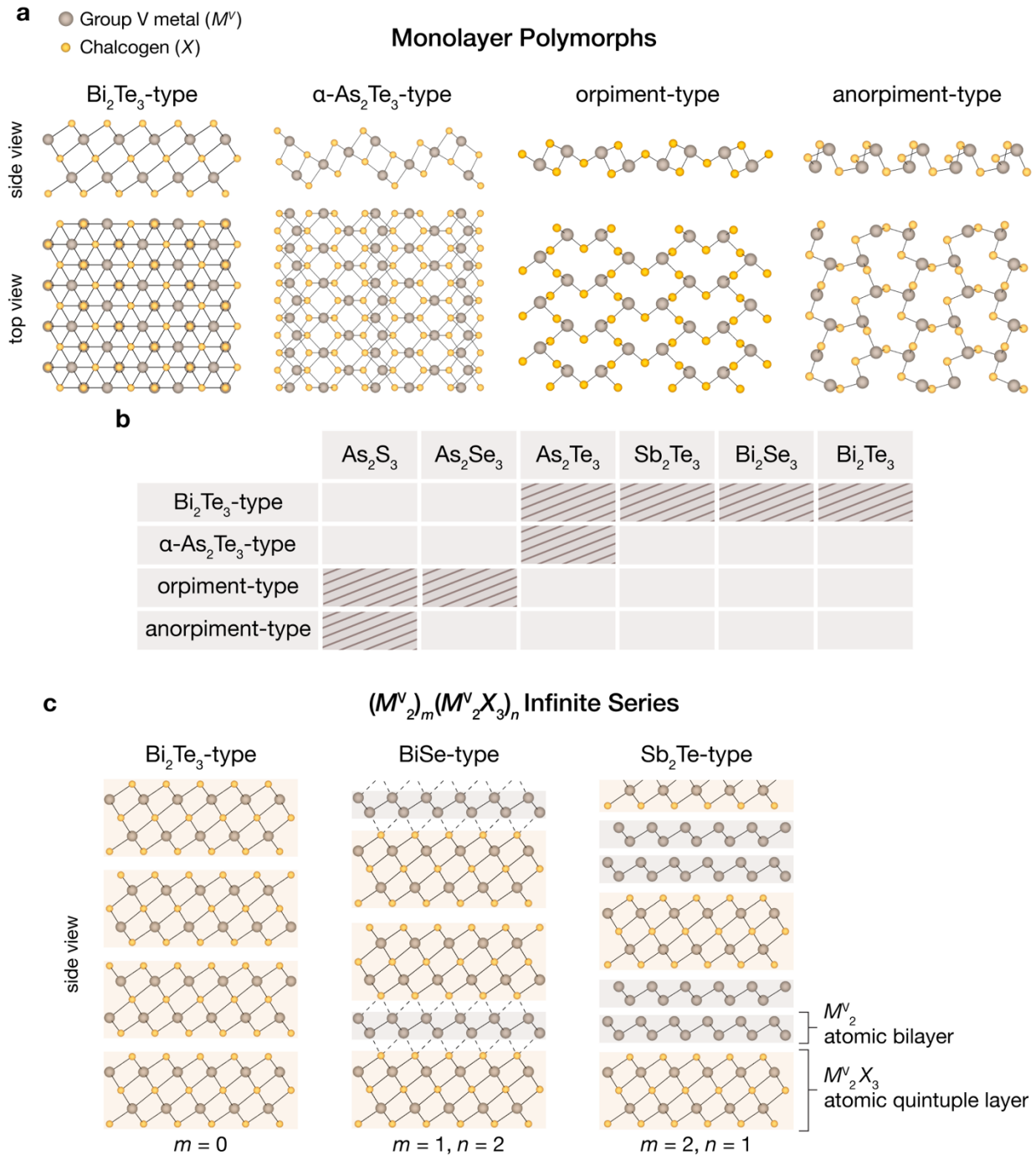


**Figure 11. 2D polymorphs of group V metal chalcogenides. a)** Structures and **b)** summary of monolayer polymorphs for the layered group V metal chalcogenides of composition $M^V_2X_3$. $As_2Te_3$ also exhibits a distorted $Bi_2Te_3$-type structure not pictured here. **c)** Illustration of the modular structures of the $(M^V_2)_m(M^V_2X_3)_n$ infinite series using $Bi_2Te_3$, BiSe, and $Sb_2Te$ as examples. The structures are composed of blocks of $M^V_2$ atomic bilayers in a hexagonally buckled arrangement and $M^V_2X_3$ atomic quintuple layers in a $Bi_2Te_3$-type structure with a ratio of $m$:$n$ $M^V_2$: $M^V_2X_3$ blocks. The dashed lines in the BiSe-type structure indicate the variable nature of the bonds, which are weakly covalent for Bi compounds and vdW for Sb compounds.

**Table 5. Structures and electronic properties of group V metal chalcogenides of composition $M^{V}_{2}X_{3}$.**

| | | name | structure type | space group | lattice parameters (Å) | electronic properties | refs |
|---|---|---|---|---|---|---|---|
| **$As_2S_3$** | bulk | orpiment | orpiment | $P2_1/c$ | $a$ = 11.48<br>$b$ =9.58<br>$c$ = 4.26<br>β = 90.7° | direct bandgap of 2.5-2.7 eV,<br>electron mobility of ~ 1 $cm^2$ $V^{-1}$ $s^{-1}$ | 498,583–586 |
| | | anorpiment | anorpiment | $P\bar{1}$ | $a$ = 5.758<br>$b$ = 8.717<br>$c$ = 10.268<br>α = 78.15<br>β = 75.82<br>γ =89.86 | indirect bandgap of ~ 2.4 eV[a] | 501,587 |
| | monolayer | - | orpiment | – | $a$ = 11.3[a] | indirect bandgap of 3 - 3.3 eV[a] | 505,554–556 |
| **$As_2Se_3$** | bulk | α-$As_2Se_3$ | orpiment | $P2_1/c$ | $a$ = 12.077<br>$b$ =9.904<br>$c$ = 4.284<br>β = 90.46° | direct bandgap of 1.75-1.85 eV | 503,583,585,588 |
| | monolayer | - | orpiment | – | $a$ = 12.1[a] | indirect bandgaps of 2.3 - 2.6 eV[a] | 554–556 |
| **$As_2Te_3$** | bulk | α-$As_2Te_3$ | α-$As_2Te_3$ | $C2/m$ | $a$ = 14.337<br>$b$ =4.015<br>$c$ = 9.887<br>β = 95.06° | bandgap of 0.43-0.48 eV,<br>$ZT$ of ~0.001 (RT)[b] | 507,508,520 |
| | | β-$As_2Te_3$ | $Bi_2Te_3$ | $R\bar{3}m$ | $a$ = 4.047<br>$c$ = 29.498 | bandgap of 0.24-0.3 eV[a],<br>Hall mobility of ~50 $cm^2$ $V^{-1}$ $s^{-1}$,<br>$ZT$ of ~0.2 (RT)[b] | 508,516,589,590 |
| | | β`-$As_2Te_3$ | β`-$As_2Te_3$ | $P2_1/m$ | $a$ = 6.996<br>$b$ =16.241<br>$c$ = 10.254<br>β = 103.43° | bandgap of 0.39 eV[a] | 508,590 |
| | monolayer | - | $Bi_2Te_3$ | – | – | indirect bandgap of 1.1 eV[a] | 555 |
| | | - | orpiment | – | $a$ = 13.1[a] | indirect bandgap of 1.8 eV[a] | 556 |
| **$Sb_2Te_3$** | bulk | α-$Sb_2Te_3$ | $Bi_2Te_3$ | $R\bar{3}m$ | $a$ = 4.264<br>$c$ = 30.46 | topological insulator,<br>bulk bandgap of 0.24 eV, Hall mobility on the order of $10^2$ $cm^2$ $V^{-1}$ $s^{-1}$ (RT),<br>$zT$ of ~0.3 (RT)[b] | 494,591–593 |
| | monolayer[c] | - | $Bi_2Te_3$ | – | $a$ = 4.3[a] | indirect bandgap of 0.7 eV,<br>$ZT$ up to 2 (RT)[a] | 533,540,541,594,595 |

| | | | | | | | |
|---|---|---|---|---|---|---|---|
| **$Bi_2Se_3$** | bulk | α-$Bi_2Se_3$ | $Bi_2Te_3$ | $R\bar{3}m$ | $a$ = 4.143<br>$c$ = 28.64 | topological insulator,<br>bulk bandgap of 0.3 eV,<br>Hall mobility on the order of $10^3$ $cm^2$ $V^{-1}$ $s^{-1}$ (RT) and $10^4$ $cm^2$ $V^{-1}$ $s^{-1}$ (~ 2 K),<br>$zT$ of ~0.1 (RT)[b] | 496,523,596,597 |
| | monolayer[c] | - | $Bi_2Te_3$ | – | $a$ = 4.1 | indirect bandgap of 0.9 eV[a] | 534–536,598,599 |
| **$Bi_2Te_3$** | bulk | α-$Bi_2Te_3$ | $Bi_2Te_3$ | $R\bar{3}m$ | $a$ = 4.395<br>$c$ = 30.44 | topological insulator,<br>bulk bandgap of 0.14-0.165 eV,<br>Hall mobility on the order of $10^2$ $cm^2$ $V^{-1}$ $s^{-1}$ (RT),<br>$zT$ of ~0.6 (RT)[b] | 495,512,522 |
| | monolayer[c] | - | $Bi_2Te_3$ | – | $a$ = 4.4 | indirect bandgap of 0.5 eV,<br>$ZT$ up to 1[a] | 537,542–544 |

[a] calculated value

[b] doping, alloying and nanostructuring is reported to improve the *ZT* value, please refer to the text and references

[c] Properties of the few layer samples are also reported, see references in the text

### 3.3.2. Polymorph control of 2D group V metal chalcogenides

**3.3.2.1. Growth.** Polymorph control *via* growth is mostly realized for the Sb-Te, Bi-Se, and Bi-Te systems within the $(M^{V}_2)_m(M^{V}_2X_3)_n$ series. In contrast, the growth of arsenic chalcogenides primarily results in amorphous films[600] and hence polymorph control *via* growth remains challenging. A review by Ginley *et al*. summarizes efforts in growing α-$Sb_2Te_3$, α-$Bi_2Se_3$, and α-$Bi_2Te_3$ compounds using MBE.[601] Precise control over the beam flux allows access to stoichiometries beyond $M^{V}_2X_3$ to other phases belonging to the $(M^{V}_2)_m(M^{V}_2X_3)_n$ series as has been demonstrated for the MBE growth of $Sb_2Te$ and SbTe,[578] $Sb_4Te_3$,[570] Bi-Se[602] and Bi-Te [570,582,603] compounds. While it is possible to achieve growth of compounds with small *m* and *n*, the pure growth of other members of the series is highly challenging due to disorder. These polymorphs are close to each other in composition and thus even small variations in the flux or other growth conditions result in a formation of stacking faults and disorder.[570,602,603] The growth of $M^{V}_2X_3$ phases and control over $(M^{V}_2)_m(M^{V}_2X_3)_n$ stoichiometry have also been realized with CVD,[604,605] MOCVD,[606–608] MOVPE,[609] PLD,[610–612] PVT,[613] sputtering,[614,615] and other methods.[616]

While polytypism is not common for the group V metal chalcogenides, Rotunno *et al*. grew the 1T polytype of $Sb_2Te_3$ (space group $P\bar{3}m1$) in the form of nanowires using MOCVD.[617] The structure consists of Te-Sb-Te-Sb-Te quintuple layers stacked exactly on top of each other in contrast to the translational offset observed in the typical 3R stacking arrangement. The 1T polytype is believed to be stabilized by the nanowire geometry and surface energy of the facets.

**3.3.2.1. Pressure and Temperature.** The application of hydrostatic pressure, often in combination with elevated temperatures, is a common strategy for altering the structures of bulk group V metal chalcogenides. These studies may provide a starting point for future work into 2D polymorph control. Several layered polymorphs of group V metal chalcogenides accessed at high pressures

are stable at ambient conditions upon releasing the pressure, and the existence of such polymorphs indicates a possibility of achieving the structures in the 2D form.

α-$As_2Se_3$ is reported to transition to β phase (α-$As_2Te_3$) at pressures of 3-5 GPa and temperatures of 300-650 °C, and subsequently changes to γ-$As_2Se_3$ at 7 GPa and 950 °C, both of which are stable at room temperature and atmospheric pressure.[618,619] The structural details of γ-$As_2Se_3$ are unknown. At 1050 °C and 7 GPa, $As_2Se_3$ is reported to disproportionate to AsSe and $AsSe_2$, the latter of which has an $MoS_2$-type structure (space group *R*3*m*).[619] Similarly, orpiment ($As_2S_3$) disproportionates above 6 GPa and 600 °C to AsS and $AsS_2$.[620] The structure of AsS (space group *Pca*2$_1$) has As–As bonds of 2.4-2.6 Å and consists of washboard-like layers separated by vdW gaps reminiscent of the *sw/aw* structure motif observed in the group V elements and group IV monochalcogenides.[621] $AsS_2$ (space group *P*2$_1$) is composed of chains with S–S bonds (2.0 – 2.1 Å) that are separated by vdW gaps.[622] Early studies report a transition of α-$As_2Te_3$ to β-$As_2Te_3$ at 6-8 GPa.[623] However, later reports assigned the 6-8 GPa transition to metallisation of α-$As_2Te_3$ followed by a structural transition to non-layered γ-$As_2Te_3$ (isostructural to γ-$Bi_2Te_3$, space group *C*2/*c*) above ~13-17 GPa.[624,625]

Bulk $Sb_2Te_3$, $Bi_2Se_3$, and $Bi_2Te_3$ display rich polymorphism at high pressure, which is detailed in the reviews by Manjón *et al.*[626] and Morozova *et al*.[627] The α phase ($Bi_2Te_3$-type) is reported to transition to a β-phase at 8-10 GPa, which is the only layered high-pressure polymorph and features heptacoordinated *M* cations. It is worth noting that at ~4 GPa, α-$Sb_2Te_3$, α-$Bi_2Se_3$ and α-$Bi_2Te_3$ undergo isostructural phase transitions associated with anomalies in mechanical, electrical, and thermodynamic properties. This transition is often assigned to an electronic topological transition (*i.e.*, a second order isostructural phase transition associated with the change of the Fermi energy surface topology),[626] although recent reports suggest alternative mechanisms

with no change of the electronic topology.[628,629] Additional layered polymorphs of $Sb_2Te_3$, $Bi_2Se_3$ and $Bi_2Te_3$ can be accessed under both high pressure and temperature. At 4 GPa and 400-850 °C, α-$Sb_2Te_3$ transitions to a structure of space group *C*2/*m* that resembles α-$As_2Te_3$.[630,631] $Bi_2Se_3$ and $Bi_2Te_3$ can adopt alternate structures belonging to the $P2_1/m$ and *R*3*m* space groups, respectively, by quenching from 7.7 GPa and 400-1127 °C.[632,633] These polymorphs are metastable at ambient conditions and transition to α-$Bi_2Te_3$ structure upon heating.

While no bismuth chalcogenides of composition Bi$X_2$ are reported at ambient conditions, high-pressure and high-temperature synthesis (5.5−7.5 GPa, 650−1200 °C) has enabled access to novel layered $BiS_2$ and $BiSe_2$ polymorphs (space group *C*2/*m*), which feature S-S or Se-Se bonds.[634,635] Although the individual layers are formally neutral, the gap between layers (1.7 Å) is much smaller in comparison to other $MX_2$ chalcogenides such as $MoS_2$ (3.2 Å).

# 4. Layered Transition Metal Halides

Layered vdW transition metal halides (TMHs) have a general formula of a $MY_n$, where *M* is transition metal, *Y* is Cl, Br or I, and n is typically 2 or 3. However, there are examples of intermediate stoichiometries (*e.g.*, n = 8/3) as well as n > 3 (see section 4.3). With the exceptions of $ZrCl_2$[636] and $ZrI_2$[637,638] where Zr has trigonal prismatic coordination, the transition metal cations in $MY_n$ compounds are octahedrally coordinated and the edge-shared octahedra form layers that are separated by vdW gaps. For n = 2, all the metal sites in the layer are occupied, resulting in a triangular net of cations (**Figure 12a**). Lowering the metal content (n > 2) can be considered as the formation of 'vacancies' in the n = 2 triangular cation net structure. This concept is analogous to the hollow hexagon polymorphs of borophene (section 2.1.1). For n = 3, the honeycomb net of

cations is formed (**Figure 12b**). The voids can be occupied by the same metal cations to form solid solutions of $MY_2$-$MY_3$[639] or by other guest cations. The former was experimentally observed in single crystals of $VI_3$[640,641] and $VBr_3$,[642] although the partial occupancy was attributed to the presence of stacking faults in the crystals.

In comparison to metal chalcogenides, metal halides feature more ionic bonding and hence greater charge separation between the metal and halogen atoms. Such charge localization generally results in lower charge carrier mobilities. In fact, most of the TMHs are Mott insulators. Moreover, the angular momentum associated with partially filled *d* orbitals of the transition metal cations gives rise to magnetic order. As a result, layered vdW TMHs present a rich spectrum of possibilities related to 2D magnetism and spintronics. Theoretical studies predict low cleavage energies for most layered vdW TMHs,[643–646] suggesting the possibility of monolayer TMHs *via* exfoliation from the bulk or bottom-up vdW epitaxy. The exploration of 2D TMHs is relatively nascent and thus much work is still required to investigate the structures and properties of their 2D forms. For more details regarding the magnetic properties of bulk TMHs please see the review by McGuire.[647]

Due to the low vdW interlayer binding strength, stacking faults or polytypes are commonly observed in layered $MY_n$ compounds, although they are often difficult to distinguish experimentally. Stacking variations can occur during heating or cooling of $MY_n$ crystals through structural transition temperatures or during growth, [648] as well upon mechanical deformation such as during micromechanical exfoliation.[649,650] Similarly, atomic force microscopy studies of layered vdW TMHs have shown that the applied tip force can alter the structure of TMH crystals. For example, Bengel *et al.* report drastic changes of the atomic force microscopy images of transition metal trichlorides produced with large applied forces and explain their observation by tip-force-

induced surface corrugation.[651] A recent single-spin magnetometry study also reports a strong change of magnetization (most likely caused by a structural change) after physical puncture of the $CrI_3$ flake on the substrate.[652] These results indicate that even if the structure of the bulk crystal is well established, control over the symmetry and stacking becomes vital for 2D TMH samples that are often produced by scotch-tape exfoliation and thus undergo mechanical deformation during preparation.

It should also be noted that most layered vdW TMHs are not stable in ambient conditions, adding further complexity to their characterization. Reaction of the TMH with ambient water starts from the edge until the entire crystal is 'dissolved' in the absorbed water.[653] As a result, most experimental studies on exfoliated TMHs are performed in gloveboxes and vacuum chambers and/or with encapsulation schemes (e.g., sandwiching the TMH flake between hBN flakes) to protect the crystals from ambient exposure.

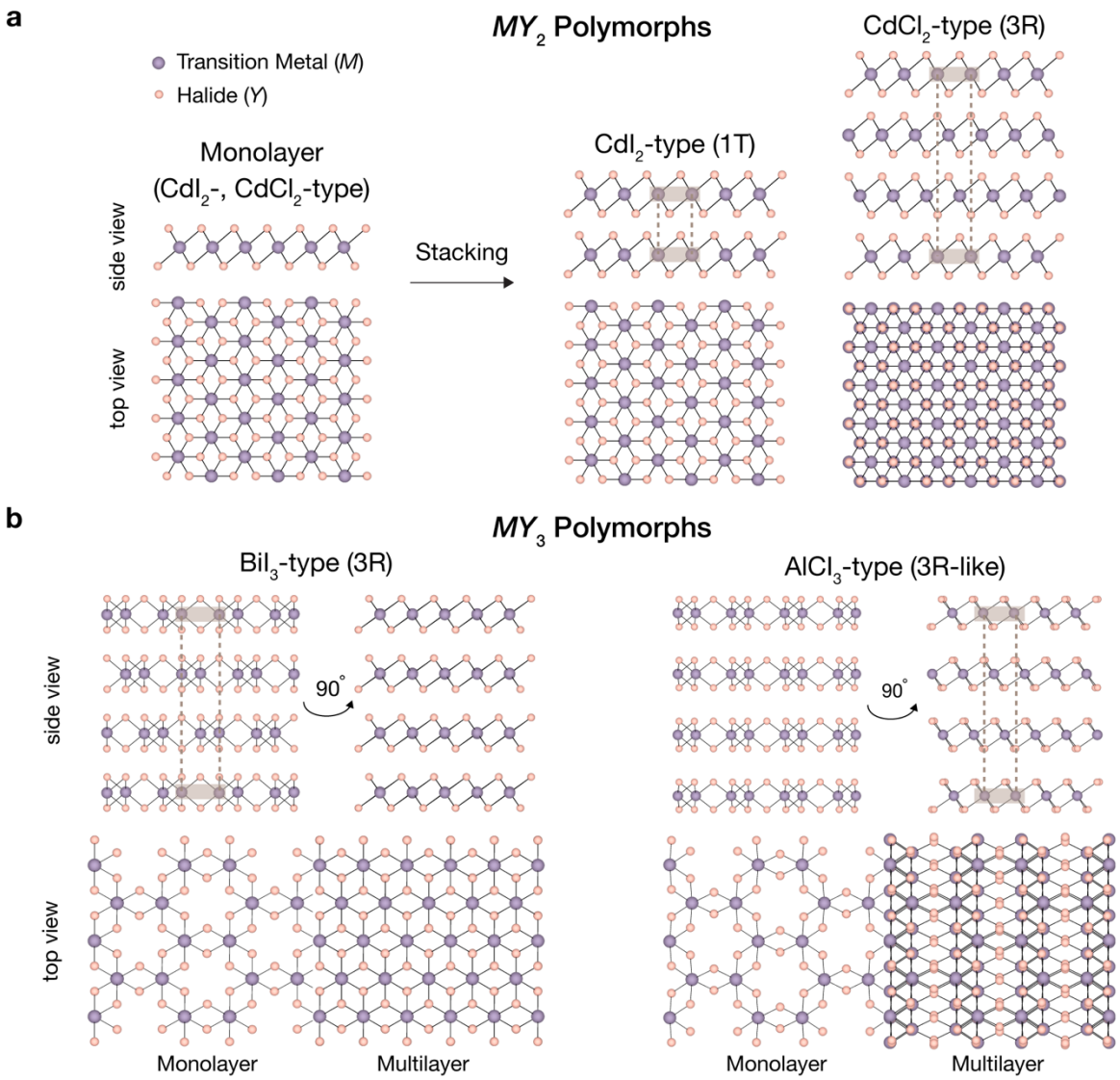


**Figure 12. 2D transition metal halide polymorphs.** Monolayer and stacking polymorphs of layered transition metal halides of composition **a)** $MY_2$ and **b)** $MY_3$. The shaded brown rectangles and dashed lines indicate the alignment of equivalent layers.

## *4.1. Transition Metal Dihalides*

### 4.1.1. Structures and properties of 2D transition metal dihalide polymorphs

Most bulk layered $MY_2$ halides crystallize in the $CdI_2$-type or $CdCl_2$-type structures, which share the same monolayer structure and differ only in their layer stacking sequence (*i.e.,* they are

polytypes). The $CdI_2$-type structure corresponds to the 1T polytype (AA stacking, space group $P\bar{3}m1$), and the $CdCl_2$-type structure corresponds to the 3R polytype (ABC stacking, space group $R\bar{3}m$). However, $ZrCl_2$ adopts an $MoS_2$-type structure[636] and $ZrI_2$ adopts both $MoTe_2$-type and $WTe_2$-type structures,[637,638] all of which correspond to trigonal prismatic coordination of the Zr cation. Limited experimental studies exist of first-row TMHs in the 2D limit, and computational studies predict octahedral coordination of the metal cation for most of these materials (**Table 6**), except the aforementioned zirconium halides as well as $TiCl_2$ and $FeY_2$. For the latter compounds, computational studies suggest that the monolayers can adopt both trigonal prismatic or octahedral coordination of the metal cation,[654–657] although a recent study by Zhou *et al.* only observed octahedrally coordinated Fe in the $FeCl_2$ monolayer grown by MBE.[658] In the 2D literature, the monolayer $MoS_2$-type structure with trigonal prismatic metal coordination is often referred to as a '2H' (or sometimes '1H') monolayer, and the monolayer $CdI_2$-type or $CdCl_2$-type structures with octahedral metal coordination are referred to as '1T' monolayers. Although the topology of the bond network in $CrY_2$ halides is similar to other $CdCl_2$-type and $CdI_2$-type compounds, the Jahn-Teller effect leads to strong distortion of the $[CrY_6]$ octahedra,[659,660] which was directly observed in the STM studies of the $CrI_2$ monolayer grown by MBE.[661,662]

Transition metal dihalides show diverse forms of magnetic order, although they remain relatively less explored compared to the trihalide family (section 4.2). In addition, most of the studies of transition metal dihalides to date have been limited to bulk materials. $MY_2$ compounds typically possess antiferromagnetic (AFM) or complex helimagnetic (HM) order with various spin structures and orientations. In particular, $VCl_2$[663–665] and $VBr_2$[663,664,666] have so-called Néel 120° magnetic structure (120° angle between neighboring spins) with spins in the *ac* plane in the bulk, while theoretical studies predict similar Néel 120° structure in monolayers but with the spins in

the *ab* plane.[667] $MnBr_2$[668] and $FeI_2$[669–671] have stripes of spins running through the crystal where the stripes are arranged with AFM order. The iron, cobalt, and nickel chlorides and bromides all exhibit ferromagnetically (FM) coupled intralayer spins with AFM interlayer interactions, although the spin orientations differ among these compounds (**Table 6**).[672,673] Finally, $MnI_2$,[668,674–676] $CoI_2$,[677–679] $NiI_2$[677,680] and $NiBr_2$[681–685] possess complex HM ground state order. These halides are also reported to show multiferroic behaviour,[676,679,685] which opens the possibility for electrical control of magnetism. Moreover, iron halide monolayers have been predicted to show half-metallicity (*i.e.*, metallic behaviour for one spin orientation and insulating for another).[645,686] A summary of the structures, properties, and magnetic ordering of $MY_2$ compounds in the bulk (experimental data) and in the monolayer form (calculated values) is presented in **Table 6**. Additionally, a review by McGuire contains further details on the magnetic properties of bulk $MY_2$ compounds.[647]

**Table 6. Structures, magnetic properties, and electronic properties of monolayer and bulk transition metal dihalides.**

| | | structure type (space group) at RT | lattice parameters (Å) | magnetic order and spin orientation | temperature of magnetic order (K) | electronic properties | ref(s) |
|---|---|---|---|---|---|---|---|
| **$TiCl_2$** | bulk | $CdI_2$ ($P\bar{3}m1$) | $a$ = 3.561, $c$ = 5.875 | AFM | 85 | – | 687–689 |
| | monolayer | trigonal prismatic | – | AFM ∥ c | – | – | 654 |
| **$TiBr_2$** | bulk | $CdI_2$ ($P\bar{3}m1$) | $a$ =3.629, $c$ = 6.492 | – | – | – | 688–690 |
| | monolayer | octahedral | – | AFM ∥ c | – | – | 654 |
| **$TiI_2$** | bulk | $CdI_2$ ($P\bar{3}m1$) | $a$ = 4.11, $c$ = 6.82 | – | – | – | 688,689,691 |
| | monolayer | octahedral | – | AFM ∥ c | – | – | 654 |
| **$ZrCl_2$** | bulk | $MoS_2$ ($R3m$) | $a$ = 3.382, $c$ = 19.378 | – | – | – | 636,688,689 |
| | monolayer | trigonal prismatic | – | – | – | – | 654 |
| **$ZrI_2$** | bulk α-$ZrI_2$ | $MoTe_2$ ($P2_1/m$) | $a$ = 6.821, $b$ = 3.741, $c$ = 14.937, β = 95.66 | – | – | – | 637,689 |
| | bulk β-$ZrI_2$ | $WTe_2$ ($Pmn2_1$) | $a$ = 3.744, $b$ =6.831, $c$ = 14.886 | – | – | – | 638 |
| | monolayer | trigonal prismatic | – | – | – | – | 654 |
| **$VCl_2$** | bulk | $CdI_2$ ($P\bar{3}m1$) | $a$ = 3.60, $c$ = 5.83 | AFM-120°, ∥ ac plane | 36 | – | 663–665,692 |
| | monolayer | octahedral | $a$ = 3.6 | AFM-120°, ⊥ c | – | insulator | 643,654,667,693–695 |
| **$VBr_2$** | bulk | $CdI_2$ ($P\bar{3}m1$) | $a$ = 3.76, $c$ = 6.18 | AFM-120°, ∥ ac plane | 30 | – | 663,664,666,691 |
| | monolayer | octahedral | $a$ = 3.81 | AFM-120°, ⊥ c | – | insulator | 643,654,667,693–695 |
| **$VI_2$** | bulk | $CdI_2$ ($P\bar{3}m1$) | $a$ = 4.057, $c$ = 6.760 | AFM | 16.3, 15 | – | 663,664,696 |
| | monolayer | octahedral | $a$ = 4.08 | AFM-120°, ⊥ c | – | insulator | 643,654,667,693–695 |
| **$CrBr_2$** | bulk | $C2/m$ | $a$ = 7.11, $b$ = 3.65, $c$ = 6.22, β = 93.88 | – | – | – | 659 |
| | monolayer | octahedral | $a$ = 3.7 | AFM | – | half-metal | 643,695 |
| **$CrI_2$** | bulk | $C2/m$ | $a$ = 7.55, $b$ = 3.93, $c$ = 7.51, β = 115.52 | – | – | – | 660 |
| | monolayer | octahedral | $a$ = 3.9 – 4.2 | FM | – | insulator | 661,662 |
| **$MnCl_2$** | bulk | $CdCl_2$ ($R\bar{3}m$) | $a$ = 3.711, $c$ = 17.59 | AFM stripe ⊥ c or HM | 2, 1.8 | insulator | 669,697,698 |
| | monolayer | octahedral | $a$ = 3.64 | multiple structures proposed | – | insulator | 643,654,693–695,699 |
| **$MnBr_2$** | bulk | $CdI_2$ ($P\bar{3}m1$)[a] | $a$ = 3.868, $c$ = 6.272 | AFM stripe ⊥ c | 2.3, 2.16 | insulator | 668,669,700 |
| | monolayer | octahedral | $a$ = 3.84 | AFM-120° or stripe ⊥ c | – | insulator | 643,654,693–695 |
| **$MnI_2$** | bulk | $CdI_2$ ($P\bar{3}m1$) | $a$ = 4.146, $c$ = 6.829 | HM | 3.95, 3.8, 3.45 | insulator multiferroic | 668,669,674–676 |
| | monolayer | octahedral | $a$ = 4.12 | AFM-120° or stripe ⊥ c | – | insulator | 643,654,693–695 |
| **$FeCl_2$** | bulk | $CdCl_2$ ($R\bar{3}m$) | $a$ = 3.598, $c$ = 17.536 | AFM ∥ c | 24 | insulator | 669,672,701 |

| | | | | | | | |
|---|---|---|---|---|---|---|---|
| | monolayer | octahedral<br>trigonal prismatic | $a$ = 3.4-3.5<br>$a$ = 3.36 | FM ‖ c | 100-160 | half-metal | 643,654–658,686,693,694,702 |
| **$FeBr_2$** | bulk | $CdI_2$ ($P\bar{3}m1$) | $a$ = 3.776, $c$ = 6.227 | AFM ‖ c | 14 | insulator | 669,672,703 |
| | monolayer | octahedral<br>trigonal prismatic | $a$ = 3.69<br>$a$ = 3.57 | FM ‖ c | 80-200 | half-metal | 643,654,656,693,694 |
| **$FeI_2$** | bulk | $CdI_2$ ($P\bar{3}m1$) | $a$ = 4.03, $c$ = 6.75 | AFM ‖ c, stripes | 9 | insulator | 669–671 |
| | monolayer | octahedral<br>trigonal prismatic | $a$ = 3.98<br>$a$ = 3.87 | FM ‖ c | 40-120 | half-metal | 643,654,656,693,694 |
| **$CoCl_2$** | bulk | $CdCl_2$ ($R\bar{3}m$) | $a$ = 3.553, $c$ = 17.359 | AFM ⊥ c | 25 | insulator | 672 |
| | monolayer | octahedral | $a$ = 3.49 | multiple structures proposed | – | half-metal | 643,654,693–695 |
| **$CoBr_2$** | bulk | $CdI_2$ ($P\bar{3}m1$) | $a$ = 3.728, $c$ = 6.169 | AFM ⊥ c | 19 | insulator | 672 |
| | monolayer | octahedral | $a$ = 3.63 | multiple structures proposed | – | insulator | 643,644,654,693–695,704 |
| **$CoI_2$** | bulk | $CdI_2$ ($P\bar{3}m1$) | $a$ = 3.985, $c$ = 6.664 | HM | 11 | insulator<br>multiferroic | 677–679 |
| | monolayer | octahedral | $a$ = 3.92 | AFM | – | insulator | 643,654,693–695 |
| **$NiCl_2$** | bulk | $CdCl_2$ ($R\bar{3}m$) | $a$ = 3.483, $c$ = 17.40 | AFM ⊥ c | 52 | insulator | 673,705,706 |
| | monolayer | octahedral | $a$ = 3.45 | FM ‖ c | 60-200 | insulator | 643,654,693–695,707–709 |
| **$NiBr_2$** | bulk | $CdCl_2$ ($R\bar{3}m$) | $a$ = 3.704, $c$ = 18.31 | AFM ⊥ c, HM | 52, 23 | insulator<br>multiferroic | 681–685,710 |
| | monolayer | octahedral | $a$ = 3.64 | FM ‖ c | 130-170 | insulator | 643,654,693–695,707–709 |
| **$NiI_2$** | bulk | $CdCl_2$ ($R\bar{3}m$)[b] | $a$ = 3.922, $c$ = 19.808 | HM | 75 | insulator<br>multiferroic | 677,680 |
| | monolayer | octahedral | $a$ = 3.92 | FM ‖ c | 130-180 | insulator | 643,654,693–695,707–709,711 |

Entries for bulk structures are based on experiment and monolayer entries are based on calculations
'Octahedral' indicates a $CdI_2$-type or $CdCl_2$-type monolayer structure with octahedral coordination of the metal cation
'Trigonal prismatic' indicates an $MoS_2$-type monolayer structure with trigonal prismatic coordination of metal cation
[a]$MnBr_2$ transitions to $CdCl_2$-type structure above 623 K
[b]$NiI_2$ transitions to monoclinic structure below 60 K

### 4.1.2. Polymorph control of 2D transition metal dihalides

Reports of 2D transition metal dihalide growth are limited to UHV-MBE $CrI_2$[661,662] and $FeCl_2$.[658] In both cases, the structure of the 2D layer resembles the bulk (*i.e.*, octahedrally coordinated Cr and Fe), although a number of theoretical studies predicted trigonal prismatic coordination for monolayer $FeCl_2$.[655–657,702] Stacking order as well as its influence on the magnetic and electronic properties of these 2D films remain to be explored. Similarly, limited studies have experimentally demonstrated polymorph control for 2D transition metal dihalides. However, the reports of structural manipulation in the bulk provide a basis for such control in the ultrathin limit. Several $MY_2$ compounds are reported to undergo temperature-induced transitions from one polymorph to another. In particular, $MnBr_2$ transitions from the $CdI_2$-type to $CdCl_2$-type structure above 623 K.[712] Furthermore, $NiI_2$ adopts a monoclinic structure below ~60 K, along with the emergence of helical antiferromagnetic order, although the exact structural details of this low-temperature $NiI_2$ phase are not yet reported.[677] Liu *et al.* report a slight decrease of the Néel temperature with decreasing thickness in PVD grown $NiI_2$,[713] although it remains to be seen whether the thickness of other $MY_2$ crystals affects the transition temperatures observed in the bulk. Multiple reports of such thickness dependencies in the transition metal trihalides (section 4.2.2) and group III metal chalcogenides (section 3.1.2.3) suggest its likelihood.

The application of hydrostatic pressure has been explored to induce structural and phase transitions in bulk $MY_2$ compounds. $FeCl_2$ transitions from the 3R polytype ($CdCl_2$-type structure) to the 1T polytype ($CdI_2$-type structure) at 0.6 GPa.[701] Two more phases of $FeCl_2$ have been reported at higher pressures, although both are of the $CdI_2$-type structure. Specifically, at pressures above 32 GPa, the spins cant away from the *c* axis and the Fe *d* electrons delocalize, leading to an insulator-to-metal transition and collapse of magnetisation at higher pressures.[714] A similar

insulator-to-metal transition has been observed for $FeI_2$.[714] $CoCl_2$ was shown to transition from the 3R polytype ($CdCl_2$-type structure) to a 2H polytype ($CdI_2$-type modification) at 0.5 GPa followed by another transition to the 1T polytype ($CdI_2$-type structure).[715] Further pressurization results in an insulator-to-metal transition at ~70 GPa. Interestingly, metallization of $CoCl_2$ was found to occur due to *p*-*d* charge-transfer bandgap closure with the 3*d* electrons still localized, meaning that metallization and magnetism can coexist until the occurrence of 3*d* electron delocalization at 180 GPa. An insulator-to-metal transition was also found for $NiI_2$ at 16 GPa and is associated with charge-transfer gap closure.[680] Since $NiI_2$ is non-magnetic above 19 GPa, the existence of a new antiferromagnetic-metallic phase has been proposed between 17 and 19 GPa.[716]

Alloying has also been used to tune the structures of $MY_2$ compounds. Specifically, since all nickel halides have the same $CdCl_2$-type structure, full solid solutions exist between $NiBr_2$ and $NiI_2$. This strategy has been demonstrated to decrease the Néel temperature upon Br substitution in $NiI_2$.[717] Additionally, $NiBr_2$ has been shown to change from the $CdCl_2$-type structure to the $CdI_2$-type structure upon Co substitution (around 56-76% of cobalt). The temperature-composition phase diagram of the magnetic transitions shows that increasing the Co content decreases the Néel temperature of the first $NiBr_2$ transition (from a non-commensurate to a commensurate antiferromagnetic structure) to 21 K at 56% Co concentration.[718]

## *4.2. Transition Metal Trihalides*

### 4.2.1. Structures and properties of 2D transition metal trihalide polymorphs

Most layered transition metal trihalides have $BiI_3$-type or $AlCl_3$-type structures.[647] In both cases, the monolayer structure is based on the honeycomb cation sublattice, which can be constructed

from the $MY_2$ monolayer by 'removing' every third metal cation. Both $MY_3$ polymorphs have similar stacking sequences: strictly 3R for $BiI_3$-type (ABC stacking, space group $R\bar{3}$) and '3R-like' for $AlCl_3$-type (ABC stacking, space group $C2/m$). The latter has a different layer shift direction compared to the $BiI_3$-type structure (**Figure 12b**). Furthermore, the $AlCl_3$-type structure has two types of crystallographic halide sites that allow for distortion of the [$MY_6$] octahedra and hence several different *M-Y* and *M-M* distances. In most cases, the distortion is minimal such that the $BiI_3$-type and $AlCl_3$-type structures can essentially be considered polytypes. However, if the distortion is strong (*e.g.*, α-$MoCl_3$ in section 4.2.1.4), then $BiI_3$-type and $AlCl_3$-type structures should be considered as polymorphs rather than polytypes.

Polymorphism and polytypism in vdW-layered $MY_3$ compounds play a crucial role in determining their properties. Similar to the previous discussions on group III and IV metal chalcogenides (section 3.1.1 and 3.2.1, respectively), the absence of an inversion center results in strong SHG. Moreover, differences in the layer stacking order yield different topology of magnetic exchange interactions, which in some cases causes different magnetic orders in two polytypes of the same material (*e.g.*, $CrI_3$ in section 4.2.1.2). Similar to the layer-dependent ferroelectric properties of SnS and SnTe,[430,436] thickness-dependent magnetism is observed in $CrBr_3$ and $CrI_3$. Furthermore, multiple $MY_3$ compounds are reported to transition from one polymorph to another upon cooling. For many $MY_3$ compounds, this transition is crucial in determining their properties, especially in the few-layer limit. A summary of the structure type, properties, and transition temperatures of $MY_3$ compounds is provided in **Table 7**.

**4.2.1.1. Vanadium triiodide.** Various crystal structures for the room-temperature and low-temperature forms of $VI_3$ have been proposed.[640,719–721] Recent Raman spectroscopy studies indicate a high-temperature $AlCl_3$-type structure ($C2/m$),[721,722] which transitions to a $BiI_3$-type

structure ($R\bar{3}$) upon cooling.[719,721] In contrast, a recent X-ray diffraction study suggests that $VI_3$ adopts a $BiI_3$-type structure at room temperature and transitions to a monoclinic phase at 79 K and to a triclinic phase at 32 K,[723] although the exact structural details are unknown.[723] Furthermore, two FM transitions are reported at ~50 K (second-order) and ~36 K (first order) that merge at a pressure of 0.6 GPa.[641,724] At 2 K, $VI_3$ has large out-of-plane magnetic anisotropy with four-fold symmetry and weak in-plane magnetic anisotropy with six-fold symmetry, but the exact ground state magnetic structure remains unknown.[725] Recent computational studies of bulk and monolayer samples suggested that $VI_3$ is a 2D Ising ferromagnet (easy *c*-axis magnetization).[726] Wide-field nitrogen-vacancy microscopy measurements allowed the imaging of magnetic domains and domain reversal (at fields < 1 T at 5 K) for few-layer $VI_3$ flakes encapsulated using hexagonal boron nitride.[727] The authors observed magnetic signal down to bilayer samples but no magnetization was observed for monolayers, possibly due to imperfect encapsulation and degradation. Moreover, for few-layer $VI_3$ (2-9 layers), the authors observed lower magnetization in comparison to bulk $VI_3$ that could be explained by AFM interlayer coupling, as supported by computation modelling.[727] In line with these findings, Wang and Long considered two possible structures of the $VI_3$ bilayer and concluded that either the FM or AFM ground state is favored depending on the stacking order.[728] These results imply that stacking sequence (*i.e.*, polytypism) in $VI_3$ has a dramatic influence on its magnetic configuration. In contrast, Long *et al*. predicted stacking-independent ferromagnetism in bilayer $VI_3$.[729] Therefore, more experimental studies are needed to clarify the magnetic order in $VI_3$ in the few-layer limit.

Experimental studies report that bulk $VI_3$ is a semiconductor with a bandgap between 0.6 and 0.7 eV.[640,720] Correspondingly, theoretical studies predicted that bulk $VI_3$ is a Mott-insulator with a gap of 0.9 to 1 eV.[719,720,726,728] However, some studies predict half-metallicity with no

bandgap.[640,730,731] While there are no experimental reports on electronic transport in 2D $VI_3$, recent theoretical studies predict that monolayer[726–728,732] and bilayer[727] $VI_3$ are Mott insulators while the trilayer is a half-metal.[727] Long *et al.* predicted bilayer $VI_3$ to also be a half-metal.[729]

**4.2.1.2. Chromium trihalides.** Chromium halides are the most studied of the transition metal halides. A number of unique properties are observed in these materials including thickness-dependent and stacking-dependent magnetism, giant tunneling magnetoresistance, and electrical control over the magnetic state. From Cl to I, the increase in atomic number results in larger SOC as well as larger Cr-Cr distances that result in weaker direct exchange and dominant super exchange interactions. All bulk $CrY_3$ halides possess a high-temperature $AlCl_3$-type structure and transition to a $BiI_3$-type structure upon cooling, although this transition occurs above room temperature for $CrBr_3$. The transition temperatures are given in **Table 7**. Notably, contrary to the bulk, micromechanically exfoliated $CrCl_3$ and $CrI_3$ do not show the transition into the rhombohedral $BiI_3$-type structure and instead show signs of the monoclinic $AlCl_3$-type structure at low temperatures. A discussion on the proposed mechanisms for this discrepancy between bulk and exfoliated samples of $CrCl_3$ and $CrI_3$ is provided in section 4.2.2.

Chromium halides possess different degrees of ambient stability with the chloride being the most stable and the iodide being the most reactive with moisture.[733] Exfoliated $CrI_3$ flakes degrade in air within minutes, and the degradation is accelerated under optical illumination.[653]All halides show insulating behavior and therefore their properties are often probed by fabricating tunneling devices. These measurements typically use graphene contacts in addition to sandwiching between two hexagonal boron nitride flakes, where the flake stacking is performed in inert environments, in an effort to minimize ambient degradation.

Chromium halides possess a range of magnetic ordering behavior, especially in the 2D thickness regime. Bulk $CrCl_3$ establishes its magnetic order in two stages (at 17 and 14 K),[734,735] and the ground state magnetic structure has interlayer AFM coupling with FM ordered in-plane spins with weak magnetic anisotropy.[734,736] In few-layer $CrCl_3$ crystals, the interlayer exchange has been observed to be an order of magnitude larger in comparison to bulk $CrCl_3$ (**Figure 13a**). Furthermore, exfoliated $CrCl_3$ flakes do not exhibit the monoclinic to rhombohedral structural transition that occurs at 240 K for bulk crystals (**Figure 13b**).[650] Both bulk $CrBr_3$[737] and $CrI_3$[648,738,739] establish FM order at low temperature (37 K and 60.5 K, respectively) with the spins lying along the *c* axis. Recent magnetometry[740], photoluminescence[741] and tunneling measurements[742] on exfoliated flakes have shown that $CrBr_3$ remains FM down to the monolayer limit. However, exfoliated $CrI_3$ crystals instead exhibit AFM order below 45 K as measured by magnetooptical Kerr effect (MOKE),[743] photoluminescence[744] and Raman spectroscopy,[745,746] and single-spin microscopy.[652] While the spins in exfoliated $CrI_3$ are still of FM order within the layer, the layers are instead AFM coupled. As a result, exfoliated $CrI_3$ crystals with an even number of layers show net AFM behavior, whereas flakes with an odd number of layers show net FM order due to the uncompensated magnetisation of a single layer. This observation has triggered significant attention for $CrI_3$ despite of its high ambient instability.

As discovered in spectroscopic and computational studies, the origin of the distinct magnetic behaviour of thin $CrI_3$ flakes (AFM below 45 K) compared to bulk crystals (FM below 60.5 K) lies in polymorphism, and more specifically, the layer stacking arrangement. Similar to $CrCl_3$, Raman spectroscopy and SHG showed that thin flakes of $CrI_3$ remain in the monoclinic $AlCl_3$-type structure and do not undergo the structural transition at 210 K to the rhombohedral $BiI_3$-type structure as observed for bulk crystals.[747,748] This insight is consistent with theoretical

studies showing that the interlayer exchange interactions of the $AlCl_3$-type structure favor AFM order while those of the $BiI_3$-type phase favor FM order.[749–752] Stacking-dependent magnetic order (FM versus AFM) has also been observed in bilayer $CrBr_3$ grown using MBE (**Figure 13c,d**) as discussed further in section 4.2.2.[753]

The fabrication of devices from exfoliated chromium trihalide crystals has enabled further investigation into their unique 2D magnetic properties. $CrCl_3$ has been exfoliated down to the monolayer limit[733,735] and fabricated into tunneling heterostructures for probing the tunneling current through $CrCl_3$ as a function of its thickness, applied magnetic field, and temperature.[650,754–756] These studies allowed the construction of the magnetic phase diagram of exfoliated $CrCl_3$ and proposed a theoretical model for the spin-flip and spin-flop transitions.[754,755] Ghazaryan *et al.* discovered magnon-assisted tunneling through $CrBr_3$, which opens the possibility for spin filtering and spin injection.[742] At room temperature, exfoliated $CrI_3$ shows *n*-type semiconducting behaviour with charge carrier field-effect mobilities on the order of 0.001 $cm^2\ V^{-1}\ s^{-1}$, whereas $CrI_3$ is insulating at low temperatures where magnetic ordering emerges.[757] Additional studies of few-layer $CrI_3$ flakes showed giant tunneling magnetoresistance due to the spin-filtering effect as a result of AFM order,[757–760] memristive behavior,[761] spin tunnel field-effect transistors,[762] in addition to other phenomena.[763] Furthermore, electrostatic control of magnetism in bilayer $CrI_3$ has been achieved by switching from AFM to FM order at an electron doping level of $\sim 3 \times 10^{13}$ [764–766] or with an electric field on the order of 1 $V\ nm^{-1}$ in a dual-gated geometry.[767–769]

**4.2.1.3. Ruthenium trichloride.** The exact structures of $RuCl_3$ are still under debate due to stacking faults in the crystals and similarities between possible polytypes. Both a trigonal phase (space group $P3_112$)[770–772] and a $AlCl_3$-type monoclinic phase[773] have been reported at room temperature. Cao *et al*. reported that the monoclinic structure persists throughout the whole

temperature range in $RuCl_3$ single crystals with minimal stacking faults.[774] However, recent reports suggest a broad hysteretic transition (from 60 to 170 K) from the monoclinic $AlCl_3$-type high-temperature phase into a rhombohedral $BiI_3$-type structure, similar to Cr$Y_3$ halides.[775–777] Additionally, a recent study by Dai *et al.* revealed reconstruction of the surface monolayer of bulk $RuCl_3$ crystals using surface-sensitive LEED.[778] The authors proposed that Cl vacancies on the surface of the flakes likely induced surface monolayer buckling and concomitant braking of the inversion symmetry. Hence, the surface of $RuCl_3$ crystals may be different from the bulk structure, which is a phenomenon also suggested for $CrI_3$ as discussed in section 4.2.2.

$RuCl_3$ crystals show stacking-dependent magnetic transitions. Crystals with a minimal amount of stacking faults generally show only one sharp transition at 7 K,[771,774] which corresponds to the so-called in-plane zigzag order and AFM alignment of layers with ABC stacking. $RuCl_3$ crystals that posses more stacking faults instead show a magnetic order transition at 14 K, or both 14 K and 7 K.[771,774,779] $RuCl_3$ powders show only the broad 14 K transition. Moreover, crystals that show the transition at 7 K can be transformed into crystals with only the 14 K transition *via* mechanical deformation.[771,774]

$RuCl_3$ has attracted significant theoretical and experimental attention as it was identified as a candidate for the realization of a Kitaev spin liquid state.[780–782] Signatures of the Kitaev spin liquid state in $RuCl_3$ (fractional magnetic excitations, Majorana fermions) have been observed by a number of techniques including neutron scattering,[783,784] NMR,[785] and half-quantized thermal Hall effect.[786,787] For more details on the topic of realization of Kitaev spin liquid states, please see the recent review by Takagi *et al*.[782] Magnetic fields can induce the transition from the ordered zigzag phase into a disordered state possibly related to the Kitaev quantum spin liquid, although the exact magnetic field–temperature phase diagram of $RuCl_3$ is not fully established.[786,788,789]

Studies of exfoliated $RuCl_3$ flakes have uncovered the effect of flake thickness on the emergence of the spin liquid state. Raman spectroscopy measurements have shown the presence of the magnetic scattering continuum down to monolayer thicknesses, indicating a persistent proximate quantum spin liquid state in the 2D limit.[790–792] Additionally, these measurements indicated a lowering of the symmetry in exfoliated $RuCl_3$ through in-plane distortions, which was found to correlate with the observed enhancement of anisotropy in the Kitaev exchange constants.[791] $RuCl_3$ is a Mott insulator with a bandgap of 0.25 eV,[793] and conductivity measurements on single flakes indicated that it becomes insulating at low temperatures.[649] Therefore, in order to access the magnetic properties of thin flakes, indirect measurements have been explored by making a heterostructure of $RuCl_3$ with graphene.[794–797] These measurements demonstrated electron transfer from graphene to $RuCl_3$, allowing the investigation of proximity effects (*e.g.*, strain) and doping on the magnetic interactions in $RuCl_3$. Additionally, while a number of electrical circuits have been proposed to probe the spin liquid state in $RuCl_3$,[798] this experimental strategy may prove to be challenging due to the low conductivity of $RuCl_3$ at low temperatures.

**4.2.1.4. Other $MY_3$ halides.** $TiCl_3$ exhibits multiple polytypes at room temperature. Early work by Natta *et al.* reports α, β and γ polymorphs, as well as a δ polymorph which was obtained by prolonged grinding of α- or γ-$TiCl_3$.[799] The α ($BiI_3$-type) and γ (space group $P3_112$) structures are both are layered and differ only by their stacking order (*i.e.*, they are polytypes).[799] Later work by Troyanov *et al.* identified four different layered polytypes of $TiCl_3$ at room temperature: I ($BiI_3$-type), II (space group $P312$), III (space group $P\bar{3}1c$), and ε (space group $P\bar{3}m1$).[800,801] These polytypes were first reported to transition into the monoclinic $AlCl_3$-type structure below 220 K,[800]

although a later study by the same group assigned triclinic low-temperature structures to $TiCl_3$ and $TiBr_3$ and revealed the presence of Ti-Ti interactions.[801,802]

Early reports showed that layered $TiCl_3$ polymorphs are paramagnetic at room temperature.[803,804] The magnetic susceptibility has a broad maximum at 260 K (suggesting AFM order) that quickly drops below 217 K.[804] No magnetic order is present at 4 K, which is possibly explained by the formation of Ti-Ti bonds below the phase transition at 217 K.[805] Cavallone *et al.* performed electrical[806] and optical[807] measurements of α-$TiCl_3$ and found semiconducting behavior, and recent theoretical work showed that layered $TiCl_3$ polymorphs are Mott insulators.[808] No experimental studies of $TiCl_3$ in the few-layer limit are reported, although Zhou *et al.* predicted half metallicity in monolayer $TiCl_3$[809] and Geng *et al.* predicted that $TiY_3$ are FM insulators.[810]

Multiple polytypes of $FeCl_3$ are reported at room temperature: $BiI_3$-type,[811] as well as structures of space group $P312$ and $P\bar{3}$.[812] $FeCl_3$ has been shown to have a HM ground state with the AFM coupled layers coupled below ~9 K,[813,814] although a higher temperature of 15 K was reported in an early neutron diffraction study.[815] Subsequent studies report a field-induced spin-flop magnetic phase transition at ~4 T.[816] Based on Mössbauer-effect measurements, $FeBr_3$ has been shown to have a transition at ~16 K and an AFM ground state similar to $FeCl_3$.[817] While no experimental results have been reported for iron halides in the few-layer limit, recent theoretical studies predict that the monolayers of all iron halides are half-metals with FM order below 116 – 175 K.[818,819] Another study by Liu *et al.* has explored possible magnetic structures of monolayer $FeCl_3$ and $FeBr_3$ under strain, which led to the proposal that $FeCl_3$ may host a spin liquid state.[820]

For $MoCl_3$, two polymorphs are observed at room temperature: α- and β-$MoCl_3$, both of which belong to the $C2/m$ space group[821,822] Specifically, α-$MoCl_3$ is of the $AlCl_3$-type structure, whereas β-$MoCl_3$ is reported to have different stacking sequence with a higher density of stacking

faults and higher degree of disorder.[821,823] At room temperature, α-$MoCl_3$ is diamagnetic due to dimerization of the Mo cations in the honeycomb lattice. Above 585 K, $MoCl_3$ is reported to transition to another $AlCl_3$-type structure[821,823] where the Mo-Mo dimers are broken such that the Mo cations form a nearly regular honeycomb lattice, resulting in the sharp increase of the magnetic susceptibility. Interestingly, McGuire *et al.* suggested the presence of strong AFM exchange within this high-temperature $MoCl_3$ phase, and calculated an order of magnitude higher magnetic exchange interaction in comparison to $CrCl_3$ and $CrBr_3$.[823] This observation suggests that if a dimerization structural transition in α-$MoCl_3$ is avoided and the high-temperature phase can be retained, much higher magnetic transition temperatures can be expected in α-$MoCl_3$ compared to Cr halides.

All Rh and Ir halides crystallize in the $AlCl_3$-type structure, and they are non-magnetic.[773,824–826] 2D $RhI_3$ was recently investigated through optoelectronic measurements and found to exhibit a responsivity of 11.5 A $W^{-1}$ and specific detectivity up to $2\times10^{10}$ Jones at 980 nm.[827] A computational study showed that semiconducting non-magnetic Rh$Y_3$ monolayers can display indirect-to-direct bandgap transitions upon application of in-plane strain and can develop net magnetic moment upon electron doping.[828]

Multiple metal halides do not have vdW-layered bulk structures, but monolayers of these compounds have been constructed and explored computationally. These materials could potentially be accessed *via* bottom-up growth methods. Recent theoretical studies derived the monolayer structures of $RuBr_3$ and $RuI_3$ from the $RuCl_3$ structure and agreed on the possibility of realizing these structures experimentally, but predicted different magnetic order and transition temperatures.[829,830] Mn$Y_3$ monolayers were predicted to be intrinsic Dirac half-metals with high charge carrier mobilities in addition to exhibiting FM order with high Curie temperatures.[831]

Motivated by the search for candidates that show the quantum anomalous Hall (QAH) effect at room temperature, Ni, Pt, and Pd halides have recently been studied computationally. All Ni$Y_3$ monolayers were identified to be intrinsic Dirac half-metals with high mobility and high-temperature ferromagnetism, which are requirements for the room-temperature QAH effect.[832–834] Similarly, $PdCl_3$ has been predicted to be a Dirac half-metal with a high Curie temperature in the monolayer form,[835] and predicted to transition to a half-metal in the bilayer form and a ferromagnetic metal with increasing number of layers.[836] Monolayers of palladium and platinum bromides and iodides have also been identified as ferromagnetic semiconductors and candidates for the high-temperature QAH effect.[837] In search of other topologically non-trivial materials, $PtCl_3$ was recently predicted to be a 2D Weyl half-semimetal.[838]

**Table 7. Structures, magnetic properties, and electronic properties of monolayer and bulk transition metal trihalides.**

| | | structure type (space group) at RT | lattice parameters (Å) | phase transition | magnetic order and spin orientation | temperature of magnetic order (K) | electronic properties | ref(s) |
|---|---|---|---|---|---|---|---|---|
| **α-$TiCl_3$**[a] | bulk | $BiI_3$ ($R\bar{3}$) | $a$ = 6.153, $c$ = 17.599 | $P\bar{1}$ below 220 K[b] | –[b] | – | insulator | 799–801,803–808 |
| | monolayer | $BiI_3$ | $a$ = 6.1-6.3 | – | FM | – | half-metal or insulator[b] | 809,810 |
| **α-$TiBr_3$** | bulk | $BiI_3$ ($R\bar{3}$) | $a$ = 6.478, $c$ = 18.632 | $P\bar{1}$ below 180 K[b] | –[b] | – | insulator | 801,802,839 |
| | monolayer | $BiI_3$ | $a$ = 6.7 | – | FM | 75 | insulator | –[810] |
| **$VCl_3$** | bulk | $BiI_3$ ($R\bar{3}$) | $a$ = 6.012, $c$ = 17.34 | – | AFM | – | – | 673,840 |
| | monolayer | $BiI_3$ | $a$ = 6.28 | – | FM ⊥ c | 80-425 | half-metal | 730,809 |
| **$VBr_3$** | bulk | $BiI_3$ ($R\bar{3}$) | $a$ = 6.371, $c$ =18.376 | 90 K, details of LT phase are unknown | AFM ∥ c | 26.5 | insulator | 642 |
| | monolayer | – | – | – | – | – | – | – |
| **$VI_3$** | bulk | $BiI_3$ ($R\bar{3}$)[b] | $a$ = 6.914, $c$ = 19.902 | Monoclinic between 79 K and 32 K, triclinic below 32 K[b] | FM[b] | 50, 36 | insulator | 640,641,719–727 |
| | few-layer | $BiI_3$ | $a$ = 7.07 | – | FM[b] | – | insulator[b] | 727–730,732 |
| **$CrCl_3$** | bulk | $AlCl_3$ ($C2/m$) | $a$ = 5.959, $b$ = 10.321, $c$ = 6.114, β = 108.50 | $BiI_3$ below 240 K | AFM ⊥ c | 17, 14 | insulator | 734–736,841 |
| | few-layer | $AlCl_3$[b] | $a$ = 5.985 | no phase transition upon cooling[b] | AFM ⊥ c[b] | ≈17 | insulator | 650,754,842,843 |
| **$CrBr_3$** | bulk | $BiI_3$ ($R\bar{3}$) | $a$ = 6.26, $c$ = 18.2 | $AlCl_3$ above 420 K | FM ∥ c | 37 | insulator | 737,844 |
| | few-layer | $BiI_3$ | $a$ = 6.3 | – | FM or AFM ∥ c[b] | ≈ 27 | insulator | 740,742,753,845 |
| **$CrI_3$** | bulk | $AlCl_3$ ($C2/m$) | $a$ = 6.866, $b$ = 11.886, $c$ = 6.984, β = 108.51 | $BiI_3$ below 210 K | FM ∥ c | 61 | insulator | 648,738,739 |
| | few-layer | $AlCl_3$[b] | $a$ = 6.95 | no phase transition upon cooling[b] | AFM ∥ c[b] | ≈ 45 | insulator | 652,661,743–745,846,847 |
| **α-$MoCl_3$**[a] | bulk | $AlCl_3$ ($C2/m$) | $a$ = 6.112, $b$ = 9.782, $c$ = 6.315, β = 108.16 | $AlCl_3$ above 585 K[b] | AFM[b] | 585[b] | insulator | 821–823 |
| | few-layer | $AlCl_3$ ($C2/m$) | – | – | – | – | – | 848 |
| **$FeCl_3$**[a] | bulk | $BiI_3$ ($R\bar{3}$)[b] | $a$ = 6.056, $c$ = 17.41 | – | HM | 9-15[b] | insulator | 811–816 |
| | monolayer | $BiI_3$ | $a$ = 5.91 | – | FM | 175 | Dirac half-metal | 818,820 |
| **$FeBr_3$** | bulk | $BiI_3$ ($R\bar{3}$) | $a$ = 6.397, $c$ =18.38 | – | AFM | 16 | insulator | 817,849 |

| | | | | | | | | |
|---|---|---|---|---|---|---|---|---|
| | monolayer | $BiI_3$ | $a$ = 6.29 | | FM | 140 | Dirac half-metal | 818–820 |
| **$FeI_3$** | bulk | – | – | – | – | – | – | – |
| | monolayer | $BiI_3$ | – | – | FM | 116 | Dirac half-metal | 818 |
| **α-$RuCl_3$** | bulk | $AlCl_3$ ($C2/m$) [b] | $a$ = 5.976, $b$ = 10.342, $c$ = 6.013, β = 108.87 | $BiI_3$ below ≈ 60-170 K[b] | AFM, Kitaev spin liquid state [b] | 14, 7[b] | insulator | 770–777,779 |
| | few-layer | $AlCl_3$[b] | $a$ = 6.0, $b$ = 10.4 | 150-180 K[b] | – [b] | 12-35[b] | insulator | 649,790–792,794,795,850,851 |

[a] Multiple polymorphs are reported at room temperature, see text

[b] See text

### 4.2.2. Polymorph control of 2D transition metal trihalides

Since the study of 2D transition metal halides is just beginning, the extent of experimental polymorph control in 2D $MY_3$ compounds is relatively limited. However, the significant influence of structures and polytypes on magnetic properties suggests that polymorph control will be a crucial engineering parameter for this class of materials. For both exfoliated $CrCl_3$ and $CrI_3$, the structural transition from the high-temperature $AlCl_3$-type structure to the $Bi_3$-type structure that is observed in the bulk is supressed. The mechanism behind the absence of this structural transition in exfoliated samples is still under investigation. However, two of the leading proposed explanations are: (1) preservation of the $AlCl_3$-type structure through mechanical deformation and stacking fault generation; (2) the $AlCl_3$-type surface reconstruction that dominates the behavior of 2D samples.

Similar to what was discovered in $RuCl_3$[771,774,779] and $RhI_3$,[827] it has been suggested that the mechanical stress generated by the exfoliation process can induce defects such as stacking faults and grain boundaries that pin the high-temperature phase. This argument suggests that thick exfoliated flakes should also show no structural transition, which was in fact observed for $CrCl_3$.[650] However, a study by Niu *et al.*[852] used cryogenic magnetic force microscopy to probe the magnetisation in $CrI_3$ flakes thicker than 25 nm and found the coexistence of both 2D-like AFM order below 45 K and bulk-like FM order below 60.5 K. The former AFM order was assigned to approximately 20 layers (*i.e.*, 13 nm thick), whereas the bulk of the crystal was asserted to be FM. Together with the earlier studies, this work suggests that below 45 K, the surface of the thick flakes has monoclinic symmetry ($AlCl_3$-type structure), whereas the bulk is rhombohedral ($BiI_3$-type). A study by Li *et al.* suggested that this structural transition is triggered by magnetic order – namely, at the onset of magnetic order, the surface layers change to the monoclinic stacking sequence while

the bulk of the crystal remains rhombohedral.[853] Overall, further work is necessary to fully understand the mechanism behind the preservation of the $AlCl_3$-type structure in ultrathin chromium halides and its influence on magnetic properties.

A recent study concerning the MBE growth of bilayer $CrBr_3$ provides a rare example of polytype and property control in vdW TMHs using synthesis methods.[753] As depicted in **Figure 13c,d**, the authors observed AFM interlayer ordering for bilayer samples where the $CrBr_3$ layers were stacked in the same orientation (rhombohedral stacking, in analogy to $AlCl_3$-type and $BiI_3$-type structures) and FM interlayer ordering when the layers were stacked with a relative 180º rotation (hexagonal stacking). The hexagonal stacking is not reported for bulk $CrBr_3$ crystals and is thus a unique polytype for thin stacked samples. In this manner, the authors achieved explicit control over interlayer magnetic ordering in 2D $CrBr_3$ *via* assembly of distinct polytypes using bottom-up methods. This study demonstrates the promise of vapor-phase growth efforts for polymorph control in TMHs, although such synthesis of $MY_3$ compounds remains challenging and is limited to $MoCl_3$,[848] $CrBr_3$[753] and $CrI_3$.[661]

The application of pressure and strain has also been employed to induce polymorph conversions in $MY_3$ compounds. Hydrostatic pressures of ~2-3 GPa were shown to irreversibly change the $AlCl_3$-type stacking order to $BiI_3$-type in bilayer and few-layer $CrI_3$ crystals, inducing an AFM to FM phase transition (**Figure 13e**).[854,855] Theoretical studies of strained few-layer $CrI_3$ indicate the possibility of achieving other magnetic ground states including zigzag, Néel, and stripy phases as well as states with in-plane spins.[856–858] Indeed, strain tuning of the spin-flip transition in bilayer $CrI_3$ was recently demonstrated.[859] In the case of bulk $RuCl_3$, the application of hydrostatic pressure resulted in a phase transition into the triclinic structure followed by Ru-Ru dimerization from the overlap of the Ru 4*d* orbitals and complete suppression of the

magnetization,[860,861] similar to the Mo and Zr trihalides (section 4.2.1.4). Raman spectroscopy studies of exfoliated $RuCl_3$ flakes revealed in-plane distortions of the $RuCl_3$ lattice in the 2D limit,[790–792] and a recent theoretical study indicated that monolayer $RuCl_3$ becomes strained when in proximity to graphene.[797]

Irradiation of 2D transition metal trihalides may also provide another means for polymorph control. Rodriguez-Vega *et al.* predicted that low-frequency IR light pulses can coherently drive Raman phonon modes in bilayer $CrI_3$, which can cause relative displacements between the layers and hence affect the exchange interactions and magnetic order.[862] Similarly, a recent theoretical study predicted that optical pumping of $RuCl_3$ monolayers could change the spin liquid phase to a ferromagnetic phase due to doping-induced lattice strain and itinerant ferromagnetism.[850]

The use of doping and lithiation of TMHs has been explored both experimentally and computationally to tune their structure and properties. Tartaglia *et al.* constructed a triangular phase diagram of $CrY_3$ compounds, which allowed tuning of the magnitude of the spin-orbit interactions in the solid solutions.[863] More studies should be performed to reveal the structural details and properties of these compounds in the 2D limit. Recently, Cr doping in bulk $RuCl_3$ was shown to destabilize the zigzag $RuCl_3$ order in favor of the spin glass state at 10% Cr doping.[864] Lithiation of bulk $RuCl_3$ was explored with both $LiBH_4$[865] and LiI,[866] resulting in a decrease of the temperature of the AFM order. It should be noted that the former account of lithiation with $LiBH_4$ also included an exfoliation and restacking procedure following lithiation. Lithiation of mono-, bi-, and trilayer $CrI_3$ has also been predicted to fill the empty sites in the cation honeycomb lattice and induce half-metallicity,[867] while lithiation of monolayer $CrBr_3$ has been predicted to induce asymmetric Jahn-Teller distortions of the $[CrBr_6]$ octahedra for multiferroicity.[868] A recent theoretical study explored doping of V into monolayer $VI_3$ (essentially a monolayer $VI_2$-$VI_3$ solid

solution) and found that the doping level can tune the electronic bandgap. For a doping level of 1/16 to 1/4, the FM state is favored, whereas a fully-doped monolayer (*i.e.* $VI_2$) shows AFM order.[639]

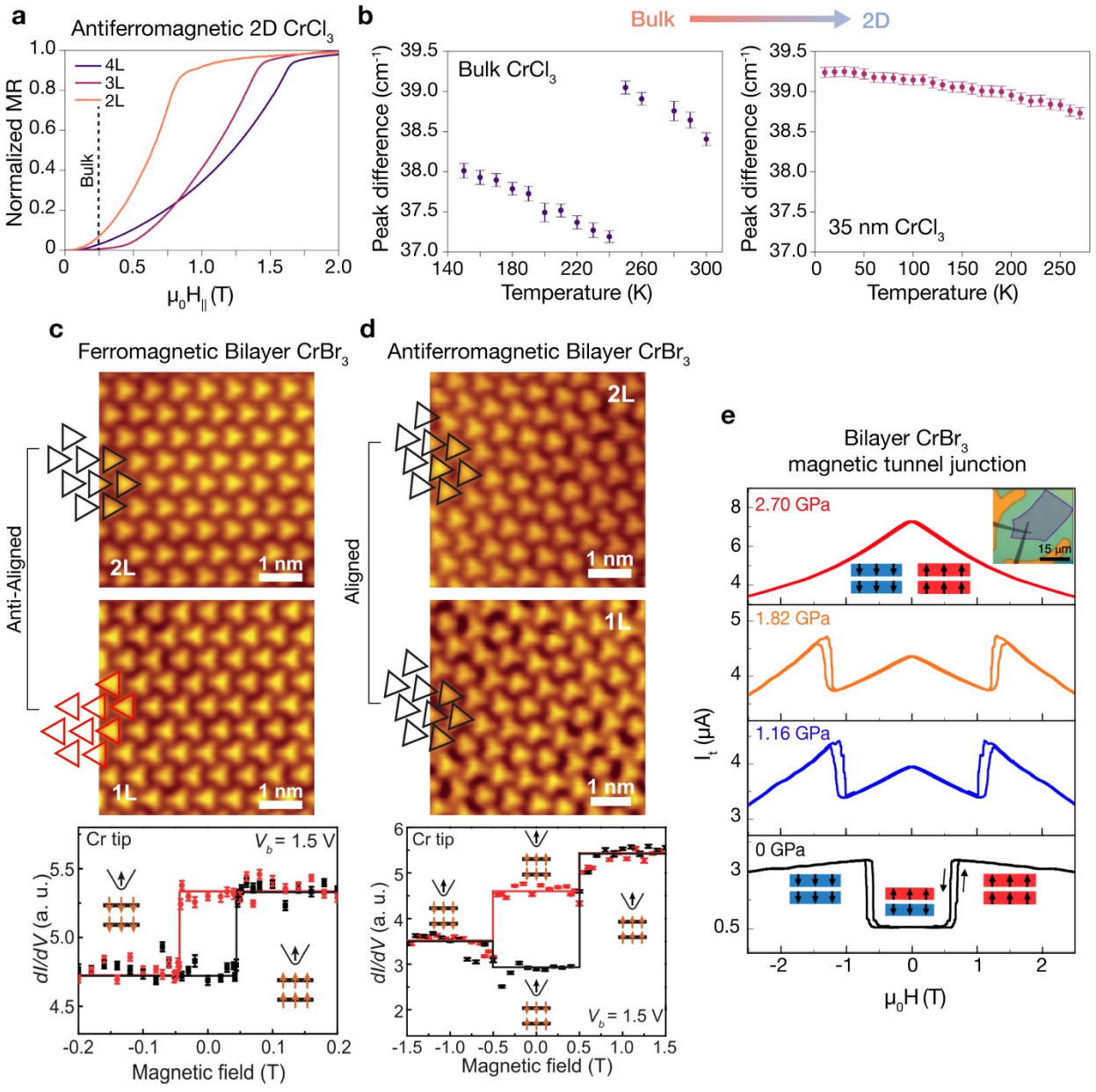


**Figure 13. Experimental demonstrations of polymorphic control in 2D transition metal halides. a)** Plot of the normalized magnetoresistance (MR) of a 2D CrCl3 crystal as a function of the in-plane magnetic field (H||). The crystals show a thickness-dependent saturation field for tetralayer (4L), trilayer (3L), and bilayer (2L) $CrCl_3$. The AFM to FM transition occurs at much higher magnetic fields than bulk crystals

(0.2-0.25 T). **b)** The high-temperature monoclinic structure of $CrCl_3$ crystals is preserved at low temperatures for 2D flakes, whereas bulk $CrCl_3$ transitions to a rhombohedral structure, as evidenced by a discontinuity in the Raman peak difference value. The figures for **a)** and **b)** were adapted with permission from Ref.[869] Copyright 2018 Springer Nature. **c)** FM versus **d)** AFM ordering in polytypes of bilayer $CrBr_3$ synthesized *via* MBE on HOPG. The STM images are shown on top, while the bottom panels show the spin-polarized tunneling spectra as a function of applied magnetic field as measured by a Cr-coated magnetized tip. Adapted from Ref.[753] Copyright 2019 The American Association for the Advancement of Science. **e)** Plot of the tunneling current ($I_t$) in a bilayer $CrI_3$ magnetic tunnel junction as a function of magnetic field (H). A pressure-induced structural transition results in AFM to FM ordering in bilayer $CrI_3$. Adapted with permission from Ref.[854] Copyright 2019 Springer Nature.

## *4.3. Transition Metal Halides of Other Stoichiometries*

A number of layered vdW transition metal halides have stoichiometries different from $MY_2$ and $MY_3$. Inspired by the properties of $RuCl_3$, McGuire *et al.* studied crystals of layered osmium chloride. Since osmium prefers a higher oxidation state, the authors observed crystals of the formula $Os_{0.55}Cl_2$ (equivalent to $OsCl_{3.6}$ or $Os_{0.8}Cl_3$).[870] The structure was indexed as $CdCl_2$-type with partial occupancy of the metal sites where the Os vacancies tend to obey 3-fold symmetry. Osmium chloride is an insulator, and the magnetic susceptibility data indicate antiferromagnetic interlayer interactions, although no magnetic order is observed down to 0.4 K. A recent theoretical study predicts monolayer $OsCl_3$ to be ferromagnetic, but with a different structure from the aforementioned experimental work.[871]

β-$MoCl_4$ was recently reported to have a layered vdW structure.[872] Similar to osmium chloride, the structure is $CdCl_2$-type with 50% occupancy of metal sites following three-fold symmetry. Based on diffraction experiments, the authors proposed two distinct models of vacancy ordering that differ by the metal site occupancy, although further studies are needed to clarify the exact structure. Contrary to α-$MoCl_3$, no Mo-Mo dimers were observed, and Weiss temperatures indicate moderate antiferromagnetic interlayer interactions.[872]

Niobium halides are known to crystallize in the $Nb_3Y_8$ stoichiometry. Their layered structure consists of $[Nb_3Y_{13}]$ clusters that are arranged in the triangular lattice. Kennedy *et al.* reported five possible polytypes of clustered $M_3Y_8$ compounds,[873] although only two are observed for Nb halides: α-type (2T, space group $P\bar{3}m1$) is reported for $Nb_3Cl_8$, and β-type (6R, space group $R\bar{3}m$) is reported for $Nb_3Br_8$ and $Nb_3I_8$, as well as intercalated $Nb_3Cl_8$ (*i.e.*, β-$A$$Nb_3Cl_8$ where $A$ is alkali metal).[873–877] α-$Nb_3Cl_8$ has been observed to transition from the room temperature trigonal phase to a monoclinic $C2/m$ structure at 90 K.[878,879] This structural transition causes a paramagnetic to nonmagnetic transition, and potential mechanisms include charge disproportionation[879] and second-order Jahn Teller distortion.[878] A recent study on exfoliated α-$Nb_3Cl_8$ flakes revealed insulating behavior and thickness-depended conductivity.[880] β-$Nb_3Br_8$ was found to possess the same paramagnetic to nonmagnetic transition as α-$Nb_3Cl_8$ at 387 K.[876] Moreover, Pasco *et al.* showed that the temperature of the phase transition can be tuned by varying the Cl/Br ratio in $Nb_3Cl_{8-x}Br_x$.[876] Recent studies of exfoliated monolayer β-$Nb_3I_8$[881] have reported semiconducting behavior with a bandgap of ~1 eV,[882] and a theoretical study predicted FM order in $Nb_3Y_8$ monolayers with Curie temperatures of 30-90 K.[883] Another theoretical report predicted thickness-dependent magnetic properties of 2D $Nb_3I_8$ as well as a Curie temperature near room temperature for the monolayer.[884] Contrary to niobium, bulk vanadium halides do not adopt the $M_3Y_8$ stoichiometry. However, it may be possible to obtain 2D forms of composition $V_3Y_8$. In particular, a recent computational study by Xiao *et al.* predicted that monolayer $V_3Cl_8$, $V_3Br_8$, and $V_3I_8$ are stable, with monolayer $V_3Cl_8$ being an intrinsic AFM semiconductor, and monolayer $V_3Br_8$ and $V_3I_8$ being FM half-metals.[885]

# 5. Conclusions and Outlook

The exploration and manipulation of structural diversity in emerging post-dichalcogenide 2D materials has only recently been undertaken and provides ample opportunity for 2D materials engineering. This polymorphism encompasses several categories of structural variation: entirely different monolayer structures (*e.g.*, the group V elemental materials), stacking polytypes (*e.g.*, the group III metal chalcogenides and TMHs), and substrate-induced monolayer reconstructions (*e.g.*, the group IV elemental materials). Since material structure dictates properties, this structural diversity gives rise to a diversity in properties. In turn, the development of precise polymorphic control methods enables explicit control and realization of desired material properties. For the discussed 2D materials, the most powerful methods of polymorph control were achieved using vapor-phase synthesis methods through the manipulation of growth conditions (*e.g.*, temperature, pressure, and precursor concentrations) and the synthesis substrate. As a result, progress in polymorph control of post-dichalcogenide 2D materials relies on developments in their synthesis *via* vapor-phase methods. Therefore, further work in developing improved vapor-phase synthesis of post-dichalcogenide 2D materials, especially the TMHs, is necessary. Furthermore, non-equilibrium synthesis methods such as pulsed laser deposition provide opportunities for targeting metastable 2D material polymorphs.[886]

Moreover, while the phase diagrams and structures of bulk materials have been studied systematically and thoroughly, this understanding is often not directly translatable to the 2D regime. As surface effects become important – if not dominant – in the atomically thin limit, the balance of forces that dictate the stability of different structures can change. For example, several of the discussed 2D materials go through thickness-driven structural transformations as they enter the 2D thickness regime. These materials include GaTe,[379] SnTe,[398,479] bismuthene,[290] and some vdW metal halides.[652,743,744,869] Furthermore, several materials exhibit 2D polymorphs that are

stable at standard temperature/pressure conditions even though they are only observed in the bulk at high temperatures/pressures, if at all. Specific examples in this category including several elemental 2D materials (*e.g.*, borophene,[30,31] antimonene,[215,216] bismuthene[218]) as well as $In_2Se_3$.[344,345] Therefore, opportunities exist for the re-evaluation of phase diagrams in the 2D regime, which may accelerate the discovery of entirely new 2D polymorphs.

## *5.1. Discovery of 2D Polymorphs*

The discovery of new 2D polymorphs can be guided using computational prediction. Computational structure prediction underlies the fundamental mission of the Materials Genome Initiative[887] and has been specifically recognized as a pathway for the identification of metastable polymorphs in the 2019 'Materials by Design' roadmap.[888] As machine learning, high-throughput screening, and non-empirical search algorithms are becoming increasingly accessible, computation methods are well positioned to uncover novel 2D structures that are beyond experimental intuition.[889] For example, several recent studies have focused on high-volume prediction of 2D structures (**Figure 14a**).[890,891] Moreover, several 2D polymorphs have been experimentally synthesized with the help of computational efforts. These materials include borophene,[41,42,44] blue phosphorene,[199] and 2D selenium and tellurium.[892,893] In addition to the elemental materials covered in this text, their alloys (*e.g.*, IV-V) could provide another emergent class of polymorphic 2D materials, where computational investigations allow for efficient exploration of an experimentally daunting phase space.[894–896] However, as evidenced by purely synthetic 2D materials such as borophene, it is imperative to widen the search for 2D polymorphs to non-vdW-layered parent materials. This concept is underlined by a computational study into 'spontaneous graphitization' by Sorokin *et al.*, wherein the authors found that the structural

preference of bulk materials with 3D bonding may spontaneously shift to a layered structure below a specific thickness (**Figure 14b**).[897] Alternatively, a computational study by Liu *et al*. found the substrate to play a significant role in facilitating interdimensional structural transformations.[893] Hence, substrate and thickness effects alter the energetic playing field in the 2D regime and justify a reconsideration of potential 2D material candidates.

## *5.2. Stabilization of 2D Polymorphs*

Along with polymorph discovery, tactics for stabilizing metastable 2D polymorphs require further research. A powerful and promising tool is substrate engineering. As discussed above, the use of substrate symmetry or the strength of film-substrate interactions are essential methods in selecting the desired 2D polymorph of a material. To template specific structures, the nature of the interaction can range from pure vdW interfaces (*e.g*., ground-state *hb*-antimonene on hexagonal $PdTe_2$[276] versus metastable *aw*-antimonene on orthorhombic $T_d$-$WTe_2$[281]) to covalent interfaces (*e.g*., planar bismuthene on SiC[242], as shown in **Figure 14c**). Due to their lack of dangling bonds, many 2D materials can grow *via* vdW epitaxy, enabling their deposition on a variety of substrates. However, substrate engineering for 2D polymorph control is limited and requires further work, especially as vapor-phase synthesis methods are being developed for emerging 2D materials. In contrast, the principle of pseudomorphism, wherein metastable phases are stabilized *via* epitaxy, has long been explored using MBE for 3D materials.[898] Furthermore, more innovative forms of epitaxy and templating have shown promise for 2D polymorphs. Specifically, confined epitaxy, wherein the 2D layer is embedded within another structure, has resulted in novel 2D polymorphs. Notably, 2D GaN was grown by Al Balushi *et al.* in between a bulk SiC substrate and a bilayer graphene overlayer.[899] Similarly, Wang *et al.* reported the growth of a $CdI_2$-type monolayer of

metastable $GeTe_2$ in a matrix of $GeSb_2Te_{4+x}$.[487] In a more unconventional scheme, Gonzalez *et al*. achieved the tailorable growth of 2D metal halides of formula $MY_2$ inside metal-organic framework templates (**Figure 14c**).[900]

Alternatively, the use of additives, dopants, or alloying presents another strategy to stabilize metastable 2D polymorphs. For the 2D TMDs, lithium intercalation has been demonstrated to stabilize both undistorted and distorted $CdI_2$-type (1T) structures of monolayer $MoS_2$, while alloying with analogous elements (*i.e*., introduction of other transition metals or chalcogens) has been shown to more subtly tune their structure.[16] Additionally, the use of an alkali element additive (potassium) during CVD of monolayer $MoS_2$ has been reported to stabilize the distorted $CdI_2$-type (1T′) phase,[901] and could prove useful for polymorph selection in other 2D metal chalcogenides. However, with the exception these specific examples in 2D TMDs, the use of additives, dopants, or alloying is under-investigated in the 2D materials research field.

In contrast, these strategies have worked well for bulk materials, highlighted here by several recent reports. For perovskites, the incorporation of different organic ligands has been shown to select between different metastable structures of $CsPbI_3$.[902] Rare-earth metal dopants have been used to stabilize metastable structures of bulk materials such as $Ag_2WO_4$[903] and $LaVO_4$,[904] while mercury impurities have been employed to stabilize black As single-crystals.[264] Furthermore, Zakutev and Lany *et al.* have recently investigated the implications of alloying materials with different ground-state structures for the purpose of stabilizing metastable phases.[905] For example, they realized wurtzite-type $MnSe_{0.5}Te_{0.5}$ by alloying rock-salt-type MnSe and nickeline MnTe (**Figure 14d**).[906] Lastly, surface functionalization of 2D materials such as the group V elements has been predicted to enable structural control.[175–177,295] This principle was

recently exemplified in a study by Fu *et al.*, who obtained metastable cubic formamidinium lead iodide at room temperature using surface functionalization with organic ligands.[907]

The search for suitable synthesis substrates, templates, or additives lends itself well to combinatorial methods, which could accelerate efforts aimed at polymorph stabilization and epitaxy. For example, Tomada *et al.* recently used combinatorial methods to explore different molecular seeds for the growth of distinct chiralities of single-walled carbon nanotubes,[908] while Wittkamper *et al.* used a polycrystalline $CoNb_2O_6$ substrate to search for grain orientations that stabilize the metastable scrutinyite-type $SnO_2$ polymorph over the ground-state rutile-type $SnO_2$ structure (**Figure 14e**).[909] Furthermore, the use of compositional or substrate temperature gradients can be used to combinatorially investigate narrow dopant concentrations or synthesis temperature windows where particular metastable structures are obtained. The insight from combinatorial synthesis can then feed directly into computational materials design and discovery, which is often hindered by a lack of reliable and high-volume experimental data.

## *5.3. Polymorph Engineering and Functionality*

Higher-order materials engineering and functionalities can be enabled by the variety of accessible 2D polymorphs and the methods used to stabilize them. Specifically, directed structural designs can be achieved by integrating different polymorphs of a single material, as can be pursed through either patterned conversion or self-assembly and growth. For instance, the patterned conversion (using methods such as thermal annealing[489] or irradiation with photons[368] or electrons[491]) of a high-resistance polymorph into a low-resistance polymorph has the potential to realize functional homojunctions for contact engineering.[910] The phase transformations themselves can also be functional, as demonstrated by Choi *et al.* with switchable polymorph conversions in exfoliated

$In_2Se_3$ for phase-change-memory devices.[378] Using self-assembly of polymorphs during growth, novel nanostructures or superlattices can also be realized. This concept is best illustrated by the self-assembly of borophene into striped periodic arrangements of its various polymorphs (**Figure 14f**),[25] which could be leveraged to form nanoscale transport channels.[52] The case of $CrI_3$ illustrates the possibility of functional surface reconstructions wherein the surface layers are of a different structure from the bulk and impart different magnetic order to the material.[852,853] Furthermore, the vapor-phase assembly of phosphorene polymorphs can enable the formation of phosphorus fullerenes, nanotubes, or nanoribbons,[911] the latter of which were recently reported using a top-down method.[912] However, an outstanding obstacle on the path to directed design of 2D polymorphs will be the technological feasibility of processing these materials. In particular, the 2D materials community consistently faces challenges in the transfer or low-temperature growth of 2D materials required for electronics fabrication processes.[913–915]

Artificial 2D polytypes can also be fabricated using directed stacking of vdW layers of a single material or several isostructural materials. As has been recently demonstrated with graphene layers, the angle at which 2D materials are stacked can potentially have a dramatic effect on their properties (**Figure 14f**). In the case of bilayer graphene, 'magic angles' (*e.g.*, $\theta = 1.1^{\circ}$) exist where the Fermi velocity goes to zero. Cao *et al.* found magic-angle twisted bilayer graphene to exhibit superconductivity, whereas conventional twist angles in bilayer graphene do not show this behavior.[13] This approach is also utilized the report by Chen *et al.* wherein the authors synthesized a bilayer $CrBr_3$ polytype not observed in the bulk and leveraged the intralayer stacking orientations to control the 2D magnetic order of the crystals. Furthermore, a recent study by Liu *et al.* investigated a method for large-area mechanical exfoliation of monolayer TMDs and their

reassembly into artificially stacked heterostructures.[916] This method could thus provide a promising pathway to investigate the benefits of 2D artificial polytypes and related twistronics.

Lastly, the ability to engineer a specific polymorph leads to the refinement of structure-specific device performance. For example, Jiang *et al.* created novel spin tunnel FETs based on vdW heterostructures by controlling the number of layers in ultrathin $CrI_3$ crystals, wherein the stacking sequence gives rise to antiferromagnetic interlayer coupling that can be switched to ferromagnetic with a gate voltage.[762] Further experimental work in identifying and tailoring 2D polymorphs for targeted applications is warranted, although some recent studies have undertaken this effort computationally.[409,917–919] A recent study by Cheema *et al.* places the entire hierarchy of polymorphic design into perspective. The authors were able to push the limits of ultrathin ferroelectricity in bulk-like Zr-doped $HfO_2$ (down to 1 nm in thickness) that was grown using ALD on $SiO_2$/Si (**Figure 14g**).[1] This result was achieved by stabilization of a metastable polar phase of $Hf_{0.8}Zr_{0.2}O_2$ (HZO).[920] In this case, the engineered stabilization mechanism was two-fold: (1) a thickness (*i.e.*, surface energy) effect that favors the higher symmetry polar phase of HZO in the ultrathin limit as opposed to the bulk-stable nonpolar phase; (2) a metal layer was deposited on the ultrathin HZO films prior to a rapid thermal annealing step to provide confinement of the structure. When both of these strategies were in place, the polar HZO phase was stabilized, resulting in ultrathin enhancement of the ferroelectric effect. Moreover, the fabrication scheme was shown to be easily integrated with $SiO_2$/Si, demonstrating the potential for monolithic fabrication of polarization-driven low-power memory applications. Therefore, this study illustrates the promise of polymorphic engineering in the 2D limit for enhanced and novel functionalities.

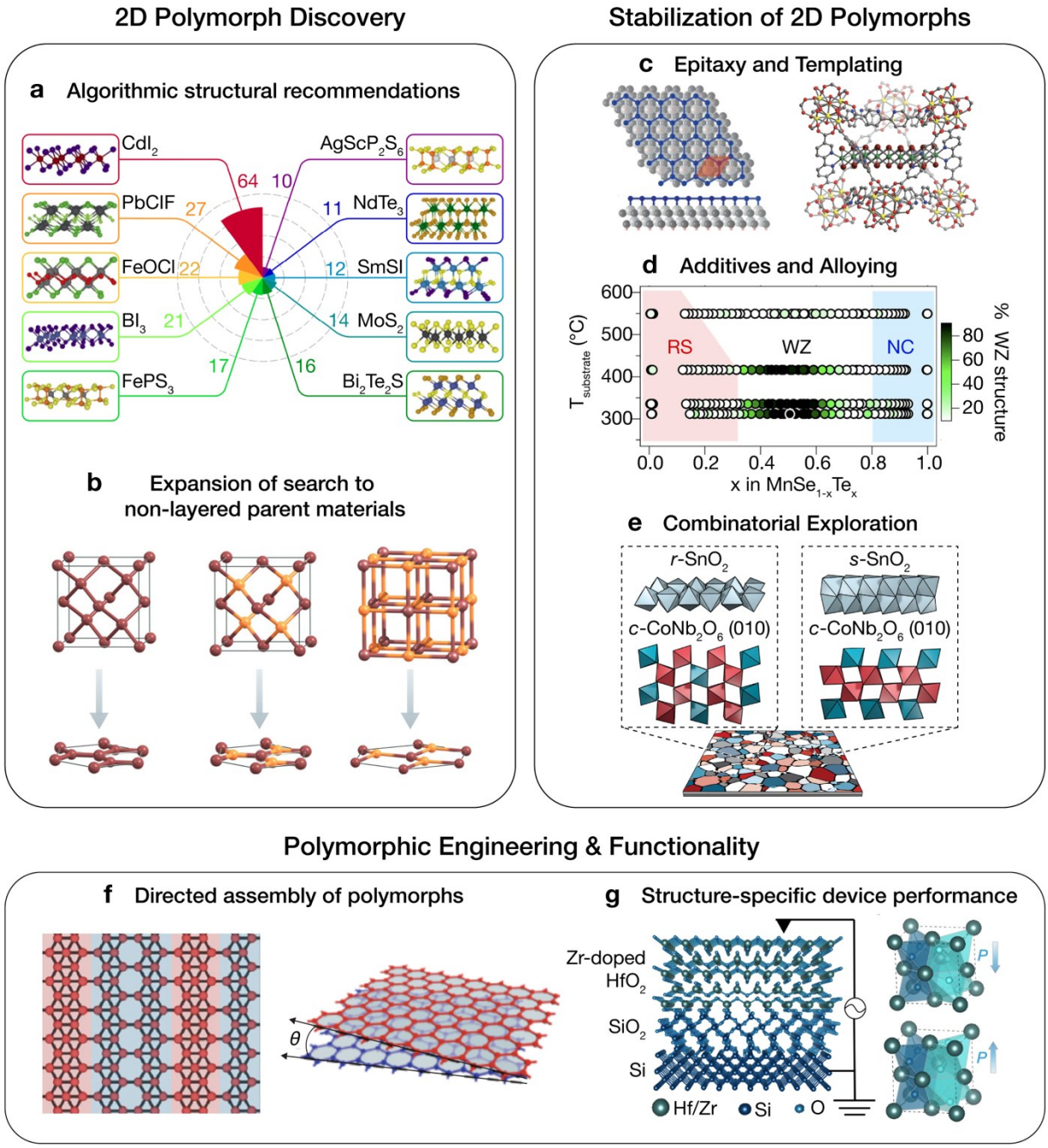


**Figure 14. Outlook for 2D Polymorphs.** *Discovery of 2D Polymorphs*: **a)** Algorithmic methods can be used to suggest novel 2D polymorphs. For example, Mounet *et al.* used high-throughput algorithmic screening to identify easily exfoliatable materials. The top 10 most common 2D structural prototypes are depicted. Adapted with permission from Ref. [890] Copyright 2018 Springer Nature. **b)** Additionally, the search for 2D polymorphs should be expanded to include non-layered parent materials. Using DFT, Sorokin *et al.* studied the 'spontaneous graphitization' of non-layered bulk materials, here depicted with the preference of certain diamond-, zincblende-, and rock-salt-type bulk structures to form layered planar hexagonal structures (graphite-like) in the ultrathin limit. Adapted with permission from Ref.[897] Copyright

2014 American Chemical Society. *Stabilization of 2D Polymorphs*: Accessing a variety of 2D polymorphs will require the stabilization of metastable structures, which can be achieved using several strategies: **c)** The use of substrate epitaxy (*i.e*., pseudomorphism) and confined epitaxy methods have been shown to template the growth of 2D materials. Left: Reis *et al.* used epitaxy to stabilize planar bismuthene on SiC. Right: Gonzalez *et al*. templated the growth of various monolayer transition metal dihalides confined inside metal-organic frameworks. The left figure was adapted with permission from Ref.[242] Copyright 2017 The American Association for the Advancement of Science. The right figure was reproduced from Ref.[900] Copyright 2019 Springer Nature. **d)** The use of additives, such as dopants or alloying, can stabilize metastable structures as demonstrated by Siol *et al.* by alloying rock-salt-type (RS) MnSe with nickleline (NC) MnTe to obtain metastable wurtzite-type (WZ) $MnSe_{1-x}Te_x$. Adapted from Ref.[906] Copyright 2018 The American Association for the Advancement of Science under a Creative Commons Attribution-NonCommercial 4.0 International Public License https://creativecommons.org/licenses/by-nc/4.0/. **e)** Combinatorial synthesis methods will accelerate the exploration of 2D polymorph stabilization, illustrated here with a study by Wittkamper *et al.,* wherein the authors used a polycrystalline substrate to combinatorially investigate the role of substrate crystallinity in obtaining metastable scrutinyite-type (*s*-) $SnO_2$ versus stable rutile-type (*r*-) $SnO_2$. Adapted with permission from Ref.[921] Copyright 2017 The American Association for the Advancement of Science. *Polymorphic Engineering and Functionality***:** Higher-order materials engineering and functionalities can be enabled by accessing and engineering 2D polymorphs. **f)** Right: the self-assembly of lateral 'stripes' of 2D borophene polymorphs could lead to nanoscale transport channels.[52] Adapted with permission from Ref.[25] Copyright 2018 Springer Nature. Left: the artificial polytype of bilayer magic angle graphene (*e.g*., $\theta = 1.1^{o}$) has been shown to exhibit novel properties such as superconductivity.[13] Adapted with permission from Ref.[922] Copyright 2016. American Chemical Society. **g)** Precise polymorph control will enable novel functionalities, as demonstrated by Cheema *et al*. Depicted here is ultrathin (down to 1 nm) ferroelectricity in Zr-doped $HfO_2$ (HZO) achieved by stabilizing the metastable polar polymorph using both thickness and confinement effects. The enhanced ultrathin ferroelectricity is enabled by this 2D polymorph, whereas 3D materials like HZO usually lose ferroelectricity beyond a critical thickness. Adapted with permission from Ref. [920] Copyright 2020 Springer Nature.

# For Table of Contents Only

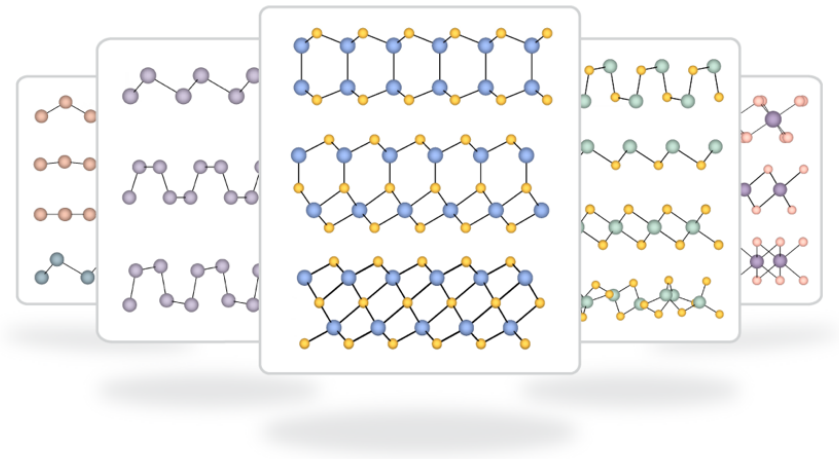

# 6. Author Information

## *6.1. Biographies*

Dr. Hadallia Bergeron recently defended her PhD in Materials Science and Engineering from Northwestern University under the supervision of Professor Mark Hersam. She obtained her B.Sc in Physics from McGill University in 2013. Her research focuses on the vapor-phase synthesis of two-dimensional metal chalcogenide semiconductors. Her efforts at understanding the phase evolution of indium selenide helped to inspire this review.

Dr. Dmitry Lebedev is currently pursuing his postdoctoral research work in the Materials Science and Engineering department at Northwestern University in the group of Professor Mark Hersam. He obtained his B.Sc. and M.Sc. in Materials from Moscow State University and his PhD in Chemistry from ETH Zurich.

Dr. Mark C. Hersam is the Walter P. Murphy Professor of Materials Science and Engineering and Director of the Materials Research Center at Northwestern University. His research interests include nanomaterials, scanning probe microscopy, nanoelectronic devices, and renewable energy technologies. He has received several honors including the Presidential Early

Career Award for Scientists and Engineers, Materials Research Society Outstanding Young Investigator Award, MacArthur Fellowship, U.S. Science Envoy, National Academy of Inventors, and AVS Medard W. Welch Award.

## 7. Acknowledgements

This research was supported by the Materials Research Science and Engineering Center (MRSEC) of Northwestern University (NSF DMR-1720139). H.B. acknowledges Dr. Bernard Beckerman for his help on proofreading parts of this manuscript. D.L. would like to thank the Swiss National Science Foundation for an Early PostDoc Mobility Fellowship (P2EZP2_181614) in addition to the U.S. National Science Foundation (NSF DMR-2004420).

## 8. References

(1) Herbstein, F. H. Diversity Amidst Similarity: A Multidisciplinary Approach to Phase Relationships, Solvates, and Polymorphs. *Cryst. Growth Des.* **2004**, *4*, 1419–1429.

(2) Davey, J. W.; Hohenlohe, P. A.; Etter, P. D.; Boone, J. Q.; Catchen, J. M.; Blaxter, M. L. Genome-Wide Genetic Marker Discovery and Genotyping Using Next-Generation Sequencing. *Nat. Rev. Genet.* **2011**, *12*, 499–510.

(3) Moulton, B.; Zaworotko, M. J. From Molecules to Crystal Engineering: Supramolecular Isomerism and Polymorphism in Network Solids. *Chem. Rev.* **2001**, *101*, 1629–1658.

(4) Blagden, N.; de Matas, M.; Gavan, P. T.; York, P. Crystal Engineering of Active Pharmaceutical Ingredients to Improve Solubility and Dissolution Rates. *Adv. Drug Deliv. Rev.* **2007**, *59*, 617–630.

(5) Brittain, H. G. *Polymorphism in Pharmaceutical Solids*; CRC Press, 2016.

(6) Chandran, M. Chapter Six - Synthesis, Characterization, and Applications of Diamond Films. In *Carbon-Based Nanofillers and Their Rubber Nanocomposites*; Yaragalla, S., Mishra, R., Thomas, S., Kalarikkal, N., Maria, H. J., Eds.; Elsevier, 2019; pp. 183–224.

(7) Trigunayat, G. C.; Verma, A. R. Polytypism and Stacking Faults in Crystals with Layer Structure. In *Crystallography and Crystal Chemistry of Materials with Layered Structures*; Lévy, F., Ed.; Physics and Chemistry of Materials with Layered Structures; Springer Netherlands: Dordrecht, 1976; pp. 269–340.

(8) Boehm, H. P.; Coughlin, R. W. Enthalpy Difference of Hexagonal and Rhombohedral Graphite. *Carbon* **1964**, *2*, 1–6.

(9) Bistritzer, R.; MacDonald, A. H. Moiré Bands in Twisted Double-Layer Graphene. *Proc. Natl. Acad. Sci.* **2011**, *108*, 12233–12237.

(10) Suárez Morell, E.; Correa, J. D.; Vargas, P.; Pacheco, M.; Barticevic, Z. Flat Bands in Slightly Twisted Bilayer Graphene: Tight-Binding Calculations. *Phys. Rev. B* **2010**, *82*, 121407.

(11) Cao, Y.; Fatemi, V.; Fang, S.; Tomarken, S. L.; Luo, J. Y.; Sanchez-Yamagishi, J. D.; Watanabe, K.; Taniguchi, T.; Kaxiras, E.; et al. Correlated Insulator Behaviour at Half-Filling in Magic-Angle Graphene Superlattices. *Nature* **2018**, *556*, 80–84.

(12) Cao, Y.; Rodan-Legrain, D.; Rubies-Bigorda, O.; Park, J. M.; Watanabe, K.; Taniguchi, T.; Jarillo-Herrero, P. Tunable Correlated States and Spin-Polarized Phases in Twisted Bilayer–Bilayer Graphene. *Nature* **2020**, *583*, 215–220.

(13) Cao, Y.; Fatemi, V.; Fang, S.; Watanabe, K.; Taniguchi, T.; Kaxiras, E.; Jarillo-Herrero, P. Unconventional Superconductivity in Magic-Angle Graphene Superlattices. *Nature* **2018**, *556*, 43–50.

(14) Yankowitz, M.; Chen, S.; Polshyn, H.; Zhang, Y.; Watanabe, K.; Taniguchi, T.; Graf, D.; Young, A. F.; Dean, C. R. Tuning Superconductivity in Twisted Bilayer Graphene. *Science* **2019**, *363*, 1059–1064.

(15) Lin, Y.; Zhang, L.; Mao, H.; Chow, P.; Xiao, Y.; Baldini, M.; Shu, J.; Mao, W. L. Amorphous Diamond: A High-Pressure Superhard Carbon Allotrope. *Phys. Rev. Lett.* **2011**, *107*, 175504.

(16) Voiry, D.; Mohite, A.; Chhowalla, M. Phase Engineering of Transition Metal Dichalcogenides. *Chem. Soc. Rev.* **2015**, *44*, 2702–2712.

(17) Wang, J.; Wei, Y.; Li, H.; Huang, X.; Zhang, H. Crystal Phase Control in Two-Dimensional Materials. *Sci. China Chem.* **2018**, *61*, 1227–1242.

(18) Xiao, Y.; Zhou, M.; Liu, J.; Xu, J.; Fu, L. Phase Engineering of Two-Dimensional Transition Metal Dichalcogenides. *Sci. China Mater.* **2019**, *62*, 759–775.

(19) Manzeli, S.; Ovchinnikov, D.; Pasquier, D.; Yazyev, O. V.; Kis, A. 2D Transition Metal Dichalcogenides. *Nat. Rev. Mater.* **2017**, *2*, 17033.

(20) Yang, H.; Kim, S. W.; Chhowalla, M.; Lee, Y. H. Structural and Quantum-State Phase Transitions in van der Waals Layered Materials. *Nature Phys.* **2017**, *13*, 931–937.

(21) Wang, X.; Song, Z.; Wen, W.; Liu, H.; Wu, J.; Dang, C.; Hossain, M.; Iqbal, M. A.; Xie, L. Potential 2D Materials with Phase Transitions: Structure, Synthesis, and Device Applications. *Adv. Mater.* **2019**, *31*, 1804682.

(22) Sokolikova, M. S.; Mattevi, C. Direct Synthesis of Metastable Phases of 2D Transition Metal Dichalcogenides. *Chem. Soc. Rev.* **2020**, *49*, 3952–3980.

(23) Motizuki, Kazuko. *Structural Phase Transitions in Layered Transition Metal Compounds*; Springer, 1986; Vol. 8.

(24) Rachel, S.; Ezawa, M. Giant Magnetoresistance and Perfect Spin Filter in Silicene, Germanene, and Stanene. *Phys. Rev. B* **2014**, *89*, 195303.

(25) Liu, X.; Zhang, Z.; Wang, L.; Yakobson, B. I.; Hersam, M. C. Intermixing and Periodic Self-Assembly of Borophene Line Defects. *Nature Mater.* **2018**, *17*, 783–788.

(26) Ramsdell, L. S. Studies on Silicon Carbide. *American Mineralogist* **1947**, *32*, 64–82.

(27) Guinier, A.; Bokij, G. B.; Boll-Dornberger, K.; Cowley, J. M.; Ďurovič, S.; Jagodzinski, H.; Krishna, P.; de Wolff, P. M.; Zvyagin, B. B.; Cox, D. E.; et al. Nomenclature of Polytype Structures. Report of the International Union of Crystallography *Ad Hoc* Committee on the Nomenclature of Disordered, Modulated and Polytype Structures. *Acta Cryst. A* **1984**, *40*, 399–404.

(28) Katzke, H.; Tolédano, P.; Depmeier, W. Phase Transitions between Polytypes and Intralayer Superstructures in Transition Metal Dichalcogenides. *Phys. Rev. B* **2004**, *69*, 134111.

(29) Pałosz, B. Reasons for Polytypism of Crystals of the Type $MX_2$ II. Clasification of Faults and Structural Series of Polytypes; Conditions of Polytypic Growth of $CdI_2$, $PbI_2$, $CdBr_2$, $SnS_2$, $SnSe_2$ and $Ti_{1.2}S_2$. *Phys. Stat. Sol. A* **1983**, *80*, 11–41.

(30) Mannix, A. J.; Zhou, X.-F.; Kiraly, B.; Wood, J. D.; Alducin, D.; Myers, B. D.; Liu, X.; Fisher, B. L.; Santiago, U.; Guest, J. R.; et al. Synthesis of Borophenes: Anisotropic, Two-Dimensional Boron Polymorphs. *Science* **2015**, *350*, 1513–1516.

(31) Feng, B.; Zhang, J.; Zhong, Q.; Li, W.; Li, S.; Li, H.; Cheng, P.; Meng, S.; Chen, L.; Wu, K. Experimental Realization of Two-Dimensional Boron Sheets. *Nature Chem.* **2016**, *8*, 563–568.

(32) Kamal, C.; Chakrabarti, A.; Ezawa, M. Aluminene as Highly Hole-doped Graphene. *New J. Phys.* **2015**, *17*, 083014.

(33) Lukačević, I.; Varga Pajtler, M.; Mužević, M.; Gupta, S. K. Prospects for Experimental Realization of Two-Dimensional Aluminium Allotropes. *J. Mater. Chem. C* **2019**, *7*, 2666–2675.

(34) Kochat, V.; Samanta, A.; Zhang, Y.; Bhowmick, S.; Manimuda, P.; Asif, S. A. S.; Stender, A. S.; Vajtai, R.; Singh, A. K.; Tiwary, C. S.; et al. Atomically Thin Gallium Layers from Solid-Melt Exfoliation. *Sci. Adv.* **2018**, *4*, e1701373.

(35) Singh, D.; Gupta, S. K.; Lukačević, I.; Sonvane, Y. Indiene 2D Monolayer: A New Nanoelectronic Material. *RSC Adv.* **2016**, *6*, 8006–8014.

(36) Mannix, A. J.; Kiraly, B.; Hersam, M. C.; Guisinger, N. P. Synthesis and Chemistry of Elemental 2D Materials. *Nat. Rev. Chem.* **2017**, *1*, 0014.

(37) Zhang, Z.; Penev, E. S.; Yakobson, B. I. Two-Dimensional Boron: Structures, Properties and Applications. *Chem. Soc. Rev.* **2017**, *46*, 6746–6763.

(38) Huang, Y.; Shirodkar, S. N.; Yakobson, B. I. Two-Dimensional Boron Polymorphs for Visible Range Plasmonics: A First-Principles Exploration. *J. Am. Chem. Soc.* **2017**, *139*, 17181–17185.

(39) Mannix, A. J.; Zhang, Z.; Guisinger, N. P.; Yakobson, B. I.; Hersam, M. C. Borophene as a Prototype for Synthetic 2D Materials Development. *Nature Nanotech.* **2018**, *13*, 444–450.

(40) Boustani, I. Systematic *Ab Initio* Investigation of Bare Boron Clusters: Determination of the Geometry and Electronic Structures of $B_N$ (N=2–14). *Phys. Rev. B* **1997**, *55*, 16426–16438.

(41) Tang, H.; Ismail-Beigi, S. Novel Precursors for Boron Nanotubes: The Competition of Two-Center and Three-Center Bonding in Boron Sheets. *Phys. Rev. Lett.* **2007**, *99*, 115501.

(42) Yang, X.; Ding, Y.; Ni, J. *Ab Initio* Prediction of Stable Boron Sheets and Boron Nanotubes: Structure, Stability, and Electronic Properties. *Phys. Rev. B* **2008**, *77*, 041402.

(43) Wu, X.; Dai, J.; Zhao, Y.; Zhuo, Z.; Yang, J.; Zeng, X. C. Two-Dimensional Boron Monolayer Sheets. *ACS Nano* **2012**, *6*, 7443–7453.

(44) Penev, E. S.; Bhowmick, S.; Sadrzadeh, A.; Yakobson, B. I. Polymorphism of Two-Dimensional Boron. *Nano Lett.* **2012**, *12*, 2441–2445.

(45) Yu, X.; Li, L.; Xu, X.-W.; Tang, C.-C. Prediction of Two-Dimensional Boron Sheets by Particle Swarm Optimization Algorithm. *J. Phys. Chem. C* **2012**, *116*, 20075–20079.

(46) Lu, H.; Mu, Y.; Bai, H.; Chen, Q.; Li, S.-D. Binary Nature of Monolayer Boron Sheets from *Ab Initio* Global Searches. *J. Chem. Phys.* **2013**, *138*, 024701.

(47) Campbell, G. P.; Mannix, A. J.; Emery, J. D.; Lee, T.-L.; Guisinger, N. P.; Hersam, M. C.; Bedzyk, M. J. Resolving the Chemically Discrete Structure of Synthetic Borophene Polymorphs. *Nano Lett.* **2018**, *18*, 2816–2821.

(48) Liu, X.; Wang, L.; Li, S.; Rahn, M. S.; Yakobson, B. I.; Hersam, M. C. Geometric Imaging of Borophene Polymorphs with Functionalized Probes. *Nat. Commun.* **2019**, *10*, 1642.

(49) Feng, B.; Zhang, J.; Liu, R.-Y.; Iimori, T.; Lian, C.; Li, H.; Chen, L.; Wu, K.; Meng, S.; Komori, F.; et al. Direct Evidence of Metallic Bands in a Monolayer Boron Sheet. *Phys. Rev. B* **2016**, *94*, 041408.

(50) Kiraly, B.; Liu, X.; Wang, L.; Zhang, Z.; Mannix, A. J.; Fisher, B. L.; Yakobson, B. I.; Hersam, M. C.; Guisinger, N. P. Borophene Synthesis on Au(111). *ACS Nano* **2019**, *13*, 3816–3822.

(51) Zhong, Q.; Zhang, J.; Cheng, P.; Feng, B.; Li, W.; Sheng, S.; Li, H.; Meng, S.; Chen, L.; u, K. Metastable Phases of 2D Boron Sheets on Ag(111). *J. Phys.: Condens. Matter* **2017**, *29*, 095002.

(52) Silvestre, G. H.; Scopel, W. L.; Miwa, R. H. Electronic Stripes and Transport Properties in Borophene Heterostructures. *Nanoscale* **2019**, *11*, 17894–17903.

(53) Feng, B.; Sugino, O.; Liu, R.-Y.; Zhang, J.; Yukawa, R.; Kawamura, M.; Iimori, T.; Kim, H.; Hasegawa, Y.; Li, H.; et al. Dirac Fermions in Borophene. *Phys. Rev. Lett.* **2017**, *118*, 096401.

(54) Feng, B.; Zhang, J.; Ito, S.; Arita, M.; Cheng, C.; Chen, L.; Wu, K.; Komori, G.; Sugino, O.; Miyamoto, K.; et al. Discovery of 2D Anisotropic Dirac Cones. *Adv. Mater.* **2018**, *30*, 1704025.

(55) Gupta, S.; Kutana, A.; Yakobson, B. I. Dirac Cones and Nodal Line in Borophene. *J. Phys. Chem. Lett.* **2018**, *9*, 2757–2762.

(56) Penev, E. S.; Kutana, A.; Yakobson, B. I. Can Two-Dimensional Boron Superconduct? *Nano Lett.* **2016**, *16*, 2522–2526.

(57) Zhao, Y.; Zeng, S.; Ni, J. Phonon-Mediated Superconductivity in Borophenes. *Appl. Phys. Lett.* **2016**, *108*, 242601.

(58) Gao, M.; Li, Q.-Z.; Yan, X.-W.; Wang, J. Prediction of Phonon-Mediated Superconductivity in Borophene. *Phys. Rev. B* **2017**, *95*, 024505.

(59) Zhang, H.; Xie, Y.; Zhang, Z.; Zhong, C.; Li, Y.; Chen, Z.; Chen, Y. Dirac Nodal Lines and Tilted Semi-Dirac Cones Coexisting in a Striped Boron Sheet. *J. Phys. Chem. Lett.* **2017**, *8*, 1707–1713.

(60) Yi, W.; Liu, W.; Botana, J.; Zhao, L.; Liu, Z.; Liu, J.; Miao, M. Honeycomb Boron Allotropes with Dirac Cones: A True Analogue to Graphene. *J. Phys. Chem. Lett.* **2017**, *8*, 2647–2653.

(61) Gao, Z.; Li, M.; Wang, J.-S. Insight into Two-Dimensional Borophene: Five-Center Bond and Phonon-Mediated Superconductivity. *ACS Appl. Mater. Interfaces* **2019**, *11*, 47279–47288.

(62) Zhang, Z.; Yang, Y.; Penev, E. S.; Yakobson, B. I. Elasticity, Flexibility, and Ideal Strength of Borophenes. *Adv. Funct. Mater.* **2017**, *27*, 1605059.

(63) Tsafack, T.; Yakobson, B. I. Thermomechanical Analysis of Two-Dimensional Boron Monolayers. *Phys. Rev. B* **2016**, *93*, 165434.

(64) Zhou, H.; Cai, Y.; Zhang, G.; Zhang, Y.-W. Superior Lattice Thermal Conductance of Single-Layer Borophene. *npj 2D Mater. Appl.* **2017**, *1*, 14.

(65) Kulish, V. V. Surface Reactivity and Vacancy Defects in Single-Layer Borophene Polymorphs. *Phys. Chem. Chem. Phys.* **2017**, *19*, 11273–11281.

(66) Xiang, P.; Chen, X.; Zhang, W.; Li, J.; Xiao, B.; Li, L.; Deng, K. Metallic Borophene Polytypes as Lightweight Anode Materials for Non-Lithium-Ion Batteries. *Phys. Chem. Chem. Phys.* **2017**, *19*, 24945–24954.

(67) Li, D.; Gao, J.; Cheng, P.; He, J.; Yin, Y.; Hu, Y.; Chen, L.; Cheng, Y.; Zhao, J. 2D Boron Sheets: Structure, Growth, and Electronic and Thermal Transport Properties. *Adv. Funct. Mater.* **2019**, 1904349.

(68) Zhang, Z.; Yang, Y.; Gao, G.; Yakobson, B. I. Two-Dimensional Boron Monolayers Mediated by Metal Substrates. *Angew. Chem. Int. Ed.* **2015**, *54*, 13022–13026.

(69) Liu, Y.; Penev, E. S.; Yakobson, B. I. Probing the Synthesis of Two-Dimensional Boron by First-Principles Computations. *Angew. Chem. Int. Ed.* **2013**, *52*, 3156–3159.

(70) Wu, R.; Drozdov, I. K.; Eltinge, S.; Zahl, P.; Ismail-Beigi, S.; Božović, I.; Gozar, A. Large-Area Single-Crystal Sheets of Borophene on Cu(111) Surfaces. *Nature Nanotech.* **2019**, *14*, 44–49.

(71) Vinogradov, N. A.; Lyalin, A.; Taketsugu, T.; Vinogradov, A. S.; Preobrajenski, A. Single-Phase Borophene on Ir(111): Formation, Structure, and Decoupling from the Support. *ACS Nano* **2019**, *13*, 14511–14518.

(72) Li, W.; Kong, L.; Chen, C.; Gou, J.; Sheng, S.; Zhang, W.; Li, H.; Chen, L.; Cheng, P.; Wu, K. Experimental Realization of Honeycomb Borophene. *Science Bulletin* **2018**, *63*, 282–286.

(73) Karmodak, N.; Jemmis, E. D. The Role of Holes in Borophenes: An *Ab Initio* Study of Their Structure and Stability with and without Metal Templates. *Angew. Chem. Int. Ed.* **2017**, *56*, 10093–10097.

(74) Wu, R.; Gozar, A.; Božović, I. Large-Area Borophene Sheets on Sacrificial Cu(111) Films Promoted by Recrystallization from Subsurface Boron. *npj Quantum Mater.* **2019**, *4*, 40.

(75) Zhang, Z.; Shirodkar, S. N.; Yang, Y.; Yakobson, B. I. Gate-Voltage Control of Borophene Structure Formation. *Angew. Chem. Int. Ed.* **2017**, *56*, 15421–15426.

(76) Şahin, H.; Cahangirov, S.; Topsakal, M.; Bekaroglu, E.; Akturk, E.; Senger, R. T.; Ciraci, S. Monolayer Honeycomb Structures of Group-IV Elements and III-V Binary Compounds: First-Principles Calculations. *Phys. Rev. B* **2009**, *80*, 155453.

(77) Molle, A.; Goldberger, J.; Houssa, M.; Xu, Y.; Zhang, S.-C.; Akinwande, D. Buckled Two-Dimensional Xene Sheets. *Nature Mater.* **2017**, *16*, 163–169.

(78) Liu, C.-C.; Jiang, H.; Yao, Y. Low-Energy Effective Hamiltonian Involving Spin-Orbit Coupling in Silicene and Two-Dimensional Germanium and Tin. *Phys. Rev. B* **2011**, *84*, 195430.

(79) Gori, P.; Kupchak, I.; Bechstedt, F.; Grassano, D.; Pulci, O. Honeycomb Silicon on Alumina: Massless Dirac Fermions in Silicene on Substrate. *Phys. Rev. B* **2019**, *100*, 245413.

(80) Cahangirov, S.; Topsakal, M.; Aktürk, E.; Şahin, H.; Ciraci, S. Two- and One-Dimensional Honeycomb Structures of Silicon and Germanium. *Phys. Rev. Lett.* **2009**, *102*, 236804.

(81) Xu, Y.; Yan, B.; Zhang, H.-J.; Wang, J.; Xu, G.; Tang, P.; Duan, W.; Zhang, S.-C. Large-Gap Quantum Spin Hall Insulators in Tin Films. *Phys. Rev. Lett.* **2013**, *111*, 136804.

(82) Huang, Z.-Q.; Hsu, C.-H.; Chuang, F.-C.; Liu, Y.-T.; Lin, H.; Su, W.-S.; Ozolins, V.; Bansil, A. Strain Driven Topological Phase Transitions in Atomically Thin Films of Group IV and V Elements in the Honeycomb Structures. *New J. Phys.* **2014**, *16*, 105018.

(83) Rivero, P.; Yan, J.-A.; García-Suárez, V. M.; Ferrer, J.; Barraza-Lopez, S. Stability and Properties of High-Buckled Two-Dimensional Tin and Lead. *Phys. Rev. B* **2014**, *90*, 241408.

(84) Vishnoi, P.; Pramoda, K.; Rao, C. N. R. 2D Elemental Nanomaterials Beyond Graphene. *ChemNanoMat* **2019**, *5*, 1062–1091.

(85) Glavin, N. R.; Rao, R.; Varshney, V.; Bianco, E.; Apte, A.; Roy, A.; Ringe, E.; Ajayan, P. M. Emerging Applications of Elemental 2D Materials. *Adv. Mater.* **2020**, *32*, 1904302.

(86) Si, N.; Yao, Q.; Jiang, Y.; Li, H.; Zhou, D.; Ji, Q.; Huang, H.; Li, H.; Niu, T. Recent Advances in Tin: From Two-Dimensional Quantum Spin Hall Insulator to Bulk Dirac Semimetal. *J. Phys. Chem. Lett.* **2020**, *11*, 1317–1329.

(87) Ni, Z.; Minamitani, E.; Ando, Y.; Watanabe, S. Germanene and Stanene on Two-Dimensional Substrates: Dirac Cone and Z 2 Invariant. *Phys. Rev. B* **2017**, *96*, 075427.

(88) Yakovkin, I. N. Spin-Orbit Band Gaps and Destruction of Dirac Cones. *Surf. Sci.* **2017**, *662*, 1–5.

(89) Ma, Y.; Dai, Y.; Guo, M.; Niu, C.; Huang, B. Intriguing Behavior of Halogenated Two-Dimensional Tin. *J. Phys. Chem. C* **2012**, *116*, 12977–12981.

(90) Chou, B.-H.; Huang, Z.-Q.; Hsu, C.-H.; Chuang, F.-C.; Liu, Y.-T.; Lin, H.; Bansil, A. Hydrogenated Ultra-Thin Tin Films Predicted as Two-Dimensional Topological Insulators. *New J. Phys.* **2014**, *16*, 115008.

(91) Si, C.; Liu, J.; Xu, Y.; Wu, J.; Gu, B.-L.; Duan, W. Functionalized Germanene as a Prototype of Large-Gap Two-Dimensional Topological Insulators. *Phys. Rev. B* **2014**, *89*, 115429.

(92) Özçelik, V. O.; Ciraci, S. Local Reconstructions of Silicene Induced by Adatoms. *J. Phys. Chem. C* **2013**, *117*, 26305–26315.

(93) Cahangirov, S.; Özçelik, V. O.; Xian, L.; Avila, J.; Cho, S.; Asensio, M. C.; Ciraci, S.; Rubio, A. Atomic Structure of the 3 × 3 Phase of Silicene on Ag(111). *Phys. Rev. B* **2014**, *90*, 035448.

(94) Özçelik, V. O.; Durgun, E.; Ciraci, S. New Phases of Germanene. *J. Phys. Chem. Lett.* **2014**, *5*, 2694–2699.

(95) Tang, P.; Chen, P.; Cao, W.; Huang, H.; Cahangirov, S.; Xian, L.; Xu, Y.; Zhang, S.-C.; Duan, W.; Rubio, A. Stable Two-Dimensional Dumbbell Stanene: A Quantum Spin Hall Insulator. *Phys. Rev. B* **2014**, *90*, 121408.

(96) Matusalem, F.; Marques, M.; Teles, L. K.; Bechstedt, F. Stability and Electronic Structure of Two-Dimensional Allotropes of Group-IV Materials. *Phys. Rev. B* **2015**, *92*, 045436.

(97) Tang, J.; Li, J.; He, C.; Zhang, C.; Ouyang, T.; Tang, C.; Xiao, H.; Zhong, J. *Ab Initio* Prediction of a New Allotrope of Two-Dimensional Silicon. *Phys. Status Solidi RRL* **2017**, *11*, 1600422.

(98) Gao, N.; Liu, H.; Zhou, S.; Bai, Y.; Zhao, J. Interaction between Post-Graphene Group-IV Honeycomb Monolayers and Metal Substrates: Implication for Synthesis and Structure Control. *J. Phys. Chem. C* **2017**, *121*, 5123–5129.

(99) Hartman, T.; Sofer, Z. Beyond Graphene: Chemistry of Group 14 Graphene Analogues: Silicene, Germanene, and Stanene. *ACS Nano* **2019**, *13*, 8566–8576.

(100) Lin, C.-L.; Arafune, R.; Kawahara, K.; Kanno, M.; Tsukahara, N.; Minamitani, E.; Kim, Y.; Kawai, M.; Takagi, N. Substrate-Induced Symmetry Breaking in Silicene. *Phys. Rev. Lett.* **2013**, *110*, 076801.

(101) Zhu, F.; Chen, W.; Xu, Y.; Gao, C.; Guan, D.; Liu, C.; Qian, D.; Zhang, S.-C.; Jia, J. Epitaxial Growth of Two-Dimensional Stanene. *Nature Mater.* **2015**, *14*, 1020–1025.

(102) Liao, M.; Zang, Y.; Guan, Z.; Li, H.; Gong, Y.; Zhu, K.; Hu, X.-P.; Zhang, D.; Xu, Y.; Wang, Y.-Y.; et al. Superconductivity in Few-Layer Stanene. *Nature Phys.* **2018**, *14*, 344–348.

(103) Lalmi, B.; Oughaddou, H.; Enriquez, H.; Kara, A.; Vizzini, S.; Ealet, B.; Aufray, B. Epitaxial Growth of a Silicene Sheet. *Appl. Phys. Lett.* **2010**, *9*, 223109.

(104) Vogt, P.; De Padova, P.; Quaresima, C.; Avila, J.; Frantzeskakis, E.; Asensio, M. C.; Resta, A.; Ealet, B.; Le Lay, G. Silicene: Compelling Experimental Evidence for Graphenelike Two-Dimensional Silicon. *Phys. Rev. Lett.* **2012**, *108*, 155501.

(105) Lin, C.-L.; Arafune, R.; Kawahara, K.; Tsukahara, N.; Minamitani, E.; Kim, Y.; Takagi, N.; Kawai, M. Structure of Silicene Grown on Ag(111). *Appl. Phys. Express* **2012**, *5*, 045802.

(106) Jamgotchian, H.; Colignon, Y.; Hamzaoui, N.; Ealet, B.; Hoarau, J. Y.; Aufray, B.; Bibérian, J. P. Growth of Silicene Layers on Ag(111): Unexpected Effect of the Substrate Temperature. *J. Phys.: Condens. Matter* **2012**, *24*, 172001.

(107) Arafune, R.; Lin, C.-L.; Kawahara, K.; Tsukahara, N.; Minamitani, E.; Kim, Y.; Takagi, N.; Kawai, M. Structural Transition of Silicene on Ag(111). *Surf. Sci.* **2013**, *608*, 297–300.

(108) Pawlak, R.; Drechsel, C.; D'Astolfo, P.; Kisiel, M.; Meyer, E.; Cerda, J. I. Quantitative Determination of Atomic Buckling of Silicene by Atomic Force Microscopy. *Proc. Natl. Acad. Sci. USA* **2020**, *117*, 228–237.

(109) Curcella, A.; Bernard, R.; Borensztein, Y.; Resta, A.; Lazzeri, M.; Prévot, G. Structure and Stability of Silicene on Ag(111) Reconstructions from Grazing Incidence X-Ray Diffraction and Density Functional Theory. *Phys. Rev. B* **2019**, *99*, 205411.

(110) Meng, L.; Wang, Y.; Zhang, L.; Du, S.; Wu, R.; Li, L.; Zhang, Y.; Li, G.; Zhou, H.; Hofer, W. A.; et al. Buckled Silicene Formation on Ir(111). *Nano Lett.* **2013**, *13*, 685–690.

(111) Huang, L.; Zhang, Y.-F.; Zhang, Y.-Y.; Xu, W.; Que, Y.; Li, E.; Pan, J.-B.; Wang, Y.-L.; Liu, Y.; Du, S.-X.; et al. Sequence of Silicon Monolayer Structures Grown on a Ru Surface: From a Herringbone Structure to Silicene. *Nano Lett.* **2017**, *17*, 1161–1166.

(112) Fleurence, A.; Friedlein, R.; Ozaki, T.; Kawai, H.; Wang, Y.; Yamada-Takamura, Y. Experimental Evidence for Epitaxial Silicene on Diboride Thin Films. *Phys. Rev. Lett.* **2012**, *108*, 245501.

(113) Aizawa, T.; Suehara, S.; Otani, S. Silicene on Zirconium Carbide (111). *J. Phys. Chem. C* **2014**, *118*, 23049–23057.

(114) Stępniak-Dybala, A.; Krawiec, M. Formation of Silicene on Ultrathin Pb(111) Films. *J. Phys. Chem. C* **2019**, *123*, 17019–17025.

(115) Li, L.; Lu, S.; Pan, J.; Qin, Z.; Wang, Y.; Wang, Y.; Cao, G.; Du, S.; Gao, H.-J. Buckled Germanene Formation on Pt(111). *Adv. Mater.* **2014**, *26*, 4820–4824.

(116) Dávila, M. E.; Xian, L.; Cahangirov, S.; Rubio, A.; Le Lay, G. Germanene: A Novel Two-Dimensional Germanium Allotrope Akin to Graphene and Silicene. *New J. Phys.* **2014**, *16*, 095002.

(117) Zhuang, J.; Gao, N.; Li, Z.; Xu, X.; Wang, J.; Zhao, J.; Dou, S. X.; Du, Y. Cooperative Electron–Phonon Coupling and Buckled Structure in Germanene on Au(111). *ACS Nano* **2017**, *11*, 3553–3559.

(118) Dávila, M. E.; Le Lay, G. Few Layer Epitaxial Germanene: A Novel Two-Dimensional Dirac Material. *Sci Rep* **2016**, *6*, 20714.

(119) Lin, C.-H.; Huang, A.; Pai, W. W.; Chen, W.-C.; Chen, T.-Y.; Chang, T.-R.; Yukawa, R.; Cheng, C.-M.; Mou, C.-Y.; Matsuda, I.; et al. Single-Layer Dual Germanene Phases on Ag(111). *Phys. Rev. Materials* **2018**, *2*, 024003.

(120) Chiniwar, S.; Huang, A.; Chen, T.-Y.; Lin, C.-H.; Hsing, C.-R.; Chen, W.-C.; Cheng, C.-M.; Jeng, H.-T.; Wei, C. M.; Pai, W. W.; et al. Substrate-Mediated Umklapp Scattering at the Incommensurate Interface of a Monatomic Alloy Layer. *Phys. Rev. B* **2019**, *99*, 155408.

(121) Derivaz, M.; Dentel, D.; Stephan, R.; Hanf, M.-C.; Mehdaoui, A.; Sonnet, P.; Pirri, C. Continuous Germanene Layer on Al(111). *Nano Lett.* **2015**, *15*, 2510–2516.

(122) Stephan, R.; Hanf, M. C.; Derivaz, M.; Dentel, D.; Asensio, M. C.; Avila, J.; Mehdaoui, A.; Sonnet, P.; Pirri, C. Germanene on Al(111): Interface Electronic States and Charge Transfer. *J. Phys. Chem. C* **2016**, *120*, 1580–1585.

(123) Endo, S.; Kubo, O.; Nakashima, N.; Iwaguma, S.; Yamamoto, R.; Kamakura, Y.; Tabata, H.; Katayama, M. $\sqrt{3} \times \sqrt{3}$ Germanene on Al(111) Grown at Nearly Room Temperature. *Appl. Phys. Express* **2018**, *11*, 019201.

(124) Qin, Z.; Pan, J.; Lu, S.; Shao, Y.; Wang, Y.; Du, S.; Gao, H.-J.; Cao, G. Direct Evidence of Dirac Signature in Bilayer Germanene Islands on Cu(111). *Adv. Mater.* **2017**, *29*, 1606046.

(125) Gou, J.; Zhong, Q.; Sheng, S.; Li, W.; Cheng, P.; Li, H.; Chen, L.; Wu, K. Strained Monolayer Germanene with $1 \times 1$ Lattice on Sb(111). *2D Mater.* **2016**, *3*, 045005.

(126) Gou, J.; Kong, L.; Li, H.; Zhong, Q.; Li, W.; Cheng, P.; Chen, L.; Wu, K. Strain-Induced Band Engineering in Monolayer Stanene on Sb(111). *Phys. Rev. Materials* **2017**, *1*, 054004.

(127) Wu, H.; Tang, J.; Liang, Q.; Shi, B.; Niu, Y.; Si, J.; Liao, Q.; Dou, W. A van der Waals Epitaxial Growth of Ultrathin Two-Dimensional Sn Film on Graphene Covered Cu(111) Substrate. *Appl. Phys. Lett.* **2019**, *115*, 141601.

(128) Yuhara, J.; Fujii, Y.; Nishino, K.; Isobe, N.; Nakatake, M.; Xian, L.; Rubio, A.; Le Lay, G. Large Area Planar Stanene Epitaxially Grown on Ag(111). *2D Mater.* **2018**, *5*, 025002.

(129) Maniraj, M.; Stadtmüller, B.; Jungkenn, D.; Düvel, M.; Emmerich, S.; Shi, W.; Stöckl, J.; Lyu, L.; Kollamana, J.; Wei, Z.; et al. A Case Study for the Formation of Stanene on a Metal Surface. *Commun. Phys.* **2019**, *2*, 12.

(130) Liu, Y.; Gao, N.; Zhuang, J.; Liu, C.; Wang, J.; Hao, W.; Dou, S. X.; Zhao, J.; Du, Y. Realization of Strained Stanene by Interface Engineering. *J. Phys. Chem. Lett.* **2019**, *10*, 1558–1565.

(131) Xu, C.-Z.; Chan, Y.-H.; Chen, Y.; Chen, P.; Wang, X.; Dejoie, C.; Wong, M.-H.; Hlevyack, J. A.; Ryu, H.; Kee, H.-Y.; et al. Elemental Topological Dirac Semimetal: α-Sn on InSb(111). *Phys. Rev. Lett.* **2017**, *118*, 146402.

(132) Xu, C.-Z.; Chan, Y.-H.; Chen, P.; Wang, X.; Flötotto, D.; Hlevyack, J. A.; Bian, G.; Mo, S.-K.; Chou, M.-Y.; Chiang, T.-C. Gapped Electronic Structure of Epitaxial Stanene on InSb(111). *Phys. Rev. B* **2018**, *97*, 035122.

(133) Rogalev, V. A.; Reis, F.; Adler, F.; Bauernfeind, M.; Erhardt, J.; Kowalewski, A.; Scholz, M. R.; Dudy, L.; Duffy, L. B.; Hesjedal, T.; et al. Tailoring the Topological Surface State in Ultrathin α-Sn(111) Films. *Phys. Rev. B* **2019**, *100*, 245144.

(134) De Crescenzi, M.; Berbezier, I.; Scarselli, M.; Castrucci, P.; Abbarchi, M.; Ronda, A.; Jardali, F.; Park, J.; Vach, H. Formation of Silicene Nanosheets on Graphite. *ACS Nano* **2016**, *10*, 11163–11171.

(135) Chiappe, D.; Scalise, E.; Cinquanta, E.; Grazianetti, C.; van den Broek, B.; Fanciulli, M.; Houssa, M.; Molle, A. Two-Dimensional Si Nanosheets with Local Hexagonal Structure on a $MoS_2$ Surface. *Adv. Mater.* **2014**, *26*, 2096–2101.

(136) Peng, W.; Xu, T.; Diener, P.; Biadala, L.; Berthe, M.; Pi, X.; Borensztein, Y.; Curcella, A.; Bernard, R.; Prévot, G.; et al. Resolving the Controversial Existence of Silicene and Germanene Nanosheets Grown on Graphite. *ACS Nano* **2018**, *12*, 4754–4760.

(137) van Bremen, R.; Yao, Q.; Banerjee, S.; Cakir, D.; Oncel, N.; Zandvliet, H. J. W. Intercalation of Si between $MoS_2$ Layers. *Beilstein J. Nanotechnol.* **2017**, *8*, 1952–1960.

(138) Gao, J.; Zhao, J. Initial Geometries, Interaction Mechanism and High Stability of Silicene on Ag(111) Surface. *Sci. Rep.* **2012**, *2*, 861.

(139) Chen, M. X.; Zhong, Z.; Weinert, M. Designing Substrates for Silicene and Germanene: First-Principles Calculations. *Phys. Rev. B* **2016**, *94*, 075409.

(140) Sone, J.; Yamagami, T.; Nakatsuji, K.; Hirayama, H. Si Growth at Graphene Surfaces on 6H-SiC(0001) Substrates. *Jpn. J. Appl. Phys.* **2016**, *55*, 035502.

(141) Guo, Z.-X.; Furuya, S.; Iwata, J.; Oshiyama, A. Absence and Presence of Dirac Electrons in Silicene on Substrates. *Phys. Rev. B* **2013**, *87*, 235435.

(142) Wang, Y.-P.; Cheng, H.-P. Absence of a Dirac Cone in Silicene on Ag(111): First-Principles Density Functional Calculations with a Modified Effective Band Structure Technique. *Phys. Rev. B* **2013**, *87*, 245430.

(143) Mahatha, S. K.; Moras, P.; Bellini, V.; Sheverdyaeva, P. M.; Struzzi, C.; Petaccia, L.; Carbone, C. Silicene on Ag(111): A Honeycomb Lattice without Dirac Bands. *Phys. Rev. B* **2014**, *89*, 201416.

(144) Feng, Y.; Liu, D.; Feng, B.; Liu, X.; Zhao, L.; Xie, Z.; Liu, Y.; Liang, A.; Hu, C.; Hu, Y.; et al. Direct Evidence of Interaction-Induced Dirac Cones in a Monolayer Silicene/Ag(111) System. *Proc Natl Acad Sci USA* **2016**, *113*, 14656–14661.

(145) Feng, B.; Zhou, H.; Feng, Y.; Liu, H.; He, S.; Matsuda, I.; Chen, L.; Schwier, E. F.; Shimada, K.; Meng, S.; et al. Superstructure-Induced Splitting of Dirac Cones in Silicene. *Phys. Rev. Lett.* **2019**, *122*, 196801.

(146) Wang, Y.; Li, J.; Xiong, J.; Pan, Y.; Ye, M.; Guo, Y.; Zhang, H.; Quhe, R.; Lu, J. Does the Dirac Cone of Germanene Exist on Metal Substrates? *Phys. Chem. Chem. Phys.* **2016**, *18* (28), 19451–19456.

(147) Mannix, A. J.; Kiraly, B.; Fisher, B. L.; Hersam, M. C.; Guisinger, N. P. Silicon Growth at the Two-Dimensional Limit on Ag(111). *ACS Nano* **2014**, *8*, 7538–7547.

(148) Shirai, T.; Shirasawa, T.; Hirahara, T.; Fukui, N.; Takahashi, T.; Hasegawa, S. Structure Determination of Multilayer Silicene Grown on Ag(111) Films by Electron Diffraction: Evidence for Ag Segregation at the Surface. *Phys. Rev. B* **2014**, *89*, 241403.

(149) Borensztein, Y.; Curcella, A.; Royer, S.; Prévot, G. Silicene Multilayers on Ag(111) Display a Cubic Diamondlike Structure and a $\sqrt{3} \times \sqrt{3}$ Reconstruction Induced by Surfactant Ag Atoms. *Phys. Rev. B* **2015**, *92*, 155407.

(150) Kawahara, K.; Shirasawa, T.; Lin, C.-L.; Nagao, R.; Tsukahara, N.; Takahashi, T.; Arafune, R.; Kawai, M.; Takagi, N. Atomic Structure of "Multilayer Silicene" Grown on Ag(111): Dynamical Low Energy Electron Diffraction Analysis. *Surf. Sci.* **2016**, *651*, 70–75.

(151) Curcella, A.; Bernard, R.; Borensztein, Y.; Lazzeri, M.; Prévot, G. The Mechanism for the Stabilization and Surfactant Properties of Epitaxial Silicene. *Nanoscale* **2018**, *10*, 2291–2300.

(152) Yabuoshi, K.; Sugimoto, Y. Evidence for Honeycomb-Chained Trimer Structure of Multilayer Silicene on Ag(111) with Noncontact Atomic Force Microscopy. *Jpn. J. Appl. Phys.* **2019**, *58*, 020903.

(153) Švec, M.; Hapala, P.; Ondráček, M.; Merino, P.; Blanco-Rey, M.; Mutombo, P.; Vondráček, M.; Polyak, Y.; Cháb, V.; Martín Gago, J. A.; et al. Silicene versus Two-Dimensional Ordered Silicide: Atomic and Electronic Structure of Si-(19 × 19) R23.4°/Pt(111). *Phys. Rev. B* **2014**, *89*, 201412.

(154) Ho, C.-S.; Banerjee, S.; Batzill, M.; Beck, D. E.; Koel, B. E. Formation and Structure of a (√19×√19)R23.4°-Ge/Pt(111) Surface Alloy. *Surf. Sci.* **2009**, *603*, 1161–1167.

(155) Wang, W.; Uhrberg, R. I. G. Investigation of the Atomic and Electronic Structures of Highly Ordered Two-Dimensional Germanium on Au(111). *Phys. Rev. Materials* **2017**, *1*, 074002.

(156) Cantero, E. D.; Solis, L. M.; Tong, Y.; Fuhr, J. D.; Martiarena, M. L.; Grizzi, O.; Sánchez, E. A. Growth of Germanium on Au(111): Formation of Germanene or Intermixing of Au and Ge Atoms? *Phys. Chem. Chem. Phys.* **2017**, *19*, 18580–18586.

(157) Martínez, E. A.; Fuhr, J. D.; Grizzi, O.; Sánchez, E. A.; Cantero, E. D. Growth of Germanene on Al(111) Hindered by Surface Alloy Formation. *J. Phys. Chem. C* **2019**, *123*, 12910–12918.

(158) Muzychenko, D. A.; Oreshkin, S. I.; Panov, V. I.; Van Haesendonck, C.; Oreshkin, A. I. Single and Multi Domain Buckled Germanene Phases on Al(111) Surface. *Nano Res.* **2019**, *12*, 2988–2996.

(159) Fang, J.; Zhao, P.; Chen, G. Germanene Growth on Al(111): A Case Study of Interface Effect. *J. Phys. Chem. C* **2018**, *122*, 18669–18681.

(160) Luh, D.-A.; Wang, C.-H.; Yang, Y.-W. Growth of Thin Sn Films on Ag(111) Studied with Low-Energy Electron Diffraction and X-Ray Photoelectron Spectroscopy. *Thin Solid Films* **2019**, *682*, 44–49.

(161) Deng, J.; Xia, B.; Ma, X.; Chen, H.; Shan, H.; Zhai, X.; Li, B.; Zhao, A.; Xu, Y.; Duan, W.; et al. Epitaxial Growth of Ultraflat Stanene with Topological Band Inversion. *Nature Mater.* **2018**, *17*, 1081–1086.

(162) Guo, Z.-X.; Furuya, S.; Iwata, J.; Oshiyama, A. Absence of Dirac Electrons in Silicene on Ag(111) Surfaces. *J. Phys. Soc. Jpn.* **2013**, *82*, 063714.

(163) Kokott, S.; Pflugradt, P.; Matthes, L.; Bechstedt, F. Nonmetallic Substrates for Growth of Silicene: An *Ab Initio* Prediction. *J. Phys.: Condens. Matter* **2014**, *26*, 185002.

(164) Cai, Y.; Chuu, C.-P.; Wei, C. M.; Chou, M. Y. Stability and Electronic Properties of Two-Dimensional Silicene and Germanene on Graphene. *Phys. Rev. B* **2013**, *88*, 245408.

(165) Matusalem, F.; Koda, D. S.; Bechstedt, F.; Marques, M.; Teles, L. K. Deposition of Topological Silicene, Germanene and Stanene on Graphene-Covered SiC Substrates. *Sci Rep* **2017**, *7*, 15700.

(166) Li, L.; Zhao, M. First-Principles Identifications of Superstructures of Germanene on Ag(111) Surface and h-BN Substrate. *Phys. Chem. Chem. Phys.* **2013**, *15*, 16853.

(167) Hsu, C.-H.; Fang, Y.; Wu, S.; Huang, Z.-Q.; Crisostomo, C. P.; Gu, Y.-M.; Zhu, Z.-Z.; Lin, H.; Bansil, A.; Chuang, F.-C.; et al. Quantum Anomalous Hall Insulator Phase in Asymmetrically Functionalized Germanene. *Phys. Rev. B* **2017**, *96*, 165426.

(168) Galbiati, M.; Motta, N.; De Crescenzi, M.; Camilli, L. Group-IV 2D Materials beyond Graphene on Nonmetal Substrates: Challenges, Recent Progress, and Future Perspectives. *Appl. Phys. Rev.* **2019**, *6*, 041310.

(169) Acun, A.; Poelsema, B.; Zandvliet, H. J. W.; van Gastel, R. The Instability of Silicene on Ag(111). *Appl. Phys. Lett.* **2013**, *103*, 263119.

(170) De Padova, P.; Generosi, A.; Paci, B.; Ottaviani, C.; Quaresima, C.; Olivieri, B.; Salomon, E.; Angot, T.; Le Lay, G. Multilayer Silicene: Clear Evidence. *2D Mater.* **2016**, *3*, 031011.

(171) Feng, B.; Ding, Z.; Meng, S.; Yao, Y.; He, X.; Cheng, P.; Chen, L.; Wu, K. Evidence of Silicene in Honeycomb Structures of Silicon on Ag(111). *Nano Lett.* **2012**, *12*, 3507–3511.

(172) Zang, Y.; Jiang, T.; Gong, Y.; Guan, Z.; Liu, C.; Liao, M.; Zhu, K.; Li, Z.; Wang, L.; Li, W.; et al. Realizing an Epitaxial Decorated Stanene with an Insulating Bandgap. *Adv. Funct. Mater.* **2018**, *28*, 1802723.

(173) Grazianetti, C.; Chiappe, D.; Cinquanta, E.; Tallarida, G.; Fanciulli, M.; Molle, A. Exploring the Morphological and Electronic Properties of Silicene Superstructures. *Appl. Surf. Sci.* **2014**, *291*, 109–112.

(174) Huang, C.; Zhou, J.; Wu, H.; Deng, K.; Jena, P.; Kan, E. Quantum Phase Transition in Germanene and Stanene Bilayer: From Normal Metal to Topological Insulator. *J. Phys. Chem. Lett.* **2016**, *7*, 1919–1924.

(175) Zhang, W. X.; Dong, M. M.; He, C. Novel Electronic and Planar Magnetic Properties of Two-Dimensional Surface Decorated Antimonene. *Mater. Res. Bull.* **2019**, *118*, 110489.

(176) Hsu, C.-H.; Huang, Z.-Q.; Chuang, F.-C.; Kuo, C.-C.; Liu, Y.-T.; Lin, H.; Bansil, A. The Nontrivial Electronic Structure of Bi/Sb Honeycombs on SiC(0001). *New J. Phys.* **2015**, *17*, 025005.

(177) Zhang, S.; Hu, Y.; Hu, Z.; Cai, B.; Zeng, H. Hydrogenated Arsenenes as Planar Magnet and Dirac Material. *Appl. Phys. Lett.* **2015**, *107*, 022102.

(178) Hsu, C.-H.; Huang, Z.-Q.; Crisostomo, C. P.; Yao, L.-Z.; Chuang, F.-C.; Liu, Y.-T.; Wang, B.; Hsu, C.-H.; Lee, C.-C.; Lin, H.; et al. Two-Dimensional Topological Crystalline

Insulator Phase in Sb/Bi Planar Honeycomb with Tunable Dirac Gap. *Sci Rep* **2016**, *6*, 18993.

(179) Fu, L. Topological Crystalline Insulators. *Phys. Rev. Lett.* **2011**, *106*, 106802.

(180) Needs, R. J.; Martin, R. M.; Nielsen, O. H. Total-Energy Calculations of the Structural Properties of the Group-V Element Arsenic. *Phys. Rev. B* **1986**, *33*, 3778–3784.

(181) Burdett, J. K.; Lee, S. Peierls Distortions in Two and Three Dimensions and the Structures of AB Solids. *J. Am. Chem. Soc.* **1983**, *105*, 1079–1083.

(182) Gunton, D. J.; Saunders, G. A. The Young's Modulus and Poisson's Ratio of Arsenic, Antimony and Bismuth. *J Mater Sci* **1972**, *7*, 1061–1068.

(183) Sturala, J.; Sofer, Z.; Pumera, M. Chemistry of Layered Pnictogens: Phosphorus, Arsenic, Antimony, and Bismuth. *Angew. Chem.* **2019**, *131*, 7631–7637.

(184) Boulfelfel, S. E.; Seifert, G.; Grin, Y.; Leoni, S. Squeezing Lone Pairs: The A 17 to A 7 Pressure-Induced Phase Transition in Black Phosphorus. *Phys. Rev. B* **2012**, *85*, 014110.

(185) Zhang, S.; Xie, M.; Li, F.; Yan, Z.; Li, Y.; Kan, E.; Liu, W.; Chen, Z.; Zeng, H. Semiconducting Group 15 Monolayers: A Broad Range of Band Gaps and High Carrier Mobilities. *Angew. Chem. Int. Ed.* **2016**, *55*, 1666–1669.

(186) Ersan, F.; Aktürk, E.; Ciraci, S. Stable Single-Layer Structure of Group-V Elements. *Phys. Rev. B* **2016**, *94*, 245417.

(187) Lin, W.; Li, J.; Wang, W.; Liang, S.-D.; Yao, D.-X. Electronic Structure and Band Gap Engineering of Two-Dimensional Octagon-Nitrogene. *Sci Rep* **2018**, *8*, 1674.

(188) Zhang, Y.; Lee, J.; Wang, W.-L.; Yao, D.-X. Two-Dimensional Octagon-Structure Monolayer of Nitrogen Group Elements and the Related Nano-Structures. *Comput. Mater. Sci.* **2015**, *110*, 109–114.

(189) Carrete, J.; Gallego, L. J.; Mingo, N. Structural Complexity and Phonon Physics in 2D Arsenenes. *J. Phys. Chem. Lett.* **2017**, *8*, 1375–1380.

(190) Kou, L.; Tan, X.; Ma, Y.; Tahini, H.; Zhou, L.; Sun, Z.; Aijun, D.; Chen, C.; Smith, S. C. Tetragonal Bismuth Bilayer: A Stable and Robust Quantum Spin Hall Insulator. *2D Mater.* **2015**, *2*, 045010.

(191) Eremets, M. I.; Gavriliuk, A. G.; Trojan, I. A.; Dzivenko, D. A.; Boehler, R. Single-Bonded Cubic Form of Nitrogen. *Nature Mater.* **2004**, *3*, 558–563.

(192) Özçelik, V. O.; Aktürk, O. Ü.; Durgun, E.; Ciraci, S. Prediction of a Two-Dimensional Crystalline Structure of Nitrogen Atoms. *Phys. Rev. B* **2015**, *92*, 125420.

(193) Harada, Y.; Yamamoto, M.; Baba, T.; Kita, T. Epitaxial Two-Dimensional Nitrogen Atomic Sheet in GaAs. *Appl. Phys. Lett.* **2014**, *104*, 041907.

(194) Gusmão, R.; Sofer, Z.; Pumera, M. Black Phosphorus Rediscovered: From Bulk Material to Monolayers. *Angew. Chem. Int. Ed.* **2017**, *56*, 8052–8072.

(195) Liu, H.; Neal, A. T.; Zhu, Z.; Luo, Z.; Xu, X.; Tománek, D.; Ye, P. D. Phosphorene: An Unexplored 2D Semiconductor with a High Hole Mobility. *ACS Nano* **2014**, *8*, 4033–4041.

(196) Lu, W.; Nan, H.; Hong, J.; Chen, Y.; Zhu, C.; Liang, Z.; Ma, X.; Ni, Z.; Jin, C.; Zhang, Z. Plasma-Assisted Fabrication of Monolayer Phosphorene and Its Raman Characterization. *Nano Res.* **2014**, *7*, 853–859.

(197) Castellanos-Gomez, A.; Vicarelli, L.; Prada, E.; Island, J. O.; Narasimha-Acharya, K. L.; Blanter, S. I.; Groenendijk, D. J.; Buscema, M.; Steele, G. A.; Alvarez, J. V.; et al. Isolation and Characterization of Few-Layer Black Phosphorus. *2D Mater.* **2014**, *1*, 025001.

(198) Jamieson, J. C. Crystal Structures Adopted by Black Phosphorus at High Pressures. *Science* **1963**, *139*, 1291–1292.

(199) Zhu, Z.; Tománek, D. Semiconducting Layered Blue Phosphorus: A Computational Study. *Phys. Rev. Lett.* **2014**, *112*, 176802.

(200) Zhang, J. L.; Zhao, S.; Han, C.; Wang, Z.; Zhong, S.; Sun, S.; Guo, R.; Zhou, X.; Gu, C. D.; Yuan, K. D.; et al. Epitaxial Growth of Single Layer Blue Phosphorus: A New Phase of Two-Dimensional Phosphorus. *Nano Lett.* **2016**, *16*, 4903–4908.

(201) Zhao, S.; Zhang, J. L.; Chen, W.; Li, Z. Structure of Blue Phosphorus Grown on Au(111) Surface Revisited. *J. Phys. Chem. C* **2020**, *124*, 2024–2029.

(202) Guan, J.; Zhu, Z.; Tománek, D. Phase Coexistence and Metal-Insulator Transition in Few-Layer Phosphorene: A Computational Study. *Phys. Rev. Lett.* **2014**, *113*, 046804.

(203) Guan, J.; Zhu, Z.; Tománek, D. Tiling Phosphorene. *ACS Nano* **2014**, *8*, 12763–12768.

(204) Wu, M.; Fu, H.; Zhou, L.; Yao, K.; Zeng, X. C. Nine New Phosphorene Polymorphs with Non-Honeycomb Structures: A Much Extended Family. *Nano Lett.* **2015**, *15*, 3557–3562.

(205) Zhao, T.; He, C. Y.; Ma, S. Y.; Zhang, K. W.; Peng, X. Y.; Xie, G. F.; Zhong, J. X. A New Phase of Phosphorus: The Missed Tricycle Type Red Phosphorene. *J. Phys.: Condens. Matter* **2015**, *27*, 265301.

(206) Han, W. H.; Kim, S.; Lee, I.-H.; Chang, K. J. Prediction of Green Phosphorus with Tunable Direct Band Gap and High Mobility. *J. Phys. Chem. Lett.* **2017**, *8*, 4627–4632.

(207) Geng, W.; Xiao, J.; Brown, J. J.; Page, A. J.; Ke, Z. New Phosphorene by Phase Combination with Tunable Electronic and Mechanical Properties. *J. Phys. Chem. C* **2019**, *123*, 10788–10794.

(208) Qiu, L.; Dong, J.; Ding, F. Highly Stable Phosphorene Isomers Based on a Buckled Honeycomb Lattice. *Nanoscale* **2019**, *11*, 7135–7139.

(209) Iwasaki, H.; Kikegawa, T. Structural Systematics of the High-Pressure Phases of Phosphorus, Arsenic, Antimony and Bismuth. *Acta Crystallogr. B Struct. Sci.* **1997**, *53*, 353–357.

(210) Pumera, M.; Sofer, Z. 2D Monoelemental Arsenene, Antimonene, and Bismuthene: Beyond Black Phosphorus. *Adv. Mater.* **2017**, *29*, 1605299.

(211) Osters, O.; Nilges, T.; Bachhuber, F.; Pielnhofer, F.; Weihrich, R.; Schöneich, M.; Schmidt, P. Synthesis and Identification of Metastable Compounds: Black Arsenic-Science or Fiction? *Angew. Chem. Int. Ed.* **2012**, *51*, 2994–2997.

(212) Zhang, Z.; Xie, J.; Yang, D.; Wang, Y.; Si, M.; Xue, D. Manifestation of Unexpected Semiconducting Properties in Few-Layer Orthorhombic Arsenene. *Appl. Phys. Express* **2015**, *8*, 055201.

(213) Kamal, C.; Ezawa, M. Arsenene: Two-Dimensional Buckled and Puckered Honeycomb Arsenic Systems. *Phys. Rev. B* **2015**, *91*, 085423.

(214) Kecik, D.; Durgun, E.; Ciraci, S. Stability of Single-Layer and Multilayer Arsenene and Their Mechanical and Electronic Properties. *Phys. Rev. B* **2016**, *94*, 205409.

(215) Aktürk, O. Ü.; Özçelik, V. O.; Ciraci, S. Single-Layer Crystalline Phases of Antimony: Antimonenes. *Phys. Rev. B* **2015**, *91*, 235446.

(216) Wang, G.; Pandey, R.; Karna, S. P. Atomically Thin Group V Elemental Films: Theoretical Investigations of Antimonene Allotropes. *ACS Appl. Mater. Interfaces* **2015**, *7*, 11490–11496.

(217) Cheng, L.; Liu, H.; Tan, X.; Zhang, J.; Wei, J.; Lv, H.; Shi, J.; Tang, X. Thermoelectric Properties of a Monolayer Bismuth. *J. Phys. Chem. C* **2014**, *118*, 904–910.

(218) Aktürk, E.; Aktürk, O. Ü.; Ciraci, S. Single and Bilayer Bismuthene: Stability at High Temperature and Mechanical and Electronic Properties. *Phys. Rev. B* **2016**, *94*, 014115.

(219) Lu, Y.; Xu, W.; Zeng, M.; Yao, G.; Shen, L.; Yang, M.; Luo, Z.; Pan, F.; Wu, K.; Das, T.; et al. Topological Properties Determined by Atomic Buckling in Self-Assembled Ultrathin Bi(110). *Nano Lett.* **2015**, *15*, 80–87.

(220) Kowalczyk, P. J.; Brown, S. A.; Maerkl, T.; Lu, Q.; Chiu, C.-K.; Liu, Y.; Yang, S. A.; Wang, X.; Zasada, I.; Genuzio, F.; et al. Realization of Symmetry-Enforced Two-Dimensional Dirac Fermions in Nonsymmorphic α-Bismuthene. *ACS Nano* **2020**, *14*, 1888–1894.

(221) Huang, Z.-Q.; Chuang, F.-C.; Hsu, C.-H.; Liu, Y.-T.; Chang, H.-R.; Lin, H.; Bansil, A. Nontrivial Topological Electronic Structures in a Single Bi(111) Bilayer on Different Substrates: A First-Principles Study. *Phys. Rev. B* **2013**, *88*, 165301.

(222) Qiao, J.; Kong, X.; Hu, Z.-X.; Yang, F.; Ji, W. High-Mobility Transport Anisotropy and Linear Dichroism in Few-Layer Black Phosphorus. *Nat. Commun.* **2014**, *5*, 4475.

(223) Fei, R.; Faghaninia, A.; Soklaski, R.; Yan, J.-A.; Lo, C.; Yang, L. Enhanced Thermoelectric Efficiency via Orthogonal Electrical and Thermal Conductances in Phosphorene. *Nano Lett.* **2014**, *14*, 6393–6399.

(224) Zeraati, M.; Vaez Allaei, S. M.; Abdolhosseini Sarsari, I.; Pourfath, M.; Donadio, D. Highly Anisotropic Thermal Conductivity of Arsenene: An *Ab Initio* Study. *Phys. Rev. B* **2016**, *93*, 085424.

(225) Yuan, H.; Liu, X.; Afshinmanesh, F.; Li, W.; Xu, G.; Sun, J.; Lian, B.; Curto, A. G.; Ye, G.; Hikita, Y.; et al. Polarization-Sensitive Broadband Photodetector Using a Black Phosphorus Vertical p–n Junction. *Nature Nanotech.* **2015**, *10*, 707–713.

(226) Wang, X.; Jones, A. M.; Seyler, K. L.; Tran, V.; Jia, Y.; Zhao, H.; Wang, H.; Yang, L.; Xu, X.; Xia, F. Highly Anisotropic and Robust Excitons in Monolayer Black Phosphorus. *Nature Nanotech.* **2015**, *10*, 517–521.

(227) Liu, X.; Ryder, C. R.; Wells, S. A.; Hersam, M. C. Resolving the In-Plane Anisotropic Properties of Black Phosphorus. *Small Methods* **2017**, *1*, 1700143.

(228) Chen, Y.; Chen, C.; Kealhofer, R.; Liu, H.; Yuan, Z.; Jiang, L.; Suh, J.; Park, J.; Ko, C.; Choe, H. S.; et al. Black Arsenic: A Layered Semiconductor with Extreme In-Plane Anisotropy. *Adv. Mater.* **2018**, *30*, 1800754.

(229) Chen, K.-X.; Lyu, S.-S.; Wang, X.-M.; Fu, Y.-X.; Heng, Y.; Mo, D.-C. Excellent Thermoelectric Performance Predicted in Two-Dimensional Buckled Antimonene: A First-Principles Study. *J. Phys. Chem. C* **2017**, *121*, 13035–13042.

(230) Xiao, J.; Long, M.; Zhang, X.; Ouyang, J.; Xu, H.; Gao, Y. Theoretical Predictions on the Electronic Structure and Charge Carrier Mobility in 2D Phosphorus Sheets. *Sci. Rep.* **2015**, *5*, 9961.

(231) Wang, Y.; Huang, P.; Ye, M.; Quhe, R.; Pan, Y.; Zhang, H.; Zhong, H.; Shi, J.; Lu, J. Many-Body Effect, Carrier Mobility, and Device Performance of Hexagonal Arsenene and Antimonene. *Chem. Mater.* **2017**, *29*, 2191–2201.

(232) Chowdhury, C.; Datta, A. Exotic Physics and Chemistry of Two-Dimensional Phosphorus: Phosphorene. *J. Phys. Chem. Lett.* **2017**, *8*, 2909–2916.

(233) Xiao, C.; Wang, F.; Yang, S. A.; Lu, Y.; Feng, Y.; Zhang, S. Elemental Ferroelectricity and Antiferroelectricity in Group-V Monolayer. *Adv. Funct. Mater.* **2018**, *28*, 1707383.

(234) Guo, Y.; Zhu, H.; Wang, Q. Large Second Harmonic Generation in Elemental α-Sb and α-Bi Monolayers. *J. Phys. Chem. C* **2020**, *124*, 5506–5513.

(235) Wada, M.; Murakami, S.; Freimuth, F.; Bihlmayer, G. Localized Edge States in Two-Dimensional Topological Insulators: Ultrathin Bi Films. *Phys. Rev. B* **2011**, *83*, 121310.

(236) Liu, Z.; Liu, C.-X.; Wu, Y.-S.; Duan, W.-H.; Liu, F.; Wu, J. Stable Nontrivial Z 2 Topology in Ultrathin Bi(111) Films: A First-Principles Study. *Phys. Rev. Lett.* **2011**, *107*, 136805.

(237) Chen, L.; Wang, Z. F.; Liu, F. Robustness of Two-Dimensional Topological Insulator States in Bilayer Bismuth against Strain and Electrical Field. *Phys. Rev. B* **2013**, *87*, 235420.

(238) Wang, Y.; Zhang, C.; Ji, W.; Zhang, R.; Li, P.; Wang, P.; Ren, M.; Chen, X.; Yuan, M. Tunable Quantum Spin Hall Effect via Strain in Two-Dimensional Arsenene Monolayer. *J. Phys. D: Appl. Phys.* **2016**, *49*, 055305.

(239) Zhang, H.; Ma, Y.; Chen, Z. Quantum Spin Hall Insulators in Strain-Modified Arsenene. *Nanoscale* **2015**, *7*, 19152–19159.

(240) Zhao, M.; Zhang, X.; Li, L. Strain-Driven Band Inversion and Topological Aspects in Antimonene. *Sci. Rep.* **2015**, *5*, 16108.

(241) Hu, Z.; Gao, J.; Zhang, S.; Zhao, J.; Zhou, W.; Zeng, H. Topologically Protected States and Half-Metal Behaviors: Defect-Strain Synergy Effects in Two-Dimensional Antimonene. *Phys. Rev. Materials* **2019**, *3*, 074005.

(242) Reis, F.; Li, G.; Dudy, L.; Bauernfeind, M.; Glass, S.; Hanke, W.; Thomale, R.; Schäfer, J.; Claessen, R. Bismuthene on a SiC Substrate: A Candidate for a High-Temperature Quantum Spin Hall Material. *Science* **2017**, *357*, 287–290.

(243) Sun, H.-H.; Wang, M.-X.; Zhu, F.; Wang, G.-Y.; Ma, H.-Y.; Xu, Z.-A.; Liao, Q.; Lu, Y.; Gao, C.-L.; Li, Y.-Y.; et al. Coexistence of Topological Edge State and Superconductivity in Bismuth Ultrathin Film. *Nano Lett.* **2017**, *17*, 3035–3039.

(244) Zhu, S.-Y.; Shao, Y.; Wang, E.; Cao, L.; Li, X.-Y.; Liu, Z.-L.; Liu, C.; Liu, L.-W.; Wang, J.-O.; Ibrahim, K.; et al. Evidence of Topological Edge States in Buckled Antimonene Monolayers. *Nano Lett.* **2019**, *19*, 6323–6329.

(245) Mi, K.; Xie, J.; Si, M. S.; Gao, C. X. Layer-Stacking Effect on Electronic Structures of Bilayer Arsenene. *EPL* **2017**, *117*, 27002.

(246) Kadioglu, Y.; Santana, J. A.; Özaydin, H. D.; Ersan, F.; Aktürk, O. Ü.; Aktürk, E.; Reboredo, F. A. Diffusion Quantum Monte Carlo and Density Functional Calculations of the Structural Stability of Bilayer Arsenene. *J. Chem. Phys.* **2018**, *148*, 214706.

(247) Zhang, S.; Guo, S.; Chen, Z.; Wang, Y.; Gao, H.; Gómez-Herrero, J.; Ares, P.; Zamora, F.; Zhu, Z.; Zeng, H. Recent Progress in 2D Group-VA Semiconductors: From Theory to Experiment. *Chem. Soc. Rev.* **2018**, *47*, 982–1021.

(248) Ersan, F.; Kecik, D.; Özçelik, V. O.; Kadioglu, Y.; Aktürk, O. Ü.; Durgun, E.; Aktürk, E.; Ciraci, S. Two-Dimensional Pnictogens: A Review of Recent Progresses and Future Research Directions. *Appl. Phys. Rev.* **2019**, *6*, 021308.

(249) Wu, Z.; Hao, J. Electrical Transport Properties in Group-V Elemental Ultrathin 2D Layers. *npj 2D Mater. Appl.* **2020**, *4*, 4.

(250) Zhuang, J.; Liu, C.; Gao, Q.; Liu, Y.; Feng, H.; Xu, X.; Wang, J.; Zhao, J.; Dou, S. X.; Hu, Z.; et al. Band Gap Modulated by Electronic Superlattice in Blue Phosphorene. *ACS Nano* **2018**, *12*, 5059–5065.

(251) Lange, S.; Schmidt, P.; Nilges, T. Au3SnP7@Black Phosphorus: An Easy Access to Black Phosphorus. *Inorg. Chem.* **2007**, *46*, 4028–4035.

(252) Akahama, Y.; Endo, S.; Narita, S. Electrical Properties of Black Phosphorus Single Crystals. *J. Phys. Soc. Jpn.* **1983**, *52*, 2148–2155.

(253) Liang, L.; Wang, J.; Lin, W.; Sumpter, B. G.; Meunier, V.; Pan, M. Electronic Bandgap and Edge Reconstruction in Phosphorene Materials. *Nano Lett.* **2014**, *14*, 6400–6406.

(254) Schiferl, D.; Barrett, C. S. The Crystal Structure of Arsenic at 4.2, 78 and 299°K. *J. Appl. Crystallogr.* **1969**, *2*, 30–36.

(255) Kecik, D.; Özçelik, V. O.; Durgun, E.; Ciraci, S. Structure Dependent Optoelectronic Properties of Monolayer Antimonene, Bismuthene and Their Binary Compound. *Phys. Chem. Chem. Phys.* **2019**, *21*, 7907–7917.

(256) Cucka, P.; Barrett, C. S. The Crystal Structure of Bi and of Solid Solutions of Pb, Sn, Sb and Te in Bi. *Acta Cryst.* **1962**, *15*, 865–872.

(257) Smith, J. B.; Hagaman, D.; Ji, H.-F. Growth of 2D Black Phosphorus Film from Chemical Vapor Deposition. *Nanotechnology* **2016**, *27*, 215602.

(258) Li, X.; Deng, B.; Wang, X.; Chen, S.; Vaisman, M.; Karato, S.; Pan, G.; Larry Lee, M.; Cha, J.; Wang, H.; et al. Synthesis of Thin-Film Black Phosphorus on a Flexible Substrate. *2D Mater.* **2015**, *2*, 031002.

(259) Li, C.; Wu, Y.; Deng, B.; Xie, Y.; Guo, Q.; Yuan, S.; Chen, X.; Bhuiyan, M.; Wu, Z.; Watanabe, K.; et al. Synthesis of Crystalline Black Phosphorus Thin Film on Sapphire. *Adv. Mater.* **2018**, *30*, 1703748.

(260) Rajabali, M.; Esfandiari, M.; Asgharian, H.; Mohajerzadeh, S. Evolution of Phosphorene Sheets through Direct Crystallization of Thin-Film Red Phosphorus. *Phys. Status Solidi RRL* **2019**, 1900432.

(261) Zhang, W.; Enriquez, H.; Tong, Y.; Bendounan, A.; Kara, A.; Seitsonen, A. P.; Mayne, A. J.; Dujardin, G.; Oughaddou, H. Epitaxial Synthesis of Blue Phosphorene. *Small* **2018**, *14*, 1804066.

(262) Hu, Y.; Qi, Z.-H.; Lu, J.; Chen, R.; Zou, M.; Chen, T.; Zhang, W.; Wang, Y.; Xue, X.; Ma, J.; et al. Van der Waals Epitaxial Growth and Interfacial Passivation of Two-Dimensional Single-Crystalline Few-Layer Gray Arsenic Nanoflakes. *Chem. Mater.* **2019**, *31*, 4524–4535.

(263) Shah, J.; Wang, W.; Sohail, H. M.; Uhrberg, R. I. G. Experimental Evidence of Monolayer Arsenene: An Exotic Two-Dimensional Semiconducting Material. *2D Mater.* **2019**, *7*, 025013.

(264) Antonatos, N.; Luxa, J.; Sturala, J.; Sofer, Z. Black Arsenic: A New Synthetic Method by Catalytic Crystallization of Arsenic Glass. *Nanoscale* **2020**, *12*, 5397–5401.

(265) Zhong, M.; Xia, Q.; Pan, L.; Liu, Y.; Chen, Y.; Deng, H.-X.; Li, J.; Wei, Z. Thickness-Dependent Carrier Transport Characteristics of a New 2D Elemental Semiconductor: Black Arsenic. *Adv. Funct. Mater.* **2018**, *28*, 1802581.

(266) Yang, Z.; Wu, Z.; Lyu, Y.; Hao, J. Centimeter-scale Growth of Two-dimensional Layered High-mobility Bismuth Films by Pulsed Laser Deposition. *InfoMat* **2019**, *1*, 98–107.

(267) Jankowski, M.; Kamiński, D.; Vergeer, K.; Mirolo, M.; Carla, F.; Rijnders, G.; Bollmann, T. R. J. Controlling the Growth of Bi(110) and Bi(111) Films on an Insulating Substrate. *Nanotechnology* **2017**, *28*, 155602.

(268) Han, N.; Gao, N.; Zhao, J. Initial Growth Mechanism of Blue Phosphorene on Au(111) Surface. *J. Phys. Chem. C* **2017**, *121*, 17893–17899.

(269) Tian, H.; Zhang, J.-Q.; Ho, W.; Xu, J.-P.; Xia, B.; Xia, Y.; Fan, J.; Xu, H.; Xie, M.; Tong, S. Y. Two-Dimensional Metal-Phosphorus Network. *Matter* **2020**, *2*, 111–118.

(270) Gao, J.; Zhang, G.; Zhang, Y.-W. The Critical Role of Substrate in Stabilizing Phosphorene Nanoflake: A Theoretical Exploration. *J. Am. Chem. Soc.* **2016**, *138*, 4763–4771.

(271) Zeng, J.; Cui, P.; Zhang, Z. Half Layer By Half Layer Growth of a Blue Phosphorene Monolayer on a GaN(001) Substrate. *Phys. Rev. Lett.* **2017**, *118*, 046101.

(272) Qiu, L.; Dong, J. C.; Ding, F. Selective Growth of Two-Dimensional Phosphorene on Catalyst Surface. *Nanoscale* **2018**, *10*, 2255–2259.

(273) Xu, Y.; Shi, X.; Zhang, Y.; Zhang, H.; Zhang, Q.; Huang, Z.; Xu, X.; Guo, J.; Zhang, H.; Sun, L.; et al. Epitaxial Nucleation and Lateral Growth of High-Crystalline Black Phosphorus Films on Silicon. *Nat. Commun.* **2020**, *11*, 1330.

(274) Lei, T.; Liu, C.; Zhao, J.-L.; Li, J.-M.; Li, Y.-P.; Wang, J.-O.; Wu, R.; Qian, H.-J.; Wang, H.-Q.; Ibrahim, K. Electronic Structure of Antimonene Grown on $Sb_2Te_3$(111) and $Bi_2Te_3$ Substrates. *J. Appl. Phys.* **2016**, *119*, 015302.

(275) Fortin-Deschênes, M.; Waller, O.; Menteş, T. O.; Locatelli, A.; Mukherjee, S.; Genuzio, F.; Levesque, P. L.; Hébert, A.; Martel, R.; Moutanabbir, O. Synthesis of Antimonene on Germanium. *Nano Lett.* **2017**, *17*, 4970–4975.

(276) Wu, X.; Shao, Y.; Liu, H.; Feng, Z.; Wang, Y.-L.; Sun, J.-T.; Liu, C.; Wang, J.-O.; Liu, Z.-L.; Zhu, S.-Y.; et al. Epitaxial Growth and Air-Stability of Monolayer Antimonene on $PdTe_2$. *Adv. Mater.* **2017**, *29*, 1605407.

(277) Niu, T.; Zhou, W.; Zhou, D.; Hu, X.; Zhang, S.; Zhang, K.; Zhou, M.; Fuchs, H.; Zeng, H. Modulating Epitaxial Atomic Structure of Antimonene through Interface Design. *Adv. Mater.* **2019**, *31*, 1902606.

(278) Jałochowski, M.; Krawiec, M. Antimonene on Pb Quantum Wells. *2D Mater.* **2019**, *6*, 045028.

(279) Niu, T.; Meng, Q.; Zhou, D.; Si, N.; Zhai, S.; Hao, X.; Zhou, M.; Fuchs, H. Large-Scale Synthesis of Strain-Tunable Semiconducting Antimonene on Copper Oxide. *Adv. Mater.* **2019**, 1906873.

(280) Sun, X.; Lu, Z.; Xiang, Y.; Wang, Y.; Shi, J.; Wang, G.-C.; Washington, M. A.; Lu, T.-M. Van der Waals Epitaxy of Antimony Islands, Sheets, and Thin Films on Single-Crystalline Graphene. *ACS Nano* **2018**, *12*, 6100–6108.

(281) Shi, Z.-Q.; Li, H.; Yuan, Q.-Q.; Song, Y.-H.; Lv, Y.-Y.; Shi, W.; Jia, Z.-Y.; Gao, L.; Chen, Y.-B.; Zhu, W.; et al. Van der Waals Heteroepitaxial Growth of Monolayer Sb in a Puckered Honeycomb Structure. *Adv. Mater.* **2019**, *31*, 1806130.

(282) Märkl, T.; Kowalczyk, P. J.; Le Ster, M.; Mahajan, I. V.; Pirie, H.; Ahmed, Z.; Bian, G.; Wang, X.; Chiang, T.-C.; Brown, S. A. Engineering Multiple Topological Phases in Nanoscale Van der Waals Heterostructures: Realisation of $\alpha$-Antimonene. *2D Mater.* **2017**, *5*, 011002.

(283) Shao, Y.; Liu, Z.-L.; Cheng, C.; Wu, X.; Liu, H.; Liu, C.; Wang, J.-O.; Zhu, S.-Y.; Wang, Y.-Q.; Shi, D.-X.; et al. Epitaxial Growth of Flat Antimonene Monolayer: A New Honeycomb Analogue of Graphene. *Nano Lett.* **2018**, *18*, 2133–2139.

(284) Yaginuma, S.; Nagao, T.; Sadowski, J. T.; Saito, M.; Nagaoka, K.; Fujikawa, Y.; Sakurai, T.; Nakayama, T. Origin of Flat Morphology and High Crystallinity of Ultrathin Bismuth Films. *Surf. Sci.* **2007**, *601*, 3593–3600.

(285) Kokubo, I.; Yoshiike, Y.; Nakatsuji, K.; Hirayama, H. Ultrathin Bi(110) Films on Si(111) $3 \times 3 - B$ Substrates. *Phys. Rev. B* **2015**, *91*, 075429.

(286) Peng, L.; Qiao, J.; Xian, J.-J.; Pan, Y.; Ji, W.; Zhang, W.; Fu, Y.-S. Unusual Electronic States and Superconducting Proximity Effect of Bi Films Modulated by a $NbSe_2$ Substrate. *ACS Nano* **2019**, *13*, 1885–1892.

(287) Yamada, K.; Souma, S.; Yamauchi, K.; Shimamura, N.; Sugawara, K.; Trang, C. X.; Oguchi, T.; Ueno, K.; Takahashi, T.; Sato, T. Ultrathin Bismuth Film on 1T-$TaS_2$ : Structural Transition and Charge-Density-Wave Proximity Effect. *Nano Lett.* **2018**, *18*, 3235–3240.

(288) Dong, X.; Li, Y.; Li, J.; Peng, X.; Qiao, L.; Chen, D.; Yang, H.; Xiong, X.; Wang, Q.; Li, X.; et al. Epitaxial Growth and Structural Properties of Bi(110) Thin Films on $TiSe_2$ Substrates. *J. Phys. Chem. C* **2019**, *123*, 13637–13641.

(289) Shen, K.; Hua, C.; Liang, Z.; Wang, Y.; Sun, H.; Hu, J.; Zhang, H.; Li, H.; Jiang, Z.; Huang, H.; et al. Epitaxial Growth of Free-Standing Bismuth Film on Graphene Embedded with Nontrivial Properties. *ACS Appl. Electron. Mater.* **2019**, *1*, 1817–1824.

(290) Nagao, T.; Sadowski, J.; Saito, M.; Yaginuma, S.; Fujikawa, Y.; Kogure, T.; Ohno, T.; Hasegawa, Y.; Hasegawa, S.; Sakurai, T. Nanofilm Allotrope and Phase Transformation of Ultrathin Bi Film on Si(111)-7×7. *Phys. Rev. Lett.* **2004**, *93*, 105501.

(291) Yaginuma, S.; Nagaoka, K.; Nagao, T.; Bihlmayer, G.; M. Koroteev, Y.; V. Chulkov, E.; Nakayama, T. Electronic Structure of Ultrathin Bismuth Films with A7 and Black-Phosphorus-like Structures. *J. Phys. Soc. Jpn.* **2008**, *77*, 014701.

(292) Walker, E. S.; Na, S. R.; Jung, D.; March, S. D.; Kim, J.-S.; Trivedi, T.; Li, W.; Tao, L.; Lee, M. L.; Liechti, K. M.; et al. Large-Area Dry Transfer of Single-Crystalline Epitaxial Bismuth Thin Films. *Nano Lett.* **2016**, *16*, 6931–6938.

(293) Kawakami, N.; Lin, C.-L.; Kawahara, K.; Kawai, M.; Arafune, R.; Takagi, N. Structural Evolution of Bi Thin Films on Au(111) Revealed by Scanning Tunneling Microscopy. *Phys. Rev. B* **2017**, *96*, 205402.

(294) Aierken, Y.; Çakır, D.; Sevik, C.; Peeters, F. M. Thermal Properties of Black and Blue Phosphorenes from a First-Principles Quasiharmonic Approach. *Phys. Rev. B* **2015**, *92*, 081408.

(295) Freitas, R. R. Q.; Rivelino, R.; de Brito Mota, F.; de Castilho, C. M. C.; Kakanakova-Georgieva, A.; Gueorguiev, G. K. Topological Insulating Phases in Two-Dimensional Bismuth-Containing Single Layers Preserved by Hydrogenation. *J. Phys. Chem. C* **2015**, *119*, 23599–23606.

(296) Chen, Y.; Shi, X.; Li, M.; Liu, Y.; Xiao, H.; Chen, X. Strain and Defect Engineering on Phase Transition of Monolayer Black Phosphorene. *Phys. Chem. Chem. Phys.* **2018**, *20*, 21832–21843.

(297) Terhell, J. C. J. M. Polytypism in the III–VI Layer Compounds. *Prog. Cryst. Growth Charact. Mater.* **1983**, *7*, 55–110.

(298) Diehl, R.; Nitsche, R. Vapour Growth of Three $In_2S_3$ Modifications by Iodine Transport. *J. Cryst. Growth* **1975**, *28*, 306–310.

(299) Han, G.; Chen, Z.-G.; Sun, C.; Yang, L.; Cheng, L.; Li, Z.; Lu, W.; Gibbs, Z. M.; Snyder, G. J.; Jack, K.; et al. A New Crystal: Layer-Structured Rhombohedral $In_3Se_4$. *CrystEngComm* **2014**, *16*, 393–398.

(300) Hogg, J. H. C.; Sutherland, H. H.; Williams, D. J. The Crystal Structure of Tetraindium Triselenide. *Acta Crystallogr. B Struct. Crystallogr. Cryst. Chem.* **1973**, *29*, 1590–1593.

(301) Hogg, J. H. C.; Sutherland, H. H. Indium Telluride. *Acta Cryst B* **1976**, *32*, 2689–2690.

(302) Serebryanaya, N. R. The Crystal Structure of Pressure-Induced Phases of $In_2Te_3$ and $Ga_2Te_3$. *Powder Diffr.* **1992**, *7*, 99–102.

(303) Wasala, M.; Sirikumara, H. I.; Raj Sapkota, Y.; Hofer, S.; Mazumdar, D.; Jayasekera, T.; Talapatra, S. Recent Advances in Investigations of the Electronic and Optoelectronic Properties of Group III, IV, and V Selenide Based Binary Layered Compounds. *J. Mater. Chem. C* **2017**, *5*, 11214–11225.

(304) Yang, Z.; Hao, J. Recent Progress in 2D Layered III–VI Semiconductors and Their Heterostructures for Optoelectronic Device Applications. *Adv. Mater. Technol.* **2019**, *4*, 1900108.

(305) Cai, H.; Gu, Y.; Lin, Y.-C.; Yu, Y.; Geohegan, D. B.; Xiao, K. Synthesis and Emerging Properties of 2D Layered III–VI Metal Chalcogenides. *Appl. Phys. Rev.* **2019**, *6*, 041312.

(306) Kolesnikov, N. N.; Borisenko, E. B.; Borisenko, D. N.; Timonina, A. V. Structure and Microstructure of GaTe Crystals Grown by High-Pressure Vertical Zone Melting. *J. Cryst. Growth* **2013**, *365*, 59–63.

(307) Sánchez-Royo, J. F.; Pellicer-Porres, J.; Segura, A.; Muñoz-Sanjosé, V.; Tobías, G.; Ordejón, P.; Canadell, E.; Huttel, Y. Angle-Resolved Photoemission Study and First-Principles Calculation of the Electronic Structure of GaTe. *Phys. Rev. B* **2002**, *65*, 115201.

(308) Bastow, T. J.; Campbell, I. D.; Whitfield, H. J. A 69Ga, 115In NQR Study of Polytypes of GaS, GaSe and InSe. *Solid State Commun.* **1981**, *39*, 307–311.

(309) Kou, L.; Du, A.; Ma, Y.; Liao, T.; Chen, C. Charging Assisted Structural Phase Transitions in Monolayer InSe. *Phys. Chem. Chem. Phys.* **2017**, *19*, 22502–22508.

(310) Autere, A.; Jussila, H.; Dai, Y.; Wang, Y.; Lipsanen, H.; Sun, Z. Nonlinear Optics with 2D Layered Materials. *Adv. Mater.* **2018**, *30*, 1705963.

(311) Cui, C.; Xue, F.; Hu, W.-J.; Li, L.-J. Two-Dimensional Materials with Piezoelectric and Ferroelectric Functionalities. *npj 2D Mater. Appl.* **2018**, *2*, 18.

(312) Li, W.; Li, J. Piezoelectricity in Two-Dimensional Group-III Monochalcogenides. *Nano Res.* **2015**, *8*, 3796–3802.

(313) Dai, M.; Wang, Z.; Wang, F.; Qiu, Y.; Zhang, J.; Xu, C.-Y.; Zhai, T.; Cao, W.; Fu, Y.; Jia, D.; et al. Two-Dimensional van der Waals Materials with Aligned In-Plane Polarization and Large Piezoelectric Effect for Self-Powered Piezoelectric Sensors. *Nano Lett.* **2019**, *19*, 5410–5416.

(314) Zhou, X.; Cheng, J.; Zhou, Y.; Cao, T.; Hong, H.; Liao, Z.; Wu, S.; Peng, H.; Liu, K.; Yu, D. Strong Second-Harmonic Generation in Atomic Layered GaSe. *J. Am. Chem. Soc.* **2015**, *137*, 7994–7997.

(315) Leisgang, N.; Roch, J. G.; Froehlicher, G.; Hamer, M.; Terry, D.; Gorbachev, R.; Warburton, R. J. Optical Second Harmonic Generation in Encapsulated Single-Layer InSe. *AIP Advances* **2018**, *8*, 105120.

(316) Huang, W.; Gan, L.; Li, H.; Ma, Y.; Zhai, T. Phase-Engineered Growth of Ultrathin InSe Flakes by Chemical Vapor Deposition for High-Efficiency Second Harmonic Generation. *Chem. Eur. J.* **2018**, *24*, 15678–15684.

(317) Hao, Q.; Yi, H.; Su, H.; Wei, B.; Wang, Z.; Lao, Z.; Chai, Y.; Wang, Z.; Jin, C.; Dai, J.; et al. Phase Identification and Strong Second Harmonic Generation in Pure ε-InSe and Its Alloys. *Nano Lett.* **2019**, *19*, 2634–2640.

(318) Zhou, J.; Shi, J.; Zeng, Q.; Chen, Y.; Niu, L.; Liu, F.; Yu, T.; Suenaga, K.; Liu, X.; Lin, J.; et al. InSe Monolayer: Synthesis, Structure and Ultra-High Second-Harmonic Generation. *2D Mater.* **2018**, *5*, 025019.

(319) Attaccalite, C.; Palummo, M.; Cannuccia, E.; Grüning, M. Second-Harmonic Generation in Single-Layer Monochalcogenides: A Response from First-Principles Real-Time Simulations. *Phys. Rev. Materials* **2019**, *3*, 074003.

(320) Hu, L.; Huang, X.; Wei, D. Layer-Independent and Layer-Dependent Nonlinear Optical Properties of Two-Dimensional GaX (X = S, Se, Te) Nanosheets. *Phys. Chem. Chem. Phys.* **2017**, *19*, 11131–11141.

(321) Plucinski, L.; Johnson, R. L.; Kowalski, B. J.; Kopalko, K.; Orlowski, B. A.; Kovalyuk, Z. D.; Lashkarev, G. V. Electronic Band Structure of GaSe(0001): Angle-Resolved Photoemission and *Ab Initio* Theory. *Phys. Rev. B* **2003**, *68*, 125304.

(322) Gomes da Costa, P.; Dandrea, R. G.; Wallis, R. F.; Balkanski, M. First-Principles Study of the Electronic Structure of γ-InSe and β-InSe. *Phys. Rev. B* **1993**, *48*, 14135–14141.

(323) Srour, J.; Badawi, M.; El Haj Hassan, F.; Postnikov, A. Comparative Study of Structural and Electronic Properties of GaSe and InSe Polytypes. *J. Chem. Phys.* **2018**, *149*, 054106.

(324) Sun, Y.; Luo, S.; Zhao, X.-G.; Biswas, K.; Li, S.-L.; Zhang, L. InSe: A Two-Dimensional Material with Strong Interlayer Coupling. *Nanoscale* **2018**, *10*, 7991–7998.

(325) Huang, S.; Tatsumi, Y.; Ling, X.; Guo, H.; Wang, Z.; Watson, G.; Puretzky, A. A.; Geohegan, D. B.; Kong, J.; Li, J.; et al. In-Plane Optical Anisotropy of Layered Gallium Telluride. *ACS Nano* **2016**, *10*, 8964–8972.

(326) Susoma, J.; Karvonen, L.; Säynätjoki, A.; Mehravar, S.; Norwood, R. A.; Peyghambarian, N.; Kieu, K.; Lipsanen, H.; Riikonen, J. Second and Third Harmonic Generation in Few-Layer Gallium Telluride Characterized by Multiphoton Microscopy. *Appl. Phys. Lett.* **2016**, *108*, 073103.

(327) Kosobutsky, A. V.; Sarkisov, S. Yu. Influence of Size Effects on the Electronic Structure of Hexagonal Gallium Telluride. *Phys. Solid State* **2018**, *60*, 1686–1690.

(328) Han, G.; Chen, Z.-G.; Drennan, J.; Zou, J. Indium Selenides: Structural Characteristics, Synthesis and Their Thermoelectric Performances. *Small* **2014**, *10*, 2747–2765.

(329) Küpers, M.; Konze, P. M.; Meledin, A.; Mayer, J.; Englert, U.; Wuttig, M.; Dronskowski, R. Controlled Crystal Growth of Indium Selenide, $In_2Se_3$ , and the Crystal Structures of α-$In_2Se_3$. *Inorg. Chem.* **2018**, *57*, 11775–11781.

(330) Liu, L.; Dong, J.; Huang, J.; Nie, A.; Zhai, K.; Xiang, J.; Wang, B.; Wen, F.; Mu, C.; Zhao, Z.; et al. Atomically Resolving Polymorphs and Crystal Structures of $In_2Se_3$. *Chem. Mater.* **2019**, *31*, 10143–10149.

(331) Li, W.; Sabino, F. P.; Crasto de Lima, F.; Wang, T.; Miwa, R. H.; Janotti, A. Large Disparity between Optical and Fundamental Band Gaps in Layered $In_2Se_3$. *Phys. Rev. B* **2018**, *98*, 165134.

(332) Zheng, C.; Yu, L.; Zhu, L.; Collins, J. L.; Kim, D.; Lou, Y.; Xu, C.; Li, M.; Wei, Z.; Zhang, Y.; et al. Room Temperature In-Plane Ferroelectricity in van der Waals $In_2Se_3$. *Science Advances* **2018**, *4*, eaar7720.

(333) Collins, J. L.; Wang, C.; Tadich, A.; Yin, Y.; Zheng, C.; Hellerstedt, J.; Grubišić-Čabo, A.; Tang, S.; Mo, S.-K.; Riley, J.; et al. Electronic Band Structure of In-Plane Ferroelectric van der Waals B′-$In_2Se_3$. *ACS Appl. Electron. Mater.* **2020**, *2*, 213–219.

(334) van Landuyt, J.; van Tendeloo, G.; Amelinckx, S. Phase Transitions in $In_2Se_3$ as Studied by Electron Microscopy and Electron Diffraction. *Phys. Stat. Sol. A* **1975**, *30*, 299–314.

(335) Zhang, F.; Wang, Z.; Dong, J.; Nie, A.; Xiang, J.; Zhu, W.; Liu, Z.; Tao, C. Atomic-Scale Observation of Reversible Thermally Driven Phase Transformation in 2D $In_2Se_3$. *ACS Nano* **2019**, *13*, 8004–8011.

(336) Dong, J.; Liu, L.; Nie, A.; Xiang, J.; Zhai, K.; Wang, B.; Wen, F.; Mu, C.; Chen, Y.; Zhao, Z.; et al. Influence of van der Waals Epitaxy on Phase Transformation Behaviors in 2D Heterostructure. *Appl. Phys. Lett.* **2020**, *116*, 021602.

(337) Liu, J.; Pantelides, S. T. Pyroelectric Response and Temperature-Induced $\alpha$ - $\beta$ Phase Transitions in $\alpha$-$In_2Se_3$ and Other $\alpha$-$III_2VI_3$ (III = Al, Ga, In; VI = S, Se) Monolayers. *2D Mater.* **2019**, *6*, 025001.

(338) Ding, W.; Zhu, J.; Wang, Z.; Gao, Y.; Xiao, D.; Gu, Y.; Zhang, Z.; Zhu, W. Prediction of Intrinsic Two-Dimensional Ferroelectrics in $In_2Se_3$ and Other $III_2$-$VI_3$ van der Waals Materials. *Nat Commun.* **2017**, *8*, 14956.

(339) Xiao, J.; Zhu, H.; Wang, Y.; Feng, W.; Yunxia; Dasgupta, A.; Han, Y.; Wang, Y.; Muller, D. A.; Martin, L. W.; et al. Intrinsic Two-Dimensional Ferroelectricity with Dipole Locking. *Phys. Rev. Lett.* **2018**, *120*, 227601.

(340) Xue, F.; Hu, W.; Lee, K.; Lu, L.; Zhang, J.; Tang, H.; Han, A.; Hsu, W.; Tu, S.; Chang, W.; et al. Room-Temperature Ferroelectricity in Hexagonally Layered A-$In_2Se_3$ Nanoflakes down to the Monolayer Limit. *Adv. Funct. Mater.* **2018**, *28*, 1803738.

(341) Cui, C.; Hu, W.-J.; Yan, X.; Addiego, C.; Gao, W.; Wang, Y.; Wang, Z.; Li, L.; Cheng, Y.; Li, P.; et al. Intercorrelated In-Plane and Out-of-Plane Ferroelectricity in Ultrathin Two-Dimensional Layered Semiconductor $In_2Se_3$. *Nano Lett.* **2018**, *18*, 1253–1258.

(342) Zhou, Y.; Wu, D.; Zhu, Y.; Cho, Y.; He, Q.; Yang, X.; Herrera, K.; Chu, Z.; Han, Y.; Downer, M. C.; et al. Out-of-Plane Piezoelectricity and Ferroelectricity in Layered α-$In_2Se_3$ Nanoflakes. *Nano Lett.* **2017**, *17*, 5508–5513.

(343) Xue, F.; Zhang, J.; Hu, W.; Hsu, W.-T.; Han, A.; Leung, S.-F.; Huang, J.-K.; Wan, Y.; Liu, S.; Zhang, J.; et al. Multidirection Piezoelectricity in Mono- and Multilayered Hexagonal α-$In_2Se_3$. *ACS Nano* **2018**, *12*, 4976–4983.

(344) Tao, X.; Gu, Y. Crystalline–Crystalline Phase Transformation in Two-Dimensional $In_2Se_3$ Thin Layers. *Nano Lett.* **2013**, *13*, 3501–3505.

(345) Feng, W.; Gao, F.; Hu, Y.; Dai, M.; Liu, H.; Wang, L.; Hu, P. Phase-Engineering-Driven Enhanced Electronic and Optoelectronic Performance of Multilayer $In_2Se_3$ Nanosheets. *ACS Appl. Mater. Interfaces* **2018**, *10*, 27584–27588.

(346) Huang, L.; Chen, Z.; Li, J. Effects of Strain on the Band Gap and Effective Mass in Two-Dimensional Monolayer GaX (X = S, Se, Te). *RSC Adv.* **2015**, *5*, 5788–5794.

(347) Ho, C. H.; Lin, S. L. Optical Properties of the Interband Transitions of Layered Gallium Sulfide. *J. Appl. Phys.* **2006**, *100*, 083508.

(348) Demirci, S.; Avazlı, N.; Durgun, E.; Cahangirov, S. Structural and Electronic Properties of Monolayer Group III Monochalcogenides. *Phys. Rev. B* **2017**, *95*, 115409.

(349) Jung, C. S.; Shojaei, F.; Park, K.; Oh, J. Y.; Im, H. S.; Jang, D. M.; Park, J.; Kang, H. S. Red-to-Ultraviolet Emission Tuning of Two-Dimensional Gallium Sulfide/Selenide. *ACS Nano* **2015**, *9*, 9585–9593.

(350) Ma, Y.; Dai, Y.; Guo, M.; Yu, L.; Huang, B. Tunable Electronic and Dielectric Behavior of GaS and GaSe Monolayers. *Phys. Chem. Chem. Phys.* **2013**, *15*, 7098.

(351) Aulich, E.; Brebner, J. L.; Mooser, E. Indirect Energy Gap in GaSe and GaS. *Phys. Stat. Sol. B* **1969**, *31*, 129–131.

(352) Kuhn, A.; Chevy, A.; Chevalier, R. Crystal Structure and Interatomic Distances in GaSe. *Phys. Stat. Sol. A* **1975**, *31*, 469–475.

(353) Shenoy, U. S.; Gupta, U.; Narang, D. S.; Late, D. J.; Waghmare, U. V.; Rao, C. N. R. Electronic Structure and Properties of Layered Gallium Telluride. *Chem. Phys. Lett.* **2016**, *651*, 148–154.

(354) Bose, D. N.; Pal, S. Photoconductivity, Low-Temperature Conductivity, and Magnetoresistance Studies on the Layered Semiconductor GaTe. *Phys. Rev. B* **2001**, *63*, 235321.

(355) Borisenko, E.; Borisenko, D.; Timonina, A.; Kolesnikov, N. Nonvariant Polymorphic Transition from Hexagonal to Monoclinic Lattice in GaTe Single Crystal. *J. Cryst. Growth* **2020**, *535*, 125548.

(356) Debbichi, L.; Eriksson, O.; Lebègue, S. Two-Dimensional Indium Selenides Compounds: An Ab Initio Study. *J. Phys. Chem. Lett.* **2015**, *6*, 3098–3103.

(357) De Blasi, C.; Micocci, G.; Mongelli, S.; Tepore, A. Large InSe Single Crystals Grown from Stoichiometric and Non-Stoichiometric Melts. *J. Cryst. Growth* **1982**, *57*, 482–486.

(358) Mudd, G. W.; Svatek, S. A.; Ren, T.; Patanè, A.; Makarovsky, O.; Eaves, L.; Beton, P. H.; Kovalyuk, Z. D.; Lashkarev, G. V.; Kudrynskyi, Z. R.; et al. Tuning the Bandgap of Exfoliated InSe Nanosheets by Quantum Confinement. *Adv. Mater.* **2013**, *25*, 5714–5718.

(359) Zhou, J.; Zeng, Q.; Lv, D.; Sun, L.; Niu, L.; Fu, W.; Liu, F.; Shen, Z.; Jin, C.; Liu, Z. Controlled Synthesis of High-Quality Monolayered α-$In_2Se_3$ via Physical Vapor Deposition. *Nano Lett.* **2015**, *15*, 6400–6405.

(360) Julien, C.; Chevy, A.; Siapkas, D. Optical Properties of $In_2Se_3$ Phases. *Phys. Stat. Sol. A* **1990**, *118*, 553–559.

(361) Almeida, G.; Dogan, S.; Bertoni, G.; Giannini, C.; Gaspari, R.; Perissinotto, S.; Krahne, R.; Ghosh, S.; Manna, L. Colloidal Monolayer β-$In_2Se_3$ Nanosheets with High Photoresponsivity. *J. Am. Chem. Soc.* **2017**, *139*, 3005–3011.

(362) Lutz, H. D.; Fischer, M.; Baldus, H.-P.; Blachnik, R. Zur polymorphie des $In_2Se_3$. *J. Less Common Met.* **1988**, *143*, 83–92.

(363) Balakrishnan, N.; Steer, E. D.; Smith, E. F.; Kudrynskyi, Z. R.; Kovalyuk, Z. D.; Eaves, L.; Patanè, A.; Beton, P. H. Epitaxial Growth of γ-InSe and α, β, and γ-$In_2Se_3$on ε-GaSe. *2D Materials* **2018**, *5*, 035026.

(364) Hu, Y.; Feng, W.; Dai, M.; Yang, H.; Chen, X.; Liu, G.; Zhang, S.; Hu, P. Temperature-Dependent Growth of Few Layer $\beta$ -InSe and $\alpha$ -$In_2Se_3$ Single Crystals for Optoelectronic Device. *Semicond. Sci. Technol.* **2018**, *33*, 125002.

(365) Lee, C. H.; Krishnamoorthy, S.; O'Hara, D. J.; Brenner, M. R.; Johnson, J. M.; Jamison, J. S.; Myers, R. C.; Kawakami, R. K.; Hwang, J.; Rajan, S. Molecular Beam Epitaxy of 2D-Layered Gallium Selenide on GaN Substrates. *J. Appl. Phys.* **2017**, *121*, 094302.

(366) Longuinhos, R.; Ribeiro-Soares, J. Ultra-Weak Interlayer Coupling in Two-Dimensional Gallium Selenide. *Phys. Chem. Chem. Phys.* **2016**, *18*, 25401–25408.

(367) Gillan, E. G.; Barron, A. R. Chemical Vapor Deposition of Hexagonal Gallium Selenide and Telluride Films from Cubane Precursors: Understanding the Envelope of Molecular Control. *Chem. Mater.* **1997**, *9*, 3037–3048.

(368) Yu, Y.; Ran, M.; Zhou, S.; Wang, R.; Zhou, F.; Li, H.; Gan, L.; Zhu, M.; Zhai, T. Phase-Engineered Synthesis of Ultrathin Hexagonal and Monoclinic GaTe Flakes and Phase Transition Study. *Adv. Funct. Mater.* **2019**, *29*, 1901012.

(369) Li, J.-B.; Record, M.-C.; Tedenac, J.-C. A Thermodynamic Assessment of the In–Se System. *MEKU* **2003**, *94*, 381–389.

(370) Lin, M.; Wu, D.; Zhou, Y.; Huang, W.; Jiang, W.; Zheng, W.; Zhao, S.; Jin, C.; Guo, Y.; Peng, H.; et al. Controlled Growth of Atomically Thin $In_2Se_3$ Flakes by van der Waals Epitaxy. *J. Am. Chem. Soc.* **2013**, *135*, 13274–13277.

(371) Zhang, X.; Lee, S.; Bansal, A.; Zhang, F.; Terrones, M.; Jackson, T. N.; Redwing, J. M. Epitaxial Growth of Few-Layer β-$In_2Se_3$ Thin Films by Metalorganic Chemical Vapor Deposition. *J. Cryst. Growth* **2020**, *533*, 125471.

(372) Bae, C. J.; McMahon, J.; Detz, H.; Strasser, G.; Park, J.; Einarsson, E.; Eason, D. B. Influence of Thickness on Crystallinity in Wafer-Scale GaTe Nanolayers Grown by Molecular Beam Epitaxy. *AIP Advances* **2017**, *7*, 035113.

(373) Yonezawa, T.; Murakami, T.; Higashimine, K.; Fleurence, A.; Oshima, Y.; Yamada-Takamura, Y. Atomistic Study of GaSe/Ge(111) Interface Formed through van der Waals Epitaxy. *Surf. Interface Anal.* **2019**, *51*, 95–99.

(374) Diep, N. Q.; Liu, C.-W.; Wu, S.-K.; Chou, W.-C.; Huynh, S. H.; Chang, E. Y. Screw-Dislocation-Driven Growth Mode in Two Dimensional GaSe on GaAs(001) Substrates Grown by Molecular Beam Epitaxy. *Sci. Rep.* **2019**, *9*, 17781.

(375) Feng, W.; Qin, F.; Yu, M.; Gao, F.; Dai, M.; Hu, Y.; Wang, L.; Hou, J.; Li, B.; Hu, P. Synthesis of Superlattice InSe Nanosheets with Enhanced Electronic and Optoelectronic Performance. *ACS Appl. Mater. Interfaces* **2019**, *11*, 18511–18516.

(376) Osman, M.; Huang, Y.; Feng, W.; Liu, G.; Qiu, Y.; Hu, P. Modulation of Opto-Electronic Properties of InSe Thin Layers via Phase Transformation. *RSC Adv.* **2016**, *6*, 70452–70459.

(377) Su, H.; Liu, X.; Wei, C.; Li, J.; Sun, Z.; Liu, Q.; Zhou, X.; Deng, J.; Yi, H.; Hao, Q.; et al. Pressure-Controlled Structural Symmetry Transition in Layered InSe. *Laser & Photonics Reviews* **2019**, *13*, 1900012.

(378) Choi, M. S.; Cheong, B.; Ra, C. H.; Lee, S.; Bae, J.-H.; Lee, S.; Lee, G.-D.; Yang, C.-W.; Hone, J.; Yoo, W. J. Electrically Driven Reversible Phase Changes in Layered $In_2Se_3$ Crystalline Film. *Adv. Mater.* **2017**, *29*, 1703568.

(379) Zhao, Q.; Wang, T.; Miao, Y.; Ma, F.; Xie, Y.; Ma, X.; Gu, Y.; Li, J.; He, J.; Chen, B.; et al. Thickness-Induced Structural Phase Transformation of Layered Gallium Telluride. *Phys. Chem. Chem. Phys.* **2016**, *18*, 18719–18726.

(380) Bletskan, D. I. Phase Equilibrium in Binary Systems AIV BVI Part. III Systems Sn-Chalcogenides. *J. Ovonic Res.* **2005**, *1*, 61–69.

(381) Bletskan, D. I. Phase Equilibrium in Binary Systems AIV BVI Part. II Systems Germanium Chalcogen. *J. Ovonic Res.* **2005**, *1*, 53–60.

(382) Skelton, J. M.; Burton, L. A.; Oba, F.; Walsh, A. Chemical and Lattice Stability of the Tin Sulfides. *J. Phys. Chem. C* **2017**, *121*, 6446–6454.

(383) Antunez, P. D.; Buckley, J. J.; Brutchey, R. L. Tin and Germanium Monochalcogenide IV–VI Semiconductor Nanocrystals for Use in Solar Cells. *Nanoscale* **2011**, *3*, 2399.

(384) Mitchell, R. S.; Fujiki, Y.; Ishizawa, Y. Structural Polytypism of $SnS_2$. *Nature* **1974**, *247*, 537–538.

(385) Littlewood, P. B. The Crystal Structure of IV-VI Compounds. I. Classification and Description. *J. Phys. C: Solid State Phys.* **1980**, *13*, 4855–4873.

(386) Fjellvåg, H.; Kongshaug, K. O.; Stølen, S. Crystal Structure of $Ge_4Se_9$: A New Germanium Selenide with $Se_2$ Pairs Breaking the Edge-Sharing $GeSe_4$ Tetrahedra in $GeSe_2$. *J. Chem. Soc., Dalton Trans.* **2001**, *7*, 1043–1045.

(387) Bletskan, D. I. Phase Equilibrium in Binary Systems AIV BVI Part. I The Systems Silicon-Chalcogen. **2005**, *1*, 47–52.

(388) Ploog, K.; Stetter, W.; Nowitzki, A.; Schönherr, E. Crystal Growth and Structure Determination of Silicon Telluride $Si_2Te_3$. *Mater. Res. Bull.* **1976**, *11*, 1147–1153.

(389) Steinberg, S.; Stoffel, R. P.; Dronskowski, R. Search for the Mysterious SiTe—An Examination of the Binary Si–Te System Using First-Principles-Based Methods. *Cryst. Growth Des.* **2016**, *16*, 6152–6155.

(390) Göbgen, K. C.; Steinberg, S.; Dronskowski, R. Revisiting the Si–Te System: $SiTe_2$ Finally Found by Means of Experimental and Quantum-Chemical Techniques. *Inorg. Chem.* **2017**, *56*, 11398–11405.

(391) Lach-hab, M.; Papaconstantopoulos, D. A.; Mehl, M. J. Electronic Structure Calculations of Lead Chalcogenides PbS, PbSe, PbTe. *J. Phys. Chem. Solids* **2002**, *63*, 833–841.

(392) Xia, F.; Wang, H.; Hwang, J. C. M.; Neto, A. H. C.; Yang, L. Black Phosphorus and Its Isoelectronic Materials. *Nat Rev Phys* **2019**, *1*, 306–317.

(393) Hu, Z.; Ding, Y.; Hu, X.; Zhou, W.; Yu, X.; Zhang, S. Recent Progress in 2D Group IV–IV Monochalcogenides: Synthesis, Properties and Applications. *Nanotechnology* **2019**, *30*, 252001.

(394) Boschker, J. E.; Wang, R.; Calarco, R. GeTe: A Simple Compound Blessed with a Plethora of Properties. *CrystEngComm* **2017**, *19*, 5324–5335.

(395) Singh, A. K.; Hennig, R. G. Computational Prediction of Two-Dimensional Group-IV Mono-Chalcogenides. *Appl. Phys. Lett.* **2014**, *105*, 042103.

(396) Ul Haq, B.; AlFaify, S.; Laref, A. Design and Characterization of Novel Polymorphs of Single-Layered Tin-Sulfide for Direction-Dependent Thermoelectric Applications Using First-Principles Approaches. *Phys. Chem. Chem. Phys.* **2019**, *21*, 4624–4632.

(397) Kafalas, J. A.; Mariano, A. N. High-Pressure Phase Transition in Tin Telluride. *Science* **1964**, *143*, 952–952.

(398) Chang, K.; Kaloni, T. P.; Lin, H.; Bedoya-Pinto, A.; Pandeya, A. K.; Kostanovskiy, I.; Zhao, K.; Zhong, Y.; Hu, X.; Xue, Q.; et al. Enhanced Spontaneous Polarization in Ultrathin SnTe Films with Layered Antipolar Structure. *Adv. Mater.* **2019**, *31*, 1804428.

(399) Shportko, K.; Kremers, S.; Woda, M.; Lencer, D.; Robertson, J.; Wuttig, M. Resonant Bonding in Crystalline Phase-Change Materials. *Nature Mater.* **2008**, *7*, 653–658.

(400) Chattopadhyay, T.; Boucherle, J. X.; vonSchnering, H. G. Neutron Diffraction Study on the Structural Phase Transition in GeTe. *J. Phys. C: Solid State Phys.* **1987**, *20*, 1431–1440.

(401) Qiao, M.; Chen, Y.; Wang, Y.; Li, Y. The Germanium Telluride Monolayer: A Two Dimensional Semiconductor with High Carrier Mobility for Photocatalytic Water Splitting. *J. Mater. Chem. A* **2018**, *6*, 4119–4125.

(402) Wan, W.; Liu, C.; Xiao, W.; Yao, Y. Promising Ferroelectricity in 2D Group IV Tellurides: A First-Principles Study. *Appl. Phys. Lett.* **2017**, *111*, 132904.

(403) Lencer, D.; Salinga, M.; Grabowski, B.; Hickel, T.; Neugebauer, J.; Wuttig, M. A Map for Phase-Change Materials. *Nature Mater.* **2008**, *7*, 972–977.

(404) Iizumi, M.; Hamaguchi, Y.; F. Komatsubara, K.; Kato, Y. Phase Transition in SnTe with Low Carrier Concentration. *J. Phys. Soc. Jpn.* **1975**, *38*, 443–449.

(405) Zhu, Z.; Guan, J.; Liu, D.; Tománek, D. Designing Isoelectronic Counterparts to Layered Group V Semiconductors. *ACS Nano* **2015**, *9*, 8284–8290.

(406) Hu, T.; Dong, J. Two New Phases of Monolayer Group-IV Monochalcogenides and Their Piezoelectric Properties. *Phys. Chem. Chem. Phys.* **2016**, *18*, 32514–32520.

(407) Alonso-Lanza, T.; Ayuela, A.; Aguilera-Granja, F. An Array of Layers in Silicon Sulfides: Chainlike and Monolayer. *Phys. Rev. B* **2016**, *94*, 245441.

(408) Yang, J.-H.; Zhang, Y.; Yin, W.-J.; Gong, X. G.; Yakobson, B. I.; Wei, S.-H. Two-Dimensional SiS Layers with Promising Electronic and Optoelectronic Properties: Theoretical Prediction. *Nano Lett.* **2016**, *16*, 1110–1117.

(409) Hu, Z.-Y.; Li, K.-Y.; Lu, Y.; Huang, Y.; Shao, X.-H. High Thermoelectric Performances of Monolayer SnSe Allotropes. *Nanoscale* **2017**, *9*, 16093–16100.

(410) Wu, M.; Wei, S.-H.; Huang, L. Origin of Polymorphism of the Two-Dimensional Group-IV Monochalcogenides. *Phys. Rev. B* **2017**, *96*, 205411.

(411) Luo, N.; Wang, C.; Jiang, Z.; Xu, Y.; Zou, X.; Duan, W. Saddle-Point Excitons and Their Extraordinary Light Absorption in 2D β-Phase Group-IV Monochalcogenides. *Adv. Funct. Mater.* **2018**, *28*, 1804581.

(412) Dong, B.; Wang, Z.; Hung, N. T.; Oganov, A. R.; Yang, T.; Saito, R.; Zhang, Z. New Two-Dimensional Phase of Tin Chalcogenides: Candidates for High-Performance Thermoelectric Materials. *Phys. Rev. Materials* **2019**, *3*, 013405.

(413) Li, Z.-Y.; Liu, M.-Y.; Huang, Y.; Chen, Q.-Y.; Cao, C.; He, Y. Tuning the Electronic Properties of Bilayer Group-IV Monochalcogenides by Stacking Order, Strain and an Electric Field: A Computational Study. *Phys. Chem. Chem. Phys.* **2018**, *20*, 214–220.

(414) Mao, Y.; Xu, C.; Yuan, J.; Zhao, H. Effect of Stacking Order and In-Plane Strain on the Electronic Properties of Bilayer GeSe. *Phys. Chem. Chem. Phys.* **2018**, *20*, 6929–6935.

(415) Yang, J.-H.; Gong, X.-G. Stacking Induced Indirect-to-Direct Bandgap Transition in Layered Group-IV Monochalcogenides for Ideal Optoelectronics. *J. Mater. Chem. C* **2019**, *7*, 11858–11867.

(416) Zhang, J.; Lang, X. Y.; Jiang, Q. Electronic and Optical Properties of Bilayer SnS with Different Stacking Orders: A First Principles Study. *J. Appl. Phys.* **2018**, *124*, 235101.

(417) Gomes, L. C.; Carvalho, A. Phosphorene Analogues: Isoelectronic Two-Dimensional Group-IV Monochalcogenides with Orthorhombic Structure. *Phys. Rev. B* **2015**, *92*, 085406.

(418) Huang, L.; Wu, F.; Li, J. Structural Anisotropy Results in Strain-Tunable Electronic and Optical Properties in Monolayer GeX and SnX (X = S, Se, Te). *J. Chem. Phys.* **2016**, *144*, 114708.

(419) Qin, G.; Qin, Z.; Fang, W.-Z.; Zhang, L.-C.; Yue, S.-Y.; Yan, Q.-B.; Hu, M.; Su, G. Diverse Anisotropy of Phonon Transport in Two-Dimensional Group IV–VI Compounds: A Comparative Study. *Nanoscale* **2016**, *8*, 11306–11319.

(420) Li, Z.; Yang, Y.; Wang, X.; Shi, W.; Xue, D.-J.; Hu, J.-S. Three-Dimensional Optical Anisotropy of Low-Symmetry Layered GeS. *ACS Appl. Mater. Interfaces* **2019**, *11*, 24247–24253.

(421) Tian, Z.; Guo, C.; Zhao, M.; Li, R.; Xue, J. Two-Dimensional SnS: A Phosphorene Analogue with Strong In-Plane Electronic Anisotropy. *ACS Nano* **2017**, *11*, 2219–2226.

(422) Xu, X.; Song, Q.; Wang, H.; Li, P.; Zhang, K.; Wang, Y.; Yuan, K.; Yang, Z.; Ye, Y.; Dai, L. In-Plane Anisotropies of Polarized Raman Response and Electrical Conductivity in Layered Tin Selenide. *ACS Appl. Mater. Interfaces* **2017**, *9*, 12601–12607.

(423) Shi, G.; Kioupakis, E. Anisotropic Spin Transport and Strong Visible-Light Absorbance in Few-Layer SnSe and GeSe. *Nano Lett.* **2015**, *15*, 6926–6931.

(424) Gomes, L. C.; Carvalho, A.; Castro Neto, A. H. Enhanced Piezoelectricity and Modified Dielectric Screening of Two-Dimensional Group-IV Monochalcogenides. *Phys. Rev. B* **2015**, *92*, 214103.

(425) Guo, Y.; Zhou, S.; Bai, Y.; Zhao, J. Oxidation Resistance of Monolayer Group-IV Monochalcogenides. *ACS Appl. Mater. Interfaces* **2017**, *9*, 12013–12020.

(426) Wang, H.; Qian, X. Two-Dimensional Multiferroics in Monolayer Group IV Monochalcogenides. *2D Mater.* **2017**, *4*, 015042.

(427) Tang, X.; Kou, L. Two-Dimensional Ferroics and Multiferroics: Platforms for New Physics and Applications. *J. Phys. Chem. Lett.* **2019**, *10*, 6634–6649.

(428) Wang, H.; Qian, X. Giant Optical Second Harmonic Generation in Two-Dimensional Multiferroics. *Nano Lett.* **2017**, *17*, 5027–5034.

(429) Chang, K.; Liu, J.; Lin, H.; Wang, N.; Zhao, K.; Zhang, A.; Jin, F.; Zhong, Y.; Hu, X.; Duan, W.; et al. Discovery of Robust In-Plane Ferroelectricity in Atomic-Thick SnTe. *Science* **2016**, *353*, 274–278.

(430) Bao, Y.; Song, P.; Liu, Y.; Chen, Z.; Zhu, M.; Abdelwahab, I.; Su, J.; Fu, W.; Chi, X.; Yu, W.; et al. Gate-Tunable In-Plane Ferroelectricity in Few-Layer SnS. *Nano Lett.* **2019**, *19*, 5109–5117.

(431) Sutter, P.; Sutter, E. Growth Mechanisms of Anisotropic Layered Group IV Chalcogenides on van der Waals Substrates for Energy Conversion Applications. *ACS Appl. Nano Mater.* **2018**, *1*, 3026–3034.

(432) Jiang, J.; Wong, C. P. Y.; Zou, J.; Li, S.; Wang, Q.; Chen, J.; Qi, D.; Wang, H.; Eda, G.; Chua, D. H. C.; et al. Two-Step Fabrication of Single-Layer Rectangular SnSe Flakes. *2D Mater.* **2017**, *4*, 021026.

(433) Kolobov, A. V.; Kim, D. J.; Giussani, A.; Fons, P.; Tominaga, J.; Calarco, R.; Gruverman, A. Ferroelectric Switching in Epitaxial GeTe Films. *APL Materials* **2014**, *2*, 066101.

(434) Polking, M. J.; Urban, J. J.; Milliron, D. J.; Zheng, H.; Chan, E.; Caldwell, M. A.; Raoux, S.; Kisielowski, C. F.; Ager, J. W.; Ramesh, R.; et al. Size-Dependent Polar Ordering in Colloidal GeTe Nanocrystals. *Nano Lett.* **2011**, *11*, 1147–1152.

(435) Lucovsky, G.; White, R. M. Effects of Resonance Bonding on the Properties of Crystalline and Amorphous Semiconductors. *Phys. Rev. B* **1973**, *8*, 660–667.

(436) Kaloni, T. P.; Chang, K.; Miller, B. J.; Xue, Q.-K.; Chen, X.; Ji, S.-H.; Parkin, S. S. P.; Barraza-Lopez, S. From an Atomic Layer to the Bulk: Low-Temperature Atomistic Structure and Ferroelectric and Electronic Properties of SnTe Films. *Phys. Rev. B* **2019**, *99*, 134108.

(437) Tanaka, Y.; Ren, Z.; Sato, T.; Nakayama, K.; Souma, S.; Takahashi, T.; Segawa, K.; Ando, Y. Experimental Realization of a Topological Crystalline Insulator in SnTe. *Nature Phys* **2012**, *8*, 800–803.

(438) Dittmar, G.; Schäfer, H. Die Kristallstruktur von H.T.-$GeS_2$. *Acta Crystallogr. B Struct. Sci.* **1975**, *31*, 2060–2064.

(439) Dittmar, G.; Schäfer, H. Die Kristallstruktur von Germaniumdiselenid. *Acta Cryst. B* **1976**, *32*, 2726–2728.

(440) Fuentes-Cabrera, M.; Wang, H.; Sankey, O. F. Phase Stability and Pressure-Induced Semiconductor to Metal Transition in Crystalline $GeSe_2$. *J. Phys.: Condens. Matter* **2002**, *14*, 9589–9600.

(441) Popović, Z. V.; Holtz, M.; Reimann, K.; Syassen, K. High-Pressure Raman Scattering and Optical Absorption Study of β-$GeS_2$. *Phys. Stat. Sol. B* **1996**, *198*, 533–537.

(442) Dittmar, W. G.; Schäfer, H. Die Kristallstruktur von L.T.-$GeS_2$. *Acta Crystallographica Section B* **1976**, *32*, 1188–1192.

(443) Yang, Y.; Liu, S.; Wang, X.; Li, Z.; Zhang, Y.; Zhang, G.; Xue, D.; Hu, J. Polarization-Sensitive Ultraviolet Photodetection of Anisotropic 2D $GeS_2$. *Adv. Funct. Mater.* **2019**, *29*, 1900411.

(444) Yang, Y.; Wang, X.; Liu, S.-C.; Li, Z.; Sun, Z.; Hu, C.; Xue, D.-J.; Zhang, G.; Hu, J.-S. Weak Interlayer Interaction in 2D Anisotropic $GeSe_2$. *Adv. Sci.* **2019**, *6*, 1801810.

(445) Yan, Y.; Xiong, W.; Li, S.; Zhao, K.; Wang, X.; Su, J.; Song, X.; Li, X.; Zhang, S.; Yang, H.; et al. Direct Wide Bandgap 2D $GeSe_2$ Monolayer toward Anisotropic UV Photodetection. *Adv. Optical Mater.* **2019**, *7*, 1900622.

(446) Lochocki, E. B.; Vishwanath, S.; Liu, X.; Dobrowolska, M.; Furdyna, J.; Xing, H. G.; Shen, K. M. Electronic Structure of $SnSe_2$ Films Grown by Molecular Beam Epitaxy. *Appl. Phys. Lett.* **2019**, *114*, 091602.

(447) Pałosz, B.; Pałosz, W.; Gierlotka, S. Structures of 26 New Polytypes of Tin Disulfide. *Acta Cryst. C* **1986**, *42*, 653–657.

(448) Acharya, S.; Srivastava, O. N. Occurrence of Polytypism in $SnSe_2$. *J. Cryst. Growth* **1981**, *55*, 395–397.

(449) Pałosz, B.; Gierlotka, S.; Lévy, F. Polytypism of $SnSe_2$ Crystals Grown by Chemical Transport: Structures of Six Large-Period Polytypes of $SnSe_2$. *Acta Crystallogr. C Cryst. Struct. Commun.* **1985**, *41*, 1404–1406.

(450) Seminovski, Y.; Palacios, P.; Wahnón, P. Effect of van der Waals Interaction on the Properties of $SnS_2$ Layered Semiconductor. *Thin Solid Films* **2013**, *535*, 387–389.

(451) Gonzalez, J. M.; Oleynik, I. I. Layer-Dependent Properties of $SnS_2$ and $SnSe_2$ Two-Dimensional Materials. *Phys. Rev. B* **2016**, *94*, 125443.

(452) Zhang, Y.-M.; Fan, J.-Q.; Wang, W.-L.; Zhang, D.; Wang, L.; Li, W.; He, K.; Song, C.-L.; Ma, X.-C.; Xue, Q.-K. Observation of Interface Superconductivity in a $SnSe_2$/Epitaxial Graphene van der Waals Heterostructure. *Phys. Rev. B* **2018**, *98*, 220508.

(453) Shao, Z.; Fu, Z.-G.; Li, S.; Cao, Y.; Bian, Q.; Sun, H.; Zhang, Z.; Gedeon, H.; Zhang, X.; Liu, L.; et al. Strongly Compressed Few-Layered $SnSe_2$ Films Grown on a $SrTiO_3$ Substrate: The Coexistence of Charge Ordering and Enhanced Interfacial Superconductivity. *Nano Lett.* **2019**, *19*, 5304–5312.

(454) Zeng, J.; Liu, E.; Fu, Y.; Chen, Z.; Pan, C.; Wang, C.; Wang, M.; Wang, Y.; Xu, K.; Cai, S.; et al. Gate-Induced Interfacial Superconductivity in 1T-$SnSe_2$. *Nano Lett.* **2018**, *18*, 1410–1415.

(455) Wu, H.; Li, S.; Susner, M.; Kwon, S.; Kim, M.; Haugan, T.; Lv, B. Spacing Dependent and Cation Doping Independent Superconductivity in Intercalated 1T 2D $SnSe_2$. *2D Mater.* **2019**, *6*, 045048.

(456) Malone, B. D.; Kaxiras, E. Quasiparticle Band Structures and Interface Physics of SnS and GeS. *Phys. Rev. B* **2013**, *87*, 245312.

(457) Vaughn, D. D.; Patel, R. J.; Hickner, M. A.; Schaak, R. E. Single-Crystal Colloidal Nanosheets of GeS and GeSe. *J. Am. Chem. Soc.* **2010**, *132*, 15170–15172.

(458) Jeong, K.; Park, S.; Park, D.; Ahn, M.; Han, J.; Yang, W.; Jeong, H.-S.; Cho, M.-H. Evolution of Crystal Structures in GeTe during Phase Transition. *Sci. Rep.* **2017**, *7*, 955.

(459) Bauer Pereira, P.; Sergueev, I.; Gorsse, S.; Dadda, J.; Müller, E.; Hermann, R. P. Lattice Dynamics and Structure of GeTe, SnTe and PbTe. *Phys. Status Solidi B* **2013**, *250*, 1300–1307.

(460) Fernandes, P. A.; Sousa, M. G.; Salomé, P. M. P.; Leitão, J. P.; da Cunha, A. F. Thermodynamic Pathway for the Formation of SnSe and $SnSe_2$ Polycrystalline Thin Films by Selenization of Metal Precursors. *CrystEngComm* **2013**, *15*, 10278.

(461) Lefebvre, I.; Szymanski, M. A.; Olivier-Fourcade, J.; Jumas, J. C. Electronic Structure of Tin Monochalcogenides from SnO to SnTe. *Phys. Rev. B* **1998**, *58*, 1896–1906.

(462) Mariano, A. N.; Chopra, K. L. Polymorphism in Some IV-VI Compounds Induced by High Pressure and Thin-Film Epitaxial Growth. *Appl. Phys. Lett.* **1967**, *10*, 282–284.

(463) Zhou, D.; Li, Q.; Ma, Y.; Cui, Q.; Chen, C. Pressure-Induced Superconductivity in SnTe: A First-Principles Study. *J. Phys. Chem. C* **2013**, *117*, 12266–12271.

(464) Mitrofanov, K. V.; Kolobov, A. V.; Fons, P.; Krbal, M.; Shintani, T.; Tominaga, J.; Uruga, T. Local Structure of the SnTe Topological Crystalline Insulator: Rhombohedral Distortions Emerging from the Rocksalt Phase. *Phys. Rev. B* **2014**, *90*, 134101.

(465) Li, Z.; Wang, X.; Shi, W.; Xing, X.; Xue, D.-J.; Hu, J.-S. Strain-Engineering the Electronic Properties and Anisotropy of $GeSe_2$ Monolayers. *RSC Adv.* **2018**, *8*, 33445–33450.

(466) Shao, G.; Xue, X.-X.; Zhou, X.; Xu, J.; Jin, Y.; Qi, S.; Liu, N.; Duan, H.; Wang, S.; Li, S.; et al. Shape-Engineered Synthesis of Atomically Thin 1T-$SnS_2$ Catalyzed by Potassium Halides. *ACS Nano* **2019**, *13*, 8265–8274.

(467) Julien, C.; Eddrief, M.; Samaras, I.; Balkanski, M. Optical and Electrical Characterizations of SnSe, $SnS_2$ and $SnSe_2$ Single Crystals. *Mater. Sci. Eng.: B* **1992**, *15*, 70–72.

(468) Schlüter, M.; Cohen, M. L. Valence-Band Density of States and Chemical Bonding for Several Non-Transition-Metal Layer Compounds: $SnSe_2$, $PbI_2$, $BiI_3$, and GaSe. *Phys. Rev. B* **1976**, *14*, 424–431.

(469) Mehboudi, M.; Fregoso, B. M.; Yang, Y.; Zhu, W.; van der Zande, A.; Ferrer, J.; Bellaiche, L.; Kumar, P.; Barraza-Lopez, S. Structural Phase Transition and Material Properties of Few-Layer Monochalcogenides. *Phys. Rev. Lett.* **2016**, *117*, 246802.

(470) Dewandre, A.; Verstraete, M. J.; Grobert, N.; Zanolli, Z. Spectroscopic Properties of Few-Layer Tin Chalcogenides. *J. Phys. Mater.* **2019**, *2*, 044005.

(471) Poudel, S. P.; Villanova, J. W.; Barraza-Lopez, S. Group-IV Monochalcogenide Monolayers: Two-Dimensional Ferroelectrics with Weak Intralayer Bonds and a Phosphorenelike Monolayer Dissociation Energy. *Phys. Rev. Materials* **2019**, *3*, 124004.

(472) Mutlu, Z.; Wu, R. J.; Wickramaratne, D.; Shahrezaei, S.; Liu, C.; Temiz, S.; Patalano, A.; Ozkan, M.; Lake, R. K.; Mkhoyan, K. A.; et al. Phase Engineering of 2D Tin Sulfides. *Small* **2016**, *12*, 2998–3004.

(473) Huang, Y.; Xu, K.; Wang, Z.; Shifa, T. A.; Wang, Q.; Wang, F.; Jiang, C.; He, J. Designing the Shape Evolution of $SnSe_2$ Nanosheets and Their Optoelectronic Properties. *Nanoscale* **2015**, *7*, 17375–17380.

(474) Burton, L. A.; Colombara, D.; Abellon, R. D.; Grozema, F. C.; Peter, L. M.; Savenije, T. J.; Dennler, G.; Walsh, A. Synthesis, Characterization, and Electronic Structure of Single-Crystal SnS, $Sn_2S_3$, and $SnS_2$. *Chem. Mater.* **2013**, *25*, 4908–4916.

(475) Li, M.; Zhu, Y.; Li, T.; Lin, Y.; Cai, H.; Li, S.; Ding, H.; Pan, N.; Wang, X. One-Step CVD Fabrication and Optoelectronic Properties of $SnS_2$/SnS Vertical Heterostructures. *Inorg. Chem. Front.* **2018**, *5*, 1828–1835.

(476) Wang, Z.; Pang, F. A Facile Way to Control Phase of Tin Selenide Flakes by Chemical Vapor Deposition. *Chem. Phys. Lett.* **2018**, *702*, 90–95.

(477) Zhang, H.; Balaji, Y.; Nalin Mehta, A.; Heyns, M.; Caymax, M.; Radu, I.; Vandervorst, W.; Delabie, A. Formation Mechanism of 2D $SnS_2$ and SnS by Chemical Vapor Deposition Using $SnCl_4$ and $H_2S$. *J. Mater. Chem. C* **2018**, *6*, 6172–6178.

(478) Ahn, J.-H.; Lee, M.-J.; Heo, H.; Sung, J. H.; Kim, K.; Hwang, H.; Jo, M.-H. Deterministic Two-Dimensional Polymorphism Growth of Hexagonal *n*-Type $SnS_2$ and Orthorhombic *p*-Type SnS Crystals. *Nano Lett.* **2015**, *15*, 3703–3708.

(479) Chang, K.; Parkin, S. S. P. The Growth and Phase Distribution of Ultrathin SnTe on Graphene. *APL Materials* **2019**, *7*, 041102.

(480) Chen, H.; Keiser, C.; Du, S.; Gao, H.-J.; Sutter, P.; Sutter, E. Termination of Ge Surfaces with Ultrathin GeS and $GeS_2$ Layers *via* Solid-State Sulfurization. *Phys. Chem. Chem. Phys.* **2017**, *19*, 32473–32480.

(481) Giussani, A.; Perumal, K.; Hanke, M.; Rodenbach, P.; Riechert, H.; Calarco, R. On the Epitaxy of Germanium Telluride Thin Films on Silicon Substrates. *Phys. Status Solidi B* **2012**, *249*, 1939–1944.

(482) Wang, R.; Zhang, W.; Momand, J.; Ronneberger, I.; Boschker, J. E.; Mazzarello, R.; Kooi, B. J.; Riechert, H.; Wuttig, M.; Calarco, R. Formation of Resonant Bonding during Growth of Ultrathin GeTe Films. *NPG Asia Mater.* **2017**, *9*, e396.

(483) Wang, R.; Campi, D.; Bernasconi, M.; Momand, J.; Kooi, B. J.; Verheijen, M. A.; Wuttig, M.; Calarco, R. Ordered Peierls Distortion Prevented at Growth Onset of GeTe Ultra-Thin Films. *Sci. Rep.* **2016**, *6*, 32895.

(484) Hilmi, I.; Lotnyk, A.; Gerlach, J. W.; Schumacher, P.; Rauschenbach, B. Influence of Substrate Dimensionality on the Growth Mode of Epitaxial 3D-Bonded GeTe Thin Films: From 3D to 2D Growth. *Materials & Design* **2019**, *168*, 107657.

(485) Simpson, R. E.; Fons, P.; Kolobov, A. V.; Krbal, M.; Tominaga, J. Enhanced Crystallization of GeTe from an $Sb_2Te_3$ Template. *Appl. Phys. Lett.* **2012**, *100*, 021911.

(486) Tsunetomo, K.; Sugishima, T.; Imura, T.; Osaka, Y. Stability of Metastable $GeTe_2$ in Thin Films. *J. Non-Cryst. Solids* **1987**, *95–96*, 509–516.

(487) Wang, J.; Ronneberger, I.; Zhou, L.; Lu, L.; Deringer, V. L.; Zhang, B.; Tian, L.; Du, H.; Jia, C.; Qian, X.; et al. Unconventional Two-Dimensional Germanium Dichalcogenides. *Nanoscale* **2018**, *10*, 7363–7368.

(488) Zhou, T.; Pang, W. K.; Zhang, C.; Yang, J.; Chen, Z.; Liu, H. K.; Guo, Z. Enhanced Sodium-Ion Battery Performance by Structural Phase Transition from Two-Dimensional Hexagonal-$SnS_2$ to Orthorhombic-SnS. *ACS Nano* **2014**, *8*, 8323–8333.

(489) Tian, Z.; Zhao, M.; Xue, X.; Xia, W.; Guo, C.; Guo, Y.; Feng, Y.; Xue, J. Lateral Heterostructures Formed by Thermally Converting N-Type $SnSe_2$ to p-Type SnSe. *ACS Appl. Mater. Interfaces* **2018**, *10*, 12831–12838.

(490) Sutter, P.; Ibragimova, R.; Komsa, H.-P.; Parkinson, B. A.; Sutter, E. Self-Organized Twist-Heterostructures via Aligned van der Waals Epitaxy and Solid-State Transformations. *Nat. Commun.* **2019**, *10*, 5528.

(491) Sutter, E.; Huang, Y.; Komsa, H.-P.; Ghorbani-Asl, M.; Krasheninnikov, A. V.; Sutter, P. Electron-Beam Induced Transformations of Layered Tin Dichalcogenides. *Nano Lett.* **2016**, *16*, 4410–4416.

(492) Zhang, X.; Yang, Z.; Chen, Y. Novel Two-Dimensional Ferroelectric PbTe under Tension: A First-Principles Prediction. *J. Appl. Phys.* **2017**, *122*, 064101.

(493) Price, L. S.; Parkin, I. P.; Hardy, A. M. E.; Clark, R. J. H.; Hibbert, T. G.; Molloy, K. C. Atmospheric Pressure Chemical Vapor Deposition of Tin Sulfides (SnS, $Sn_2S_3$ , and $SnS_2$) on Glass. *Chem. Mater.* **1999**, *11*, 1792–1799.

(494) Anderson, T. L.; Krause, H. B. Refinement of the $Sb_2Te_3$ and $Sb_2Te_2Se$ Structures and Their Relationship to Nonstoichiometric $Sb_2Te_{3-y}Se_y$ Compounds. *Acta Crystallogr. B Struct. Sci.* **1974**, *30*, 1307–1310.

(495) Feutelais, Y.; Legendre, B.; Rodier, N.; Agafonov, V. A Study of the Phases in the Bismuth - Tellurium System. *Mater. Res. Bull.* **1993**, *28*, 591–596.

(496) Nakajima, S. The Crystal Structure of $Bi_2Te_{3-x}Se_x$. *J. Phys. Chem. Solids* **1963**, *24*, 479–485.

(497) Morimoto, N. The Crystal Structure of Orpiment ($As_2S_3$) Refined. *Mineral. J.* **1954**, *1*, 160–169.

(498) Mullen, D. J. E.; Nowacki, W. Refinement of the Crystal Structures of Realgar, AsS and Orpiment, $As_2S_3$. *Z. Kristallogr. Cryst. Mater.* **1972**, *136*, 48–65.

(499) Gibbs, G. V.; Wallace, A. F.; Zallen, R.; Downs, R. T.; Ross, N. L.; Cox, D. F.; Rosso, K. M. Bond Paths and van der Waals Interactions in Orpiment, $As_2S_3$. *J. Phys. Chem. A* **2010**, *114*, 6550–6557.

(500) Makovicky, E. Crystal Structures of Sulfides and Other Chalcogenides. *Rev. Mineral. Geochem.* **2006**, *61*, 7–125.

(501) Kampf, A. R.; Downs, R. T.; Housley, R. M.; Jenkins, R. A.; Hyršl, J. Anorpiment, $As_2S_3$, the Triclinic Dimorph of Orpiment. *Mineral. Mag.* **2011**, *75*, 2857–2867.

(502) Vaipolin, A. Refining the Structure of Crystalline $As_2Se_3$ by Finding Probable Corrections to the Atomic Coordinates. *Sov. Phys. Crystallogr.* **1966**, *10*, 509.

(503) Stergiou, A. C.; Rentzeperis, P. J. The Crystal Structure of Arsenic Selenide, $As_2S_3$. *Z. Krystallog.* **1985**, *173*, 185–191.

(504) Espeau, P.; Tamarit, J. Ll.; Barrio, M.; López, D. Ó.; Perrin, M. A.; Allouchi, H.; Céolin, R. Solid State Studies on Synthetic and Natural Crystalline Arsenic(III) Sulfide, $As_2S_3$ (Orpiment): New Data for an Old Compound. *Chem. Mater.* **2006**, *18*, 3821–3826.

(505) Šiškins, M.; Lee, M.; Alijani, F.; van Blankenstein, M. R.; Davidovikj, D.; van der Zant, H. S. J.; Steeneken, P. G. Highly Anisotropic Mechanical and Optical Properties of 2D Layered $As_2S_3$ Membranes. *ACS Nano* **2019**, *13*, 10845–10851.

(506) Ghosh, B.; Kothiyal, G. P. Vapour Phase Growth of Arsenic Chalcogenide Crystals and Their Characterization. *Prog. Cryst. Growth Charact. Mater.* **1983**, *6*, 393–413.

(507) Carron, G. J. The Crystal Structure and Powder Data for Arsenic Telluride. *Acta Cryst.* **1963**, *16*, 338–343.

(508) Morin, C.; Corallini, S.; Carreaud, J.; Vaney, J.-B.; Delaizir, G.; Crivello, J.-C.; Lopes, E. B.; Piarristeguy, A.; Monnier, J.; Candolfi, C.; et al. Polymorphism in Thermoelectric $As_2Te_3$. *Inorg. Chem.* **2015**, *54*, 9936–9947.

(509) Toscani, S.; Dugué, J.; Ollitrault, R.; Céolin, R. Polymorphism of $As_2Te_3$: Structural Studies and Thermal Behaviour of Rhombohedral β-$As_2Te_3$. *Thermochimica Acta* **1991**, *186*, 247–251.

(510) Chen, Y.; Liao, X.; Shi, X.; Xiao, H.; Liu, Y.; Chen, X. Three-Dimensional Auxetic Properties in Group V–VI Binary Monolayer Crystals $X_3M_2$ (X = S, Se; M = N, P, As). *Phys. Chem. Chem. Phys.* **2019**, *21*, 5916–5924.

(511) Xiao, H.; Shi, X.; Liao, X.; Zhang, Y.; Chen, X. Prediction of a Two-Dimensional $S_3N_2$ Solid for Optoelectronic Applications. *Phys. Rev. Materials* **2018**, *2*, 024002.

(512) Witting, I. T.; Chasapis, T. C.; Ricci, F.; Peters, M.; Heinz, N. A.; Hautier, G.; Snyder, G. J. The Thermoelectric Properties of Bismuth Telluride. *Adv. Electron. Mater.* **2019**, *5*, 1800904.

(513) Hong, M.; Chen, Z.-G.; Zou, J. Fundamental and Progress of $Bi_2Te_3$-Based Thermoelectric Materials. *Chinese Phys. B* **2018**, *27*, 048403.

(514) Heremans, J. P.; Cava, R. J.; Samarth, N. Tetradymites as Thermoelectrics and Topological Insulators. *Nat. Rev. Mater.* **2017**, *2*, 17049.

(515) Xu, N.; Xu, Y.; Zhu, J. Topological Insulators for Thermoelectrics. *npj Quant. Mater.* **2017**, *2*, 51.

(516) Vaney, J.-B.; Delaizir, G.; Piarristeguy, A.; Monnier, J.; Alleno, E.; Lopes, E. B.; Gonçalves, A. P.; Pradel, A.; Dauscher, A.; Candolfi, C.; et al. High-Temperature Thermoelectric Properties of the β-$As_{2-x}Bi_xTe_3$ Solid Solution. *APL Materials* **2016**, *4* , 104901.

(517) Vaney, J.-B.; Delaizir, G.; Wiendlocha, B.; Tobola, J.; Alleno, E.; Piarristeguy, A.; Gonçalves, A. P.; Gendarme, C.; Malaman, B.; Dauscher, A.; et al. Effect of Isovalent Substitution on the Electronic Structure and Thermoelectric Properties of the Solid Solution α-$As_2Te_{3-x}Se_x$ ($0 \leq x \leq 1.5$). *Inorg. Chem.* **2017**, *56*, 2248–2257.

(518) Vaney, J.-B.; Carreaud, J.; Delaizir, G.; Pradel, A.; Piarristeguy, A.; Morin, C.; Alleno, E.; Monnier, J.; Gonçalves, A. P.; Candolfi, C.; et al. High-Temperature Thermoelectric Properties of Sn-Doped β-$As_2Te_3$. *Adv. Electron. Mater.* **2015**, *1*, 1400008.

(519) Vaney, J.-B.; Carreaud, J.; Delaizir, G.; Morin, C.; Monnier, J.; Alleno, E.; Piarristeguy, A.; Pradel, A.; Gonçalves, A. P.; Lopes, E. B.; et al. Thermoelectric Properties of the α-$As_2Te_3$ Crystalline Phase. *J. Elec. Mater.* **2016**, *45*, 1447–1452.

(520) Vaney, J. B.; Carreaud, J.; Delaizir, G.; Piarristeguy, A.; Pradel, A.; Alleno, E.; Monnier, J.; Lopes, E. B.; Gonçalves, A. P.; Dauscher, A.; et al. High Thermoelectric Performance in Sn-Substituted α-$As_2Te_3$. *J. Mater. Chem. C* **2016**, *4*, 2329–2338.

(521) Zhang, H.; Liu, C.-X.; Qi, X.-L.; Dai, X.; Fang, Z.; Zhang, S.-C. Topological Insulators in Bi2Se3, Bi2Te3 and Sb2Te3 with a Single Dirac Cone on the Surface. *Nature Phys* **2009**, *5* (6), 438–442. https://doi.org/10.1038/nphys1270.

(522) Chen, Y. L.; Analytis, J. G.; Chu, J.-H.; Liu, Z. K.; Mo, S.-K.; Qi, X. L.; Zhang, H. J.; Lu, D. H.; Dai, X.; Fang, Z.; et al. Experimental Realization of a Three-Dimensional Topological Insulator, $Bi_2Te_3$. *Science* **2009**, *325*, 178–181.

(523) Xia, Y.; Qian, D.; Hsieh, D.; Wray, L.; Pal, A.; Lin, H.; Bansil, A.; Grauer, D.; Hor, Y. S.; Cava, R. J.; et al. Observation of a Large-Gap Topological-Insulator Class with a Single Dirac Cone on the Surface. *Nature Phys.* **2009**, *5*, 398–402.

(524) Hsieh, D.; Xia, Y.; Qian, D.; Wray, L.; Meier, F.; Dil, J. H.; Osterwalder, J.; Patthey, L.; Fedorov, A. V.; Lin, H.; et al. Observation of Time-Reversal-Protected Single-Dirac-Cone Topological-Insulator States in $Bi_2Te_3$ and $Sb_2Te_3$. *Phys. Rev. Lett.* **2009**, *103*, 146401.

(525) Hsieh, D.; Xia, Y.; Qian, D.; Wray, L.; Dil, J. H.; Meier, F.; Osterwalder, J.; Patthey, L.; Checkelsky, J. G.; Ong, N. P.; et al. A Tunable Topological Insulator in the Spin Helical Dirac Transport Regime. *Nature* **2009**, *460*, 1101–1105.

(526) Hor, Y. S.; Richardella, A.; Roushan, P.; Xia, Y.; Checkelsky, J. G.; Yazdani, A.; Hasan, M. Z.; Ong, N. P.; Cava, R. J. P -Type $Bi_2Se_3$ for Topological Insulator and Low-Temperature Thermoelectric Applications. *Phys. Rev. B* **2009**, *79*, 195208.

(527) Hasan, M. Z.; Kane, C. L. *Colloquium* : Topological Insulators. *Rev. Mod. Phys.* **2010**, *82*, 3045–3067.

(528) Sacépé, B.; Oostinga, J. B.; Li, J.; Ubaldini, A.; Couto, N. J. G.; Giannini, E.; Morpurgo, A. F. Gate-Tuned Normal and Superconducting Transport at the Surface of a Topological Insulator. *Nat. Commun.* **2011**, *2*, 575.

(529) Kong, D.; Chen, Y.; Cha, J. J.; Zhang, Q.; Analytis, J. G.; Lai, K.; Liu, Z.; Hong, S. S.; Koski, K. J.; Mo, S.-K.; et al. Ambipolar Field Effect in the Ternary Topological Insulator $(Bi_xSb_{1-x})_2Te_3$ by Composition Tuning. *Nature Nanotech.* **2011**, *6*, 705–709.

(530) Chen, J.; Qin, H. J.; Yang, F.; Liu, J.; Guan, T.; Qu, F. M.; Zhang, G. H.; Shi, J. R.; Xie, X. C.; Yang, C. L.; et al. Gate-Voltage Control of Chemical Potential and Weak Antilocalization in $Bi_2Se_3$. *Phys. Rev. Lett.* **2010**, *105*, 176602.

(531) Liu, M.; Chang, C.-Z.; Zhang, Z.; Zhang, Y.; Ruan, W.; He, K.; Wang, L.; Chen, X.; Jia, J.-F.; Zhang, S.-C.; et al. Electron Interaction-Driven Insulating Ground State in $Bi_2Se_3$ Topological Insulators in the Two-Dimensional Limit. *Phys. Rev. B* **2011**, *83*, 165440.

(532) Kim, Y. S.; Brahlek, M.; Bansal, N.; Edrey, E.; Kapilevich, G. A.; Iida, K.; Tanimura, M.; Horibe, Y.; Cheong, S.-W.; Oh, S. Thickness-Dependent Bulk Properties and Weak Antilocalization Effect in Topological Insulator $Bi_2Se_3$. *Phys. Rev. B* **2011**, *84*, 073109.

(533) Jiang, Y.; Wang, Y.; Chen, M.; Li, Z.; Song, C.; He, K.; Wang, L.; Chen, X.; Ma, X.; Xue, Q.-K. Landau Quantization and the Thickness Limit of Topological Insulator Thin Films of $Sb_2Te_3$. *Phys. Rev. Lett.* **2012**, *108*, 016401.

(534) Zhang, Y.; He, K.; Chang, C.-Z.; Song, C.-L.; Wang, L.-L.; Chen, X.; Jia, J.-F.; Fang, Z.; Dai, X.; Shan, W.-Y.; et al. Crossover of the Three-Dimensional Topological Insulator $Bi_2Se_3$ to the Two-Dimensional Limit. *Nat. Phys.* **2010**, *6*, 584–588.

(535) Lang, M.; He, L.; Kou, X.; Upadhyaya, P.; Fan, Y.; Chu, H.; Jiang, Y.; Bardarson, J. H.; Jiang, W.; Choi, E. S.; et al. Competing Weak Localization and Weak Antilocalization in Ultrathin Topological Insulators. *Nano Lett.* **2013**, *13*, 48–53.

(536) Wang, M.-X.; Liu, C.; Xu, J.-P.; Yang, F.; Miao, L.; Yao, M.-Y.; Gao, C. L.; Shen, C.; Ma, X.; Chen, X.; et al. The Coexistence of Superconductivity and Topological Order in the $Bi_2Se_3$ Thin Films. *Science* **2012**, *336*, 52–55.

(537) Li, Y. Y.; Wang, G.; Zhu, X. G.; Liu, M. H.; Ye, C.; Chen, X.; Wang, Y. Y.; He, K.; Wang, L. L.; Ma, X. C.; et al. Intrinsic Topological Insulator $Bi_2Te_3$ Thin Films on Si and Their Thickness Limit. *Adv. Mater.* **2010**, *22*, 4002–4007.

(538) Ivanov, Y. V.; Burkov, A. T.; Pshenay-Severin, D. A. Thermoelectric Properties of Topological Insulators. *Phys. Status Solidi B* **2018**, *255*, 1800020.

(539) Zahid, F.; Lake, R. Thermoelectric Properties of $Bi_2Te_3$ Atomic Quintuple Thin Films. *Appl. Phys. Lett.* **2010**, *97*, 212102.

(540) Xu, B.; Zhang, J.; Yu, G.; Ma, S.; Wang, Y.; Wang, Y. Thermoelectric Properties of Monolayer $Sb_2Te_3$. *J. Appl. Phys.* **2018**, *124*, 165104.

(541) Li, Z.; Miao, N.; Zhou, J.; Sun, Z.; Liu, Z.; Xu, H. High Thermoelectric Performance of Few-Quintuple $Sb_2Te_3$ Nanofilms. *Nano Energy* **2018**, *43*, 285–290.

(542) Zhang, J.; Liu, H. J.; Cheng, L.; Wei, J.; Shi, J.; Tang, X. F.; Uher, C. Enhanced Thermoelectric Performance of a Quintuple Layer of $Bi_2Te_3$. *J. Appl. Phys.* **2014**, *116*, 023706.

(543) Li, X.; Ren, H.; Luo, Y. Electronic Structure of Bismuth Telluride Quasi-Two-Dimensional Crystal: A First Principles Study. *Appl. Phys. Lett.* **2011**, *98*, 083113.

(544) Liang, J.; Cheng, L.; Zhang, J.; Liu, H.; Zhang, Z. Maximizing the Thermoelectric Performance of Topological Insulator $Bi_2Te_3$ Films in the Few-Quintuple Layer Regime. *Nanoscale* **2016**, *8*, 8855–8862.

(545) Ghaemi, P.; Mong, R. S. K.; Moore, J. E. In-Plane Transport and Enhanced Thermoelectric Performance in Thin Films of the Topological Insulators $Bi_2Te_3$ and $Bi_2Se_3$. *Phys. Rev. Lett.* **2010**, *105*, 166603.

(546) Li, Z.; Peng, L.; Li, J.; Zhou, J.; Sun, Z. Mechanical and Transport Properties of $Bi_xSb_{2-x}Te_3$ Single Quintuple Layers. *Comput. Mater. Sci.* **2019**, *170*, 109182.

(547) Li, Z.; Han, S.; Pan, Y.; Miao, N.; Zhou, J.; Xu, H.; Sun, Z. Origin of High Thermoelectric Performance with a Wide Range of Compositions for $Bi_xSb_{2-x}Te_3$ Single Quintuple Layers. *Phys. Chem. Chem. Phys.* **2019**, *21*, 1315–1323.

(548) Chen, Y.; Wu, Y.; Xu, K.; Ma, C.; Lu, Z.; Zhang, X.; Zhang, H.; Zhu, H.; Fang, Z. New $Sb_2Te_{3-x}Se_x$ Monolayers with High Electron Mobilities and Wide Absorption Range. *ACS Appl. Mater. Interfaces* **2019**, *11*, 37216–37228.

(549) Sun, Y.; Cheng, H.; Gao, S.; Liu, Q.; Sun, Z.; Xiao, C.; Wu, C.; Wei, S.; Xie, Y. Atomically Thick Bismuth Selenide Freestanding Single Layers Achieving Enhanced Thermoelectric Energy Harvesting. *J. Am. Chem. Soc.* **2012**, *134*, 20294–20297.

(550) Teweldebrhan, D.; Goyal, V.; Balandin, A. A. Exfoliation and Characterization of Bismuth Telluride Atomic Quintuples and Quasi-Two-Dimensional Crystals. *Nano Lett.* **2010**, *10*, 1209–1218.

(551) Goyal, V.; Teweldebrhan, D.; Balandin, A. A. Mechanically-Exfoliated Stacks of Thin Films of $Bi_2Te_3$ Topological Insulators with Enhanced Thermoelectric Performance. *Appl. Phys. Lett.* **2010**, *97*, 133117.

(552) Hinsche, N. F.; Zastrow, S.; Gooth, J.; Pudewill, L.; Zierold, R.; Rittweger, F.; Rauch, T.; Henk, J.; Nielsch, K.; Mertig, I. Impact of the Topological Surface State on the Thermoelectric Transport in $Sb_2Te_3$ Thin Films. *ACS Nano* **2015**, *9*, 4406–4411.

(553) Guo, M.; Wang, Z.; Xu, Y.; Huang, H.; Zang, Y.; Liu, C.; Duan, W.; Gan, Z.; Zhang, S.-C.; He, K.; et al. Tuning Thermoelectricity in a $Bi_2Se_3$ Topological Insulator via Varied Film Thickness. *New J. Phys.* **2016**, *18*, 015008.

(554) Miao, N.; Zhou, J.; Sa, B.; Xu, B.; Sun, Z. Few-Layer Arsenic Trichalcogenides: Emerging Two-Dimensional Semiconductors with Tunable Indirect-Direct Band-Gaps. *J. Alloys Compd.* **2017**, *699*, 554–560.

(555) Debbichi, L.; Kim, H.; Björkman, T.; Eriksson, O.; Lebègue, S. First-Principles Investigation of Two-Dimensional Trichalcogenide and Sesquichalcogenide Monolayers. *Phys. Rev. B* **2016**, *93*, 245307.

(556) Mortazavi, B.; Shojaei, F.; Azizi, M.; Rabczuk, T.; Zhuang, X. $As_2S_3$, $As_2Se_3$ and $As_2Te_3$ Nanosheets: Superstretchable Semiconductors with Anisotropic Carrier Mobilities and Optical Properties. *J. Mater. Chem. C* **2020**, *8*, 2400–2410.

(557) Shelimova, L. E.; Karpinskii, O. G.; Kretova, M. A.; Kosyakov, V. I.; Shestakov, V. A.; Zemskov, V. S.; Kuznetsov, F. A. Homologous Series of Layered Tetradymite-like Compounds in the Sb-Te and GeTe-$Sb_2Te_3$ Systems. *Inorg Mater* **2000**, *36*, 768–775.

(558) Govaerts, K.; Sluiter, M. H. F.; Partoens, B.; Lamoen, D. Stability of Sb-Te Layered Structures: First-Principles Study. *Phys. Rev. B* **2012**, *85*, 144114.

(559) Semiletov, S.; Pinsker, Z. The Electron Diffraction Analysis of the System of Alloys Bi-Se. In *Dokl. AN SSSR* **1955**, *100*, 1079–1082.

(560) Lind, H.; Lidin, S.; Häussermann, U. Structure and Bonding Properties of $(Bi_2Se_3)_m(Bi_2)_n$ Stacks by First-Principles Density Functional Theory. *Phys. Rev. B* **2005**, *72*, 184101.

(561) Lind, H.; Lidin, S. A General Structure Model for Bi–Se Phases Using a Superspace Formalism. *Solid State Sciences* **2003**, *5*, 47–57.

(562) Cook, N. J.; Ciobanu, C. L.; Wagner, T.; Stanley, C. J. Minerals of the System Bi-Te-Se-S Related to the Tetradymite Archetype: Review of Classification and Compositional Variation. *The Canadian Mineralogist* **2007**, *45*, 665–708.

(563) Stasova, M. Crystal Structure of Bismuth Selenides and Bismuth and Antimony Tellurides. *J. Struct. Chem.* **1967**, *8*, 584–589.

(564) Ciobanu, C. L.; Pring, A.; Cook, N. J.; Self, P.; Jefferson, D.; Dima, G. I.; Melnikov, V. Chemical-Structural Modularity in the Tetradymite Group: A HRTEM Study. *American Mineralogist* **2009**, *94*, 517–534.

(565) Samanta, M.; Pal, K.; Waghmare, U. V.; Biswas, K. Intrinsically Low Thermal Conductivity and High Carrier Mobility in Dual Topological Quantum Material, N-Type BiTe. *Angew. Chem. Int. Ed.* **2020**, *59*, 4822–4829.

(566) Brebrick, R. F. Characterization of Phases in the 50–60 at. % Te Region of the Bi–Te System by X-Ray Powder Diffraction Patterns. *J Appl Crystallogr* **1968**, *1*, 241–246.

(567) Agafonov, V.; Rodier, N.; Céolin, R.; Bellissent, R.; Bergman, C.; Gaspard, J. P. Structure of Sb2Te. *Acta Crystallogr. C Cryst. Struct. Commun.* **1991**, *47*, 1141–1143.

(568) Bos, J. W. G.; Zandbergen, H. W.; Lee, M.-H.; Ong, N. P.; Cava, R. J. Structures and Thermoelectric Properties of the Infinitely Adaptive Series $(Bi_2)_m(Bi_2Te_3)_n$. *Phys. Rev. B* **2007**, *75*, 195203.

(569) Stillwell, R. L.; Jenei, Z.; Weir, S. T.; Vohra, Y. K.; Jeffries, J. R. Superconducting $Bi_2Te$: Pressure-Induced Universality in the $(Bi_2)_m(Bi_2Te_3)_n$ Series. *Phys. Rev. B* **2016**, *93*, 094511.

(570) Cecchi, S.; Dragoni, D.; Kriegner, D.; Tisbi, E.; Zallo, E.; Arciprete, F.; Holý, V.; Bernasconi, M.; Calarco, R. Interplay between Structural and Thermoelectric Properties in Epitaxial $Sb_{2+x}Te_3$ Alloys. *Adv. Funct. Mater.* **2019**, *29*, 1805184.

(571) Stasova, M. The Crystal Structure of Bismuthum Selenide $Bi_4Se_3$. *Izvestiya Akad Nauk SSSR Neorg Materialy* **1968**, *4*, 28–31.

(572) Yamana, K.; Kihara, K.; Matsumoto, T. Bismuth Tellurides: BiTe and $Bi_4Te_3$. *Acta Crystallogr. B Struct. Sci.* **1979**, *35*, 147–149.

(573) Khalil, L.; Papalazarou, E.; Caputo, M.; Nilforoushan, N.; Perfetti, L.; Taleb-Ibrahimi, A.; Kandyba, V.; Barinov, A.; Gibson, Q. D.; Cava, R. J.; et al. Electronic Band Structure for Occupied and Unoccupied States of the Natural Topological Superlattice Phase $Sb_2Te$. *Phys. Rev. B* **2017**, *95*, 085118.

(574) Johannsen, J. C.; Autès, G.; Crepaldi, A.; Moser, S.; Casarin, B.; Cilento, F.; Zacchigna, M.; Berger, H.; Magrez, A.; Bugnon, Ph.; et al. Engineering the Topological Surface States in the $(Sb_2)_m{-}Sb_2Te_3$ (m = 0–3) Superlattice Series. *Phys. Rev. B* **2015**, *91*, 201101.

(575) Eschbach, M.; Lanius, M.; Niu, C.; Młyńczak, E.; Gospodarič, P.; Kellner, J.; Schüffelgen, P.; Gehlmann, M.; Döring, S.; Neumann, E.; et al. BiTe Is a Dual Topological Insulator. *Nat. Commun.* **2017**, *8*, 14976.

(576) Poudeu, P. F. P.; Kanatzidis, M. G. Design in Solid State Chemistry Based on Phase Homologies. $Sb_4Te_3$ and $Sb_8Te_9$ as New Members of the Series $(Sb_2Te_3)_m{\cdot}(Sb_2)_n$. *Chem. Commun.* **2005**, *21*, 2672.

(577) Kifune, K.; Kubota, Y.; Matsunaga, T.; Yamada, N. Extremely Long Period-Stacking Structure in the Sb–Te Binary System. *Acta Crystallogr. B Struct. Sci.* **2005**, *61*, 492–497.

(578) Takagaki, Y.; Giussani, A.; Tominaga, J.; Jahn, U.; Calarco, R. Transport Properties in a Sb–Te Binary Topological-Insulator System. *J. Phys.: Condens. Matter* **2013**, *25*, 345801.

(579) Govaerts, K.; Park, K.; De Beule, C.; Partoens, B.; Lamoen, D. Effect of Bi Bilayers on the Topological States of $Bi_2Se_3$: A First-Principles Study. *Phys. Rev. B* **2014**, *90*, 155124.

(580) Gibson, Q. D.; Schoop, L. M.; Weber, A. P.; Ji, H.; Nadj-Perge, S.; Drozdov, I. K.; Beidenkopf, H.; Sadowski, J. T.; Fedorov, A.; Yazdani, A.; et al. Termination-Dependent Topological Surface States of the Natural Superlattice Phase $Bi_4Se_3$. *Phys. Rev. B* **2013**, *88*, 081108.

(581) Chagas, T.; Ribeiro, G. A. S.; Gonçalves, P. H. R.; Calil, L.; Silva, W. S.; Malachias, Â.; Mazzoni, M. S. C.; Magalhães-Paniago, R. $Bi_2$:$Bi_2Te_3$ Stacking Influence on the Surface Electronic Response of the Topological Insulator $Bi_4Te_3$. *Electron. Struct.* **2020**, *2*, 015002.

(582) Rodrigues-Junior, G.; Marçal, L. A. B.; Ribeiro, G. A. S.; Rappl, P. H. de O.; Abramof, E.; Sciammarella, P. V.; Guimarães, L. de M.; Pérez, C. A.; Malachias, Â. Direct Observation of Large Strain through van der Waals Gaps on Epitaxial $Bi_2Te_3$/Graphite: Pseudomorphic Relaxation and the Role of $Bi_2$ Layers on the $Bi_xTe_y$ Topological Insulator Series. *Phys. Rev. Materials* **2020**, *4*, 023602.

(583) Zallen, R.; Drews, R. E.; Emerald, R. L.; Slade, M. L. Electronic Structure of Crystalline and Amorphous $As_2S_3$ and $As_2Se_3$. *Phys. Rev. Lett.* **1971**, *26*, 1564–1567.

(584) Blossey, D. F.; Zallen, R. Surface and Bulk Photoresponse of Crystalline $As_2S_3$. *Phys. Rev. B* **1974**, *9*, 4306–4313.

(585) Zallen, R.; Blossey, D. F. The Optical Properties, Electronic Structure, and Photoconductivity of Arsenic Chalcogenide Layer Crystals. In *Optical and Electrical Properties*; Springer, 1976; pp. 231–272.

(586) Schein, L. B. Temperature Independent Drift Mobility along the Molecular Direction of $As_2S_3$. *Phys. Rev. B* **1977**, *15*, 1024–1034.

(587) Mohammed, L.; Saeed, M. A.; Zhang, Q.; Musa, A. Core-Level Excitation in Polymorph of $As_2S_3$ and β-$In_2S_3$. *J. Comput. Phys.* **2018**, *28*, 11–17.

(588) Wu, C.-C. Structure and Optical Characterization of Sulfur Incorporated $As_2Se_3$ Crystals. *J. Appl. Phys.* **2007**, *101*, 063533.

(589) Deng, H. Theoretical Prediction of the Structural, Electronic, Mechanical and Thermodynamic Properties of the Binary α-$As_2Te_3$ and β-$As_2Te_3$. *J. Alloys Compd.* **2016**, *656*, 695–701.

(590) Vaney, J.-B.; Crivello, J.-C.; Morin, C.; Delaizir, G.; Carreaud, J.; Piarristeguy, A.; Monnier, J.; Alleno, E.; Pradel, A.; Lopes, E. B.; et al. Electronic Structure, Low-Temperature Transport and Thermodynamic Properties of Polymorphic β-$As_2Te_3$. *RSC Adv.* **2016**, *6*, 52048–52057.

(591) Kim, H.-S.; Heinz, N. A.; Gibbs, Z. M.; Tang, Y.; Kang, S. D.; Snyder, G. J. High Thermoelectric Performance in $(Bi_{0.25}Sb_{0.75})_2Te_3$ Due to Band Convergence and Improved by Carrier Concentration Control. *Materials Today* **2017**, *20*, 452–459.

(592) Sehr, R.; Testardi, L. R. The Optical Properties of P-Type $Bi_2Te_3$-$Sb_2Te_3$ Alloys between 2–15 Microns. *J. Phys. Chem. Solids* **1962**, *23*, 1219–1224.

(593) Stordeur, M.; Stölzer, M.; Sobotta, H.; Riede, V. Investigation of the Valence Band Structure of Thermoelectric $(Bi_{1-x}Sb_x)_2Te_3$ Single Crystals. *Phys. Stat. Sol. B* **1988**, *150*, 165–176.

(594) Jacobs-Gedrim, R. B.; Murphy, M. T.; Yang, F.; Jain, N.; Shanmugam, M.; Song, E. S.; Kandel, Y.; Hesamaddin, P.; Yu, H. Y.; Anantram, M. P.; et al. Reversible Phase-Change Behavior in Two-Dimensional Antimony Telluride ($Sb_2Te_3$) Nanosheets. *Appl. Phys. Lett.* **2018**, *112*, 133101.

(595) Xu, B.; Cao, Y.; An, X.; Zhang, J.; Ma, S.; Wang, Y.; Chen, J.; Chen, L.; Yi, L. Electronic and Optical Properties of Monolayer $Sb_2Te_3$ Using Biaxial Strain. *J. Phys. Soc. Jpn.* **2019**, *88*, 124712.

(596) Kang, Y.; Zhang, Q.; Fan, C.; Hu, W.; Chen, C.; Zhang, L.; Yu, F.; Tian, Y.; Xu, B. High Pressure Synthesis and Thermoelectric Properties of Polycrystalline $Bi_2Se_3$. *J. Alloys Compd.* **2017**, *700*, 223–227.

(597) Butch, N. P.; Kirshenbaum, K.; Syers, P.; Sushkov, A. B.; Jenkins, G. S.; Drew, H. D.; Paglione, J. Strong Surface Scattering in Ultrahigh-Mobility $Bi_2Se_3$ Topological Insulator Crystals. *Phys. Rev. B* **2010**, *81*, 241301.

(598) Sapkota, Y. R.; Alkabsh, A.; Walber, A.; Samassekou, H.; Mazumdar, D. Optical Evidence for Blue Shift in Topological Insulator Bismuth Selenide in the Few-Layer Limit. *Appl. Phys. Lett.* **2017**, *110*, 181901.

(599) Yazyev, O. V.; Kioupakis, E.; Moore, J. E.; Louie, S. G. Quasiparticle Effects in the Bulk and Surface-State Bands of $Bi_2Se3$ and $Bi_2Te_3$ Topological Insulators. *Phys. Rev. B* **2012**, *85*, 161101.

(600) Usanov, D.; Nezhdanov, A.; Kudryashov, M.; Krivenkov, I.; Markelov, A.; Trushin, V.; Mochalov, L.; Gogova, D.; Mashin, A. Some Insights into the Mechanism of Photoluminescence of As-S-Based Films Synthesized by PECVD. *J. Non-Cryst. Solids* **2019**, *513*, 120–124.

(601) Ginley, T.; Wang, Y.; Law, S. Topological Insulator Film Growth by Molecular Beam Epitaxy: A Review. *Crystals* **2016**, *6*, 154.

(602) Springholz, G.; Wimmer, S.; Groiss, H.; Albu, M.; Hofer, F.; Caha, O.; Kriegner, D.; Stangl, J.; Bauer, G.; Holý, V. Structural Disorder of Natural $Bi_mSe_n$ Superlattices Grown by Molecular Beam Epitaxy. *Phys. Rev. Materials* **2018**, *2*, 054202.

(603) Steiner, H.; Volobuev, V.; Caha, O.; Bauer, G.; Springholz, G.; Holý, V. Structure and Composition of Bismuth Telluride Topological Insulators Grown by Molecular Beam Epitaxy. *J. Appl. Crystallogr.* **2014**, *47*, 1889–1900.

(604) Heo, H.; Sung, J. H.; Ahn, J.-H.; Ghahari, F.; Taniguchi, T.; Watanabe, K.; Kim, P.; Jo, M.-H. Frank-van der Merwe Growth versus Volmer-Weber Growth in Successive Stacking of a Few-Layer $Bi_2Te_3/Sb_2Te_3$ by van der Waals Heteroepitaxy: The Critical Roles of Finite Lattice-Mismatch with Seed Substrates. *Adv. Electron. Mater.* **2017**, *3*. 1600375.

(605) Liu, M.; Liu, F. Y.; Man, B. Y.; Bi, D.; Xu, X. Y. Multi-Layered Nanostructure $Bi_2Se_3$ Grown by Chemical Vapor Deposition in Selenium-Rich Atmosphere. *Appl. Surf. Sci.* **2014**, *317*, 257–261.

(606) Venkatasubramanian, R.; Colpitts, T.; Watko, E.; Lamvik, M.; ElMasry, N. MOCVD of $Bi_2Te_3$, $Sb_2Te_3$ and Their Superlattice Structures for Thin-Film Thermoelectric Applications. *J. Cryst. Growth* **1997**, *170*, 817–821.

(607) Alegria, L. D.; Schroer, M. D.; Chatterjee, A.; Poirier, G. R.; Pretko, M.; Patel, S. K.; Petta, J. R. Structural and Electrical Characterization of $Bi_2Se_3$ Nanostructures Grown by Metal-Organic Chemical Vapor Deposition. *Nano Lett.* **2012**, *12*, 4711–4714.

(608) Giani, A.; Boulouz, A.; Pascal-Delannoy, F.; Foucaran, A.; Charles, E.; Boyer, A. Growth of $Bi_2Te_3$ and $Sb_2Te_3$ Thin Films by MOCVD. *Mat. Sci. Eng. B-Solid* **1999**, *64*, 19–24.

(609) Kuznetsov, P. I.; Shchamkhalova, B. S.; Yapaskurt, V. O.; Shcherbakov, V. D.; Luzanov, V. A.; Yakushcheva, G. G.; Jitov, V. A.; Sizov, V. E. MOVPE Deposition of $Sb_2Te_3$ and Other Phases of Sb-Te System on Sapphire Substrate. *J. Cryst. Growth* **2017**, *471*, 1–7.

(610) Hilmi, I.; Lotnyk, A.; Gerlach, J. W.; Schumacher, P.; Rauschenbach, B. Research Update: Van-Der-Waals Epitaxy of Layered Chalcogenide $Sb_2Te_3$ Thin Films Grown by Pulsed Laser Deposition. *APL Materials* **2017**, *5*, 050701.

(611) Dauscher, A.; Thomy, A.; Scherrer, H. Pulsed Laser Deposition of $Bi_2Te_3$ Thin Films. *Thin Solid Films* **1996**, *280*, 61–66.

(612) Bailini, A.; Donati, F.; Zamboni, M.; Russo, V.; Passoni, M.; Casari, C. S.; Li Bassi, A.; Bottani, C. E. Pulsed Laser Deposition of $Bi_2Te_3$ Thermoelectric Films. *Appl. Surf. Sci.* **2007**, *254*, 1249–1254.

(613) Concepción, O.; Galván-Arellano, M.; Torres-Costa, V.; Climent-Font, A.; Bahena, D.; Manso Silván, M.; Escobosa, A.; de Melo, O. Controlling the Epitaxial Growth of $Bi_2Te_3$, BiTe, and $Bi_4Te_3$ Pure Phases by Physical Vapor Transport. *Inorg. Chem.* **2018**, *57*, 10090–10099.

(614) Kim, D.-H.; Byon, E.; Lee, G.-H.; Cho, S. Effect of Deposition Temperature on the Structural and Thermoelectric Properties of Bismuth Telluride Thin Films Grown by Co-Sputtering. *Thin Solid Films* **2006**, *510*, 148–153.

(615) Saito, Y.; Fons, P.; Makino, K.; Mitrofanov, K. V.; Uesugi, F.; Takeguchi, M.; Kolobov, A. V.; Tominaga, J. Compositional Tuning in Sputter-Grown Highly-Oriented Bi–Te Films and Their Optical and Electronic Structures. *Nanoscale* **2017**, *9*, 15115–15121.

(616) Akshay, V. R.; Suneesh, M. V.; Vasundhara, M. Tailoring Thermoelectric Properties through Structure and Morphology in Chemically Synthesized N-Type Bismuth Telluride Nanostructures. *Inorg. Chem.* **2017**, *56*, 6264–6274.

(617) Rotunno, E.; Longo, M.; Wiemer, C.; Fallica, R.; Campi, D.; Bernasconi, M.; Lupini, A. R.; Pennycook, S. J.; Lazzarini, L. A Novel $Sb_2Te_3$ Polymorph Stable at the Nanoscale. *Chem. Mater.* **2015**, *27*, 4368–4373.

(618) Kirkinskii, V.; Yakushev, V. A New Polymorphic Modification of Arsenic Selenide Obtained at High Presssures. In *Doklady Chemistry*; 1968; Vol. 182, p. 896.

(619) Lityagina, L. M.; Kulikova, L. F.; Zibrov, I. P.; Dyuzheva, T. I.; Nikolaev, N. A.; Brazhkin, V. V. Structural Transformations in the As–Se System under High Pressures and Temperatures. *J. Alloys Compd.* **2015**, *644*, 799–803.

(620) Bolotina, N. B.; Brazhkin, V. V.; Dyuzheva, T. I.; Katayama, Y.; Kulikova, L. F.; Lityagina, L. V.; Nikolaev, N. A. High-Pressure Polymorphism of $As_2S_3$ and New $AsS_2$ Modification with Layered Structure. *Jetp Lett.* **2014**, *98*, 539–543.

(621) Brazhkin, V. V.; Bolotina, N. B.; Dyuzheva, T. I.; Gavriliuk, A. G.; Lyapin, A. G.; Popova, S. V.; Samulski, S. AsS Layered-Structure Compound: New Kind of Covalent Crystals. *CrystEngComm* **2011**, *13*, 2599.

(622) Bolotina, N. B.; Brazhkin, V. V.; Dyuzheva, T. I.; Lityagina, L. M.; Kulikova, L. F.; Nikolaev, N. A.; Verin, I. A. Crystal Structure of New AsS2 Compound. *Crystallogr. Rep.* **2013**, *58*, 61–64.

(623) Scheidemantel, T. J.; Meng, J. F.; Badding, J. V. Thermoelectric Power and Phase Transition of Polycrystalline $As_2Te_3$ under Pressure. *J. Phys. Chem. Solids* **2005**, *66*, 1744–1747.

(624) Zhao, J.; Yang, L.; Yu, Z.; Wang, Y.; Li, C.; Yang, K.; Liu, Z.; Wang, Y. Structural Phase Transitions and Metallized Phenomena in Arsenic Telluride under High Pressure. *Inorg. Chem.* **2016**, *55*, 3907–3914.

(625) Cuenca-Gotor, V. P.; Sans, J. A.; Ibáñez, J.; Popescu, C.; Gomis, O.; Vilaplana, R.; Manjón, F. J.; Leonardo, A.; Sagasta, E.; Suárez-Alcubilla, A.; et al. Structural, Vibrational, and Electronic Study of α-$As_2Te_3$ under Compression. *J. Phys. Chem. C* **2016**, *120*, 19340–19352.

(626) Manjón, F. J.; Vilaplana, R.; Gomis, O.; Pérez-González, E.; Santamaría-Pérez, D.; Marín-Borrás, V.; Segura, A.; González, J.; Rodríguez-Hernández, P.; Muñoz, A.; et al. High-Pressure Studies of Topological Insulators $Bi_2Se_3$, $Bi_2Te_3$, and $Sb_2Te_3$. *Phys. Status Solidi B* **2013**, *250*, 669–676.

(627) Morozova, N. V.; Korobeinikov, I. V.; Ovsyannikov, S. V. Strategies and Challenges of High-Pressure Methods Applied to Thermoelectric Materials. *J. Appl. Phys.* **2019**, *125*, 220901.

(628) Bera, A.; Pal, K.; Muthu, D. V. S.; Waghmare, U. V.; Sood, A. K. Pressure-Induced Phase Transition in $Bi_2Se_3$ at 3 GPa: Electronic Topological Transition or Not? *J. Phys.: Condens. Matter* **2016**, *28*, 105401.

(629) Zhu, H.; Dong, J.; Li, P.; Wang, Y.; Guo, Z.; Shan, X.; Gong, Y.; An, P.; Li, X.; Zhang, J.; et al. Bi-Centric View of the Isostructural Phase Transitions in α-$Bi_2Se_3$ and α-$Bi_2Te_3$: Bi-Centric View of Isostructural Phase Transitions in $Bi_2Se_3$ and $Bi_2Te_3$. *Phys. Status Solidi B* **2017**, *254*, 1700007.

(630) Serebryanaya, N.; Tatyanin, E.; Buga, S.; Kruglov, I.; Lvova, N.; Blank, V. Monoclinic Structure and Electrical Properties of Metastable $Sb_2Te_3$ and $Bi_{0.4}Sb_{1.6}Te_3$ Phases: Structure and Properties of Metastable $Sb_2Te_3$ and $Bi_{0.4}Sb_{1.6}Te_3$ Phases. *Phys. Status Solidi B* **2015**, *252*, 267–273.

(631) Buga, S. G.; Serebryanaya, N. R.; Dubitskiy, G. A.; Semenova, E. E.; Aksenenkov, V. V.; Blank, V. D. Structure and Electrical Properties of $Sb_2Te_3$ and $Bi_{0.4}Sb_{1.6}Te_3$ Metastable Phases Obtained by HPHT Treatment. *High Pressure Research* **2011**, *31*, 86–90.

(632) Kulbachinskii, V. A.; Buga, S. G.; Serebryanaya, N. R.; Perov, N. S.; Kytin, V. G.; Tarelkin, S. A.; Bagramov, R. H.; Eliseev, N. N.; Blank, V. D. Superconductivity, Magnetoresistance, Magnetic Anomaly and Crystal Structure of New Phases of Topological Insulators $Bi_2Se_3$ and $Sb_2Te_3$. *J. Phys.: Conf. Ser.* **2018**, *969*, 012152.

(633) Buga, S. G.; Kulbachinskii, V. A.; Kytin, V. G.; Kytin, G. A.; Kruglov, I. A.; Lvova, N. A.; Perov, N. S.; Serebryanaya, N. R.; Tarelkin, S. A.; Blank, V. D. Superconductivity in Bulk Polycrystalline Metastable Phases of $Sb_2Te_3$ and $Bi_2Te_3$ Quenched after High-Pressure–High-Temperature Treatment. *Chem. Phys. Lett.* **2015**, *631–632*, 97–102.

(634) Yamamoto, A.; Hashizume, D.; Bahramy, M. S.; Tokura, Y. Coexistence of Monochalocogen and Dichalocogen Ions in $BiSe_2$ and $BiS_2$ Crystals Prepared at High Pressure. *Inorg. Chem.* **2015**, *54*, 4114–4119.

(635) Kevy, S. M.; Nielsen, M. B.; Lundegaard, L. F.; Ceresoli, D.; Chen, Y.-S.; Reardon, H.; Parisiades, P.; Bremholm, M. Investigation of the High Pressure Phase $BiS_2$: Temperature-Resolved Structure and Compression Behavior to 60 GPa. *J. Alloys Compd.* **2019**, *789*, 588–594.

(636) Cisar, A.; Corbett, J. D.; Daake, R. L. The Zirconium Dichloride Phase Region. Synthesis, Structure, and Photoelectron Spectral Studies of 3R-$ZrCl_2$, 6T-$Zr_{1.05}Cl_2$, and Related Phases. *Inorg. Chem.* **1979**, *18*, 836–843.

(637) Guthrie, D. H.; Corbett, J. D. Synthesis and Structure of an Infinite-Chain Form of $ZrI_2$ (α). *Journal of Solid State Chemistry* **1981**, *37*, 256–263.

(638) Corbett, J. D.; Guthrie, D. H. A Second Infinite-Chain Form of Zirconium Diiodide (β) and Its Coherent Intergrowth with α-Zirconium Diiodide. *Inorg. Chem.* **1982**, *21*, 1747–1751.

(639) Baskurt, M.; Eren, I.; Yagmurcukardes, M.; Sahin, H. Vanadium Dopant- and Strain-Dependent Magnetic Properties of Single-Layer $VI_3$. *Appl. Surf. Sci.* **2020**, *508*, 144937.

(640) Kong, T.; Stolze, K.; Timmons, E. I.; Tao, J.; Ni, D.; Guo, S.; Yang, Z.; Prozorov, R.; Cava, R. J. $VI_3$ — A New Layered Ferromagnetic Semiconductor. *Adv. Mater.* **2019**, *31*, 1808074.

(641) Gati, E.; Inagaki, Y.; Kong, T.; Cava, R. J.; Furukawa, Y.; Canfield, P. C.; Bud'ko, S. L. Multiple Ferromagnetic Transitions and Structural Distortion in the van der Waals Ferromagnet $VI_3$ at Ambient and Finite Pressures. *Phys. Rev. B* **2019**, *100*, 094408.

(642) Kong, T.; Guo, S.; Ni, D.; Cava, R. J. Crystal Structure and Magnetic Properties of the Layered van der Waals Compound $VBr_3$. *Phys. Rev. Materials* **2019**, *3*, 084419.

(643) Kulish, V. V.; Huang, W. Single-Layer Metal Halides $MX_2$ (X = Cl, Br, I): Stability and Tunable Magnetism from First Principles and Monte Carlo Simulations. *J. Mat. Chem. C* **2017**, *5*, 8734–8741.

(644) Chen, P.; Zou, J.-Y.; Liu, B.-G. Intrinsic Ferromagnetism and Quantum Anomalous Hall Effect in a $CoBr_2$ Monolayer. *Phys. Chem. Chem. Phys.* **2017**, *19*, 13432–13437.

(645) Ashton, M.; Gluhovic, D.; Sinnott, S. B.; Guo, J.; Stewart, D. A.; Hennig, R. G. Two-Dimensional Intrinsic Half-Metals With Large Spin Gaps. *Nano Lett.* **2017**, *17*, 5251–5257.

(646) Zhang, W. B.; Qu, Q.; Zhu, P.; Lam, C. H. Robust Intrinsic Ferromagnetism and Half Semiconductivity in Stable Two-Dimensional Single-Layer Chromium Trihalides. *J. Mater. Chem. C* **2015**, *3*, 12457–12468.

(647) McGuire, M. A. Crystal and Magnetic Structures in Layered, Transition Metal Dihalides and Trihalides. *Crystals* **2017**, *7*, 121.

(648) McGuire, M. A.; Dixit, H.; Cooper, V. R.; Sales, B. C. Coupling of Crystal Structure and Magnetism in the Layered, Ferromagnetic Insulator $CrI_3$. *Chem. Mater.* **2015**, *27*, 612–620.

(649) Mashhadi, S.; Weber, D.; Schoop, L. M.; Schulz, A.; Lotsch, B. V.; Burghard, M.; Kern, K. Electrical Transport Signature of the Magnetic Fluctuation-Structure Relation in α-$RuCl_3$ Nanoflakes. *Nano Lett.* **2018**, *18*, 3203–3208.

(650) Klein, D. R.; MacNeill, D.; Song, Q.; Larson, D. T.; Fang, S.; Xu, M.; Ribeiro, R. A.; Canfield, P. C.; Kaxiras, E.; Comin, R.; et al. Enhancement of Interlayer Exchange in an Ultrathin Two-Dimensional Magnet. *Nat. Phys.* **2019**, *15*, 1255–1260.

(651) Bengel, H.; Cantow, H.-J.; Magonov, S. N.; Hillebrecht, H.; Thiele, G.; Liang, W.; Whangbo, M.-H. Tip-Force Induced Surface Corrugation in Layered Transition Metal Trichlorides $MCl_3$ (M = Ru, Mo, Rh, Ir). *Surf. Sci.* **1995**, *343*, 95–103.

(652) Thiel, L.; Wang, Z.; Tschudin, M. A.; Rohner, D.; Gutierrez-Lezama, I.; Ubrig, N.; Gibertini, M.; Giannini, E.; Morpurgo, A. F.; Maletinsky, P. Probing Magnetism in 2D Materials at the Nanoscale with Single-Spin Microscopy. *Science* **2019**, *364*, 973–976.

(653) Shcherbakov, D.; Stepanov, P.; Weber, D.; Wang, Y.; Hu, J.; Zhu, Y.; Watanabe, K.; Taniguchi, T.; Mao, Z.; Windl, W.; et al. Raman Spectroscopy, Photocatalytic Degradation, and Stabilization of Atomically Thin Chromium Tri-Iodide. *Nano Lett.* **2018**, *18*, 4214–4219.

(654) Li, X.; Zhang, Z.; Zhang, H. High Throughput Study on Magnetic Ground States with Hubbard *U* Corrections in Transition Metal Dihalide Monolayers. *Nanoscale Adv.* **2020**, *2*, 495–501.

(655) Hu, H.; Tong, W.-Y.; Shen, Y.-H.; Wan, X.; Duan, C.-G. Concept of the Half-Valley-Metal and Quantum Anomalous Valley Hall Effect. *npj Computational Materials* **2020**, *6*, 129.

(656) Kong, X.; Li, L.; Liang, L.; Peeters, F. M.; Liu, X.-J. The Magnetic, Electronic, and Light-Induced Topological Properties in Two-Dimensional Hexagonal $FeX_2$ (X = Cl, Br, I) Monolayers. *Appl. Phys. Lett.* **2020**, *116*, 192404.

(657) Zhao, P.; Ma, Y.; Wang, H.; Huang, B.; Kou, L.; Dai, Y. Intrinsic Valley Polarization and Anomalous Valley Hall Effect in Single-Layer 2H-$FeCl_2$. **2020**, *arXiv:2003.04561*.

(658) Zhou, X.; Brzostowski, B.; Durajski, A.; Liu, M.; Xiang, J.; Jiang, T.; Wang, Z.; Chen, S.; Li, P.; Zhong, Z.; et al. Atomically Thin 1T-$FeCl_2$ Grown by Molecular-Beam Epitaxy. *J. Phys. Chem. C* **2020**, *124*, 9416–9423.

(659) Tracy, J. W.; Gregory, N. W.; Lingafelter, E. C. Crystal Structure of Chromium(II) Bromide. *Acta Cryst* **1962**, *15*, 672–674.

(660) Tracy, J. W.; Gregory, N. W.; Stewart, J. M.; Lingafelter, E. C. The Crystal Structure of Chromium(II) Iodide. *Acta Cryst* **1962**, *15*, 460–463.

(661) Li, P.; Wang, C.; Zhang, J.; Chen, S.; Guo, D.; Ji, W.; Zhong, D. Single-Layer $CrI_3$ Grown by Molecular Beam Epitaxy. *Science Bulletin* **2020**, *65*, 1064–1071.

(662) Peng, L.; Zhao, J.; Cai, M.; Hua, G.-Y.; Liu, Z.-Y.; Xia, H.-N.; Yuan, Y.; Zhang, W.-H.; Xu, G.; Zhao, L.-X.; et al. Mott Phase in a van der Waals Transition-Metal Halide at Single-Layer Limit. *Phys. Rev. Research* **2020**, *2*, 023264.

(663) Niel, M.; Cros, C.; Le Flem, G.; Pouchard, M.; Hagenmuller, P. Magnetic Behaviour of Vanadium +II in One- and Two-Dimensional Systems. *Physica B+C* **1977**, *86–88*, 702–704.

(664) Hirakawa, K.; Kadowaki, H.; Ubukoshi, K. Study of Frustration Effects in Two-Dimensional Triangular Lattice Antiferromagnets–Neutron Powder Diffraction Study of $VX_2$ , X≡Cl, Br and I. *J. Phys. Soc. Jpn.* **1983**, *52*, 1814–1824.

(665) Kadowaki, H.; Ubukoshi, K.; Hirakawa, K.; L. Martínez, J.; Shirane, G. Experimental Study of New Type Phase Transition in Triangular Lattice Antiferromagnet $VCl_2$. *J. Phys. Soc. Jpn.* **1987**, *56*, 4027–4039.

(666) Kadowaki, H.; Ubukoshi, K.; Hirakawa, K. Neutron Scattering Study of the Triangular-Lattice Antiferromagnet $VBr_2$. *J. Phys. Soc. Jpn.* **1985**, *54*, 363–373.

(667) Abdul Wasey, A. H. M.; Karmakar, D.; Das, G. P. Manifestation of Long-Range Ordered State in Layered $VX_2$ (X = Cl, Br, I) Systems. *J. Phys.: Condens. Matter* **2013**, *25*, 476001.

(668) Sato, T.; Kadowaki, H.; Iio, K. Successive Phase Transitions in the Hexagonal-Layered Heisenberg Antiferromagnets $MnX_2$ (X = Br, I). *Physica B: Condensed Matter* **1995**, *213–214*, 224–226.

(669) Park, J.; Ryu, S.; Han, M.; Oh, S.-J. Charge-Transfer Satellites in the 2 *p* Core-Level Photoelectron Spectra of Heavy-Transition-Metal Dihalides. *Phys. Rev. B* **1988**, *37*, 10867–10875.

(670) Gelard, J.; Fert, A. R.; Meriel, P.; Allain, Y. Magnetic Structure of $FeI_2$ by Neutron Diffraction Experiments. *Solid State Commun.* **1974**, *14*, 187–189.

(671) Katsumata, K.; Katori, H. A.; Kimura, S.; Narumi, Y.; Hagiwara, M.; Kindo, K. Phase Transition of a Triangular Lattice Ising Antiferromagnet $FeI_2$. *Phys. Rev. B* **2010**, *82*, 104402.

(672) Wilkinson, M. K.; Cable, J. W.; Wollan, E. O.; Koehler, W. C. Neutron Diffraction Investigations of the Magnetic Ordering in Fe $Br_2$, $CoBr_2$, $FeCl_2$, and $CoCl_2$. *Phys. Rev.* **1959**, *113*, 497–507.

(673) Starr, C.; Bitter, F.; Kaufmann, A. R. The Magnetic Properties of the Iron Group Anhydrous Chlorides at Low Temperatures. I. Experimental. *Phys. Rev.* **1940**, *58*, 977–983.

(674) Cable, J. W.; Wilkinson, M. K.; Wollan, E. O.; Koehler, W. C. Neutron Diffraction Investigation of the Magnetic Order in $MnI_2$. *Phys. Rev.* **1962**, *125*, 1860–1864.

(675) Utesov, O. I.; Syromyatnikov, A. V. Cascades of Phase Transitions in Spiral Magnets Caused by Dipolar Forces. *Phys. Rev. B* **2017**, *95*, 214420.

(676) Kurumaji, T.; Seki, S.; Ishiwata, S.; Murakawa, H.; Tokunaga, Y.; Kaneko, Y.; Tokura, Y. Magnetic-Field Induced Competition of Two Multiferroic Orders in a Triangular-Lattice Helimagnet $MnI_2$. *Phys. Rev. Lett.* **2011**, *106*, 167206.

(677) Kuindersma, S. R.; Sanchez, J. P.; Haas, C. Magnetic and Structural Investigations on $NiI_2$ and $CoI_2$. *Physica B+C* **1981**, *111*, 231–248.

(678) Mekata, M.; Kuriyama, H.; Ajiro, Y.; Mitsuda, S.; Yoshizawa, H. First-Order Magnetic Transition in $CoI_2$. *J. Magn. Magn. Mater.* **1992**, *104–107*, 859–860.

(679) Kurumaji, T.; Seki, S.; Ishiwata, S.; Murakawa, H.; Kaneko, Y.; Tokura, Y. Magnetoelectric Responses Induced by Domain Rearrangement and Spin Structural Change in Triangular-Lattice Helimagnets $NiI_2$ and $CoI_2$. *Phys. Rev. B* **2013**, *87*, 014429.

(680) Chen, A. L.; Yu, P. Y.; Taylor, R. D. Closure of the Charge-Transfer Energy Gap and Metallization of $NiI_2$ under Pressure. *Phys. Rev. Lett.* **1993**, *71*, 4011–4014.

(681) Adam, A.; Billerey, D.; Terrier, C.; Mainard, R.; Regnault, L. P.; Rossat-Mignod, J.; Mériel, P. Neutron Diffraction Study of the Commensurate and Incommensurate Magnetic Structures of $NiBr_2$. *Solid State Commun.* **1980**, *35*, 1–5.

(682) Day, P.; Dinsdale, A.; Krausz, E. R.; Robbins, D. J. Optical and Neutron Diffraction Study of the Magnetic Phase Diagram of $NiBr_2$. *J. Phys. C: Solid State Phys.* **1976**, *9*, 2481–2490.

(683) Day, P.; Ziebeck, K. R. A. Incommensurate Spin Structure in the Low-Temperature Magnetic Phase of $NiBr_2$. *J. Phys. C: Solid State Phys.* **1980**, *13*, L523–L525.

(684) Babu, S.; Prokeš, K.; Huang, Y. K.; Radu, F.; Mishra, S. K. Magnetic-Field-Induced Incommensurate to Collinear Spin Order Transition in $NiBr_2$. *J. Appl. Phys.* **2019**, *125*, 093902.

(685) Tokunaga, Y.; Okuyama, D.; Kurumaji, T.; Arima, T.; Nakao, H.; Murakami, Y.; Taguchi, Y.; Tokura, Y. Multiferroicity in $NiBr_2$ with Long-Wavelength Cycloidal Spin Structure on a Triangular Lattice. *Phys. Rev. B* **2011**, *84*, 060406.

(686) Torun, E.; Sahin, H.; Singh, S. K.; Peeters, F. M. Stable Half-Metallic Monolayers of $FeCl_2$. *Appl. Phys. Lett.* **2015**, *106*, 192404.

(687) Baenziger, N. C.; Rundle, R. E. The Structure of $TiCl_2$. *Acta Cryst* **1948**, *1*, 274.

(688) Lewis, J.; Machin, D. J.; Newnham, I. E.; Nyholm, R. S. The Magnetic Properties of Some Halides of Titanium and Zirconium. *J. Chem. Soc.* **1962**, 2036.

(689) Maule, C. H.; Tothill, J. N.; Strange, P.; Wilson, J. A. An Optical Investigation into the $3d^1$ and $3d^2$ Transition-Metal Halides and Oxyhalides, Compounds near to Delocalisation. *J. Phys. C: Solid State Phys.* **1988**, *21*, 2153–2179.

(690) Ehrlich, P.; Gutsche, W.; Seifert, H.-J. Darstellung und Kristallstruktur von Titandibromid. *Z. Anorg. Allg. Chem.* **1961**, *312*, 80–86.

(691) Klemm, W.; Grimm, L. Zur Kenntnis der Dihalogenide des Titans und Vanadins. *Z. Anorg. Allg. Chem.* **1942**, *249*, 198–208.

(692) Villadsen, J.; Hauge, S.; Jørgensen, P. M.; Refn, S. Note on the Crystal Structure of Vanadium Dichloride. *Acta Chem. Scand.* **1959**, *13*, 2146.

(693) Feng, Y.; Wu, X.; Han, J.; Gao, G. Robust Half-Metallicities and Perfect Spin Transport Properties in 2D Transition Metal Dichlorides. *J. Mater. Chem. C* **2018**, *6*, 4087–4094.

(694) Botana, A. S.; Norman, M. R. Electronic Structure and Magnetism of Transition Metal Dihalides: Bulk to Monolayer. *Phys. Rev. Mater.* **2019**, *3*, 044001.

(695) Kovaleva, E. A.; Melchakova, I.; Mikhaleva, N. S.; Tomilin, F. N.; Ovchinnikov, S. G.; Baek, W.; Pomogaev, V. A.; Avramov, P.; Kuzubov, A. A. The Role of Strong Electron Correlations in Determination of Band Structure and Charge Distribution of Transition Metal Dihalide Monolayers. *J. Phys. Chem. Solids* **2019**, *134*, 324–332.

(696) Kuindersma, S. R.; Haas, C.; Sanchez, J. P.; Al, R. Magnetic Structures and Properties of $VI_2$. *Solid State Commun.* **1979**, *30*, 403–408.

(697) Wiesler, D. G.; Suzuki, M.; Suzuki, I. S.; Rosov, N. Determination of Anomalous Superexchange in $MnCl_2$ and Its Graphite Intercalation Compound. *Phys. Rev. Lett.* **1995**, *75*, 942–945.

(698) Tornero, J. D.; Fayos, J. Single Crystal Structure Refinement of $MnCl_2$. *Z. Kristallogr. Cryst. Mater.***1990**, *192*, 147–148.

(699) Prayitno, T. B.; Ishii, F. First-Principles Study of Spiral Spin Density Waves in Monolayer $MnCl_2$ Using Generalized Bloch Theorem. *J. Phys. Soc. Jpn.* **2019**, *88*, 104705.

(700) Wollan, E. O.; Koehler, W. C.; Wilkinson, M. K. Neutron Diffraction Study of the Magnetic Properties of $MnBr_2$. *Phys. Rev.* **1958**, *110*, 638–646.

(701) Vettier, C.; Yelon, W. B. The Structure of $FeCl_2$ at High Pressures. *J. Phys. Chem. Solids* **1975**, *36*, 401–405.

(702) Zheng, H.; Han, H.; Zheng, J.; Yan, Y. Strain Tuned Magnetocrystalline Anisotropy in Ferromagnetic H-$FeCl_2$ Monolayer. *Solid State Commun.* **2018**, *271*, 66–70.

(703) Haberecht, J.; Borrmann, H.; Kniep, R. Refinement of the Crystal Structure of Iron Dibromide, $FeBr_2$. *Z. Krystallog. - New Crystal Structures* **2001**, *216*, 510.

(704) Lv, H. Y.; Lu, W. J.; Luo, X.; Zhu, X. B.; Sun, Y. P. Strain- and Carrier-Tunable Magnetic Properties of a Two-Dimensional Intrinsically Ferromagnetic Semiconductor: $CoBr_2$ Monolayer. *Phys. Rev. B* **2019**, *99*, 134416.

(705) Busey, R. H.; Giauque, W. F. The Heat Capacity of Anhydrous $NiCl_2$ from 15 to 300°K. The Antiferromagnetic Anomaly near 52°K. Entropy and Free Energy. *J. Am. Chem. Soc.* **1952**, *74*, 4443–4446.

(706) Ferrari, A.; Braibanti, A.; Bigliardi, G. Refinement of the Crystal Structure of $NiCl_2$ and of Unit-Cell Parameters of Some Anhydrous Chlorides of Divalent Metals. *Acta Cryst* **1963**, *16*, 846–847.

(707) Lu, M.; Yao, Q. S.; Xiao, C. Y.; Huang, C. X.; Kan, E. J. Mechanical, Electronic, and Magnetic Properties of $NIX_2$ (X = Cl, Br, I) Layers. *ACS Omega* **2019**, *4*, 5714–5721.

(708) Mushtaq, M.; Zhou, Y.; Xiang, X. $NiX_2$ (X = Cl and Br) Sheets as Promising Spin Materials: A First-Principles Study. *RSC Adv.* **2017**, *7*, 22541–22547.

(709) Amoroso, D.; Barone, P.; Picozzi, S. Spontaneous Skyrmionic Lattice from Anisotropic Symmetric Exchange in a Ni-Halide Monolayer. *Nat. Commun.* **2020**, *11*, 5784.

(710) Nasser, J. A.; Kiat, J. M.; Gabilly, R. X-Ray Investigation of Magnetostriction in $NiBr_2$. *Solid State Commun.* **1992**, *82*, 49–54.

(711) Stavropoulos, P. P.; Pereira, D.; Kee, H.-Y. Microscopic Mechanism for Higher-Spin Kitaev Model. *Phys. Rev. Lett.* **2019**, *123*, 037203.

(712) Schneider, M.; Kuske, P.; Lutz, H. D. Novel High-Temperature Polymorphs of $MgBr_2$ and $MnBr_2$ - Limits of Powder Diffraction for Structure Determination. *Acta Crystallogr. B Struct. Sci.* **1992**, *48*, 761–763.

(713) Liu, H.; Wang, X.; Wu, J.; Chen, Y.; Wan, J.; Wen, R.; Yang, J.; Liu, Y.; Song, Z.; Xie, L. Vapor Deposition of Magnetic Van der Waals $NiI_2$ Crystals. *ACS Nano* **2020**, *14*, 10544–10551.

(714) Rozenberg, G. Kh.; Pasternak, M. P.; Gorodetsky, P.; Xu, W. M.; Dubrovinsky, L. S.; Le Bihan, T.; Taylor, R. D. Pressure-Induced Structural, Electronic, and Magnetic Phase Transitions in $FeCl_2$ Studied by X-Ray Diffraction and Resistivity Measurements. *Phys. Rev. B* **2009**, *79*, 214105.

(715) Barreda-Argüeso, J. A.; Nataf, L.; Aguado, F.; Hernández, I.; González, J.; Otero-de-la-Roza, A.; Luaña, V.; Jia, Y.; Jin, C.; Kim, B.; et al. Pressure-Induced Spin Transition and Site-Selective Metallization in $CoCl_2$. *Sci Rep* **2019**, *9*, 5448.

(716) Pasternak, M. P.; Taylor, R. D.; Chen, A.; Meade, C.; Falicov, L. M.; Giesekus, A.; Jeanloz, R.; Yu, P. Y. Pressure-Induced Metallization and the Collapse of the Magnetic State in the Antiferromagnetic Insulator $NiI_2$. *Phys. Rev. Lett.* **1990**, *65*, 790–793.

(717) Tang, J.; Davis, M. D.; O'Connor, C. J.; Wu, B. Doping Studies on the Origin of the Band Gaps in $NiI_{2-x}Br_x$. *Physica B: Condensed Matter* **1994**, *199–200*, 637–639.

(718) Rai, B. K.; Christianson, A. D.; Mandrus, D.; May, A. F. Influence of Cobalt Substitution on the Magnetism of $NiBr_2$. *Phys. Rev. Materials* **2019**, *3*, 034005.

(719) Tian, S.; Zhang, J. F.; Li, C.; Ying, T.; Li, S.; Zhang, X.; Liu, K.; Lei, H. Ferromagnetic van der Waals Crystal $VI_3$. *J. Am. Chem. Soc.* **2019**, *141*, 5326–5333.

(720) Son, S.; Coak, M. J.; Lee, N.; Kim, J.; Kim, T. Y.; Hamidov, H.; Cho, H.; Liu, C.; Jarvis, D. M.; Brown, P. A. C.; et al. Bulk Properties of the van der Waals Hard Ferromagnet $VI_3$. *Phys. Rev. B* **2019**, *99*, 041402.

(721) Lyu, B.; Gao, Y.; Zhang, Y.; Wang, L.; Wu, X.; Chen, Y.; Zhang, J.; Li, G.; Huang, Q.; Zhang, N.; et al. Probing the Ferromagnetism and Spin Wave Gap in $VI_3$ by Helicity-Resolved Raman Spectroscopy. *Nano Lett.* **2020**, *20*, 6024–6031.

(722) Wang, Y.-M.; Tian, S.-J.; Li, C.-H.; Jin, F.; Ji, J.-T.; Lei, H.-C.; Zhang, Q.-M. Raman Scattering Study of Two-Dimensional Magnetic van der Waals Compound $VI_3$. *Chinese Phys. B* **2020**, *29*, 056301.

(723) Doležal, P.; Kratochvílová, M.; Holý, V.; Čermák, P.; Sechovský, V.; Dušek, M.; Míšek, M.; Chakraborty, T.; Noda, Y.; Son, S.; et al. Crystal Structures and Phase Transitions of the van der Waals Ferromagnet $VI_3$. *Phys. Rev. Materials* **2019**, *3*, 121401.

(724) Liu, Y.; Abeykoon, M.; Petrovic, C. Critical Behavior and Magnetocaloric Effect in $VI_3$. *Phys. Rev. Research* **2020**, *2*, 013013.

(725) Yan, J.; Luo, X.; Chen, F. C.; Gao, J. J.; Jiang, Z. Z.; Zhao, G. C.; Sun, Y.; Lv, H. Y.; Tian, S. J.; Yin, Q. W.; et al. Anisotropic Magnetic Entropy Change in the Hard Ferromagnetic Semiconductor $VI_3$. *Phys. Rev. B* **2019**, *100*, 094402.

(726) Yang, K.; Fan, F.; Wang, H.; Khomskii, D. I.; Wu, H. $VI_3$: A Two-Dimensional Ising Ferromagnet. *Phys. Rev. B* **2020**, *101*, 100402.

(727) Broadway, D. A.; Scholten, S. C.; Tan, C.; Dontschuk, N.; Lillie, S. E.; Johnson, B. C.; Zheng, G.; Wang, Z.; Oganov, A. R.; Tian, S.; et al. Imaging Domain Reversal in an Ultrathin van der Waals Ferromagnet. *Adv. Mater.* **2020**, *32*, 2003314.

(728) Wang, Y.-P.; Long, M.-Q. Electronic and Magnetic Properties of van der Waals Ferromagnetic Semiconductor $VI_3$. *Phys. Rev. B* **2020**, *101*, 024411.

(729) Long, C.; Wang, T.; Jin, H.; Wang, H.; Dai, Y. Stacking-Independent Ferromagnetism in Bilayer $VI_3$ with Half-Metallic Characteristic. *J. Phys. Chem. Lett.* **2020**, *11*, 2158–2164.

(730) He, J.; Ma, S.; Lyu, P.; Nachtigall, P. Unusual Dirac Half-Metallicity with Intrinsic Ferromagnetism in Vanadium Trihalide Monolayers. *J. Mater. Chem. C* **2016**, *4*, 2518–2526.

(731) Li, Y.; Liu, Y.; Wang, C.; Wang, J.; Xu, Y.; Duan, W. Electrically Tunable Valleytronics in Quantum Anomalous Hall Insulating Transition Metal Trihalides. *Phys. Rev. B* **2018**, *98*, 201407.

(732) Subhan, F.; Hong, J. Magnetic Anisotropy and Curie Temperature of Two-Dimensional $VI_3$ Monolayer. *J. Phys.: Condens. Matter* **2020**, *32*, 245803.

(733) Kazim, S.; Ali, M.; Palleschi, S.; D'Olimpio, G.; Mastrippolito, D.; Politano, A.; Gunnella, R.; Di Cicco, A.; Renzelli, M.; Moccia, G.; et al. Mechanical Exfoliation and Layer Number Identification of Single Crystal Monoclinic $CrCl_3$. *Nanotechnology* **2020**, *31*, 395706.

(734) Kuhlow, B. Magnetic Ordering in $CrCl_3$ at the Phase Transition. *Phys. Stat. Sol. A* **1982**, *72*, 161–168.

(735) McGuire, M. A.; Clark, G.; Santosh, K. C.; Chance, W. M.; Jellison, G. E.; Cooper, V. R.; Xu, X. D.; Sales, B. C. Magnetic Behavior and Spin-Lattice Coupling in Cleavable van der Waals Layered $CrCl_3$ Crystals. *Phys. Rev. Mater.* **2017**, *1*, 014001.

(736) Cable, J. W.; Wilkinson, M. K.; Wollan, E. O. Neutron Diffraction Investigation of Antiferromagnetism in $CrCl_3$. *J. Phys. Chem. Solids* **1961**, *19*, 29–34.

(737) Tsubokawa, I. On the Magnetic Properties of a $CrBr_3$ Single Crystal. *J. Phys. Soc. Jpn.* **1960**, *15*, 1664–1668.

(738) Dillon, J. F.; Olson, C. E. Magnetization, Resonance, and Optical Properties of the Ferromagnet $CrI_3$. *J. Appl. Phys.* **1965**, *36*, 1259–1260.

(739) Chen, L.; Chung, J.-H.; Chen, T.; Duan, C.; Schneidewind, A.; Radelytskyi, I.; Voneshen, D. J.; Ewings, R. A.; Stone, M. B.; Kolesnikov, A. I.; et al. Magnetic Anisotropy in Ferromagnetic $CrI_3$. *Phys. Rev. B* **2020**, *101*, 134418.

(740) Kim, M.; Kumaravadivel, P.; Birkbeck, J.; Kuang, W.; Xu, S. G.; Hopkinson, D. G.; Knolle, J.; McClarty, P. A.; Berdyugin, A. I.; Ben Shalom, M.; et al. Micromagnetometry of Two-Dimensional Ferromagnets. *Nat. Electron.* **2019**, *2*, 457–463.

(741) Zhang, Z.; Shang, J.; Jiang, C.; Rasmita, A.; Gao, W.; Yu, T. Direct Photoluminescence Probing of Ferromagnetism in Monolayer Two-Dimensional $CrBr_3$. *Nano Lett.* **2019**, *19*, 3138–3142.

(742) Ghazaryan, D.; Greenaway, M. T.; Wang, Z.; Guarochico-Moreira, V. H.; Vera-Marun, I. J.; Yin, J.; Liao, Y.; Morozov, S. V.; Kristanovski, O.; Lichtenstein, A. I.; et al. Magnon-Assisted Tunnelling in van der Waals Heterostructures Based on $CrBr_3$. *Nat. Electron.* **2018**, *1*, 344–349.

(743) Huang, B.; Clark, G.; Navarro-Moratalla, E.; Klein, D. R.; Cheng, R.; Seyler, K. L.; Zhong, D.; Schmidgall, E.; McGuire, M. A.; Cobden, D. H.; et al. Layer-Dependent Ferromagnetism in a van der Waals Crystal down to the Monolayer Limit. *Nature* **2017**, *546*, 270–273.

(744) Seyler, K. L.; Zhong, D.; Klein, D. R.; Gao, S.; Zhang, X.; Huang, B.; Navarro-Moratalla, E.; Yang, L.; Cobden, D. H.; McGuire, M. A.; et al. Ligand-Field Helical Luminescence in a 2D Ferromagnetic Insulator. *Nature Physics* **2017**, *14*, 277–281.

(745) Huang, B.; Cenker, J.; Zhang, X.; Ray, E. L.; Song, T.; Taniguchi, T.; Watanabe, K.; McGuire, M. A.; Xiao, D.; Xu, X. Tuning Inelastic Light Scattering via Symmetry Control in the Two-Dimensional Magnet $CrI_3$. *Nat. Nanotechnol.* **2020**, *15*, 212-216.

(746) Cenker, J.; Huang, B.; Suri, N.; Thijssen, P.; Miller, A.; Song, T.; Taniguchi, T.; Watanabe, K.; McGuire, M. A.; Xiao, D.; et al. Direct Observation of Two-Dimensional Magnons in Atomically Thin $CrI_3$. *Nat. Phys.* **2020**, *17*, 20-25.

(747) Ubrig, N.; Wang, Z.; Teyssier, J.; Taniguchi, T.; Watanabe, K.; Giannini, E.; Morpurgo, A. F.; Gibertini, M. Low-Temperature Monoclinic Layer Stacking in Atomically Thin $CrI_3$ Crystals. *2D Mater.* **2019**, *7*, 015007.

(748) Sun, Z.; Yi, Y.; Song, T.; Clark, G.; Huang, B.; Shan, Y.; Wu, S.; Huang, D.; Gao, C.; Chen, Z.; et al. Giant Nonreciprocal Second-Harmonic Generation from Antiferromagnetic Bilayer $CrI_3$. *Nature* **2019**, *572*, 497–501.

(749) Sivadas, N.; Okamoto, S.; Xu, X.; Fennie, C. J.; Xiao, D. Stacking-Dependent Magnetism in Bilayer $CrI_3$. *Nano Lett.* **2018**, *18*, 7658–7664.

(750) Soriano, D.; Cardoso, C.; Fernández-Rossier, J. Interplay between Interlayer Exchange and Stacking in $CrI_3$ Bilayers. *Solid State Commun.* **2019**, *299*, 113662.

(751) Jang, S. W.; Jeong, M. Y.; Yoon, H.; Ryee, S.; Han, M. J. Microscopic Understanding of Magnetic Interactions in Bilayer $CrI_3$. *Phys. Rev. Mater.* **2019**, *3*, 031001.

(752) Jiang, P.; Wang, C.; Chen, D.; Zhong, Z.; Yuan, Z.; Lu, Z.-Y.; Ji, W. Stacking Tunable Interlayer Magnetism in Bilayer $CrI_3$. *Phys. Rev. B* **2019**, *99*, 144401.

(753) Chen, W.; Sun, Z.; Wang, Z.; Gu, L.; Xu, X.; Wu, S.; Gao, C. Direct Observation of van der Waals Stacking-Dependent Interlayer Magnetism. *Science* **2019**, *366*, 983–987.

(754) Wang, Z.; Gibertini, M.; Dumcenco, D.; Taniguchi, T.; Watanabe, K.; Giannini, E.; Morpurgo, A. F. Determining the Phase Diagram of Atomically Thin Layered Antiferromagnet $CrCl_3$. *Nat. Nanotechnol.* **2019**, *14*, 1116–1122.

(755) Cai, X.; Song, T.; Wilson, N. P.; Clark, G.; He, M.; Zhang, X.; Taniguchi, T.; Watanabe, K.; Yao, W.; Xiao, D.; et al. Atomically Thin $CrCl_3$: An In-Plane Layered Antiferromagnetic Insulator. *Nano Lett.* **2019**, *19*, 3993–3998.

(756) Kim, H. H.; Yang, B.; Li, S.; Jiang, S.; Jin, C.; Tao, Z.; Nichols, G.; Sfigakis, F.; Zhong, S.; Li, C.; et al. Evolution of Interlayer and Intralayer Magnetism in Three Atomically Thin Chromium Trihalides. *Proc. Natl. Acad. Sci. USA* **2019**, *116*, 11131–11136.

(757) Wang, Z.; Gutiérrez-Lezama, I.; Ubrig, N.; Kroner, M.; Gibertini, M.; Taniguchi, T.; Watanabe, K.; Imamoğlu, A.; Giannini, E.; Morpurgo, A. F. Very Large Tunneling Magnetoresistance in Layered Magnetic Semiconductor $CrI_3$. *Nat. Commun.* **2018**, *9*, 2516.

(758) Klein, D. R.; MacNeill, D.; Lado, J. L.; Soriano, D.; Navarro-Moratalla, E.; Watanabe, K.; Taniguchi, T.; Manni, S.; Canfield, P.; Fernández-Rossier, J.; et al. Probing Magnetism in 2D van der Waals Crystalline Insulators via Electron Tunneling. *Science* **2018**, *360*, 1218–1222.

(759) Song, T.; Cai, X.; Tu, M. W.; Zhang, X.; Huang, B.; Wilson, N. P.; Seyler, K. L.; Zhu, L.; Taniguchi, T.; Watanabe, K.; et al. Giant Tunneling Magnetoresistance in Spin-Filter van der Waals Heterostructures. *Science* **2018**, *360*, 1214–1218.

(760) Kim, H. H.; Yang, B.; Tian, S.; Li, C.; Miao, G.-X.; Lei, H.; Tsen, A. W. Tailored Tunnel Magnetoresistance Response in Three Ultrathin Chromium Trihalides. *Nano Lett.* **2019**, *19*, 5739–5745.

(761) Kim, H. H.; Jiang, S.; Yang, B.; Zhong, S.; Tian, S.; Li, C.; Lei, H.; Shan, J.; Mak, K. F.; Tsen, A. W. Magneto-Memristive Switching in a 2D Layer Antiferromagnet. *Adv. Mater.* **2020**, *32*, 1905433.

(762) Jiang, S.; Li, L.; Wang, Z.; Shan, J.; Mak, K. F. Spin Tunnel Field-Effect Transistors Based on Two-Dimensional van der Waals Heterostructures. *Nat. Electron.* **2019**, *2*, 159–163.

(763) Jin, W.; Kim, H. H.; Ye, Z.; Li, S.; Rezaie, P.; Diaz, F.; Siddiq, S.; Wauer, E.; Yang, B.; Li, C.; et al. Raman Fingerprint of Two Terahertz Spin Wave Branches in a Two-Dimensional Honeycomb Ising Ferromagnet. *Nat. Commun.* **2018**, *9*, 5122.

(764) Jiang, S.; Li, L.; Wang, Z.; Mak, K. F.; Shan, J. Controlling Magnetism in 2D $CrI_3$ by Electrostatic Doping. *Nat. Nanotechnol.* **2018**, *13*, 549–553.

(765) Soriano, D.; Katsnelson, M. I. Magnetic Polaron and Antiferromagnetic-Ferromagnetic Transition in Doped Bilayer $CrI_3$. *Phys. Rev. B* **2020**, *101*, 041402.

(766) Huang, B.; Clark, G.; Klein, D. R.; MacNeill, D.; Navarro-Moratalla, E.; Seyler, K. L.; Wilson, N.; McGuire, M. A.; Cobden, D. H.; Xiao, D.; et al. Electrical Control of 2D Magnetism in Bilayer $CrI_3$. *Nat. Nanotechnol.* **2018**, *13*, 544–548.

(767) Jiang, S.; Shan, J.; Mak, K. F. Electric-Field Switching of Two-Dimensional van der Waals Magnets. *Nat. Mater.* **2018**, *17*, 406–410.

(768) Suárez Morell, E.; León, A.; Miwa, R. H.; Vargas, P. Control of Magnetism in Bilayer $CrI_3$ by an External Electric Field. *2D Mater.* **2019**, *6*, 025020.

(769) Xu, R.; Zou, X. Electric Field-Modulated Magnetic Phase Transition in van der Waals $CrI_3$ Bilayers. *J. Phys. Chem. Lett.* **2020**, *11*, 3152–3158.

(770) Stroganov, E. V.; Ovchinnikov, K. V. Crystal Structure of Ruthenium Trichloride. *Vestn. Leningr. Univ. Ser. Fiz. i Khim.* **1957**, *22*, 152.

(771) Banerjee, A.; Bridges, C. A.; Yan, J. Q.; Aczel, A. A.; Li, L.; Stone, M. B.; Granroth, G. E.; Lumsden, M. D.; Yiu, Y.; Knolle, J.; et al. Proximate Kitaev Quantum Spin Liquid Behaviour in a Honeycomb Magnet. *Nat. Mater*. **2016**, *15*, 733–740.

(772) Gronke, M.; Schmidt, P.; Valldor, M.; Oswald, S.; Wolf, D.; Lubk, A.; Buchner, B.; Hampel, S. Chemical Vapor Growth and Delamination of Alpha-$RuCl_3$ Nanosheets down to the Monolayer Limit. *Nanoscale* **2018**, *10*, 19014–19022.

(773) Brodersen, K.; Moers, F.; Schnering, H. G. Zur Struktur des Iridium(III)- und des Ruthenium(III)-chlorids. *Naturwissenschaften* **1965**, *52*, 205–206.

(774) Cao, H. B.; Banerjee, A.; Yan, J.-Q.; Bridges, C. A.; Lumsden, M. D.; Mandrus, D. G.; Tennant, D. A.; Chakoumakos, B. C.; Nagler, S. E. Low-Temperature Crystal and Magnetic Structure of $\alpha$−$RuCl_3$. *Phys. Rev. B* **2016**, *93*, 134423.

(775) Reschke, S.; Mayr, F.; Wang, Z.; Do, S.-H.; Choi, K.-Y.; Loidl, A. Electronic and Phonon Excitations in α−$RuCl_3$. *Phys. Rev. B* **2017**, *96*, 165120.

(776) Reschke, S.; Mayr, F.; Widmann, S.; von Nidda, H.-A. K.; Tsurkan, V.; Eremin, M. V.; Do, S.-H.; Choi, K.-Y.; Wang, Z.; Loidl, A. Sub-Gap Optical Response in the Kitaev Spin-Liquid Candidate $\alpha$-$RuCl_3$. *J. Phys.: Condens. Matter* **2018**, *30*, 475604.

(777) Park, S.-Y.; Do, S.-H.; Choi, K.-Y.; Jang, D.; Jang, T.-H.; Schefer, J.; Wu, C.-M.; Gardner, J. S.; Park, J. M. S.; Park, J.-H.; et al. Emergence of the Isotropic Kitaev Honeycomb Lattice with Two-Dimensional Ising Universality in α-$RuCl_3$. **2016**, *arXiv:1609.05690 [cond-mat]*.

(778) Dai, Z.; Yu, J.-X.; Zhou, B.; Tenney, S.; Lampen-Kelley, P.; Yan, J.; Mandrus, D. G.; Henriksen, E.; Zang, J.; Pohl, K.; et al. Crystal Structure Reconstruction in the Surface Monolayer of the Quantum Spin Liquid Candidate α-$RuCl_3$. *2D Mater.* **2020**. *7*, 035004.

(779) Johnson, R. D.; Williams, S. C.; Haghighirad, A. A.; Singleton, J.; Zapf, V.; Manuel, P.; Mazin, I. I.; Li, Y.; Jeschke, H. O.; Valentí, R.; et al. Monoclinic Crystal Structure of α−$RuCl_3$ and the Zigzag Antiferromagnetic Ground State. *Phys. Rev. B* **2015**, *92*, 235119.

(780) Kitaev, A. Anyons in an Exactly Solved Model and Beyond. *Annals of Physics* **2006**, *321*, 2–111.

(781) Kim, H.-S.; V., V. S.; Catuneanu, A.; Kee, H.-Y. Kitaev Magnetism in Honeycomb $RuCl_3$ with Intermediate Spin-Orbit Coupling. *Phys. Rev. B* **2015**, *91*, 241110.

(782) Takagi, H.; Takayama, T.; Jackeli, G.; Khaliullin, G.; Nagler, S. E. Concept and Realization of Kitaev Quantum Spin Liquids. *Nat. Rev. Phys.* **2019**, *1*, 264–280.

(783) Banerjee, A.; Yan, J.; Knolle, J.; Bridges, C. A.; Stone, M. B.; Lumsden, M. D.; Mandrus, D. G.; Tennant, D. A.; Moessner, R.; Nagler, S. E Neutron Scattering in the Proximate Quantum Spin Liquid Alpha-$RuCl_3$. *Science* **2017**, *356*, 1055–1059.

(784) Do, S.-H.; Park, S.-Y.; Yoshitake, J.; Nasu, J.; Motome, Y.; Kwon, Y. S.; Adroja, D. T.; Voneshen, D. J.; Kim, K.; Jang, T. H.; et al. Majorana Fermions in the Kitaev Quantum Spin System α-$RuCl_3$. *Nature Physics* **2017**, *13*, 1079–1084.

(785) Janša, N.; Zorko, A.; Gomilšek, M.; Pregelj, M.; Krämer, K. W.; Biner, D.; Biffin, A.; Rüegg, C.; Klanjšek, M. Observation of Two Types of Fractional Excitation in the Kitaev Honeycomb Magnet. *Nature Phys.* **2018**, *14*, 786–790.

(786) Kasahara, Y.; Ohnishi, T.; Mizukami, Y.; Tanaka, O.; Ma, S.; Sugii, K.; Kurita, N.; Tanaka, H.; Nasu, J.; Motome, Y.; et al. Majorana Quantization and Half-Integer Thermal Quantum Hall Effect in a Kitaev Spin Liquid. *Nature* **2018**, *559*, 227–231.

(787) Yokoi, T.; Ma, S.; Kasahara, Y.; Kasahara, S.; Shibauchi, T.; Kurita, N.; Tanaka, H.; Nasu, J.; Motome, Y.; Hickey, C.; et al. Half-Integer Quantized Anomalous Thermal Hall Effect in the Kitaev Material α-$RuCl_3$. **2020**, *arXiv:2001.01899 [cond-mat]*.

(788) Balz, C.; Lampen-Kelley, P.; Banerjee, A.; Yan, J.; Lu, Z.; Hu, X.; Yadav, S. M.; Takano, Y.; Liu, Y.; Tennant, D. A.; et al. Finite Field Regime for a Quantum Spin Liquid in α−$RuCl_3$. *Phys. Rev. B* **2019**, *100*, 060405.

(789) Gass, S.; Cônsoli, P. M.; Kocsis, V.; Corredor, L. T.; Lampen-Kelley, P.; Mandrus, D. G.; Nagler, S. E.; Janssen, L.; Vojta, M.; Büchner, B.; et al. Field-Induced Transitions in the

Kitaev Material α−$RuCl_3$ Probed by Thermal Expansion and Magnetostriction. *Phys. Rev. B* **2020**, *101*, 245158.

(790) Du, L.; Huang, Y.; Wang, Y.; Wang, Q.; Yang, R.; Tang, J.; Liao, M.; Shi, D.; Shi, Y.; Zhou, X.; et al. 2D Proximate Quantum Spin Liquid State in Atomic-Thin α-$RuCl_3$. *2D Materials* **2018**, *6*, 015014.

(791) Lin, D.; Ran, K.; Zheng, H.; Xu, J.; Gao, L.; Wen, J.; Yu, S.-L.; Li, J.-X.; Xi, X. Anisotropic Scattering Continuum Induced by Crystal Symmetry Reduction in Atomically Thin α–$RuCl_3$. *Phys. Rev. B* **2020**, *101*, 045419.

(792) Zhou, B.; Wang, Y.; Osterhoudt, G. B.; Lampen-Kelley, P.; Mandrus, D.; He, R.; Burch, K. S.; Henriksen, E. A. Possible Structural Transformation and Enhanced Magnetic Fluctuations in Exfoliated α-$RuCl_3$. *J. Phys. Chem. Solids* **2019**, *128*, 291–295.

(793) Ziatdinov, M.; Banerjee, A.; Maksov, A.; Berlijn, T.; Zhou, W.; Cao, H. B.; Yan, J.-Q.; Bridges, C. A.; Mandrus, D. G.; Nagler, S. E.; et al. Atomic-Scale Observation of Structural and Electronic Orders in the Layered Compound α-$RuCl_3$. *Nat. Commun.* **2016**, *7*, 13774.

(794) Mashhadi, S.; Kim, Y.; Kim, J.; Weber, D.; Taniguchi, T.; Watanabe, K.; Park, N.; Lotsch, B.; Smet, J. H.; Burghard, M.; et al. Spin-Split Band Hybridization in Graphene Proximitized with α-$RuCl_3$ Nanosheets. *Nano Lett.* **2019**, *19*, 4659–4665.

(795) Zhou, B.; Balgley, J.; Lampen-Kelley, P.; Yan, J.-Q.; Mandrus, D. G.; Henriksen, E. A. Evidence for Charge Transfer and Proximate Magnetism in Graphene–α−$RuCl_3$ Heterostructures. *Phys. Rev. B* **2019**, *100*, 165426.

(796) Gerber, E.; Yao, Y.; Arias, T. A.; Kim, E.-A. *Ab Initio* Mismatched Interface Theory of Graphene on α−$RuCl_3$: Doping and Magnetism. *Phys. Rev. Lett.* **2020**, *124*, 106804.

(797) Biswas, S.; Li, Y.; Winter, S. M.; Knolle, J.; Valentí, R. Electronic Properties of α−$RuCl_3$ in Proximity to Graphene. *Phys. Rev. Lett.* **2019**, *123*, 237201.

(798) Aasen, D.; Mong, R. S. K.; Hunt, B. M.; Mandrus, D.; Alicea, J. Electrical Probes of the Non-Abelian Spin Liquid in Kitaev Materials. *Phys. Rev. X* **2020**, *10*, 031014.

(799) Natta, G.; Corradini, P.; Allegra, G. The Different Crystalline Modifications of $TiCl_3$, a Catalyst Component for the Polymerization of α-Olefins. I: α-, β-, γ-$TiCl_3$. II: δ-$TiCl_3$. *J. Polym. Sci.* **1961**, *51*, 399–410.

(800) Troyanov, S. I.; Snigireva, E. M.; Rybakov, V. B. An X-Ray Structural Investigation of the Phase Transition in α-$TiCl_3$. *Russ. J. Inorg. Chem.* **1991**, *36*, 1117–1123.

(801) Troyanov, S. I.; Snigireva, E. M. Crystal Structures of Transition-Metal Halides $TiCl_4$, α-$TiCl_3$, $WCl_4$, and $TiI_2$. *Russ. J. Inorg. Chem.* **2000**, *45*, 580–585.

(802) Snigireva, E. M.; Pisarevskii, A. P.; Yanovskii, A. I.; Struchkov, Y. T.; Troyanov, S. I. Crystal Structure of Low-Temperature Modification of α-$TiBr_3$. *Russ. J. Inorg. Chem.* **1994**, *39*, 374–377.

(803) Klemm, W.; Krose, E. Magnetochemische Untersuchungen XLIX. Das magnetische Verhalten der Titantrihalogenide. *Z. Anorg. Chem.* **1947**, *253*, 209–217.

(804) Ogawa, S. Magnetic Transition in $TiCl_3$. *J. Phys. Soc. Jpn.* **1960**, *15*, 1901.

(805) Emeis, C. A.; Reinders, F. J.; Drent, E. Far-Infrared Investigation of the Phase Transition at 217 K in Layer-Structured $TiCl_3$. *Solid State Commun.* **1975**, *16*, 239–242.

(806) Cavallone, F.; Pollini, I.; Spinolo, G. Electrical Properties of α-$TiCl_3$ Crystals. *Lett. Nuovo Cimento* **1970**, *4*, 764–766.

(807) Cavallone, F.; Pollini, I.; Spinolo, G. Optical Properties of α-$TiCl_3$ at the Magnetic Transition Temperature. *Phys. Stat. Sol. B* **1971**, *45*, 405–410.

(808) Sementa, L.; D'Amore, M.; Barone, V.; Busico, V.; Causa, M. A Quantum Mechanical Study of $TiCl_3$ α, β and γ Crystal Phases: Geometry, Electronic Structure and Magnetism. *Phys. Chem. Chem. Phys.* **2009**, *11*, 11264–11275.

(809) Zhou, Y.; Lu, H.; Zu, X.; Gao, F. Evidencing the Existence of Exciting Half-Metallicity in Two-Dimensional $TiCl_3$ and $VCl_3$ Sheets. *Sci. Rep.* **2016**, *6*, 19407.

(810) Geng, J.; Chan, I. N.; Ai, H.; Lo, K. H.; Kawazoe, Y.; Ng, K. W.; Pan, H. Magnetic and Electronic Properties of 2D $TiX_3$ (X = F, Cl, Br and I). *Phys. Chem. Chem. Phys.* **2020**, *22*, 17632–17638.

(811) Hashimoto, S.; Forster, K.; Moss, S. C. Structure Refinement of an $FeCl_3$ Crystal Using a Thin Plate Sample. *J. Appl. Crystallogr.* **1989**, *22*, 173–180.

(812) Troyanov, S. Crystal Structure of $FeCl_3$ Polytypes. *Russian J. Inorg. Chem.* **1993**, *38*, 1821–1824.

(813) Jones, E. R.; Morton, O. B.; Cathey, L.; Auel, T.; Amma, E. L. Low-Temperature Magnetic Susceptibility of $FeCl_3$. *J. Chem. Phys.* **1969**, *50*, 4755–4757.

(814) Stampfel, J. P.; Oosterhuis, W. T.; Window, B.; Barros, F. deS. Mössbauer-Effect Measurements in Antiferromagnetic $FeCl_3$. *Phys. Rev. B* **1973**, *8*, 4371–4382.

(815) Cable, J. W.; Wilkinson, M. K.; Wollan, E. O.; Koehler, W. C. Neutron-Diffraction Study of Antiferromagnetic $FeCl_3$. *Phys. Rev.* **1962**, *127*, 714–717.

(816) Johnson, P. B.; Friedberg, S. A.; Rayne, J. A. Field-Induced Magnetic Phase Transitions in $FeCl_3$. *J. Appl. Phys.* **1981**, *52*, 1932–1934.

(817) Oosterhuis, W. T.; Window, B.; Spartalian, K. Sublattice Magnetization in $FeBr_3$ below the Critical Region. *Phys. Rev. B* **1974**, *10*, 4616–4620.

(818) Li, P. Prediction of Intrinsic Two Dimensional Ferromagnetism Realized Quantum Anomalous Hall Effect. *Phys. Chem. Chem. Phys.* **2019**, *21*, 6712–6717.

(819) Zhang, S.-H.; Liu, B.-G. Intrinsic 2D Ferromagnetism, Quantum Anomalous Hall Conductivity, and Fully-Spin-Polarized Edge States of $FeBr_3$ Monolayer. **2017**, *arXiv:1706.08943 [cond-mat]*.

(820) Liu, P.; Luo, X.; Cheng, Y.; Wang, X.-W.; Wang, W.; Liu, H.; Cho, K.; Wang, W.-H.; Lu, F. Physical Realization of 2D Spin Liquid State by *Ab Initio* Design and Strain Engineering in $FeX_3$. *J. Phys.: Condens. Matter* **2018**, *30*, 325801.

(821) Hillebrecht, H.; Schmidt, P. J.; Rotter, H. W.; Thiele, G.; Zönnchen, P.; Bengel, H.; Cantow, H.-J.; Magonov, S. N.; Whangbo, M.-H. Structural and Scanning Microscopy Studies of Layered Compounds $MCl_3$ (M = Mo, Ru, Cr) and $MOCl_2$ (M = V, Nb, Mo, Ru, Os). *J. Alloys Compd.* **1997**, *246*, 70–79.

(822) Schäfer, H.; Schnering, H.-G. V.; Tillack, J.; Kuhnen, F.; Wöhrle, H.; Baumann, H. Neue Untersuchungen über die Chloride des Molybdäns. *Z. Anorg. Allg. Chem.* **1967**, *353*, 281–310.

(823) McGuire, M. A.; Yan, J.; Lampen-Kelley, P.; May, A. F.; Cooper, V. R.; Lindsay, L.; Puretzky, A.; Liang, L.; Kc, S.; Cakmak, E.; et al. High-Temperature Magnetostructural Transition in van der Waals-Layered α−$MoCl_3$. *Phys. Rev. Materials* **2017**, *1*, 064001.

(824) Bärnighausen, H.; Handa, B. K. Die Kristallstruktur von Rhodium(III)-chlorid. *J. Less Common Met.* **1964**, *6*, 226–231.

(825) Brodersen, K.; Thiele, G.; Recke, I. Strukturuntersuchungen an Rhodiumhalogeniden. *J. Less Common Met.* **1968**, *14*, 151–152.

(826) Brodersen, K.; Thiele, G.; Ohnsorge, H.; Recke, I.; Moers, F. Die Struktur des $IrBr_3$ und über die Ursachen der Fehlordnungserscheinungen bei den in Schichtenstrukturen Kristallisierenden Edelmetalltrihalogeniden. *J. Less Common Met.* **1968**, *15*, 347–354.

(827) Wang, F.; Zhang, Z.; Zhang, Y.; Nie, A.; Zhao, W.; Wang, D.; Huang, F.; Zhai, T. Honeycomb $RhI_3$ Flakes with High Environmental Stability for Optoelectronics. *Adv. Mater.* **2020**, *32*, 001979.

(828) Kadioglu, Y.; Ozdemir, I.; Aktürk, O. Ü.; Gökoğlu, G.; Akıncı, Ü.; Aktürk, E. Tuning the Electronic Structure of $RhX_3$ (X = Cl, Br, I) Nonmagnetic Monolayers: Effects of Charge-Injection and External Strain. *Phys. Chem. Chem. Phys.* **2020**, *22*, 4561–4573.

(829) Ersan, F.; Vatansever, E.; Sarikurt, S.; Yüksel, Y.; Kadioglu, Y.; Ozaydin, H. D.; Aktürk, O. Ü.; Akıncı, Ü.; Aktürk, E. Exploring the Electronic and Magnetic Properties of New

Metal Halides from Bulk to Two-Dimensional Monolayer: $RuX_3$ (X = Br, I). *J. Magn. Magn. Mater.* **2019**, *476*, 111–119.

(830) Huang, C.; Zhou, J.; Wu, H.; Deng, K.; Jena, P.; Kan, E. Quantum Anomalous Hall Effect in Ferromagnetic Transition Metal Halides. *Phys. Rev. B* **2017**, *95*, 045113.

(831) Sun, Q.; Kioussis, N. Prediction of Manganese Trihalides as Two-Dimensional Dirac Half-Metals. *Phys. Rev. B* **2018**, *97*, 094408.

(832) He, J.; Li, X.; Lyu, P.; Nachtigall, P. Near-Room-Temperature Chern Insulator and Dirac Spin-Gapless Semiconductor: Nickel Chloride Monolayer. *Nanoscale* **2017**, *9*, 2246–2252.

(833) Li, Z.; Zhou, B.; Luan, C. Strain-Tunable Magnetic Anisotropy in Two-Dimensional Dirac Half-Metals: Nickel Trihalides. *RSC Adv.* **2019**, *9*, 35614–35623.

(834) Liu, J.; Chen, X.; Huang, Y.; Yuan, H.; Chen, H. Thermoelectric Properties of $NiCl_3$ Monolayer: A First-Principles-Based Transport Study. *Nanomaterials* **2020**, *10*, 411.

(835) Wang, Y.; Li, S.; Zhang, C.; Zhang, S.; Ji, W.; Li, P.; Wang, P. High-Temperature Dirac Half-Metal $PdCl_3$: A Promising Candidate for Realizing Quantum Anomalous Hall Effect. *J. Mater. Chem. C* **2018**, *6*, 10284–10291.

(836) Bafekry, A.; Stampfl, C.; Peeters, F. M. Dirac Half-Metallicity of Thin $PdCl_3$ Nanosheets: Investigation of the Effects of External Fields, Surface Adsorption and Defect Engineering on the Electronic and Magnetic Properties. *Sci. Rep.* **2020**, *10*, 213.

(837) You, J.-Y.; Zhang, Z.; Gu, B.; Su, G. Two-Dimensional Room-Temperature Ferromagnetic Semiconductors with Quantum Anomalous Hall Effect. *Phys. Rev. Applied* **2019**, *12*, 024063.

(838) You, J. Y.; Chen, C.; Zhang, Z.; Sheng, X. L.; Yang, S. Y. A.; Su, G. Two-Dimensional Weyl Half-Semimetal and Tunable Quantum Anomalous Hall Effect. *Phys. Rev. B* **2019**, *100*, 064408.

(839) Troyanov, S.; Ionov, V.; Rybakov, V. The Synthesis and Crystal Structures of $TiBr_4$, $TiBr_3$, and $Ti(AlBr_4)_2$. *Žurnal Neorganičeskoj Himii* **1990**, *35*, 882–887.

(840) Klemm, W.; Krose, E. Die Kristallstrukturen von $ScCl_3$, $TiCl_3$ und $VCl_3$. *Z. Anorg. Chem.* **1947**, *253*, 218–225.

(841) Morosin, B.; Narath, A. X-Ray Diffraction and Nuclear Quadrupole Resonance Studies of Chromium Trichloride. *J. Chem. Phys.* **1964**, *40*, 1958–1967.

(842) Gao, Y.; Wang, J.; Li, Y.; Xia, M.; Li, Z.; Gao, F. Point-Defect-Induced Half Metal in $CrCl_3$ Monolayer. *Phys. Status Solidi RRL* **2018**, *12*, 1800105.

(843) Lu, X.; Fei, R.; Yang, L. Meron-Like Topological Spin Defects in Monolayer $CrCl_3$. **2020**, *Nat. Commun.* **2020**, *11*, 4724.

(844) Handy, L. L.; Gregory, N. W. Structural Properties of Chromium(III) Iodide and Some Chromium(III) Mixed Halides. *J. Am. Chem. Soc.* **1952**, *74*, 891–893.

(845) Yang, J.; Wang, J.; Liu, Q.; Xu, R.; Sun, Y.; Li, Z.; Gao, F.; Xia, M. Band Engineering in Intrinsically Magnetic $CrBr_3$ Monolayer. *J. Magn. Magn. Mater.* **2020**, *502*, 166608.

(846) Gao, Y.; Wang, J.; Li, Z.; Yang, J.; Xia, M.; Hao, X.; Xu, Y.; Gao, F. On the Ferromagnetism and Band Tailoring of $CrI_3$ Single Layer. *Phys. Status Solidi RRL* **2019**, *13*, 1800410.

(847) Kashin, I. V.; Mazurenko, V. V.; Katsnelson, M. I.; Rudenko, A. N. Orbitally-Resolved Ferromagnetism of Monolayer $CrI_3$. *2D Mater.* **2020**, *7*, 025036.

(848) Grönke, M.; Pohflepp, D.; Schmidt, P.; Valldor, M.; Oswald, S.; Wolf, D.; Hao, Q.; Steiner, U.; Büchner, B.; Hampel, S. Simulation and Synthesis of α-$MoCl_3$ Nanosheets on Substrates by Short Time Chemical Vapor Transport. *Nano-Structures & Nano-Objects* **2019**, *19*, 100324.

(849) Armbruster, M.; Ludwig, T.; Rotter, H.; Thiele, G.; Oppermann, H. Über Eisentribromid: Untersuchungen von Gleichgewichten, Kristallstruktur Und Spektroskopische Charakterisierung. *Z. Anorg. Allg. Chem.* **2000**, *626*, 187–195.

(850) Tian, Y.; Gao, W.; Henriksen, E. A.; Chelikowsky, J. R.; Yang, L. Optically Driven Magnetic Phase Transition of Monolayer $RuCl_3$. *Nano Lett.* **2019**, *19*, 7673–7680.

(851) Sarikurt, S.; Kadioglu, Y.; Ersan, F.; Vatansever, E.; Aktürk, O. Ü.; Yüksel, Y.; Akıncı, Ü.; Aktürk, E. Electronic and Magnetic Properties of Monolayer α-$RuCl_3$ : A First-Principles and Monte Carlo Study. *Phys. Chem. Chem. Phys.* **2018**, *20*, 997–1004.

(852) Niu, B.; Su, T.; Francisco, B. A.; Ghosh, S.; Kargar, F.; Huang, X.; Lohmann, M.; Li, J.; Xu, Y.; Taniguchi, T.; et al. Coexistence of Magnetic Orders in Two-Dimensional Magnet $CrI_3$. *Nano Lett.* **2020**, *20*, 553–558.

(853) Li, S.; Ye, Z.; Luo, X.; Ye, G.; Kim, H. H.; Yang, B.; Tian, S.; Li, C.; Lei, H.; Tsen, A. W.; et al. Magnetic-Field-Induced Quantum Phase Transitions in a van der Waals Magnet. *Phys. Rev. X* **2020**, *10*, 011075.

(854) Song, T.; Fei, Z.; Yankowitz, M.; Lin, Z.; Jiang, Q.; Hwangbo, K.; Zhang, Q.; Sun, B.; Taniguchi, T.; Watanabe, K.; et al. Switching 2D Magnetic States via Pressure Tuning of Layer Stacking. *Nat. Mater.* **2019**, *18*, 1298–1302.

(855) Li, T.; Jiang, S.; Sivadas, N.; Wang, Z.; Xu, Y.; Weber, D.; Goldberger, J. E.; Watanabe, K.; Taniguchi, T.; Fennie, C. J.; et al. Pressure-Controlled Interlayer Magnetism in Atomically Thin $CrI_3$. *Nat. Mater.* **2019**, *18*, 1303–1308.

(856) Leon, A.; González, J.; de Lima, F. D. C.; Mejia, J.; Suarez Morell, E. Strain-Induced Phase Transition in $CrI_3$ Bilayers. *2D Mater.* **2020**, *7*, 035008.

(857) Pizzochero, M.; Yazyev, O. V. Inducing Magnetic Phase Transitions in Monolayer $CrI_3$ *via* Lattice Deformations. *J. Phys. Chem. C* **2020**, *124*, 7585–7590.

(858) Yang, B.; Zhang, X.; Yang, H.; Han, X.; Yan, Y. Strain Controlling Transport Properties of Heterostructure Composed of Monolayer $CrI_3$. *Appl. Phys. Lett.* **2019**, *114*, 192405.

(859) Jiang, S.; Xie, H.; Shan, J.; Mak, K. F. Exchange Magnetostriction in Two-Dimensional Antiferromagnets. *Nat. Mater.* **2020**, *19*, 1295–1299.

(860) Bastien, G.; Garbarino, G.; Yadav, R.; Martinez-Casado, F. J.; Beltrán Rodríguez, R.; Stahl, Q.; Kusch, M.; Limandri, S. P.; Ray, R.; Lampen-Kelley, P.; et al. Pressure-Induced Dimerization and Valence Bond Crystal Formation in the Kitaev-Heisenberg Magnet α−$RuCl_3$. *Phys. Rev. B* **2018**, *97*, 241108.

(861) Li, G.; Chen, X.; Gan, Y.; Li, F.; Yan, M.; Ye, F.; Pei, S.; Zhang, Y.; Wang, L.; Su, H.; et al. Raman Spectroscopy Evidence for Dimerization and Mott Collapse in α−$RuCl_3$ under Pressures. *Phys. Rev. Materials* **2019**, *3*, 023601.

(862) Rodriguez-Vega, M.; Lin, Z.-X.; Leonardo, A.; Ernst, A.; Chaudhary, G.; Vergniory, M. G.; Fiete, G. A. Phonon-Mediated Dimensional Crossover in Bilayer $CrI_3$. *Phys. Rev. B* **2020**, *102*, 081117.

(863) Tartaglia, T. A.; Tang, J. N.; Lado, J. L.; Bahrami, F.; Abramchuk, M.; McCandless, G. T.; Doyle, M. C.; Burch, K. S.; Ran, Y.; Chan, J. Y.; et al. Accessing New Magnetic Regimes by Tuning the Ligand Spin-Orbit Coupling in van der Waals Magnets. *Sci. Adv.* **2020**, *6*, eabb9379.

(864) Bastien, G.; Roslova, M.; Haghighi, M. H.; Mehlawat, K.; Hunger, J.; Isaeva, A.; Doert, T.; Vojta, M.; Büchner, B.; Wolter, A. U. B. Spin-Glass State and Reversed Magnetic Anisotropy Induced by Cr Doping in the Kitaev Magnet α−$RuCl_3$. *Phys. Rev. B* **2019**, *99*, 214410.

(865) Weber, D.; Schoop, L. M.; Duppel, V.; Lippmann, J. M.; Nuss, J.; Lotsch, B. V. Magnetic Properties of Restacked 2D Spin 1/2 Honeycomb $RuCl_3$ Nanosheets. *Nano Lett.* **2016**, *16*, 3578–3584.

(866) Imai, Y.; Konno, K.; Hasegawa, Y.; Aoyama, T.; Ohgushi, K. Hydrated Lithium Intercalation into the Kitaev Spin Liquid Candidate Material A−$RuCl_3$. *Phys. Rev. B* **2019**, *99*, 245141.

(867) Guo, Y.; Yuan, S.; Wang, B.; Shi, L.; Wang, J. Half-Metallicity and Enhanced Ferromagnetism in Li-Adsorbed Ultrathin Chromium Triiodide. *J. Mater. Chem. C* **2018**, *6*, 5716–5720.

(868) Huang, C.; Du, Y.; Wu, H.; Xiang, H.; Deng, K.; Kan, E. Prediction of Intrinsic Ferromagnetic Ferroelectricity in a Transition-Metal Halide Monolayer. *Phys. Rev. Lett.* **2018**, *120*, 147601.

(869) Klein, D. R.; MacNeill, D.; Song, Q.; Larson, D. T.; Fang, S.; Xu, M.; Ribeiro, R. A.; Canfield, P. C.; Kaxiras, E.; Comin, R.; et al. Enhancement of Interlayer Exchange in an Ultrathin Two-Dimensional Magnet. *Nature Physics* **2019**, *15*, 1255–1260.

(870) McGuire, M. A.; Zheng, Q.; Yan, J.; Sales, B. C. Chemical Disorder and Spin-Liquid-like Magnetism in the van der Waals Layered 5 d Transition Metal Halide $Os_{0.55}Cl_2$. *Phys. Rev. B* **2019**, *99*, 214402.

(871) Sheng, X.-L.; Nikolić, B. K. Monolayer of the 5 d Transition Metal Trichloride $OsCl_3$: A Playground for Two-Dimensional Magnetism, Room-Temperature Quantum Anomalous Hall Effect, and Topological Phase Transitions. *Phys. Rev. B* **2017**, *95*, 201402.

(872) McGuire, M. A.; Sales, B. C. Spin-Glass Behavior and Vacancy Order in van der Waals Layered β−$MoCl_4$. *Phys. Rev. Materials* **2018**, *2*, 074007.

(873) Kennedy, J. R.; Simon, A. Chemical Intercalation of Sodium into Niobium Chloride, α-$Nb_3Cl_8$. *Inorg. Chem.* **1991**, *30*, 2564–2567.

(874) Kennedy, J. R.; Adler, P.; Dronskowski, R.; Simon, A. Experimental and Theoretical Electronic Structure Investigations on α-$Nb_3Cl_8$ and the Intercalated Phase β-$NaNb_3Cl_8$. *Inorg. Chem.* **1996**, *35*, 2276–2282.

(875) v. Schnering, H.-G.; Wöhrle, H.; Schäfer, H. Die Kristallstruktur der Verbindung $Nb_3Cl_8$. *Naturwissenschaften* **1961**, *48*, 159.

(876) Pasco, C. M.; El Baggari, I.; Bianco, E.; Kourkoutis, L. F.; McQueen, T. M. Tunable Magnetic Transition to a Singlet Ground State in a 2D van der Waals Layered Trimerized Kagomé Magnet. *ACS Nano* **2019**, *13*, 9457–9463.

(877) Habermehl, K.; Meyer, G. Triniobiumoctabromide, $Nb_3Br_8$, Revisited. *Zeitschrift für Naturforschung B* **2010**, *65*, 770–772.

(878) Sheckelton, J. P.; Plumb, K. W.; Trump, B. A.; Broholm, C. L.; McQueen, T. M. Rearrangement of van der Waals Stacking and Formation of a Singlet State at T = 90 K in a Cluster Magnet. *Inorg. Chem. Front.* **2017**, *4*, 481–490.

(879) Haraguchi, Y.; Michioka, C.; Ishikawa, M.; Nakano, Y.; Yamochi, H.; Ueda, H.; Yoshimura, K. Magnetic–Nonmagnetic Phase Transition with Interlayer Charge Disproportionation of $Nb_3$ Trimers in the Cluster Compound $Nb_3Cl_8$. *Inorg. Chem.* **2017**, *56*, 3483–3488.

(880) Yoon, J.; Lesne, E.; Sklarek, K.; Sheckelton, J.; Pasco, C.; Parkin, S.; McQueen, T. M.; Ali, M. N. Anomalous Thickness-Dependent Electrical Conductivity in van der Waals Layered Transition Metal Halide, $Nb_3Cl_8$. *J. Phys.: Condens. Matter* **2020**, *32*, 304004.

(881) Kim, B. J.; Jeong, B. J.; Oh, S.; Chae, S.; Choi, K. H.; Nanda, S. S.; Nasir, T.; Lee, S. H.; Kim, K.-W.; Lim, H. K.; et al. Structural and Electrical Properties of $Nb_3I_8$ Layered Crystal. *Phys. Status Solidi RRL* **2019**, *13*, 1800448.

(882) Oh, S.; Choi, K. H.; Chae, S.; Kim, B. J.; Jeong, B. J.; Lee, S. H.; Jeon, J.; Kim, Y.; Nanda, S. S.; Shi, L.; et al. Large-Area Synthesis of van der Waals Two-Dimensional Material $Nb_3I_8$ and Its Infrared Detection Applications. *J. Alloys Compd.* **2020**, *831*, 154877.

(883) Jiang, J.; Liang, Q.; Meng, R.; Yang, Q.; Tan, C.; Sun, X.; Chen, X. Exploration of New Ferromagnetic, Semiconducting and Biocompatible $Nb_3X_8$ (X = Cl, Br or I) Monolayers with Considerable Visible and Infrared Light Absorption. *Nanoscale* **2017**, *9*, 2992–3001.

(884) Conte, F.; Ninno, D.; Cantele, G. Layer-Dependent Electronic and Magnetic Properties of $Nb_3I_8$. *Phys. Rev. Research* **2020**, *2*, 033001.

(885) Xiao, H.; Wang, X.; Wang, R.; Xu, L.; Liang, S.; Yang, C. Intrinsic Magnetism and Biaxial Strain Tuning in Two-Dimensional Metal Halides $V_3X_8$ (X = F, Cl, Br, I) from First Principles and Monte Carlo Simulation. *Phys. Chem. Chem. Phys.* **2019**, *21*, 11731–11739.

(886) Willmott, P. R.; Huber, J. R. Pulsed Laser Vaporization and Deposition. *Rev. Mod. Phys.* **2000**, *72*, 315–328.

(887) Holdren, J. P. Materials Genome Initiative for Global Competitiveness. National Science and Technology Council and Office of Science and Technology Policy, **2011**.

(888) Alberi, K.; Nardelli, M. B.; Zakutayev, A.; Mitas, L.; Curtarolo, S.; Jain, A.; Fornari, M.; Marzari, N.; Takeuchi, I.; Green, M. L.; et al. The 2019 Materials by Design Roadmap. *J. Phys. D: Appl. Phys.* **2019**, *52*, 013001.

(889) Oganov, A. R.; Pickard, C. J.; Zhu, Q.; Needs, R. J. Structure Prediction Drives Materials Discovery. *Nat. Rev. Mater.* **2019**, *4*, 331–348.

(890) Mounet, N.; Gibertini, M.; Schwaller, P.; Campi, D.; Merkys, A.; Marrazzo, A.; Sohier, T.; Castelli, I. E.; Cepellotti, A.; Pizzi, G.; et al. Two-Dimensional Materials from High-Throughput Computational Exfoliation of Experimentally Known Compounds. *Nature Nanotech.* **2018**, *13*, 246–252.

(891) Schleder, G. R.; Acosta, C. M.; Fazzio, A. Exploring Two-Dimensional Materials Thermodynamic Stability via Machine Learning. *ACS Appl. Mater. Interfaces* **2019**, *12*, 20149–20157.

(892) Zhu, Z.; Cai, X.; Yi, S.; Chen, J.; Dai, Y.; Niu, C.; Guo, Z.; Xie, M.; Liu, F.; Cho, J.-H.; et al. Multivalency-Driven Formation of Te-Based Monolayer Materials: A Combined First-Principles and Experimental Study. *Phys. Rev. Lett.* **2017**, *119*, 106101.

(893) Liu, D.; Lin, X.; Tománek, D. Microscopic Mechanism of the Helix-to-Layer Transformation in Elemental Group VI Solids. *Nano Lett.* **2018**, *18*, 4908–4913.

(894) Ashton, M.; Sinnott, S. B.; Hennig, R. G. Computational Discovery and Characterization of Polymorphic Two-Dimensional IV–V Materials. *Appl. Phys. Lett.* **2016**, *109*, 192103.

(895) Lin, J.-H.; Zhang, H.; Cheng, X.-L.; Miyamoto, Y. Single-Layer Group IV-V and Group V-IV-III-VI Semiconductors: Structural Stability, Electronic Structures, Optical Properties, and Photocatalysis. *Phys. Rev. B* **2017**, *96*, 035438.

(896) Özdamar, B.; Özbal, G.; Çınar, M. N.; Sevim, K.; Kurt, G.; Kaya, B.; Sevinçli, H. Structural, Vibrational, and Electronic Properties of Single-Layer Hexagonal Crystals of Group IV and V Elements. *Phys. Rev. B* **2018**, *98*, 045431.

(897) Sorokin, P. B.; Kvashnin, A. G.; Zhu, Z.; Tománek, D. Spontaneous Graphitization of Ultrathin Cubic Structures: A Computational Study. *Nano Lett.* **2014**, *14*, 7126–7130.

(898) Farrow, R. F. C. The Stabilization of Metastable Phases by Epitaxy. *J. Vac. Sci. Technol. B* **1983**, *1*, 222.

(899) Al Balushi, Z. Y.; Wang, K.; Ghosh, R. K.; Vilá, R. A.; Eichfeld, S. M.; Caldwell, J. D.; Qin, X.; Lin, Y.-C.; DeSario, P. A.; Stone, G.; et al. Two-Dimensional Gallium Nitride Realized via Graphene Encapsulation. *Nature Mater.* **2016**, *15*, 1166–1171.

(900) Gonzalez, M. I.; Turkiewicz, A. B.; Darago, L. E.; Oktawiec, J.; Bustillo, K.; Grandjean, F.; Long, G. J.; Long, J. R. Confinement of Atomically Defined Metal Halide Sheets in a Metal-Organic Framework. *Nature* **2020**, *577*, 64–68.

(901) Liu, L.; Wu, J.; Wu, L.; Ye, M.; Liu, X.; Wang, Q.; Hou, S.; Lu, P.; Sun, L.; Zheng, J.; et al. Phase-Selective Synthesis of 1T′ $MoS_2$ Monolayers and Heterophase Bilayers. *Nature Mater.* **2018**, *17*, 1108–1114.

(902) Fu, Y.; Rea, M. T.; Chen, J.; Morrow, D. J.; Hautzinger, M. P.; Zhao, Y.; Pan, D.; Manger, L. H.; Wright, J. C.; Goldsmith, R. H.; et al. Selective Stabilization and Photophysical Properties of Metastable Perovskite Polymorphs of $CsPbI_3$ in Thin Films. *Chem. Mater.* **2017**, *29*, 8385–8394.

(903) Gupta, S. K.; Sudarshan, K.; Ghosh, P. S.; Mukherjee, S.; Kadam, R. M. Doping-Induced Room Temperature Stabilization of Metastable β-$Ag_2WO_4$ and Origin of Visible Emission in α- and β-$Ag_2WO_4$: Low Temperature Photoluminescence Studies. *J. Phys. Chem. C* **2016**, *120*, 7265–7276.

(904) Rastogi, C. K.; Sharma, S. K.; Patel, A.; Parthasarathy, G.; Pala, R. G. S.; Kumar, J.; Sivakumar, S. Dopant Induced Stabilization of Metastable Zircon-Type Tetragonal $LaVO_4$. *J. Phys. Chem. C* **2017**, *121*, 16501–16512.

(905) Holder, A. M.; Siol, S.; Ndione, P. F.; Peng, H.; Deml, A. M.; Matthews, B. E.; Schelhas, L. T.; Toney, M. F.; Gordon, R. G.; Tumas, W.; et al. Novel Phase Diagram Behavior and Materials Design in Heterostructural Semiconductor Alloys. *Sci. Adv.* **2017**, *3*, e1700270.

(906) Siol, S.; Holder, A.; Steffes, J.; Schelhas, L. T.; Stone, K. H.; Garten, L.; Perkins, J. D.; Parilla, P. A.; Toney, M. F.; Huey, B. D.; et al. Negative-Pressure Polymorphs Made by Heterostructural Alloying. *Sci. Adv.* **2018**, *4*, eaaq1442.

(907) Fu, Y.; Wu, T.; Wang, J.; Zhai, J.; Shearer, M. J.; Zhao, Y.; Hamers, R. J.; Kan, E.; Deng, K.; Zhu, X.-Y.; et al. Stabilization of the Metastable Lead Iodide Perovskite Phase via Surface Functionalization. *Nano Lett.* **2017**, *17*, 4405–4414.

(908) Tomada, J.; Dienel, T.; Hampel, F.; Fasel, R.; Amsharov, K. Combinatorial Design of Molecular Seeds for Chirality-Controlled Synthesis of Single-Walled Carbon Nanotubes. *Nat. Commun.* **2019**, *10*, 3278.

(909) Wittkamper, J.; Xu, Z.; Kombaiah, B.; Ram, F.; De Graef, M.; Kitchin, J. R.; Rohrer, G. S.; Salvador, P. A. Competitive Growth of Scrutinyite ($\alpha$-$PbO_2$) and Rutile Polymorphs of $Sn_2$ on All Orientations of Columbite $CoNb_2O_6$ Substrates. *Cryst. Growth Des.* **2017**, *17*, 3929–3939.

(910) Cho, S.; Kim, S.; Kim, J. H.; Zhao, J.; Seok, J.; Keum, D. H.; Baik, J.; Choe, D.-H.; Chang, K. J.; Suenaga, K.; et al. Phase Patterning for Ohmic Homojunction Contact in $MoTe_2$. *Science* **2015**, *349*, 625–628.

(911) Guan, J.; Zhu, Z.; Tománek, D. High Stability of Faceted Nanotubes and Fullerenes of Multiphase Layered Phosphorus: A Computational Study. *Phys. Rev. Lett.* **2014**, *113*, 226801.

(912) Watts, M. C.; Picco, L.; Russell-Pavier, F. S.; Cullen, P. L.; Miller, T. S.; Bartuś, S. P.; Payton, O. D.; Skipper, N. T.; Tileli, V.; Howard, C. A. Production of Phosphorene Nanoribbons. *Nature* **2019**, *568*, 216–220.

(913) Liu, Y.; Huang, Y.; Duan, X. Van der Waals Integration before and beyond Two-Dimensional Materials. *Nature* **2019**, *567*, 323–333.

(914) Fan, S.; Vu, Q. A.; Tran, M. D.; Adhikari, S.; Lee, Y. H. Transfer Assembly for Two-Dimensional van der Waals Heterostructures. *2D Mater.* **2020**, *7*, 022005.

(915) Kozhakhmetov, A.; Torsi, R.; Chen, C. Y.; Robinson, J. A. Scalable Low-Temperature Synthesis of Two-Dimensional Materials beyond Graphene. *J. Phys. Mater.* **2020**, *4*, 012001.

(916) Liu, F.; Wu, W.; Bai, Y.; Chae, S. H.; Li, Q.; Wang, J.; Hone, J.; Zhu, X.-Y. Disassembling 2D van der Waals Crystals into Macroscopic Monolayers and Reassembling into Artificial Lattices. *Science* **2020**, *367*, 903–906.

(917) Zhu, L.; Lu, Y.; Wang, L. Tuning Ferroelectricity by Charge Doping in Two-Dimensional SnSe. *J. Appl. Phys.* **2020**, *127*, 014101.

(918) Liu, C.; Guan, S.; Yin, H.; Wan, W.; Wang, Y.; Zhang, Y. γ-GeSe: A Two-Dimensional Ferroelectric Material with Doping-Induced Ferromagnetism. *Appl. Phys. Lett.* **2019**, *115*, 252904.

(919) Ji, Y.; Yang, M.; Dong, H.; Hou, T.; Wang, L.; Li, Y. Two-Dimensional Germanium Monochalcogenide Photocatalyst for Water Splitting under Ultraviolet, Visible to Near-Infrared Light. *Nanoscale* **2017**, *9*, 8608–8615.

(920) Cheema, S. S.; Kwon, D.; Shanker, N.; dos Reis, R.; Hsu, S.-L.; Xiao, J.; Zhang, H.; Wagner, R.; Datar, A.; McCarter, M. R.; et al. Enhanced Ferroelectricity in Ultrathin Films Grown Directly on Silicon. *Nature* **2020**, *580*, 478–482.

(921) Pandya, S.; Martin, L. W. Epitaxy on Polycrystalline Substrates. *Science* **2017**, *358*, 587–588.

(922) Tan, Z.; Yin, J.; Chen, C.; Wang, H.; Lin, L.; Sun, L.; Wu, J.; Sun, X.; Yang, H.; Chen, Y.; et al. Building Large-Domain Twisted Bilayer Graphene with van Hove Singularity. *ACS Nano* **2016**, *10*, 6725–6730.